Influence of the Reactor Coil Material on Coke Formation during Steam Cracking of Hydrocarbons

Invloed van het reactormateriaal op de cokesvorming tijdens het stoomkraken van koolwaterstoffen

Andres Muñoz Gandarillas

Promotoren: prof. dr. ir. G. B. Marin, prof. dr. M.-F. Reyniers
Proefschrift ingediend tot het behalen van de graad van
Doctor in de Ingenieurswetenschappen: Chemische Technologie

Vakgroep Chemische Proceskunde en Technische Chemie
Voorzitter: prof. dr. ir. G. B. Marin
Faculteit Ingenieurswetenschappen en Architectuur
Academiejaar 2014 - 2015

UNIVERSITEIT
GENT

ISBN 978-90-8578-733-4
NUR 952
Wettelijk depot: D/2014/10.500/79

Promotoren:

prof. dr. ir. Guy B. Marin
Laboratorium voor Chemische Technologie
Vakgroep Chemische Proceskunde en Technische Chemie
Universiteit Gent

prof. dr. Marie-Françoise Reyniers
Laboratorium voor Chemische Technologie
Vakgroep Chemische Proceskunde en Technische Chemie
Universiteit Gent

Decaan: Prof. dr. ir. Rik Van de Walle

Rector: Prof. dr. Anne De Paepe

De auteur genoot tijdens de onderzoeksactiviteiten de steun van de langdurige en structurele *Methusalem* financiering van de Vlaamse Overheid [BOF09/01M00409].

EXAMENCOMMISSIE

Leescommissie

Prof. dr. Marie-Françoise Reyniers [promotor]
Vakgroep Chemische Proceskunde en Chemische Technologie
Faculteit Ingenieurswetenschappen en Architectuur
Universiteit Gent

Prof. dr. ir. Geraldine Heynderickx
Laboratorium voor Chemische Technologie
Vakgroep Chemische Proceskunde en Technische Chemie
Universiteit Gent

Prof. dr. Kim Verbeken
Vakgroep Toegepaste Materiaalwetenschappen
Faculteit Ingenieurswetenschappen en Architectuur
Universiteit Gent

Dr. Ir. Valérie Vanrysselberghe
Département Procédés Raffinage & Base Chem
TOTAL Research & Technology Feluy

Prof. Dr. Ing. Nicolas Gascoin
PRISME Laboratory, Pyrolysis and Propulsion group
INSA, Centre Val de Loire

Andere leden

Prof. dr. ir. Guy B. Marin [promotor]
Laboratorium voor Chemische Technologie
Vakgroep Chemische Proceskunde en Technische Chemie
Universiteit Gent

Prof. dr. ir. Kevin Van Geem
Laboratorium voor Chemische Technologie
Vakgroep Chemische Proceskunde en Technische Chemie
Universiteit Gent

Prof. dr. ir. Hendrik Van Landeghem [voorzitter]
Vakgroep Technische Bedrijfsvoering
Universiteit Gent

A mis padres…

Acknowledgements:

I would like to start thanking God, for having taken me to this moment through such an amazing journey.

I want to thank my promotors Prof. Guy B. Marin and Prof. Marie-Françoise Reyniers. You gave me a great opportunity, and guided me exceptionally well through my thesis. I also want to thank you for all the effort you made to correct and improve this text.

I also want to thank Prof. Van Geem. Kevin, you have not only been a great influence on my work and a great reviewer for my texts, but also a model to follow and a friend. Thank you for all the help and encouragement, back from the days when I was just an intern at the lab.

The people from the industrial partner of this project deserve also great recognition. The interaction I had with you was very enriching for my research and professional life.

Quiero además agradecer a mis padres y abuela. Sé que este doctorado también fue duro para ustedes, pero siempre estuvieron allí para darme apoyo, fuerza y motivación para seguir adelante. Sin su cariño y la formación que me brindaron esto nunca hubiera sido posible. ¡Esta tesis va dedicada a ustedes!

Ik moet natuurlijk ook de technici en administratief personeel van het LCT bedanken. Het is jullie hulp die ervoor zorgt dat onze experimenten goed lopen. Dankzij jullie sympathie en steun kan ik jullie nu ook in het Nederlands bedanken.

I also want to mention Thomas, José, Matthias, Mathias and Emma. Coaching your theses and working with you was a great experience. I hope you learned from me as much as I learned from you.

I would also like to thank all the colleagues I met at LCT, who gave me support, great discussions, good professional and personal advice and, especially, amazing friendships. Marcel, Nick, Aäron, Kostas, Maarten, Gonzalo, Jelena, Steven, Carl, Panos, Maria, Thomas, Amit, Kaustav, Marko, Nenad, Ruben, Ruben, Natalia, Pieter, Aditya, Stamatis, Yu, Hassan, Marita…

I also have to thank all the great people I have met during these years in Gent, to whom I now have the honor of referring to as friends. Damian and Magda, not only were you my flatmates but, more importantly, the best friends one could imagine. Fabian, Lindsey, Germán, Peter, Dirk, Alex, Hendrik, Stefanie, Isa... So many names come to mind that I cannot type them all. A big thanks to you all for leaving a great mark in my personal life during my PhD, and for allowing me to know more about the world through you. Simón, Daniel, Juan y Juan también deben ser mencionados. Ustedes han sido mis amigos de la vida y, a pesar de la distancia, han sido y serán siempre mis hermanos.

Ik wil ook België en de stad Gent bedanken. Het was een unieke ervaring om mijn doctoraat te hebben gedaan in zo een fantastische omgeving.

Gracias, bedankt, dziękuję, danke, ďakujem, хвала, ευχαριστώ, 谢谢, धन्यवाद… Thanks for being part of the best experience of my life so far!

Andrés E. Muñoz G.
Gent, 2014

Contents

Notation

Roman

A	Pre-exponential factor of a reaction with order n	$[kg \cdot s^{-1} \cdot m^{-2} \cdot m_r^{3n} \cdot mol^{-n}]$
A_i	Peak area of compound i on a chromatogram.	
^{14}C	Carbon-14	
C_i	Concentration of component i	$[mol \cdot m^{-3}]$
D	Penetration depth	[m]
Ea	Activation energy	$[kJ \cdot mol^{-1}]$
Ei	Activation energy for reaction i	$[kJ \cdot mol^{-1}]$
F_i	Mass flow rate of component i	$[kg \cdot s^{-1}]$
f_i	Relative response factor for component i	
h	Nominal thickness of coke layer	[m]
h_{fil}	Height of catalytic coke filaments	[m]
i CC	Coked coupon after i coking-decoking cycles	
i^{th} CC	Coking-decoking cycle number i	
k	Coking rate coefficient	$[kg \cdot s^{-1} \cdot m^{-2} \cdot m_r^{3n} \cdot mol^{-n}]$
m_c	Mass of catalytic cokes	$[kg \cdot m^{-2}]$
M_i	Molecular mass of compound i	$[kg \cdot mol^{-1}]$

m_f	Experimentally measured mass of coke after 6-hour cracking	[kg]
m_{tj}	Mass of coke registered at time j	[kg]
n	Reaction order	
N_{Ci}	Number of carbon atoms in a molecule of compound i	
P	Pressure	[Pa]
preox	Coupon after preoxidation	
R	Universal gas constant	8.314 [$J \cdot mol^{-1} \cdot K^{-1}$]
R•	Surface radical	
R_a	Mean surface roughness	[μm]
R_c	Coking rate	[$kg \cdot s^{-1} \cdot m^{-2}$]
$R_{c,asym}$	Asymptotic coking rate	[$kg \cdot s^{-1} \cdot m^{-2}$]
$R_{c,cat}$	Rate of growth of catalytic cokes	[$kg \cdot s^{-1} \cdot m^{-2}$]
$R_{c,init}$	Initial coking rate	[$kg \cdot s^{-1} \cdot m^{-2}$]
S	Surface area of coupon	[m^2]
T	Temperature	[K]
t	Time	[s]
$T_{process,gas}$	Process gas temperature	[K]
T_{wall}	Reactor wall temperature	[K]
X_i	Conversion of component i	[%]

Greek

δ	dilution	[$kg \cdot kg^{-1}$]
σ	Standard deviation	

ρ	Volumetric density	$[kg \cdot m^{-3}]$
τ	Mean residence time	[s]

Acronyms

AGO	Atmospheric gas oil
CIT	Coil inlet temperature
CFD	Computational fluid dynamics
COP	Coil outlet pressure
COT	Coil outlet temperature
CPD	Cyclopentadiene
CSTR	Continuously stirred tank reactor
DFT	Density functional theory
DMDS	Dimethyl disulfide
DMS	Dimethyl sulfide
EDX	Energy dispersive X-ray microscopy
FID	Flame ionization detector
GC	Gas chromatography
HC	Hydrocarbon
HDO	Hydrodeoxygenation
HDO-CTO	Hydrodeoxygenated crude tall oil
HDO-DTO	Hydrodeoxygenated distilled tall oil
HDO-TOFA	Hydrodeoxygenated tall oil fatty acids

HRTEM	High-resolution transmission electron microscopy
JSR	Jet stirred reactor
MFC	Mass flow controller
MOT	Maximum operating temperature
PAH	Polyaromatic hydrocarbons
PFR	Plug-flow reactor
RGA	Refinery gas analyzer
SEM	Scanning electron microscopy
TCD	Thermal conductivity detector
TLE	Transfer line heat exchanger
TMT	Tube metal temperature
VGO	Vacuum gas oil

Subscripts

Arom.	Aromatics
E	Ethylene
Int std	Internal standard
P	Propylene
r	Reactor

Samenvatting

Tegenwoordig is stoomkraken het belangrijkste proces voor de productie van ethyleen en andere waardevolle basischemicaliën. In dit proces worden koolwaterstoffen verdund met stoom gekraakt in tubulaire reactoren vervaardigd uit staallegeringen met een hoge temperatuur resistentie. Een brede waaier aan producten wordt vervaardigd vertrekkende van ethyleen als belangrijkste startmateriaal en dit in verschillende takken van de industrie. Momenteel bedraagt de wereldwijde ethyleenproductie meer dan 150 miljoen ton per jaar en de verwachtingen zijn dat deze zal blijven stijgen in de komende jaren. De meest gebruikte voedingen zijn nafta en ethaan. Cokes is een ongewenst product dat gevormd wordt door bijreacties tijdens kraken. De accumulatie van cokes in de reactor heeft een negatief effect op het proces en dwingt procesoperatoren om de productie op periodieke basis te onderbreken om de reactor te ontkolen. Deze periodes zonder productie hebben een significante impact op de economische rendabiliteit van het proces. Verder hebben de cyclische veranderingen tussen reducerende en oxiderende condities op de lange termijn een negatieve invloed op het reactormateriaal.

De chemische samenstelling van de binnenwand van de reactor heeft een grote invloed op de vormingssnelheid van de cokeslaag. Een aantal metalen die typisch deel uitmaken van de legering, zoals nikkel en ijzer, bevorderen cokesvorming. Deze metalen succesvol isoleren van de binnenwand van de reactor kan dan ook de runlengte verhogen en zodoende de economische rendabiliteit van het proces bevorderen. In het laatste decennium, zijn verscheidene

gespecialiseerde legeringen en coatings ontwikkeld die de cokesvorming trachten te reduceren. Twee types gespecialiseerde oppervlakken kunnen onderscheiden worden, namelijk chromium-mangaan gemengde oxides en alumina lagen.

In deze context, is de doelstelling van dit werk het uitvoeren van een uitgebreide en systematische studie en vergelijking van de weerstand tegen cokesvorming van een reeks nieuwe gespecialiseerde materialen, specifiek ontwikkeld voor stoomkraakreactoren.

Met behulp van een elektrobalans opstelling, beschreven in Hoofdstuk 3, zijn experimenten uitgevoerd met ethaan en nafta als voeding onder industrieel relevante proces condities. Een klein, rechthoekig plaatje (10 mm × 8 mm × 1 mm) wordt geplaatst in een jet-geroerde reactor (JSR) vervaardigd uit kwarts. Het plaatje hangt aan de arm van de elektrobalans zodat het gewicht van het plaatje en dus de hoeveelheid cokes continue gemeten kan worden.

Voordat het kraakexperiment begint, worden de plaatjes in-situ gepreoxideerd, zodat hun oppervlak in dezelfde, geoxideerde toestand is zoals in industriële reactoren het geval is bij aanvang van een nieuwe productiecyclus. De snelheid waarmee cokes zich afzet op de plaatjes verandert continu doorheen de tijd. Bij de start van het experiment, wordt een hoge snelheid waargenomen. Dit is de zogenaamde initiële cokesvormingssnelheid en is een indicatie van vorming van cokes via een katalytisch mechanisme. Naarmate het experiment vordert, vermindert de katalytische cokesvorming doordat de katalytisch actieve metaaldeeltjes ingekapseld worden door cokes en ten gevolge daalt de cokesvormingssnelheid continu tot een constante waarde, de zogenaamde asymptotische snelheid. Door de korte duur van het kraakexperiment (6u), wordt de totale hoeveelheid cokes afgezet op het plaatje bepaald door zowel het katalytische als heterogeen niet-katalytische (radicalaire) mechanisme. Echter, in Hoofdstuk 2 wordt aangetoond dat in industriële reactoren het radicalaire mechanisme veruit het belangrijkste mechanisme is door de

korte duur van het katalytische regime (tussen een aantal uur tot 2 dagen) in vergelijking met de totale runlengte (ongeveer 40 dagen).

Een vergelijking van de experimenteel gemeten cokesvormingssnelheden wordt gemaakt in Hoofdstuk 4 en laat toe een rangschikking te maken van de geteste materialen op basis van hun weerstand tegen cokesvorming. Tien verschillende materialen (gelabeld A tot J) werden getest tijdens het kraken van ethaan. Eén van deze materialen (materiaal A) is een conventionele reactorlegering die als referentiebasis dient. De toegepaste kraaktemperatuur is T = 1159 K en de ethaanconversie is X_{C2H6} = 73%. Materiaal H, een alumina vormende legering, vertoont de hoogste weerstand tegen cokesvorming, gevolgd door materiaal D, een voorbehandelde legering met Cr-Mn oxides aan het oppervlak. De weerstand tegen cokesvorming van materiaal J (een coating aangebracht op een conventionele legering) is zeer gelijkaardig aan die van materiaal A.

Stoomkraakexperimenten met een lichte nafta als voeding werden uitgevoerd om het effect van de voeding op de weerstand tegen cokesvorming te onderzoeken van materiaal D en H (de twee materialen die het meeste weerstand tegen cokesvorming vertoonden tijdens de ethaanexperimenten). Materiaal A werd ook getest als referentiebasis. De gebruikte nafta bevat geen zwavel, aangezien dit element een groot en ietwat onvoorspelbaar effect heeft op de cokesvormingssnelheid. Ook de voorbehandeling van de plaatjes is exact dezelfde als bij de experimenten met ethaan als voeding. Hierdoor is het verschil in cokesvorming exclusief te wijten aan de voeding en de verschillende materiaaleigenschappen. De kraaktemperatuur is T = 1098 K en de propyleen-ethyleen verhouding (P/E) is ongeveer 0.4.

De cokesvormingssnelheden gemeten tijdens het kraken van nafta tonen aan dat, zoals bij de ethaanexperimenten, materiaal H de hoogste weerstand tegen cokesvorming heeft, gevolgd door materiaal D en A. Het verschil in vermindering van de cokesvormingssnelheid door materiaal H

ten opzichte van materiaal A is iets minder uitgesproken bij het kraken van nafta (40%) dan bij het kraken van ethaan (50%).

Om inzicht te krijgen in de chemische samenstelling van de plaatjes, wat helpt de geobserveerde cokesvormingssnelheden te begrijpen, werden rasterelektronenmicroscoop (SEM) en energie-dispersieve X-stralen (EDX) analyses uitgevoerd van het bovenoppervlak en de doorsnede van de plaatjes van materialen A, C, D, G, H en J. De doorsnedes van plaatjes na preoxidatie en na kraken werden geanalyseerd met EDX lijnscans en "element mappings" werden uitgevoerd van de doorsnedes van de plaatjes na kraken.

In Hoofdstuk 4 en 5, werden de plaatjes voor preoxidatie, na preoxidatie en na drie opeenvolgende kraakcycli geanalyseerd. Het oppervlak van de plaatjes verandert significant tijdens oxidatie door de vorming van oxidelagen. Typisch worden Cr, Mn, Al en gemengde oxides (spinels) gevormd aan het oppervlak. Scans van het bovenoppervlak bevestigen dat deze elementen het meest voorkomen aan het oppervlak van de plaatjes na preoxidatie en dat de concentraties van Fe en Ni aan het oppervlak verwaarloosbaar zijn. Thermodynamische berekeningen geven aan dat Cr_2O_3, $MnCr_2O_4$ en Al_2O_3 de meest voorkomende oxides zijn. De vorming van kleine hoeveelheden SiO_2 wordt ook voorspeld. De verhouding van de relatieve concentraties van de oxides en hun uniformiteit van de bedekking van de bulk van de legering varieert over de verschillende materialen.

"Element mappings" van de doorsnedes van de plaatjes na stoomkraken van ethaan en nafta tonen aan dat ook hier, net zoals waargenomen in de plaatjes na preoxidatie, chromium en mangaan de meest voorkomende elementen aan het oppervlak zijn. Het kan dus aangenomen worden dat er tijdens het kraken geen grote veranderingen plaats vinden in de samenstelling aan het oppervlak. Voor de Al-bevattende materialen, wordt een sterke weerstand tegen cokesvorming bereikt door de vorming van een dunne uniforme laag alumina aan het oppervlak

met een onderlaag van mangaan aluminaat. Wanneer de legering geen Al bevat, verstrekt een continue laag van mangaan chromiet een goede bescherming. Een onderlaag van silica bevordert de weerstand tegen cokesvorming verder. Hoewel alumina een goede bescherming tegen cokesvorming verstrekt, kan een excessieve hoeveelheid Al in de legering leiden tot interne oxidatie. Dit is verantwoordelijk voor de lage weerstand tegen cokesvorming van sommige Al-bevattende legeringen.

Verschillende materialen vertonen een verschillende weerstand tegen cokesvorming tijdens het stoomkraken van ethaan of nafta. De vermindering van de cokesvormingssnelheid door toepassing van materiaal H ten opzichte van referentiemateriaal A is 10% lager bij het kraken van nafta dan bij het kraken van ethaan. De voorspelde stijging in runlengte door toepassing van materiaal H ten opzichte van het referentiemateriaal is 100% voor stoomkraken van ethaan en slechts 50% bij stoomkraken van nafta. Dit verklaart waarom de toepassing van gespecialiseerde reactormaterialen in de industrie enkel nuttig geacht wordt bij het kraken van lichte voedingen. Desalniettemin, is de stijging in runlengte significant voor beide voedingen wat het belang van een geschikte materiaalselectie aantoont.

Summary

To date, steam cracking is the most important process for the production of ethylene and other valuable base chemicals. This process involves the high temperature cracking of a hydrocarbon feed using steam as a diluent, and is usually carried out in tubular reactors (radiant coils) constructed of high-temperature steels. A very broad range of products serving different industries are made using ethylene as their main building block. Currently, more than 150 million tons of ethylene are produced annually worldwide, and this value is expected to keep growing in the upcoming years. The dominant feeds for this process are naphthas and ethane.

Coke is an undesired product that forms due to side reactions during cracking. Its accumulation in the reactor coil has an negative effect on the process, and forces operators to halt production regularly to perform decoking operations. The time during which the production is stopped has a significant impact on the economics of the process, and the cyclic changes between reducing and oxidizing conditions age the coil, which affects its long-term performance.

Among other influential parameters, the chemical composition of the internal surface of the reactor coil has a large impact on the rates of coke deposition. Since coke promoting metals, e.g. Ni and Fe, are part of the reactor alloy, successfully isolating them from the surface of the coil can provide large benefits in run length and, consequently, the economics of the process. Various specialized alloys and coatings have been developed in the last decade trying to achieve a

reduction of coking. Mainly two types of specialized surfaces have been subject of interest, which are chromium-manganese mixed oxides, and alumina layers.

In this context, the objective of this work is to carry out an extensive and systematic study and comparison of the resistance to coking of a series of new specialized materials, specifically developed for use in steam cracking coils.

Using an electrobalance setup, described in Chapter 3, ethane and naphtha steam cracking experiments are carried out under a set of industrially representative conditions. Small rectangular coupons (10 mm × 8 mm × 1 mm) are placed inside a quartz jet stirred reactor (JSR), hanging from the arm of an electrobalance. This allows to continuously monitor the mass of the coupons and, consequently, measure the amount of coke depositing over the coupons during cracking operation.

Before being submitted to cracking conditions, the coupons are preoxidized in-situ, so that their surface is in the same oxidized condition as industrial reactors before the start of a cracking run.

The rate at which coke deposits on the surface of the coupons continuously changes with time. At the beginning of the experiments, a high coking rate is observed. This is referred to as the initial coking rate, and it is taken as an indication of the formation of cokes of catalytic origin. As cracking proceeds, the catalytic activity is gradually reduced due to encapsulation of the catalytic metal particles by coke, and the coking rate continuously decreases until it reaches a constant value, the so-called asymptotic rate. Because of the short duration of the cracking experiments (6 hours), the absolute amount of coke deposited on the coupons is determined by the combined action of the catalytic and heterogeneous noncatalytic (radical) mechanisms. However, Chapter 2 shows that for industrial coils the radical mechanism is largely dominant because of the short duration of the catalytic regime (ranging from a few hours up to 2 days) with respect to the absolute run length (40 days).

Comparison of the experimentally measured coking rates is presented in Chapter 4, and allows to rank the tested materials based on their coking resistance. During ethane cracking, ten different materials (labeled A to J) were tested. One of them (material A) is a traditional reactor alloy, which serves as a reference. The cracking temperature is T = 1159 K, and conversion is X_{C2H6} = 73%. Material H, which is an alumina forming alloy, exhibits the highest coking resistance, followed by material D, a pretreated alloy with Cr-Mn oxides on its surface. The coking resistance exhibited by material J (coating applied on top of a regular base alloy) is very similar to that of material A.

In Chapter 5, experiments of steam cracking of a light naphtha are carried out to observe the effect of a different feed on the coking resistance of materials D and H, i.e. the most coke resistant materials during ethane cracking experiments. Material A is also included, to serve as a reference for comparison. The used naphtha is free of sulfur, because this element has a large and somewhat unpredictable impact on the rates of coke deposition. Also the pretreatment of the coupons is exactly the same as the one applied for ethane cracking. The different coking behaviors can be, therefore, attributed only to the change of cracking conditions due to the different feeds, or to the differences between the materials. The temperature is T = 1098 K, and a propylene to ethylene ratio (P/E) of approximately 0.4 is obtained.

The coking rates measured during naphtha cracking experiments reveal that, as was the case for ethane, material H shows the highest coking resistance, followed by material D, and then by material A. The difference in coking rate reduction exhibited by material H compared to material A is only slightly less pronounced (40 %) than during ethane cracking (50 %).

To gain insight into the chemical composition of the coupons, which helps to understand the observed coking behavior, scanning electron microscopy (SEM) and energy dispersive X-ray analyzes (EDX) are performed over the top surface and cross section of coupons of materials A,

C, D, G, H and J. The cross sections of preoxidized and coked coupons are analyzed with EDX line scans, and element mappings are performed for the cross sections of coked coupons.

In Chapters 4 and 5, the coupons are analyzed before preoxidation, after preoxidation, and after three consecutive coking cycles. The surface of the coupons changes significantly after preoxidation compared to their blank state, due to the formation of oxide layers. Typically Cr, Mn and Al oxides form at the surface, as well as mixed oxides (spinels). Top surface scans confirm that these are the most abundant elements at the surface of the preoxidized coupons, and that the concentration of Fe and Ni at the surface is negligible. Thermodynamic calculations suggest that the most common oxides at the surface are Cr_2O_3, $MnCr_2O_4$ and Al_2O_3. Small amounts of SiO_2 are also predicted to form. The ratios of the relative concentrations of the oxides, as well as their uniformity of coverage of the bulk, vary depending on the material.

Element mappings of the cross section of coked coupons (after ethane and naphtha cracking) also show that chromium and manganese are the most abundant elements at the surface, similarly to what is observed after preoxidation. It can therefore be assumed that no major changes take place in the surface composition of the coupons during cracking. For the Al-containing materials, high resistance to coking is achieved by formation of a thin uniform layer of alumina with a sublayer of manganese aluminate covering the coupon. If no Al is present in the alloy, a continuous layer of manganese chromite provides a good protection. A sublayer of silica also enhances the coking resistance. Although alumina provides a good protection against coking, excessive amounts of Al in the alloy can lead to internal oxidation. This phenomenon is responsible for the low coking resistance of some Al-enhanced alloys.

Different materials exhibit different levels of resistance to coking during ethane and naphtha steam cracking. The coking rate reduction of material H compared to material A is 10 % lower during naphtha cracking. However, the predicted run length extension for material H was 100%

for ethane cracking and only 50% for naphtha cracking. This explains why, in industry, specialized coil materials are believed to be useful only for cracking of light feeds. Nevertheless, the run length increase is very significant for both feeds, showing the importance of an adequate selection of reactor coil materials.

Glossary

Arrhenius activation energy	The coefficient E_a catching the temperature dependency of the rate constant $k = A\ e^{-E_a/RT}$ with A the temperature independent pre-exponential factor.
Arrhenius equation	See Arrhenius activation energy.
Arrhenius pre-exponential factor	See Arrhenius activation energy.
Bond dissociation energy	The bond dissociation energy (BDE) is the enthalpy change when cleaving a bond by homolysis.
Catalytic coking mechanism	Mechanism that explains the formation of coke by action of a catalyst (typically Fe or Ni) during steam cracking processes
Coke	Solid carbonaceous residue that deposits inside the reactor and downstream equipment.
Comprehensive two-dimensional gas chromatography	Advanced analytical technique that provides two-dimensional separation by combining two different analytical columns connected with an interface, called the modulator, that ensures that the entire sample is

	comprehensively subjected to both separations.
Condensation coking mechanism	Mechanism that explains the formation of coke when heavy polynuclear aromatics condense either directly on the wall or in the bulk gas phase and subsequently collect on the wall.
Elementary reaction	A chemical reaction in which one or more species react to products in a single step and with a single transition state.
Energy dispersive X-ray analysis	EDX is an analytical technique that determines the elemental chemical composition of a sample by aiming a beam of high-energy electrons to it, and then quantifying the X-ray spectra emitted by the sample.
Gas phase heterogeneous coking mechanism	Mechanism that explains the formation of coke due to the interaction of precursors in the gas phase with active sites in the surface of previously deposited coke.
Gas phase homogeneous coking mechanism	See condensation coking mechanism.
Gibbs free energy	The Gibbs free energy is a thermodynamic quantity that is calculated as $G = H - TS$ with H the enthalpy, T the temperature and S the entropy.
Green olefins	Platform chemicals like ethene, propene and 1,3-butadiene produced from renewable resources in a sustainable production process.
Hydrodeoxygenation	A catalytic process which, in the presence of hydrogen, removes oxygen from organic components in the form of

	water. Common side-reactions are decarboxylation and decarbonylation producing carbon dioxide and carbon monoxide respectively.
Internal oxidation	Formation of encroachments perpendicular to the surface and towards the bulk of an alloy, frequently observed when Al-enhanced alloys are oxidized and the amount of this element is too high.
Jet stirred reactor	Type of ideal continuously stirred tank reactor which is well suited for gas-phase kinetic studies.
Mechanism	Step by step sequence of elementary reactions by which an overall reaction occurs.
Pyrolysis	The uncatalysed decomposition of organic components resulting from exposure to high temperature, in the absence of molecular oxygen.
Radical coking mechanism	See gas phase heterogeneous coking mechanism.
Reaction family	A class of reactions that are characterized by the same pattern of electron rearrangement steps.
Scanning electron microscope	SEM is a type of electron microscope that produces images of a sample by scanning it with a focused beam of electrons.
Steam cracking	A petrochemical process in which saturated hydrocarbons are converted into small unsaturated hydrocarbons by exposure to high temperature in the presence of steam. It has sometimes been referred to as “the big daddy” of petrochemical processes.

Tall oil	A viscous yellow-black odorous liquid obtained as a byproduct of the Kraft process of wood pulp manufacture when pulping mainly coniferous trees. The name originated as an Anglicization of the Swedish "tallolja" ("pine oil"). Crude tall oil can be fractionated into several fractions, including so-called tall oil fatty acids (TOFA) and distilled tall oil (DTO).

Chapter 1: Introduction

1.1 Petrochemicals and a focus on ethylene

The last hundred years have witnessed a previously unforeseeable scenario of permanent and ever-accelerating development of technology improving our lives: Electricity powers cities, with the energy being produced and distributed from a central network in most urban areas; short and long distance commuting became faster, safer and more accessible for the average person; lighter and more resistant materials have been developed, enhancing the performance and safety of transport and machinery; medicine underwent enormous improvements, in great part due to the usage of tools made of synthetic and often disposable materials; computers and mobile devices appeared rather recently and revolutionized the way we work, communicate and, ultimately, think. All of these impressive achievements –among many others– have been fueled, to a significant extent, by petroleum. However, crude oil is rarely useful in its raw form. Therefore, it is converted into various products suited for specific applications using a variety of refining and post-refining techniques. First, separation of the different components of crude oil to facilitate their subsequent treatment is carried out to obtain a wide spectrum of other products of interest, which can serve as final products or as intermediates for the production of higher added value products. Figure 1.1 presents the shares of the products obtained from crude oil processing. It

indicates that more than 80% of the oil goes to the production of fuels, whereas chemicals consume approximately 3-5% of it [1, 2].

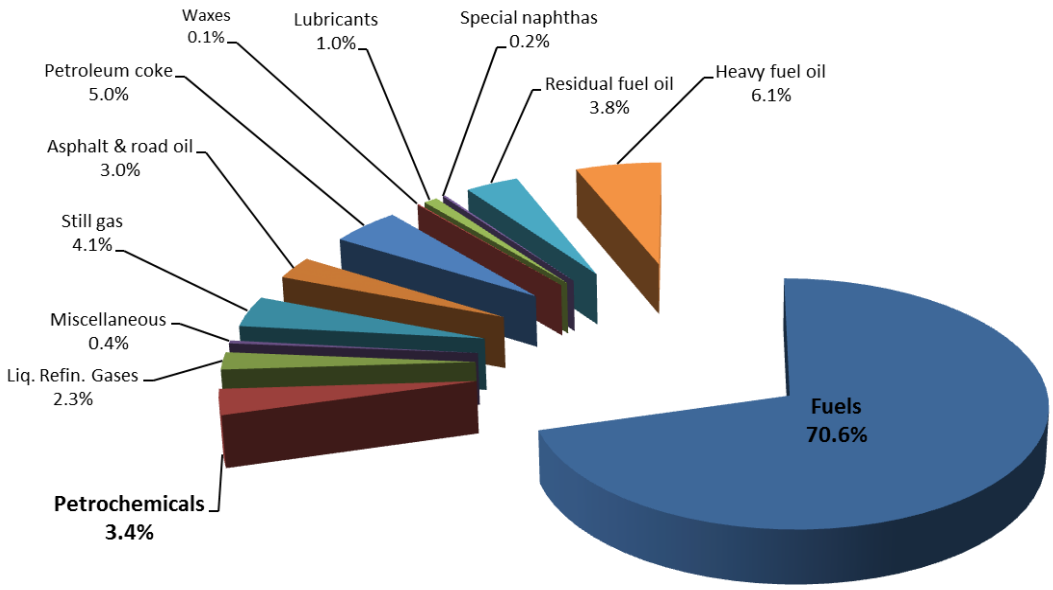

Figure 1.1: Oil barrel breakdown: production of fuels and chemicals from crude oil [3].

Fuels consume twenty times more crude oil than petrochemicals, making the latter seem rather irrelevant for the overall business in terms of volumes. However, the importance of the added value that petrochemicals have in terms of economics is unquestionable, considering the turnover they produce: In the United States alone, petrochemicals had a turnover of approximately $375 billion in 2009, almost matching the $385 billion of transportation fuels [3].

One of the processes used for the production of petrochemicals is the thermal cracking of hydrocarbons with steam, commonly called steam cracking. It is often considered “the heart” of a petrochemical plant, and is the main worldwide process for the commercial production of a wide range of base chemicals such as ethylene, propylene and other lower olefins and aromatics [4, 5]. The products of steam cracking are of immense value for many industries, among which electronics, automotive, food and textiles are probably the most remarkable. To obtain an overview of the variety of products and usefulness of this process, a very detailed presentation of

the products of steam cracking, as well as their most frequent uses, can be consulted on the website of the Association of Petrochemical Producers in Europe [6].

Ethylene (C_2H_4) is the main product obtained from this process and has been widely used for more than 60 years. Prior to World War II, the consumption of ethylene was rather small, and its usage very limited. However, the demand for styrene and polyethylene significantly raised after the war, consequently leading to the construction of olefin plants that could provide the ethylene to meet such requirements. Nowadays, ethylene is used also for the production of ethylbenzene (precursor for styrene), ethylene dichloride (precursor to vinyl chloride), ethylene oxide, vinyl acetate, alpha olefins and linear alcohols, as presented in Figure 1.2 [7, 8].

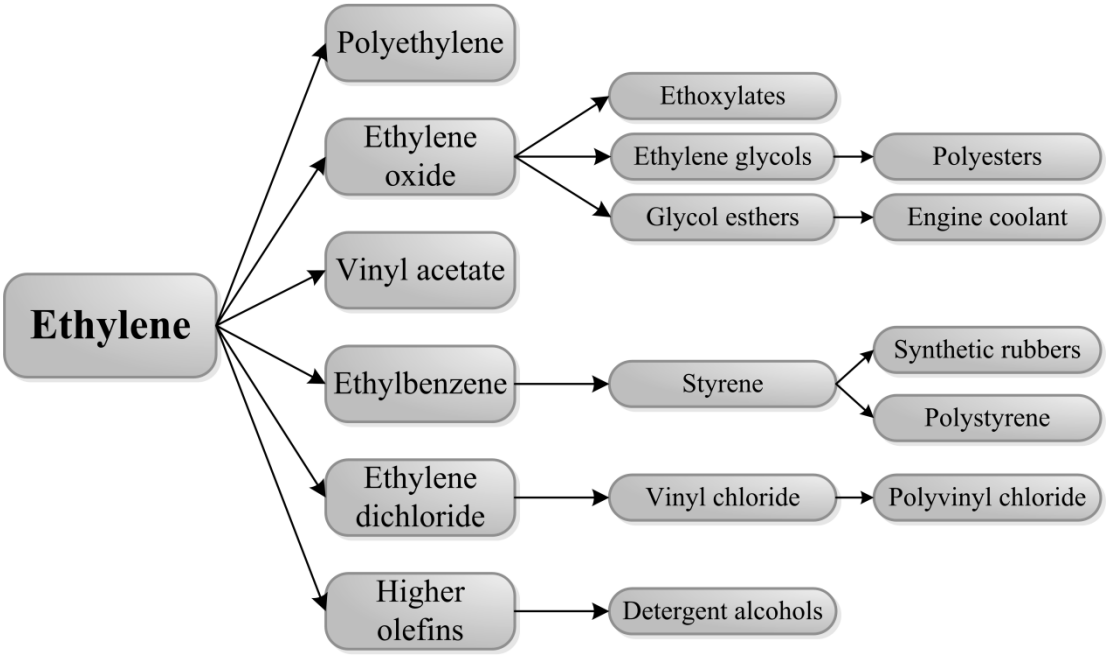

Figure 1.2: Common ethylene derivative products[8]

Propylene, C_3H_6, is also a very interesting product that is made during steam cracking. Its main uses are polypropylene (about half of the propylene is used for this purpose), propylene oxide, isopropyl alcohol, cumene, oxo alcohols, acrylic acids, and acrylonitrile.

Given the large scale and sustained growth of the industries that this process serves, steam cracking units, also frequently referred to as ethylene crackers, keep being added to the production grid with larger capacities, sometimes bordering values as high as 3 million ton per year (tpy), and with average capacities of world-scale crackers of roughly 1.5 million tpy of ethylene [9]. Predictions indicate that during 2014 more than 150 million ton of ethylene will be produced [9, 10]. The sector is predicted to grow, in the United States alone, by 25 % in the next 10 years due to the rising availability of shale gas [11].

1.2 Steam cracking technology

1.2.1 Feedstock and products

All chemical processes involve feeding a substance to a reactor, its reaction to form products, and the handling of such products coming out of the reactor [12].

The process of steam cracking is no exception. A wide variety of feeds –virtually all hydrocarbons– can be fed to this endothermic process [13]. In industrial practice, however, the span of used feeds is somewhat restricted due to availability and economics, and is mostly comprised of ethane, propane, naphthas and gas oil. Ethane has the great advantage of yielding high amounts of ethylene, while naphthas are easy to transport and are largely available in some regions, in comparison with ethane. These facts mark the landscape of the consumption of different feeds for steam cracking, as can be seen in Figure 1.3. In general, naphthas feed most of the industry, although ethane prevails in North America and the Middle East [1, 14, 15]. However, the scenario is expected to be inverted within the next three years, with ethane ruling over

naphtha worldwide, considering the large increase in availability of shale gas, mostly in North America, which has even led recently to agreements concerning exports of ethane from the U.S. to use as feedstock by INEOS in their European crackers [16, 17].

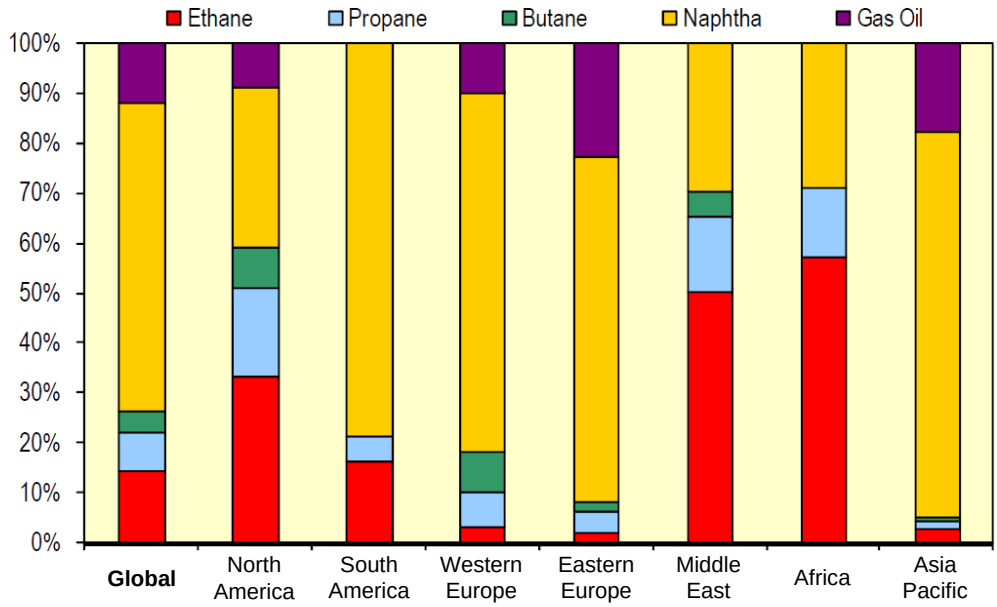

Figure 1.3: Breakdown of steam cracker feeds by region in 2010 [14].

The feedstock selection has two main implications on the process: the product distribution of the process is different depending on the feed (among other process parameters), and the process technology has also to be adjusted based on the characteristics of the feed.

Renewable feedstocks for production of "green olefins" have become object of interest recently, due to environmental concerns and the rising price of fossil feeds [18]. Various feeds, such as waste vegetal fats [18], crude tall oil (CTO) [19], distilled tall oil (DTO) [20] and tall oil fatty acids (TOFA) [21] can be fed to steam cracking processes after a hydrodeoxygenation (HDO) step, either as pure components, or blended with traditional fossil feeds.

Table 1.1: Typical product yields (wt %) of steam cracking of various fossil and renewable feeds.

Product yield (wt%)	Fossil feeds[22]						Renewable feeds			
							Tall oil			HDO Fats[18]
	Ethane†	Propane	Butane	Medium-range naphtha	AGO	VGO	HDO-DTO[20]	HDO-TOFA[21]	HDO-CTO[19]	
Hydrogen	8.8	2.3	1.6	1.5	0.9	0.8	0.6	0.7	0.9	0.9
Methane	6.3	27.5	22.0	17.2	11.2	8.8	12.8	11.8	15.8	16.3
Ethylene	77.8	42.0	40.0	33.6	26.0	20.5	38.1	36.9	32.1	30.9
Propylene	2.8	16.8	17.3	15.6	16.1	14.0	17.9	16.3	11.0	17.6
Butadiene	1.9	3.0	3.5	4.5	4.5	5.3	7.1	6.1	4.3	5.4
Others [C_2 - C_4]	0.7	1.3	6.8	4.2	4.8	6.3	10.8	7.7	6.3	10.3
Pyrol. gasoline [C_5 - C_9]										
Benzene	0.9	2.5	3.0	6.7	6.0	3.7	6.6	6.8	9.3	5.6
Toluene	0.1	0.5	0.8	3.4	2.9	2.9	1.5	3.3	5.2	2.1
Xylenes	-	-	0.4	1.8	2.2	1.9	0.1	0.5	1.2	N/A
Others	0.7	3.6	2.9	6.8	7.3	10.8	3.1	7.9	3.9	0.8
Pyrol. fuel oil [C_{10} - C_{30}]	-	0.5	1.7	4.7	18.1	25.0	0.9	1.9	N/A	N/A

*N/A: Product yield not reported.

†Includes ethane recycle

Table 1.1 presents typical yields of products obtained from steam cracking of various common fossil feeds, as well as yields reported for cracking of some renewable feeds. The highest ethylene yields are achieved for ethane, and as the feed becomes heavier, larger amounts of heavier olefins and aromatics are produced, at the expense of ethylene [7, 23, 24]. The yields obtained when cracking renewable feeds are similar to those obtained when cracking naphtha, showing that they can be a good substitute in terms of yields. However, they are not in commercial use due to their low volumes, besides being still more expensive than traditional fossil feeds.

1.2.2 Reactions during steam cracking

Steam cracking of hydrocarbons is a complex process in which, even when fed by a pure component, tens or even hundreds of products are formed, and can be therefore detected in the reactor effluent. It has been widely accepted that, during high temperature cracking of hydrocarbons, the dominating mechanism is radical in nature [25-27]. Logically, the specific reactions taking place vary depending on the feed used but three main elementary reaction families can be distinguished in this mechanism [28-31].

The first one is the scission of carbon-carbon and carbon-hydrogen bonds, and the reverse recombination of radicals, as presented in equation (1.1). The cracking is initiated by breaking the feed molecules into radicals. Evidently, the scission occurs in the weakest bond of the molecule, and in most cases the reaction rates of C-H scissions can be neglected, in comparison to those of C-C bonds.

$$R_1 - R_2 \rightleftharpoons R_1^{\bullet} + R_2^{\bullet} \tag{1.1}$$

The second elementary reaction family is formed by hydrogen abstractions, both intra and intermolecular, as presented in equation (1.2). These reactions transfer hydrogen atoms from a molecule to a radical, forming a new radical and a new molecule. Vinyl and phenyl radicals are known to be the most active radicals, whereas allylic and benzyl radicals are the least active [29].

$$R_1 - H + R_2^{\bullet} \rightleftharpoons R_1^{\bullet} + R_2 - H \tag{1.2}$$

Finally, radical addition to olefins and the reverse β scission of radicals (both intra- and intermolecular) form the third elementary reaction family:

$$R_1^{\bullet} + R_2 = R_3 \rightleftharpoons R_1 - R_2 - R_3^{\bullet} \tag{1.3}$$

Via this mechanism, some of the formed olefins can be turned into the heavier products that are present in the effluent [32].

The proposed mechanisms help to understand the formation of the vast span of products that steam cracking of hydrocarbons produces, and illustrate the enormous number of interactions that need to be taken into account if attempting to accurately model cracking.

1.2.3 Steam cracking process

Cracking units can be divided in two sections: a hot section, where the cracking takes place; and a cold section, in which the products are separated [29]. Industrially, this process starts by heating up the hydrocarbon feed (evaporating it if liquid) by means of heat exchange with flue gas. Then the hydrocarbons are mixed with the diluting steam in the desired proportions to form a homogeneous mixture, and then further heated to temperatures slightly lower than those required for cracking to proceed (800 – 950 K, depending on the feed) [30]. The steam is added to reduce the partial pressure of hydrocarbons, which favors the formation of olefins. The heated mixture is

then fed to a fired tubular reactor (also known as the radiant coil) made of heat-resistant steels (see section 2.5) with diameters in the range of 0.03 – 0.13 m [27] and lengths ranging from 10 to 100 m depending on the design. The gas phase reaches temperatures in the range of 900-1050 K in the reactor, due to the action of burners located in the bottom and/or walls of the furnace. The residence time of the feed in the reactor varies in accordance with the feedstock used and the design of the reactor coil [33, 34], but it is normally in the range of 0.1-0.5 s [30].

When the process gas leaves the reactor, it enters the cold section, in which the first step is to rapidly quench it, reducing the effluent temperature to around 600-750 K by exchanging heat with high pressure boiler water in a Transfer Line heat Exchanger (TLE) [4]. This prevents the highly reactive effluent molecules from further reacting, which could affect the olefin yields. The effluent stream is then fed to a fractionation section composed of a series of separation columns, in order to obtain separate streams of the different products. Figure 1.4 presents a simplified scheme of the process for ethane cracking, which is noticeably simpler than the one for cracking of naphtha (or other liquid feeds, e.g. gas oils), presented in Figure 1.5.

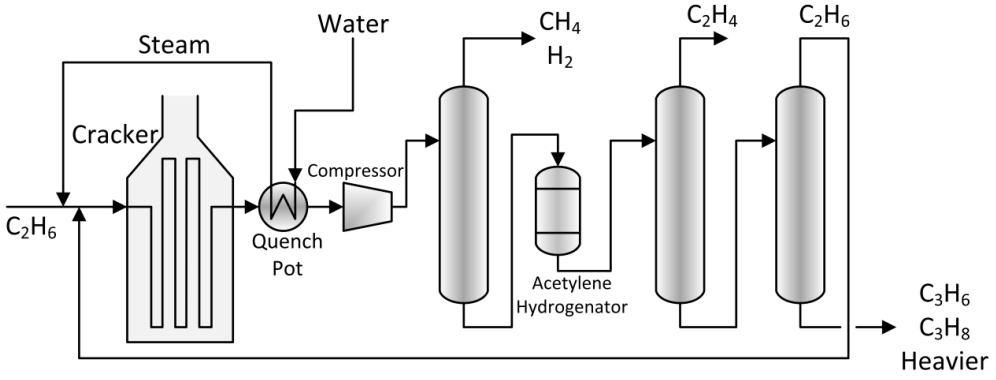

Figure 1.4: Schematic view of the process for steam cracking of ethane [7, 29].

The main difference between them is that the cold section for liquid feed plants is more developed, due to the larger variety of products that this process can form. Additionally, in most

cases a naphtha cracking plant incorporates also an ethane cracker [7], to handle the recycle stream of this hydrocarbon, which forms in significant amounts when cracking naphtha or gas oil [30, 35].

The effluent is liquefied, in order to carry out the separation of products. This is achieved by the combined action of a compressor to increase the pressure and a cold box that refrigerates the products stream. The presence of an acetylene hydrogenation unit is necessary because even traces of acetylene in ethylene can be harmful for downstream operations, particularly the manufacturing of polyethylene.

Given the high temperatures applied in the cracking process, heat resistant materials are required, i.e. materials that maintain their properties even at the high temperatures of cracking. Therefore, Fe-Cr-Ni alloy steels are typically used. Despite their good mechanical properties, a problem associated with these alloys is their propensity to promote the deposition of a carbonaceous solid residue, called coke.

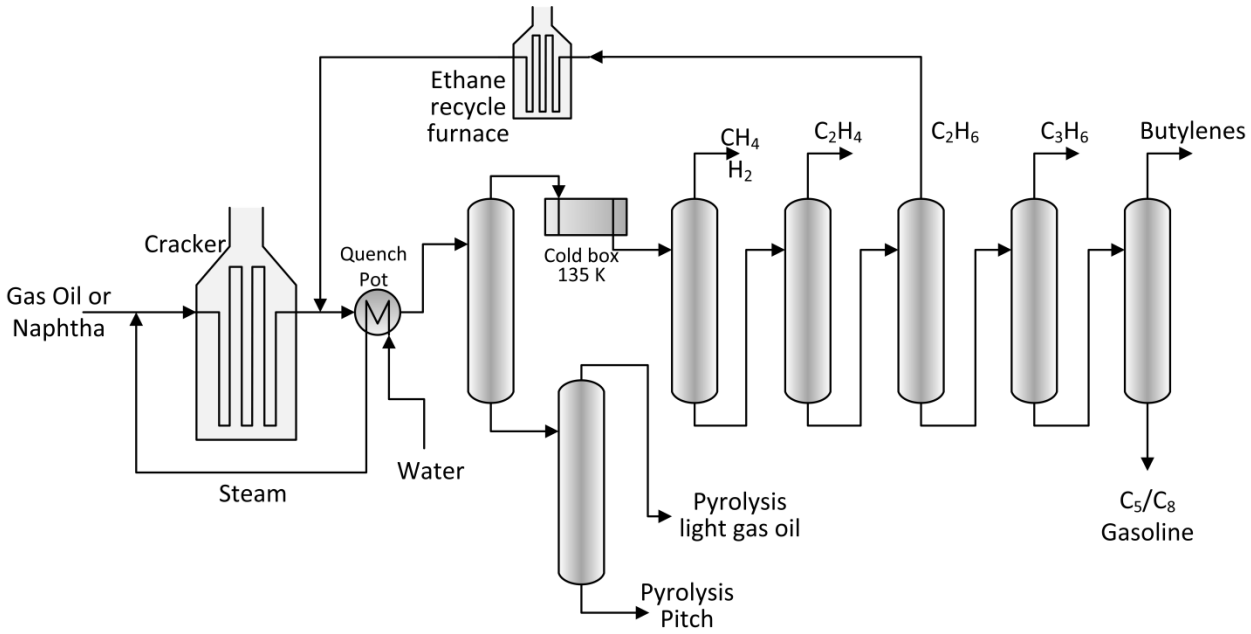

Figure 1.5: Schematic view of the process for steam cracking of liquid feeds [7, 29].

1.3 Coke deposition during steam cracking

Coke is an undesired product that forms due to side reactions during cracking. Its accumulation in the reactor coil has a negative effect on the process, as a consequence of two parallel phenomena: temperature increase and pressure drop increase.

As coke accumulates inside the coil, it forms a layer that continuously increases in thickness, like the one presented in Figure 1.6. Such layer acts as a thermal insulator [36], impeding an adequate transfer of heat from the firebox to the process gas, thus forcing operators to increase the heat input to the process, in order to keep the process gas at constant temperature. This implies a higher fuel consumption (even 5% higher at the end of a run), besides submitting the outer wall of the reactor coil to higher temperatures, which leads to weakening of the alloy and can eventually cause a mechanical failure [37].

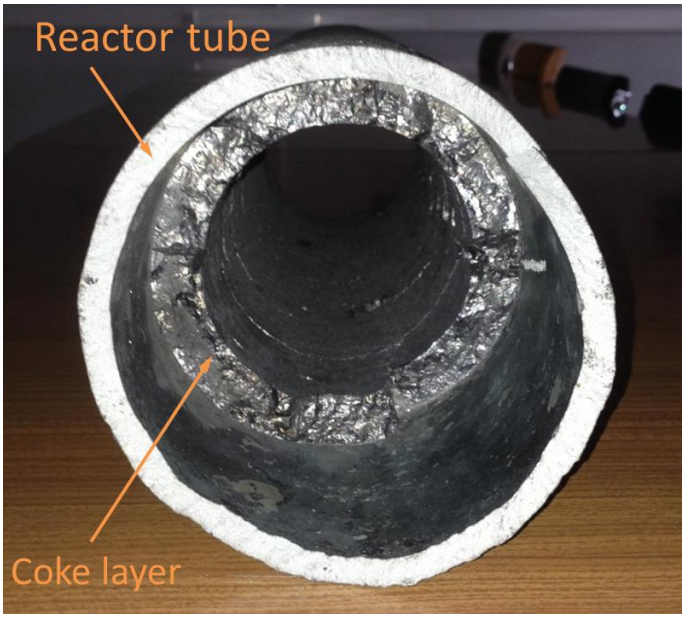

Figure 1.6: Industrial cracking coil with a thick coke layer deposited on its internal surface [38].

At the same time, the pressure drop along the coil increases due to the reduction of the cross sectional area of the reactor [39]. The higher pressure leads to a reduction of the olefins yield,

because it favors bimolecular addition reactions over monomolecular reactions, thus consuming desired light olefins [33].

Additionally, the deposited coke can react with the steam added as a diluent to the feed. This leads to the formation of carbon monoxide [40], which acts as a temporary poison for the catalyst used downstream in the hydrogenation of acetylene, methylacetylene, and propadiene [41].

CO forms through a well-known reaction, called steam reforming [42], represented in equation (1.4) and is catalyzed by nickel, available from the reactor alloy. The carbon monoxide is partly consumed and transformed to carbon dioxide by the so-called water gas shift reaction, represented in equation (1.5).

$$C_nH_m + nH_2O \leftrightarrows nCO + \left(\frac{n+m}{2}\right)H_2 \tag{1.4}$$

$$CO + H_2O \leftrightarrows CO_2 + H_2 \tag{1.5}$$

Typically, after 30-60 days of cracking either the maximum operation temperature of the reactor material or an excessive pressure drop over the reactor are reached due to the accumulation of cokes. This forces to halt the cracking operations for removal of the cokes. This decoking operation is carried out by feeding air, steam or a mix thereof to the reactor and takes approximately 48 hours, during which no products are obtained, having therefore a negative impact on the economics of the process. It has been estimated that the worldwide loss due to decoking is higher than US$ 1 billion [43]. In the light of these facts, it is very understandable that ethylene producers are largely interested in reducing the frequency of decoking operations to a minimum.

Coke forms via three main mechanisms, namely catalytic, radical and condensation mechanisms, and several process parameters, e.g. temperature, dilution and feedstock composition, influence

the rate of coke deposition. Other characteristics inherent to the reactor, such as its design, alloy composition and internal surface roughness also have an impact on the rate of coking [44].

While attempting to reduce coking to a minimum, different strategies have been developed and implemented throughout the years. The most frequent are the usage of additives during cracking, which are also often helpful to reduce the concentration of CO; modification of the internal geometry of the coils (so-called 3D geometries) for improved heat transfer; application of inert coatings to the internal surface; pretreatments of the reactor coil surface (e.g. preoxidation, prereduction, presulfidation, …); and the application of specialized alloys for the construction of coils with developed inert surfaces, capable of substantially reducing the amount of coke accumulating during the process.

It is the latter, i.e. the study of the coking resistance of specialized coil alloys and materials, that forms the subject of this work. The interest in investigating this field can be easily understood using some simple calculations to illustrate the economic advantages that the application of better coil materials (and consequently run length extensions) can bring, if compared to currently existing alloys.

To illustrate the potential benefits of utilizing specialized coils, the run length of an industrial ethane cracker as the one described by Van Geem et al. [45] was simulated using COILSIM1D. A summary of the main process conditions used in the simulation is presented in Table 1.2. This simulation assumes that the coil is made of a typical high-temperature alloy and is, therefore, taken as a base case.

Implementing the same process conditions, new simulations calculating the run length were carried out, while gradually reducing the coking rate in steps of 5%, analogous to the work of Wang et al. concerning run length extension by the use of additives [46].

Table 1.2: Process conditions and reactor characteristics for the simulation of an ethane cracking furnace

Type of reactor used	Swaged coil
Number of reactors	4
Number of passes	8
Reactor length	110.96 m
Ethane flow per reactor	2800 kg/h
Coil Inlet Temperature (CIT)	929 K
Coil Outlet Pressure (COP)	1.95×10^5 Pa
Dilution	0.365 kg_{H2O} / kg_{C2H6}
Ethane conversion	63.4%

The base case simulation predicted a run length of 48 days, and the effect on the run length of a reduction of coking rate can be observed in Figure 1.7, which also presents the decoking annual downtime as a function of the coking rate reduction.

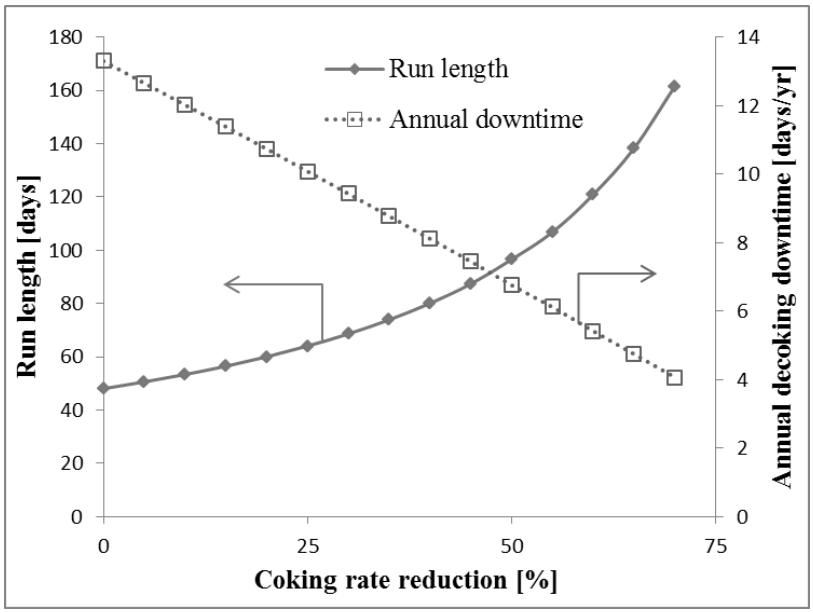

Figure 1.7: Simulated run length and net annual decoking downtime of an industrial ethane cracker as a function of the reduction of the coking rate.

Obviously, the implementation of specialized coils represents an additional cost, compared to the usage of regular high-temperature alloys. Brown presented an economic evaluation for finned coils [47]. The same methodology can be adapted to the conditions of the simulated furnace, in

order to estimate the potential benefit of using specialized coils. The additional cracking time and the corresponding additional cash margin that are obtained by a certain reduction of the coking rate are used to determine the pay back time for the additional cost of specialized coils.

Three different ethylene cash margins are used for the calculations (i.e. 1000 US$, 500 US$ and 350 US$), which represent an optimistic, a realistic, and a pessimistic case [48]. Additionally, the price of a specialized coil is estimated to be 1.5 times that of a regular coil. Taking a price of 45000 US$ per assembled coil of regular alloy, the price of a specialized coil is 67500 US$. Taking into account that the simulated furnace includes 4 coils, the additional overall cost of coils per furnace is estimated to be 90000 US$. The furnace simulation indicated that the yield of ethylene was 49.5 wt%, and an operation year was taken as 8000 hours.

Table 1.3: Economic evaluation of special coils pay back time, and benefits of a 10% coking rate reduction for the simulated ethane cracker.

		Typical coil	Special coil		
Ethylene Cash Margin	US$/t		1000	500	350
Furnace feed (incl. recycle)	kg/h	11200	11200	11200	11200
Ethylene yield	wt%	49.5	49.5	49.5	49.5
Run length	h	1154	1282	1282	1282
Run length	days	48.08	53.42	53.42	53.42
Annual on-stream time	h/yr	7681	7711	7711	7711
Ethylene production	t/yr	42581	42751	42751	42751
Incremental ethylene production	t/yr	-	170	170	170
Incremental cash margin	US$/yr	-	170454	85227	59659
Incremental coil cost	US$	-	90000	90000	90000
Pay back time	months	-	6.3	12.7	18.1

Table 1.3 shows the calculations made for the case of a 10% coking rate reduction. It can be seen that a time between 6 and 18 months (depending on the ethylene cash margin) is needed to pay back the investment on special coils. The most realistic case (500 US$/t) indicates that 13 months are needed. With typical coil lifetimes of around 5 years [30], it is evident that a 10% reduction of coking rate is already beneficial, as just slightly after a year, the profit margin of the furnace will roughly increase by 85000 US$ per year, compared to a typical coil.

Evidently, the pay back time varies depending on the percentage of reduction of the coking rate achieved. Making calculations like the one presented in Table 1.3 for various other percentages, the pay back time can be plotted (see Figure 1.8) as a function of the percentage of coking rate reduction.

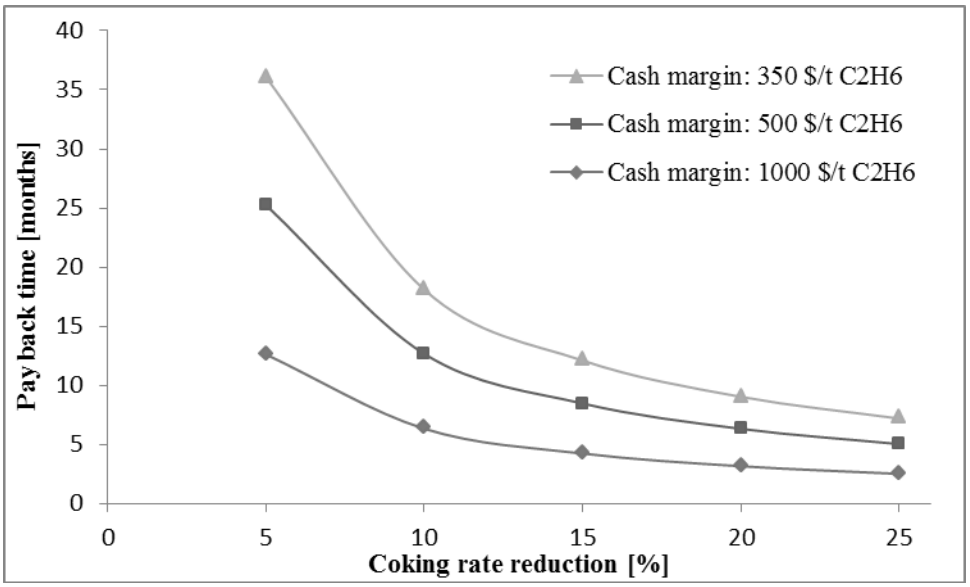

Figure 1.8: Pay back time of the investment in specialized coils as a function of the coking rate reduction in the simulated industrial furnace.

Although these values are only estimations, they illustrate the relative magnitude of the investment cost and potential benefit of coke reducing alloys and materials. It is thus easy to understand and justify the interest on developing materials that could reduce coking and, most importantly, increase profits.

1.4 Objectives and outline of this work

In section 1.1 steam cracking was introduced, and it was shown that it has a very important place in the (petro)chemical industry, not only due to its large scale but also in virtue of the high value of its products. Section 1.2 has given an insight on the technical aspects of this process, with special attention to the feedstocks used, and the implications that the feed selection carries along, mainly in terms of product yields and equipment required. Finally, in Section 1.3, coke deposition has been presented as an unavoidable phenomenon taking place during the process, indicating its implications in the operation of the crackers, and mentioning the strategies typically applied to diminish it. The use of special alloys and materials has been pointed out as one of the most remarkable areas in which improvement of the process can be achieved, due to the economic and operational benefits it can report.

In this context, the extensive and systematic study and comparison of the resistance to coking of a series of specialized and recently developed alloys and materials, specifically aimed for use in steam cracking coils becomes very interesting, and is therefore the general objective of this work.

Three specific objectives have been delineated:

- Comparison of the resistance to coking of ten different recently developed materials and alloys under steam cracking of ethane, in order to establish a ranking of the materials, based on their resistance to coking.
- Selection of three materials that were tested during ethane cracking, to submit them to light naphtha cracking conditions, so that their beneficial impact on coke deposition can be evaluated for a different feedstock.
- The behavior of the materials should also be understood and explained in terms of their microscopic structure after the cracking tests. A description of the ideal structure for a

material will be made, based on the observations comparing coking behavior and material structure.

In the following chapters, the work aiming at attaining these objectives is presented.

Chapter 2 presents a review of the three mechanisms through which coke forms. Additionally, a review of the influence on coking of alloys and their pretreatments is included. Then, some of the coking models that have been developed in the past are presented. Finally, simple calculations are presented to illustrate (i) the relative influence of temperature and gas phase composition on the coking rate, and (ii) that the duration of the initial coking regime (prevalence of catalytic mechanism) is negligible in comparison to the duration of the asymptotic regime (prevalence of radical mechanism) in an industrial coil.

Chapter 3 presents a detailed description of the experimental setups that have been used, as well as of the procedures applied during the experimental campaign.

In Chapter 4, the results obtained when testing the coking resistance under ethane steam cracking conditions of nine different materials and one coating are presented. With these data, a ranking of the studied materials has been made, based on their resistance to coking. Additionally, the results obtained from SEM and EDX analyses of top surfaces and cross sections of the studied materials are presented and, combined with thermodynamic stability calculations, are used to explain the observations.

In Chapter 5, three materials that were tested during ethane cracking (the two best performing, and a commonly used alloy) are selected and, using a protocol similar to that of ethane cracking, they are submitted to naphtha cracking, so that their coking resistance using this feed can be evaluated. Also SEM and EDX analyses are carried out over the material samples, as well as thermodynamic stability calculations, allowing to obtain a good understanding of how the change of feedstock effects the relative behaviors of the materials.

Finally, Chapter 6 summarizes the main findings of this work, emphasizing the influence of the surface composition and structure of reactor materials on the rates of coke formation. In addition, future prospects of research on the subject are presented, with the specific aim of building up on the dataset this work provides, to evaluate the effect of other parameters and their magnitude.

References

[1] Pyl, S. Sustainable production of light olefins: from fossil to renewable resources. PhD thesis, Ghent University, Ghent, Belgium, **2012**.

[2] The outlook for energy: A view to 2040. Exxon Mobil Corp.; USA, **2012**.

[3] Rinaldi, R.; Schuth, F. Design of solid catalysts for the conversion of biomass. *Energy Environ. Sci.* **2009**, *2* (6), 610-626.

[4] Van Geem, K. M.; Dhuyvetter, I.; Prokopiev, S.; Reyniers, M. F.; Viennet, D.; Marin, G. B. Coke Formation in the Transfer Line Exchanger during Steam Cracking of Hydrocarbons. *Ind. Eng. Chem. Res.* **2009**, *48* (23), 10343-10358.

[5] Speight, J. G. The chemistry and physics of coking. *Korean J. Chem. Eng.* **1998**, *15* (1), 1-8.

[6] Petrochemicals make things happen. Association of Petrochemical Producers in Europe. URL: http://www.petrochemistry.eu/flowchart/appe-flowchart.pdf, last accessed: 07/02/2013.

[7] Burdick, D. L.; Leffler, W. L., *Petrochemicals in nontechnical language.* 4th. ed.; PennWell Corporation: Tulsa, OK, USA, **2010**.

[8] Petrochemical industry ethylene plant. Siemens Industry, Inc.; USA, **2013**.

[9] True, W. R. Global ethylene capacity poised for major expansion. *Oil Gas J.* **2013**, *111* (7), 90-95.

[10] Global ethylene equivalent production capacity and demand. Ministry of Economy, Trade and Industry of Japan. URL: http://www.meti.go.jp/english/press/data/pdf/20090825_03a.pdf, last accessed: 11/02/2014.

[11] Swift, T. K.; Moore, M. G.; Sanchez, E. Shale gas and new petrochemicals investment: Benefits for the economy, jobs, and US manufacturing. American Chemistry Council. **2011**.

[12] Himmelblau, D. M.; Riggs, J. B., *Basic principles and calculations in chemical engineering.* 8th. ed.; Pearson Education, Inc.: USA, **2012**.

[13] Chauhan, A. P. S. Coke resistant coating technology for applications in ethylene pyrolysis heaters. PhD thesis, Stony Brook University, NY, U.S.A., **2007**.

[14] Nizamoff, A. J. Renewable Liquids as Steam Cracker Feedstocks - PERP09/10S12. Chemsystems PERP Program. **2010**.

[15] Ren, T.; Patel, M.; Blok, K. Olefins from conventional and heavy feedstocks: Energy use in steam cracking and alternative processes. *Energy* **2006**, *31* (4), 425-451.

[16] INEOS reaches deal with Consol to buy US ethane for offtake to Europe. *Hydrocarb. Process.* 14/02/2014, **2014**.

[17] INEOS expands plan to ship US ethane feedstocks to Norway, Scotland. *Hydrocarb. Process.* 08/05/2014, **2014**.

[18] Pyl, S. P.; Schietekat, C. M.; Reyniers, M. F.; Abhari, R.; Marin, G. B.; Van Geem, K. M. Biomass to olefins: Cracking of renewable naphtha. *Chem. Eng. J.* **2011**, *176*, 178-187.

[19] De Bruycker, R.; Anthonykuttyb, J. M.; Linnekoski, J.; Harlin, A.; Lehtonen, J.; Van Geem, K. M.; Räsänen, J.; Marin, G. B. Assessing the potential of crude tall oil for the production of green-base chemicals: an experimental and kinetic modeling study. *Ind. Eng. Chem. Res.* **2014**, *Submitted*.

[20] Dijkmans, T.; Pyl, S. P.; Reyniers, M. F.; Abhari, R.; Van Geem, K. M.; Marin, G. B. Production of bio-ethene and propene: alternatives for bulk chemicals and polymers. *Green Chem.* **2013**, *15* (11), 3064-3076.

[21] Pyl, S. P.; Dijkmans, T.; Antonykutty, J. M.; Reyniers, M. F.; Harlin, A.; Van Geem, K. M.; Marin, G. B. Wood-derived olefins by steam cracking of hydrodeoxygenated tall oils. *Bioresour. Technol.* **2012**, *126*, 48-55.

[22] Chauvel, A.; Lefebvre, G., *Petrochemical Process, Technical and Economic Characteristics, 1 Synthesis-Gas Derivatives and Major Hydrocarbons.* Gulf Publishing Company: Paris, **1989**.

[23] Glasier, G. F.; Filfil, R.; Pacey, P. D. Formation of polycyclic aromatic hydrocarbons coincident with pyrolytic carbon deposition. *Carbon* **2001**, *39* (4), 497-506.

[24] Kopinke, F. D.; Zimmermann, G.; Reyniers, G. C.; Froment, G. F. Relative rates of coke formation from hydrocarbons in steam cracking of naphtha .3. Aromatic-hydrocarbons. *Ind. Eng. Chem. Res.* **1993**, *32* (11), 2620-2625.

[25] Rice, F. O. The thermal decomposition of organic compounds from the standpoint of free radicals. I. Saturated hydrocarbons. *J. Am. Chem. Soc.* **1931**, *53* (5), 1959-1972.

[26] Froment, G. F. Thermal cracking for olefins production. Fundamentals and their application to industrial problems. *Chem. Eng. Sci.* **1981**, *36* (8), 1271-1282.

[27] Dente, M.; Bozzano, G.; Faravelli, T.; Marongiu, A.; Pierucci, S.; Ranzi, E., Kinetic Modelling of Pyrolysis Processes in Gas and Condensed Phase. In *Advances in Chemical Engineering*, Marin, G. B., Ed. Academic Press: **2007**; Vol. 32, pp 51-166.

[28] Back, M. H.; Back, R. A., Thermal decomposition and reactions of methane. In *Pyrolysis - Theory and industrial practice*, Albright, L. F.; Crynes, B. L.; Corcoran, W. H., Eds. Academic Press, Inc: New York, **1983**; pp 1-24.

[29] Van Geem, K. M. Single event microkinetic model for steam cracking of hydrocarbons. PhD thesis, Ghent University, Ghent, Belgium, **2006**.

[30] Zimmermann, H.; Walzl, R., Ethylene. In *Ullmann's Encyclopedia of Industrial Chemistry*, Wiley-VCH Verlag GmbH & Co. KGaA: Weinheim, **2009**.

[31] Sabbe, M. K.; Van Geem, K. M.; Reyniers, M. F.; Marin, G. B. First Principle-Based Simulation of Ethane Steam Cracking. *Aiche J.* **2011**, *57* (2), 482-496.

[32] Chen, C. J.; Back, M. H.; Back, R. A. The thermal decomposition of methane. II. Secondary reactions, autocatalysis and carbon formation; non-Arrhenius behaviour in the reaction of CH3 with ethane. *Can. J. Chem.* **1976**, *54* (20), 3175-3184.

[33] Van Geem, K. M.; Reyniers, M. F.; Marin, G. B. Two severity indices for scale-up of steam cracking coils. *Ind. Eng. Chem. Res.* **2005**, *44* (10), 3402-3411.

[34] Van Geem, K. M.; Heynderickx, G. J.; Marin, G. B. Effect of radial temperature profiles on yields in steam cracking. *Aiche J.* **2004**, *50* (1), 173-183.

[35] Froment, G. F. Fouling of heat transfer surfaces by coke formation in petrochemical reactors. Fouling of heat transfer equipment, **1981.** Sommerscales, E.; Knudsen, J. G., Eds. Hemisphere Publ. Corp.

[36] Ranzi, E.; Dente, M.; Pierucci, S.; Barendregt, S.; Cronin, P. Coking Simulation Aids On-Stream Time. *Oil Gas J.* **1985**, *83* (35), 49-52.

[37] Goossens, A. G.; Dente, M.; Ranzi, E. Improve steam cracking operation. *Hydrocarb. Process.* **1978**, *57* (9), 227-236.

[38] Muñoz G., A. E.; Van Geem, K. M.; Reyniers, M. F.; Marin, G. B. Assessing the influence of alloy composition on coke formation in steam cracking reactors. 25th. Ethylene Producers' Conference, San Antonio - TX, USA, 2 May, **2013.**

[39] Gascoin, N.; Abraham, G.; Gillard, P. Thermal and Hydraulic Effects of Coke Deposit in Hydrocarbon Pyrolysis Process. *J. Thermophys. Heat Transf.* **2012**, *26* (1), 57-65.

[40] McConnell, C. F.; Head, B. D., Pyrolysis of ethane and propane. In *Pyrolysis - Theory and industrial practice,* Albright, L. F.; Crynes, B. L.; Corcoran, W. H., Eds. ACADEMIC PRESS, INC: New York, **1983**; pp 25-45.

[41] Reyniers, M.-F.; Froment, G. F. Influence of metal-surface and sulfur addition on coke deposition in the thermal-cracking of hydrocarbons. *Ind. Eng. Chem. Res.* **1995**, *34* (3), 773-785.

[42] Chorkendorff, I.; Niemantsverdriet, J. W., *Concepts of modern catalysis and kinetics.* 2nd ed.; Wiley-VCH: Germany, **2007**.

[43] Kolmetz, K.; Kivlen, J.; Gray, J.; Sim, C.; Soyza, C. Advances in cracking furnace technology. Refining Technology Conference, Dubai, 14-18 Dec, **2002.**

[44] Cai, H. Y.; Krzywicki, A.; Oballa, M. C. Coke formation in steam crackers for ethylene production. *Chem. Eng. Process.* **2002**, *41* (3), 199-214.

[45] Van Geem, K. M.; Pyl, S. P.; Reyniers, M. F.; Marin, G. B. Effect of operating conditions and feedstock composition on run lengths of steam cracking coils. 21st. Ethylene Producers' Conference, Tampa - FL, USA, 28 April, **2009.**

[46] Wang, J. D.; Reyniers, M. F.; Van Geem, K. M.; Marin, G. B. Influence of silicon and silicon/sulfur-containing additives on coke formation during steam cracking of hydrocarbons. *Ind. Eng. Chem. Res.* **2008**, *47* (5), 1468-1482.

[47] Brown, D. J. Internally Finned Radiant Coils: a Valuable Tool for Improving Ethylene Plant Economics. 6th EMEA Petrochemicals Technology Conference, London, UK, **2004.**

[48] Lippe, D. Ethylene production prospects clouded by first-half turnarounds. *Oil Gas J.* **2013**, *111* (9), 102-111.

Chapter 2: Principles of coke formation

Abstract:

Coke formation is a phenomenon that inevitably occurs during steam cracking of hydrocarbons. In order to provide an insight into the main principles of coke formation, this chapter explains the three main mechanisms for coke formation, and discusses their relative importance. Literature and calculations indicate that the heterogeneous noncatalytic mechanism is the most important for industrial coils. Also, coke deposition models with different levels of complexity are presented. These models require the input of process temperature and the concentration of selected coke precursors –typically olefins and aromatics– to provide coke formation rates. Simple calculations are presented in this chapter, which illustrate that temperature affects the coking rate more strongly than the gas phase composition. Finally, the development of coil reactor materials is reviewed. Besides the chemical composition, modifications motivated by the need to enhance mechanical properties, coil pretreatments and the usage of inert and active coatings are also discussed.

Keywords: Steam cracking; coke formation mechanisms; coke deposition models; reactor coil materials; coatings.

2.1 Coking mechanisms

2.1.1 Catalytic coke formation

When hydrocarbons are brought in contact with a bare reactor coil surface at sufficiently high temperatures, coke is formed through a catalytic mechanism, in which the metals of the coil surface act as catalysts. The properties of the metals are very important in this mechanism, and the metals of the reactor surface (specifically nickel and iron) are very active towards coke deposition if compared to, e.g., copper [1, 2]. Evidently, the composition of the reactor coil surface has a large impact on the rates of coke formation [3-5].

In this mechanism, a hydrocarbon molecule is chemisorbed on the metal, forming CH, CH_2, CH_3, … groups on the surface. These groups lose hydrogen atoms which recombine and desorb into the gas phase as H_2. The carbon atoms that are consequently formed at the surface dissolve in and diffuse through the metal particles. These metal particles can be lifted from the surface if the pressure that the carbon exerts is higher than the tensile strength of the metal [3]. Carbon crystallizes at the rear end of the particle and, as it accumulates, it forms then a carbon stem which carries the metal particle on the tip. As carbon precipitates, structural deficiencies in the carbon lattice can occur and create reactive centers along the filament skin. Radicals and other molecules from the gas phase can be incorporated at these reactive sites, leading to lateral growth of the filament. Eventually encapsulation of the metal particle, impeding further growth of the filament can occur. Recent work [6] has shown, by means of in-situ high-resolution transmission electron microscopy (HRTEM) and density functional theory (DFT), that step sites are preferred for the growth of graphene, leading to encapsulation of the metal.

The rate at which encapsulation of the active particles occurs depends strongly on the relative rates of surface carbon growth, carbon gasification, dissolution and diffusion. A schematic illustration of this mechanism is presented in Figure 2.1.

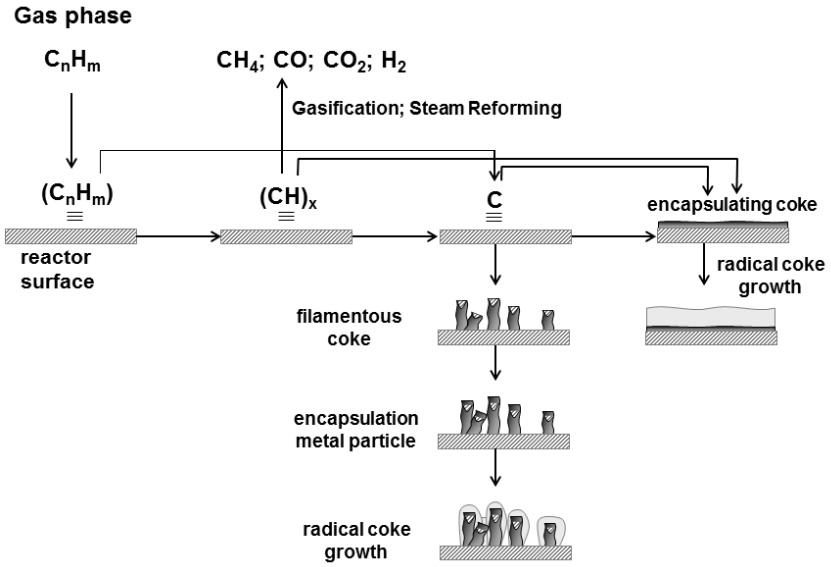

Figure 2.1: Schematic diagram of the heterogeneous catalytic mechanism for coke deposition

Carbon gasification occurs due to the dissociative chemisorption of water molecules on the metal, which produces highly active oxygen in the surface. These oxygen atoms can then react with hydrocarbons or carbon atoms from the surface forming CO, which desorbs into the gas phase.

Dissolution and diffusion of carbon play also an important role, because filaments form only on metals with high solubility for carbon. Metals with low carbon solubility, e.g. platinum, tend to deposit only encapsulating carbon at their surface. Interstitially dissolved carbon diffuses through the particle, and the driving force for this has been largely debated. Some authors [7, 8] have claimed the temperature gradient motivates the diffusion, whereas others [9-13] attributed it to the concentration gradient.

The consideration of temperature as the drive for diffusion is based on observations made by Baker et al. when decomposing acetylene over nickel [7]. The acetylene decomposition at the

interface between the gas and the metal is exothermic, whereas the precipitation of graphite at the opposite side of the particle is endothermic. This generates a heat sink, which can therefore drive the diffusion.

This mechanism straightforwardly explains the formation of filaments when the decomposition of hydrocarbons is exothermic. However, filaments are also formed during the endothermic decomposition of e.g., propane. The incongruence that this presents with the proposed mechanism has been discussed by Keep et al. [14]. They observed that during the decomposition of propane at 973 K, only the yields of ethylene, propylene and benzene were affected by the presence of nickel, leading to the conclusion that those are the actual species decomposing at the surface of the nickel particles. The decomposition to carbon of such molecules is exothermic, reconciling again the observations with the proposed thermally driven diffusion of carbon.

On the other hand, when considering a concentration gradient as the driving force for the diffusion of carbon through nickel, the difference in solubility of carbon at the metal/gas interface and the metal/carbon filament interface becomes the key point. According to the model proposed by Snoeck et al. [13] the nucleation of filamentous carbon is caused by the formation of a solution of carbon in nickel that is supersaturated with respect to filamentous carbon. The degree of supersaturation is determined by the affinity for carbon formation of the gas phase. This way, a concentration gradient is formed over the particle, providing a drive for the diffusion of carbon.

As stated earlier, the formation of carbon filaments comprises various steps. The work of Baker et al. [7, 15] helped to distinguish the rate-determining step for filament growth. Their work lead to the conclusion that the diffusion of carbon through the metal particle is the rate-determining step, because the activation energies of the filament growth coincide with those of the carbon diffusion on iron, cobalt, chromium and nickel.

2.1.2 Heterogeneous noncatalytic coke formation

This mechanism is the most important source of coke in the reactor during steam cracking. Over time, the catalytic mechanism loses importance due to the continuous encapsulation of the catalytic particles, whereas the heterogeneous non-catalytic mechanism operates over the entire run length [3]. It has been extensively discussed by several authors [16-20]. It is based on the fact that the coke layer formed on the reactor surface is not inert, because the polyaromatic structure at the surface is not entirely dehydrogenated. Consequently, with the presence of significant amounts of radicals in the gas phase –very characteristic of cracking environments– hydrogen abstraction reactions from the surface can occur easily. The most active species for the abstraction are hydrogen, methyl and ethyl radicals, and the number of active sites in the surface depends on the composition of the gas phase, which is therefore a determining factor in the deposition of coke.

Radicals or molecules from the gas phase can then react with the surface radicals via addition reactions, contributing to the growth of the coke layer. Albright and Marek [16] presented an example of the reaction of a radical from the coke layer surface with methyl radicals from the gas phase, depicted in Figure 2.2.

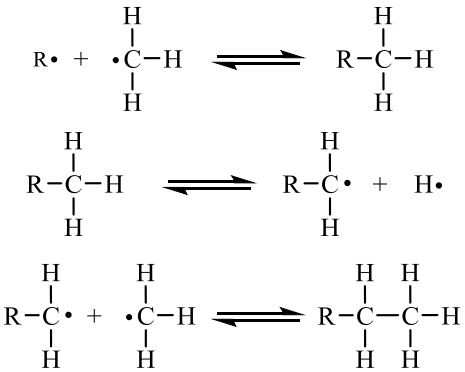

Figure 2.2: Contribution to the growth of the coke layer by reaction of surface radicals (R•) with a methyl radical [16].

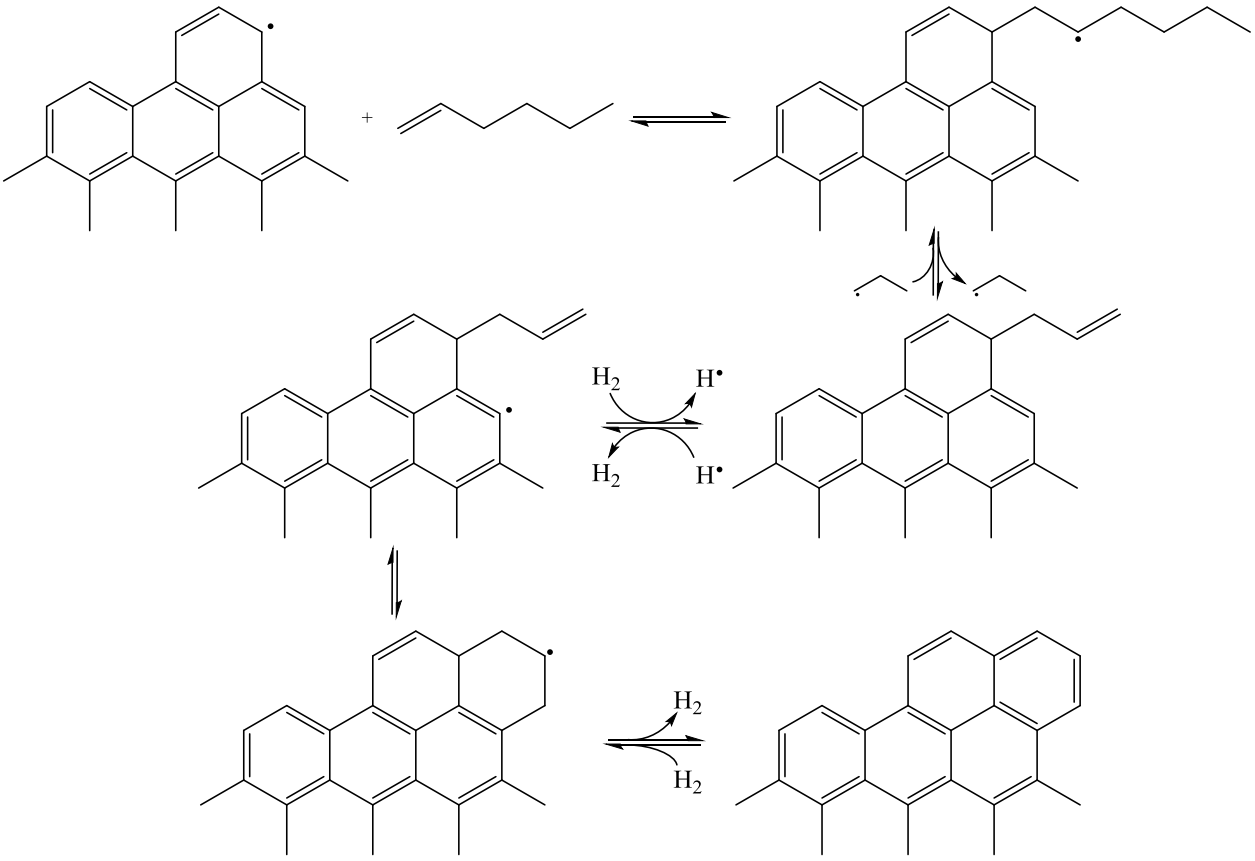

Figure 2.3: Growth of the coke layer by reaction of surface radicals with 1-hexene [18]

Another example of a reaction leading to the growth of the coke layer has been presented by Reyniers et al. [18] using 1-hexene as precursor. It is presented in Figure 2.3, and it shows that a radical at the coke surface reacts with the 1-hexene, integrating the aliphatic chain to the coke structure. After a few steps, an aromatic ring is formed, contributing this way to the growth of the coke layer. Further dehydrogenation allows the formation of new surface radicals that continue to deposit coke.

Not all the surface sites have the same reactivity. According to Wauters and Marin [20], the reactivity of a site (C-H bond in the surface of the coke layer) depends mainly on the close environment of the surface site. They grouped the sites into six different types, presented in Figure 2.4. The reactivity of each site was estimated by using the bond dissociation energy (BDE)

of the C-H bond marked with a dot. The ranking of site reactivity (from highest to lowest) is, therefore, as follows: Dibenzo[c,g]-phenanthrene > benzophenanthrene > phenanthrene, naphthalene, benzene > anthracene. Although the benzene-, naphthalene-, and phenanthrene-like sites have similar reactivities, these sites are also considered separately because of structural differences.

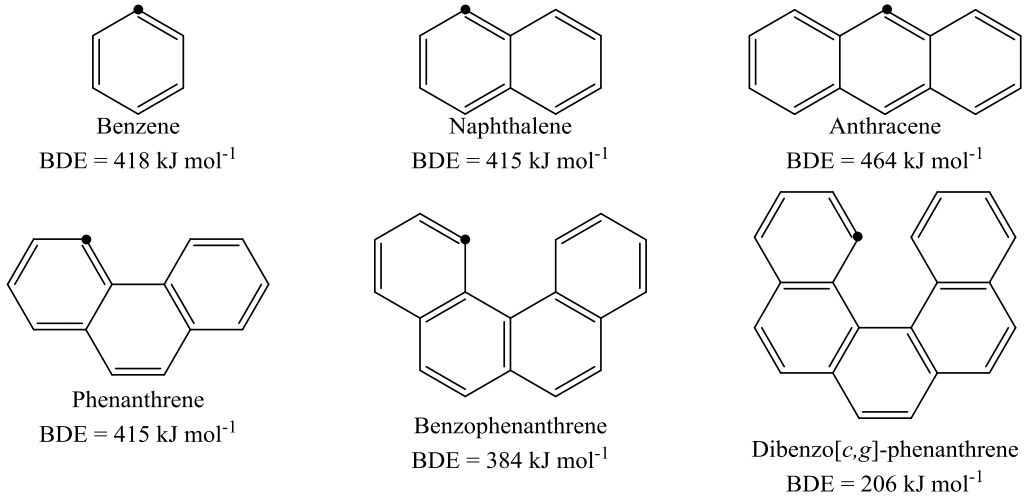

Figure 2.4: Types of coke surface sites with the corresponding BDE of the C-H bond marked with a black dot [20].

Virtually every molecule from the gas phase can act as a coke precursor, but some species are more active than others. The ^{14}C experiments of Kopinke et al. [17, 21, 22] provided a ranking of the coking tendency for a broad variety of molecules, which have been summarized by Wang [23] and are presented below in decreasing order of coking propensity:

Acetylene ≥ methylanthracenes > anthracenes > methylnaphthalenes, acetylenes (C_4^+) > cyclopentadiene, tricyclic naphthenes, mono-olefins (C_4^+), mono- and dicyclic naphthenes > propylene, ethylbenzene, xylenes, naphthenes > ethylene, paraffins, toluene > benzene > ethane > methane.

The coking propensity is not the only factor determining the contribution of each component to the coke deposition. The concentration of the components is also important. This way, although

the coking propensity of acetylene is significantly higher than that of ethylene, the contribution to coking of the latter is very important, since it is a very abundant species in the gas phase.

The large amount of potential coke precursors that are found in the gas phase implies that the number of reactions that could lead to coke formation is enormous. Nevertheless, the reactions that take place during the deposition of coke through this mechanism can be summarized following the work of Wauters and Marin [19, 20]. In order to generate a coking model that accounts for elementary reactions and that could be used independently of the feedstock, they grouped the reactions taking place during the heterogeneous non-catalytic mechanism into five classes of reversible reactions, listed below:

- Hydrogen abstraction from the surface by gas phase radicals and reverse reactions.
- Substitution by radicals at the coke surface and reverse reactions.
- Addition of a radical surface species to a gas phase olefin and the inverse β-scission of a radical surface species in a smaller surface species and a gas phase olefin.
- Addition of a gas phase radical to an olefinic bond in the coke surface and the inverse decomposition of a radical surface species to a gas phase radical and an olefinic surface species.
- Cyclization of a radical species in the coke surface and decyclization.

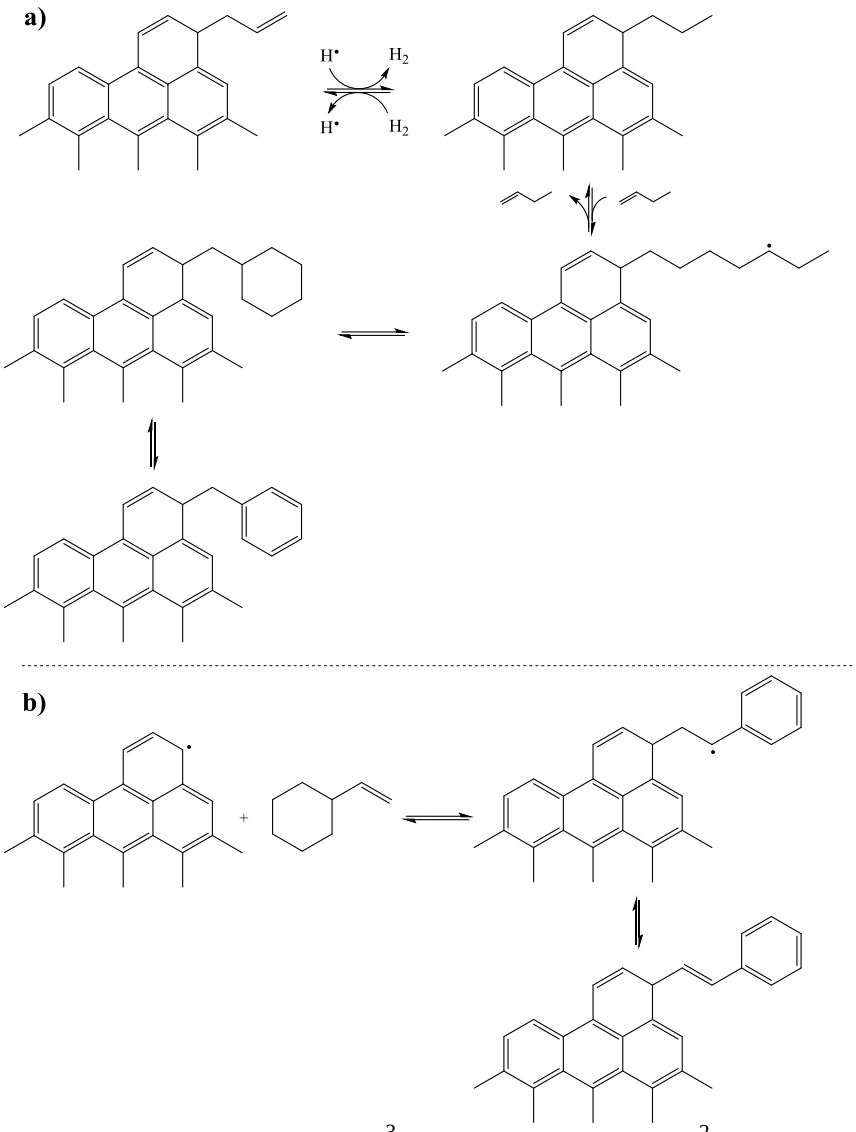

Figure 2.5: Cross-linking with (a) sp^3 carbon atom and (b) sp^2 carbon atom [18].

Typically, coke samples from ethane and naphtha crackers exhibit very low hydrogen contents [24]. This can be explained by the large amount of carbons in sp^2 hybridization that form the coke layer. These coke deposits are also very hard to drill and are not easily removed, which occurs due to cross linking with sp^2 or sp^3 carbon atoms from different layers, as suggested by Reyniers et al. [18] and presented in Figure 2.5.

2.1.3 Homogeneous noncatalytic coke formation

This mechanism is also frequently referred to as the homogeneous droplets condensation or the tar deposition mechanism. It is relevant mainly when cracking heavy feeds, such as gas oils, vacuum residue and bitumen, and in sections where the cracked gas is cooled.

The gas flowing through the reactor contains small tar droplets, giving it the appearance of a haze. Albright and Marek [16] refer to observations made by Bennett who, using an electron microscope, observed such small droplets hitting the solid surfaces. Some of the droplets that reach the surface rebound back to the gas phase, but some others adhere to the surface. It is generally accepted that these droplets consist of polyaromatic hydrocarbons (PAH) which can be present in the feed, or form as a consequence of e.g. Diels-Alder reactions [25].

With increasing cracking severity, the yields of olefins of interest (ethylene, propylene and butadiene) increase. They then reach a maximum, and eventually start to decrease. Nevertheless, the yields of other products such as hydrogen, methane and aromatic hydrocarbons keep increasing with increasing severity. This change of selectivity suggests that the olefins forming in the process successively react to form aromatic structures. Not all the gas phase hydrocarbons are equally active towards aromatization. Kopinke et al. [26] determined that 5-6 member cycloalkanes, mono and diolefins and acetylene are the most active aromatic precursors.

Sakai et al. [27] suggested an example, see Figure 2.6, of the Diels-Alder addition of butadiene to olefins yielding cyclic hydrocarbons, which ultimately produce aromatics via dehydrogenation.

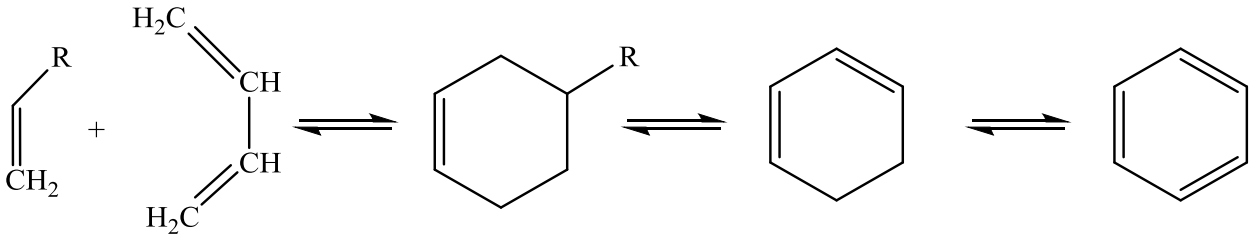

Figure 2.6: Reaction of an olefin with butadiene to ultimately yield an aromatic [27].

Another example of a reaction leading to the formation of aromatics has been suggested by Froment [28] and is presented in Figure 2.7, which considers the cyclization of higher olefins.

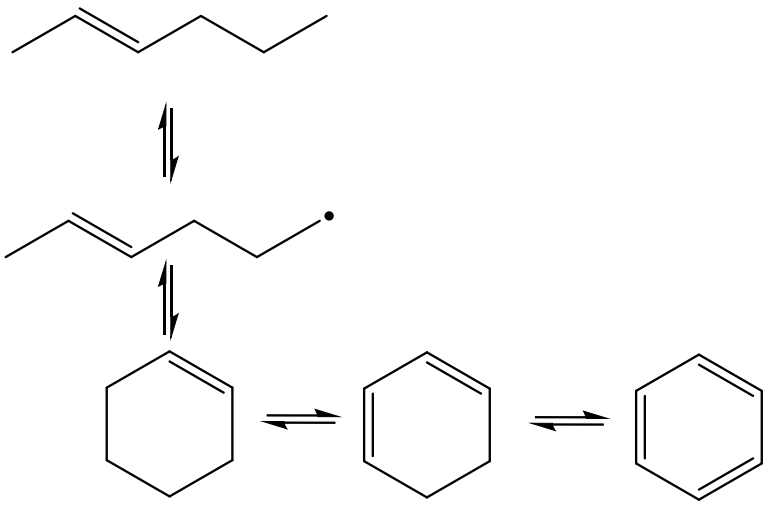

Figure 2.7: Cyclization of a higher olefin (2-hexene) yielding an aromatic [28].

The aromatics that form via the previously mentioned mechanisms react with other aromatics and other precursors, e.g. acetylene, to generate small polycyclic aromatics. Figure 2.8 presents the reaction path suggested by Frenklach et al. [29] based on studies of pyrolysis of benzene.

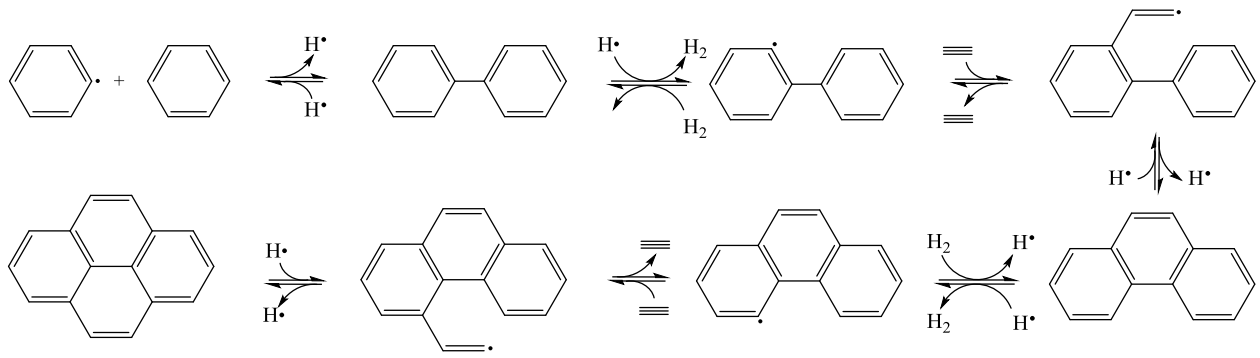

Figure 2.8: Dominant reaction pathway for the formation of small polycyclic aromatics in pyrolysis of benzene [29].

The route that the formed PAHs follow to form coke has been described by Lahaye et al [30, 31]. By nucleation and condensation, the polyaromatics form small tar droplets in the gas phase. The agglomeration of nuclei and particles can be described using the theory of collisions in the free molecular regime. Solidification occurs very slowly at temperatures below 1373 K. Therefore, under typical steam cracking conditions, solidification occurs exclusively at the reactor walls. The droplets that impinge on the surface and stay attached to it form semitar droplets, which undergo dehydrogenation until coke is formed. A schematic of the path from polynuclear aromatics to coke is presented in Figure 2.9.

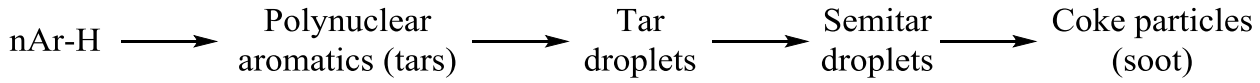

Figure 2.9: Schematic of the steps leading to formation of condensation coke [16].

The morphology of the deposited cokes depends on the porosity and wettability of the surfaces on which the droplets impinge. Higher affinity between the tars and surfaces produces smoother coke structures, whereas globular cokes are characteristic of particles with less affinity for the surface, thus conserving their spherical shape [30, 32].

2.1.4 Relevance of the coking mechanisms

Three mechanisms leading to the deposition of coke have been described. Although the three of them can eventually operate at the same time, typically one of them prevails over the other two under a given set of process conditions.

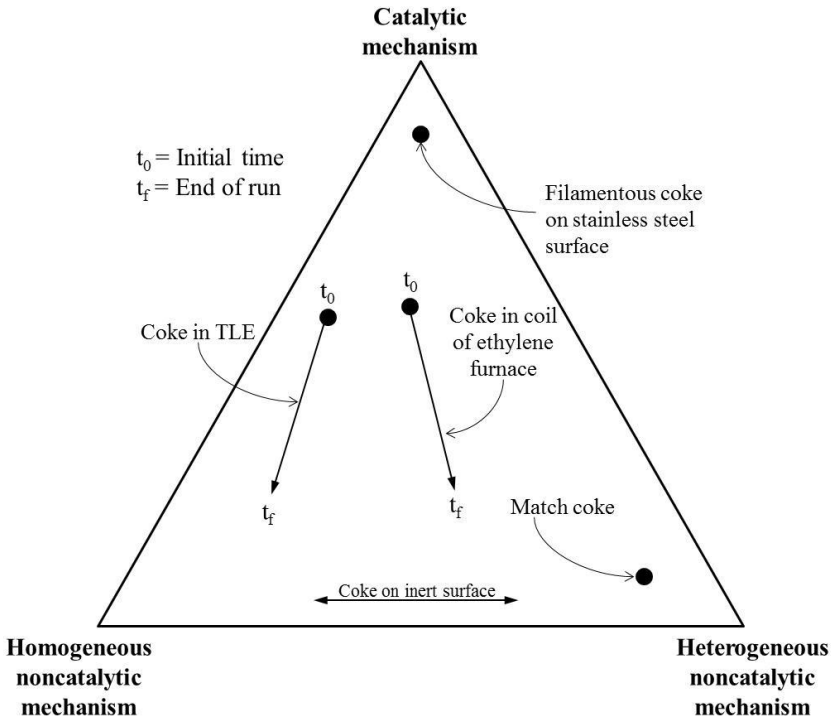

Figure 2.10: Comparison of the relative importance of the three coking mechanisms [16]

Under the typical conditions of a steam cracking reactor, the catalytic mechanism is dominant only during the early stages of cracking, while the catalytic metal particles of the coil surface are largely available. However, as the cracking run proceeds, these catalytic sites are encapsulated by the deposition of coke that forms due to the heterogeneous noncatalytic mechanism. This mechanism gains importance over time in comparison to the catalytic deposition, and becomes predominant after a few hours, which in an industrial cracking furnace is an insignificant period of time [3, 13, 17].

Finally, the homogeneous noncatalytic mechanism gains relevance when the effluent is cooled [25], as this favors condensation of heavy hydrocarbons, or if cracking temperatures are very high (above 1200K) due to the large concentration of acetylene and aromatics produced at these high temperatures [18]. This mechanism is therefore particularly important for the TLE, and almost negligible for the coil, unless heavy liquid feeds are cracked.

The interplay of these three mechanisms has been well represented by Albright and Marek [16], via the diagram presented in Figure 2.10, which illustrates the influence of each mechanism on the formation of coke in the radiant coil and TLE, taking into consideration also the time evolution as the cracking run proceeds.

2.2 Relative importance of the catalytic regime

In section 2.1.4 it was explained that, industrially, the contribution of the catalytic mechanism is practically insignificant for the total amount of coke that deposits, due to the short period of prevalence of this regime. To illustrate the relatively low importance of this mechanism, calculations for ethane and naphtha cracking have been performed.

Using experimental data obtained in an electrobalance reactor, coking rates over samples of a typical coil reactor material were determined for naphtha and ethane cracking in the initial and asymptotic regimes. The initial regime is the period at the beginning of a cracking run, when the catalytic mechanism, see section 2.1.1, is predominant. The asymptotic regime, on the other hand, refers to a later stage of the cracking run in which the heterogeneous noncatalytic mechanism is predominant, see sections 2.1.2 and 2.1.4, and the coking rate has a constant –asymptotic– value.

To do so, small rectangular coupons cut off from industrial tubes were placed inside a reactor, hanging from the arm of an electrobalance in which steam cracking of ethane and naphtha were carried out at industrially relevant conditions. The mass of the coupons was continuously

recorded, enabling to determine the rates of deposition of coke on the coupons as a function of time. Further details of the reactor, coupons, experiments and their conditions are presented in Chapter 3.

2.2.1 Naphtha cracking

Figure 2.11 presents the coking rate measured on the steel sample during a naphtha cracking experiment. It indicates that the coking rate dropped rapidly from an initial value of around 23×10^{-7} kg·m^{-2}·s^{-1} to a practically constant value of approximately 5.5×10^{-7} kg·m^{-2}·s^{-1}.

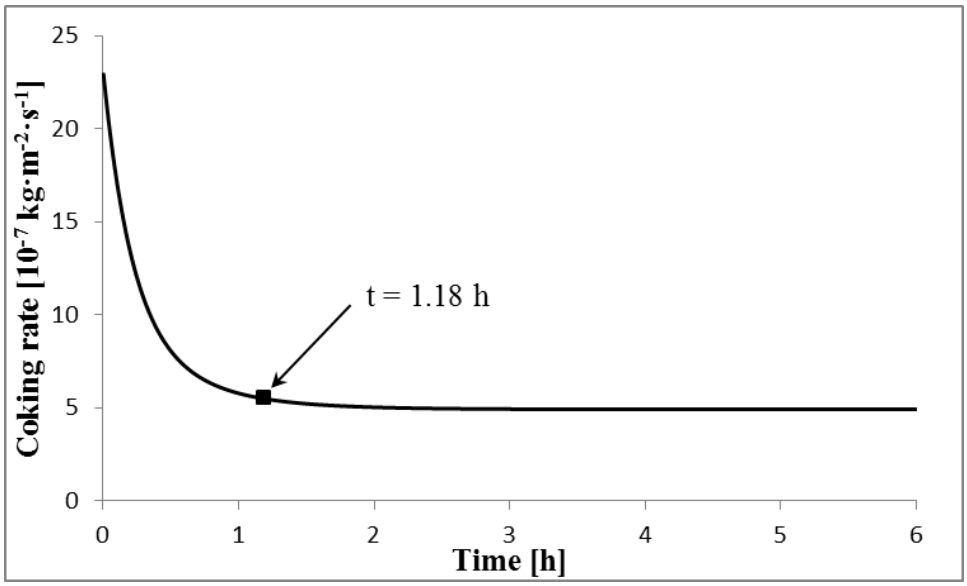

Figure 2.11: Coking rate on a steel sample as a function of cracking time during a light naphtha cracking experiment at 1098 K

The time required for the coking rate to reach the asymptotic regime is t = 1.18 hours (4260 s), as indicated in Figure 2.11. Numerical integration of the coking rate (R_c) over this time interval gives the mass of catalytic coke per unit of surface of the sample:

$$\int_0^t R_c dt = m_c \qquad (2.1)$$

Solving (2.1), the mass of coke over the sample is estimated to be $m_c = 4.95\times10^{-3}$ kg·m^{-2}. This allows to estimate a mean catalytic coking rate $R_{c,cat}$, as follows:

$$R_{c,cat} = \frac{m_c}{t} = \frac{4.95 \times 10^{-3}\ [kg \cdot m^{-2}]}{4260\ [s]} = 1.16 \times 10^{-6}\ [kg \cdot m^{-2} \cdot s^{-1}] \quad (2.2)$$

With this information and using the Arrhenius equation, a pre-exponential factor (A) can be estimated, as presented in equation (2.3). The cracking temperature of the experiments, T = 1098K, was used together with an activation energy E_a = 96.93 kJ/mol, based on the experiments of Broutin et al. [33]. The activation energy calculations can be found in Appendix A.

$$R_{c,cat} = \frac{dm_c}{dt} = A\, e^{-\frac{E_a}{R\,T}} \quad (2.3)$$

$$1.16 \times 10^{-6}\ [kg \cdot m^{-2} \cdot s^{-1}] = A\, e^{-\frac{96930\ [J \cdot mol^{-1}]}{8.314\ [J \cdot K^{-1} \cdot mol^{-1}]\ 1098\ [K]}}$$

$$A = 47.4 \times 10^{-3}\ [kg \cdot m^{-2} \cdot s^{-1}]$$

Knowing the activation energy and the pre-exponential factor, the following temperature-dependent expression for the mean catalytic coking rate can be formulated:

$$R_{c,cat} = 47.4 \times 10^{-3}\ [kg \cdot m^{-2} \cdot s^{-1}]\, e^{-\frac{96930\ [J \cdot mol^{-1}]}{8.314\ [J \cdot K^{-1} \cdot mol^{-1}]\ T\ [K]}} \quad (2.4)$$

In order to determine the duration of the catalytic coking regime in an industrial coil, data obtained by Bennett and Price [34] is used. They determined that the density of coke that had accumulated at the surface of an industrial reactor was $\rho = 1.6\times10^{3}$ kg·m^{-3}, and the thickness of the layer of catalytic coke filaments was estimated to be $h_{fil} = 1\times10^{-4}$ m. These values allow to calculate the mass of catalytic coke per unit of surface of an industrial coil (m_c):

$$m_c = h_{fil} \cdot \rho = 1 \times 10^{-4}\ [m] \times 1.6 \times 10^{3}\ [kg \cdot m^{-3}] = 0.16\ [kg \cdot m^{-2}] \quad (2.5)$$

Equation (2.3) can be rewritten in the following form:

$$dm_c = 47.4 \times 10^{-3}\ [kg \cdot m^{-2} \cdot s^{-1}]\ e^{-\frac{96930\ [J \cdot mol^{-1}]}{8.314\ [J \cdot K^{-1} \cdot mol^{-1}]\ T\ [K]}}\ dt \quad (2.6)$$

Equation (2.6) can be solved using the value estimated in equation (2.5) as boundary condition, which implies that $m_c = 0.16\ kg \cdot m^{-2}$ for a time t, allowing to formulate the following expression, which estimates the duration of the catalytic regime as a function of temperature:

$$t\ [s] = \frac{0.16\ [kg \cdot m^{-2}]}{47.4 \times 10^{-3}\ [kg \cdot m^{-2} \cdot s^{-1}]\ e^{-\frac{96930\ [J \cdot mol^{-1}]}{8.314\ [J \cdot K^{-1} \cdot mol^{-1}]\ T\ [K]}}} \quad (2.7)$$

One final consideration must be made: during the cracking experiments in the electrobalance, the metal sample was heated only by contact with the gas phase. Thus, the temperature of the gas phase was the same as that of the metal, and the gas-metal interface. Industrially, however, the heat is transferred from the coil to the gas. Hence, the temperature of the metal is higher than that of the gas, even at the gas-metal interface, which is where the catalytic reactions take place. Simulations of a naphtha cracker have indicated that the temperature at the gas-metal interface is, on average along the length of the coil, 130 K higher than the temperature of the gas [35].

Consequently, equation (2.7) has to be adjusted taking this into account so that, provided the temperature of the gas phase, the duration of the catalytic regime can be estimated:

$$t\ [s] = \frac{0.16\ [kg \cdot m^{-2}]}{47.4 \times 10^{-3}\ [kg \cdot m^{-2} \cdot s^{-1}]\ e^{-\frac{96930\ [J \cdot mol^{-1}]}{8.314\ [J \cdot K^{-1} \cdot mol^{-1}]\ (T+130)\ [K]}}} \quad (2.8)$$

With equation (2.8), the time required to reach the asymptotic regime in an industrial coil can be plotted as a function of the gas temperature.

Figure 2.12 indicates that for gas temperatures above 1100 K the asymptotic regime is reached in less than 12 hours, which accounts for less than 1% of the usual industrial run length (40 days). This shows that the asymptotic rate is vastly predominant during a naphtha cracking run.

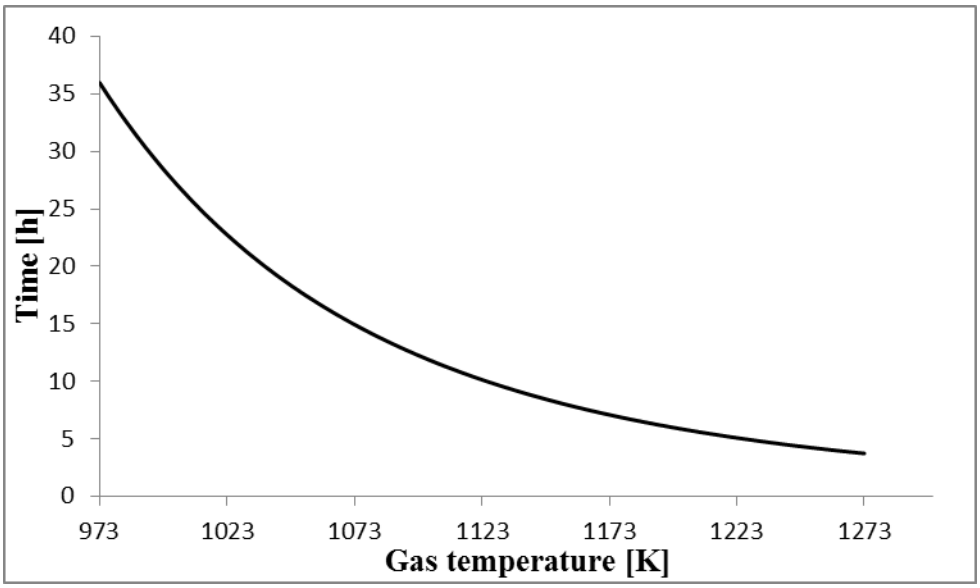

Figure 2.12: Estimated time to reach the asymptotic coking regime as a function of the gas phase temperature in an industrial coil made of a typical steel during steam cracking of a light naphtha.

2.2.2 Ethane cracking

Analogous to what was done for naphtha cracking, Figure 2.13 presents the coking rate measured during ethane cracking over a sample of the same typical alloy used for the naphtha cracking experiments. The coking rate rapidly dropped from 25×10^{-7} kg·m^{-2}·s^{-1} to an asymptotic rate of 4.2×10^{-7} kg·m^{-2}·s^{-1}.

The experimental data for ethane cracking indicates that the time to reach this asymptotic rate was t= 3.04 hours (10960 s), as indicated in Figure 2.13. Solving (2.1) with these values, m_c is estimated to be 9.90×10^{-3} kg·m^{-2}.

The mean catalytic coking rate can then be calculated, implementing the appropriate values for ethane cracking in equation (2.2):

$$R_{c,cat} = \frac{m_c}{t} \tag{2.2}$$

$$R_{c,cat} = \frac{9.90 \times 10^{-3}\ [kg \cdot m^{-2}]}{10960\ [s]} = 9.03 \times 10^{-7}\ [kg \cdot m^{-2} \cdot s^{-1}]$$

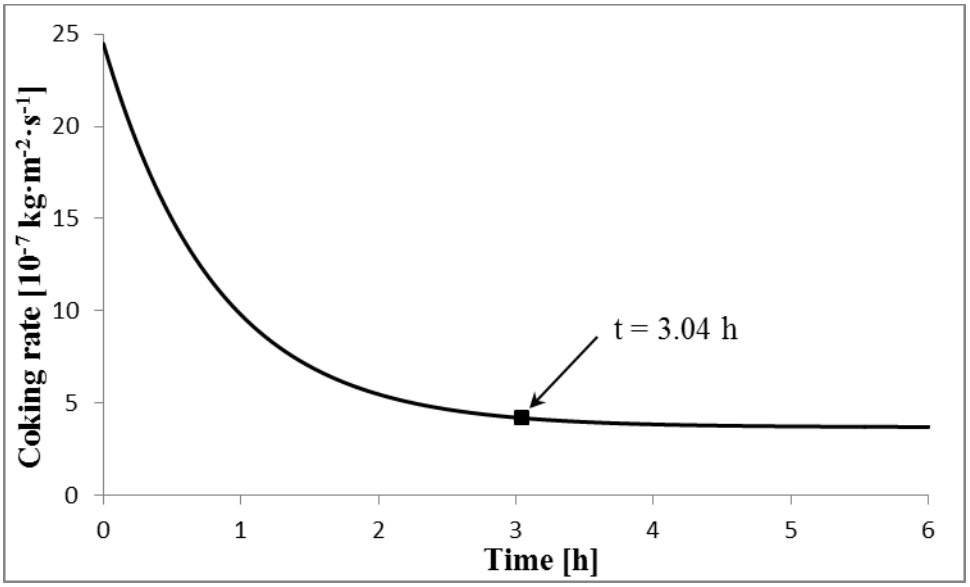

Figure 2.13: Coking rate on a steel sample as a function of cracking time during ethane cracking at 1159 K

A Pre-exponential factor (A) can be calculated using equation (2.3), using an activation energy E_a = 167.5 kJ/mol and the temperature used in the experiments, T = 1159 K.

$$R_{c,cat} = \frac{dm_c}{dt} = A\, e^{-\frac{E_a}{R\,T}} \tag{2.3}$$

$$9.03 \times 10^{-7}\ [kg \cdot m^{-2} \cdot s^{-1}] = A\, e^{-\frac{167500\ [J \cdot mol^{-1}]}{8.314\ [J \cdot K^{-1} \cdot mol^{-1}]\ 1159\ [K]}}$$

$$A = 32.0 \times 10^{-3}\ [kg \cdot m^{-2} \cdot s^{-1}]$$

This allows to propose an expression for the mean catalytic coking rate as a function of temperature, analogous to equation (2.4):

$$R_{c,cat} = 32.0 \times 10^{-3}\ [kg \cdot m^{-2} \cdot s^{-1}]\ e^{-\frac{167500\ [J \cdot mol^{-1}]}{8.314\ [J \cdot K^{-1} \cdot mol^{-1}]\ T\ [K]}} \quad (2.9)$$

As mentioned in the calculations for naphtha cracking, the gas temperature is not the same as that of the gas-metal interface in an industrial coil. For ethane cracking, the difference of the gas and gas-metal interface temperatures was estimated to be 60 K along the length of the coil [36]. Implementing this into equation (2.9), and assuming that the same mass of catalytic cokes deposits per unit of surface area as in the calculation for naphtha cracking (0.16 $kg \cdot m^{-2}$), an analogous expression to (2.8) can be presented, to calculate the time t required to reach the asymptotic regime during ethane cracking in an industrial coil, as a function of its gas temperature.

$$t\ [s] = \frac{0.16\ [kg \cdot m^{-2}]}{32.0 \times 10^{-3}\ [kg \cdot m^{-2} \cdot s^{-1}]\ e^{-\frac{167500\ [J \cdot mol^{-1}]}{8.314\ [J \cdot K^{-1} \cdot mol^{-1}]\ (T+60)\ [K]}}} \quad (2.10)$$

Using equation (2.10), it can be determined that, above 1123 K, the catalytic activity should last 35 hours. This corresponds to less than 4% of the usual run length. Figure 2.14 shows the estimated time required to reach the asymptotic regime for a vast range of relevant temperatures.

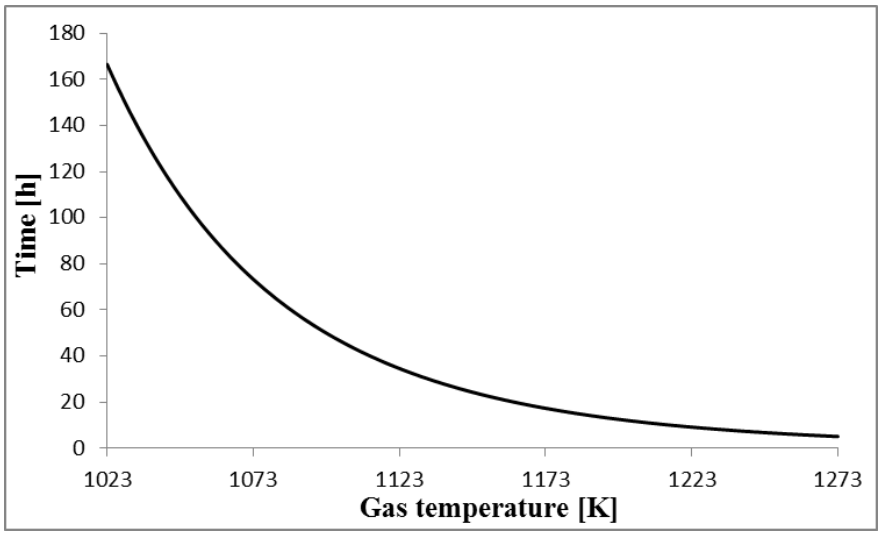

Figure 2.14: Estimated time to reach the asymptotic coking regime as a function of the gas phase temperature in an industrial coil made of a typical steel during steam cracking of ethane.

The results confirm that the coke deposited during the catalytic regime of ethane cracking have a very low impact on the total amount of cokes deposited through an entire industrial operation cycle.

2.2.3 Comparison of naphtha and ethane cracking

With the results obtained for both feedstocks, a comparison can be made between the length of the catalytic regime over the same coil material for different feedstocks. From Figure 2.15 it is obvious that the catalytic effect is significantly less pronounced during naphtha cracking than during ethane cracking.

Although for ethane it takes roughly four times longer to reach the asymptotic regime than for naphtha cracking, in both cases the amount deposited during the catalytic stage is practically negligible, supporting the statement that the asymptotic coking rate is the one that actually determines the amount of cokes that will be deposited inside the coil after a normal industrial run.

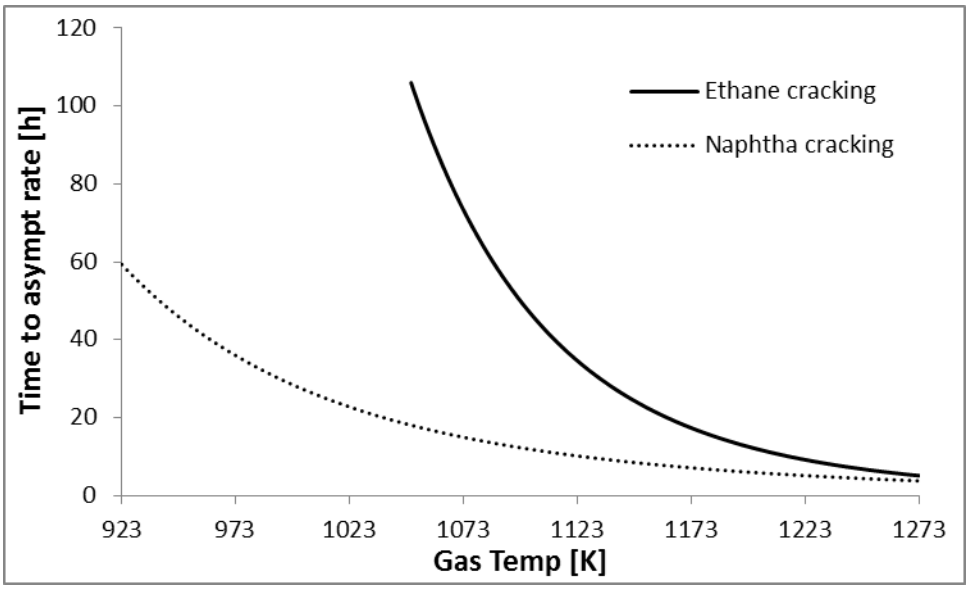

Figure 2.15: Comparison of the time required to reach asymptotic regime during steam cracking of ethane and naphtha as a function of temperature in a coil made of a typical steel.

2.3 Kinetic models for coke formation

As shown in Sections 1.3 and 1.4 of Chapter 1, the deposition of coke has a large impact on the process and its economics. This has motivated a vast number of investigations leading to propose models that could estimate the rates of coke deposition for a determined set of conditions, allowing thus to predict run lengths.

The coking models that have been developed can be grouped into three different categories, namely empirical, semi-empirical and fundamental models. Empirical models use a simple overall reaction rate equation which is then fitted to experimental data. Semi-empirical models are more elaborate, because they consider the reactions assumed to be the most important, while keeping the model still relatively simple. Finally, fundamental models take into account a vast set of elementary reactions leading to coke formation.

2.3.1 Empirical models

Sundaram and Froment postulated a model based on their experimental study of coke formation during propane pyrolysis using a CSTR equipped with an electrobalance [37]. Their proposed mechanism is presented in equations (2.11) and (2.12).

$$C_3H_8 \xrightarrow{K_1} \text{Products} \tag{2.11}$$

$$C_3H_6 \xrightarrow{K_2} \text{Coke} \tag{2.12}$$

The rate equation for this model is presented in Table 2.1, which also includes the rate equations of the other empirical models described in this section. For all of them, the activation energy is expressed in $J \cdot mol^{-1}$.

Table 2.1: Coking rate expressions of some empirical coke formation models

Model	Coking rate equation	Rate units
Sundaram and Froment (C_3H_6)	$R_c = 1.08 \times 10^9 \, e^{(-313700/R\cdot T)} \, C_{C_3H_6}$	[kg·m^{-2}·s^{-1}]
Sundaram and Froment (C_2H_4)	$R_c = 8.55 \times 10^2 \, e^{(-118100/R\cdot T)} \, C_{C_2H_4}$	[kg·m^{-2}·s^{-1}]
Pramanik and Kunzru	$R_c = 7.54 \times 10^9 \, e^{(-98400/R\cdot T)} \, C_{C_2H_4}^{2.4}$	[kg·m^{-2}·s^{-1}]
Zou et al. (C_3H_6)	$R_c = 9.82 \times 10^6 e^{(-230290/R\cdot T)} \, C_{C_2H_4} + 3.68 \times 10^4 e^{(-165220/R\,T)} \, C_{C_3H_6}^{1/3}$	[kg·m^{-2}·s^{-1}]
Zou et al. (AGO)	$R_c = 5.00 \times 10^8 e^{(-224000/R\cdot T)} \, C_{C_2H_4}^{1.34} + 1.39 \times 10^6 e^{(-141000/R\,T)} \, C_{C_{Arom.}}^{1.37}$	[kg·m^{-2}·s^{-1}]

In later work, Sundaram et al. [38] developed another model, this time for ethane cracking. Analogous to the one for propane cracking, their proposed model is based on equations (2.13) and (2.14), which indicate that C_4^+ components (butadiene and benzene**)** are considered the main precursors. For the rate expression, C_{C4+} is expressed in $kg_{C4+}\cdot m^{-3}$.

$$C_2H_6 \xrightarrow{K_1} \text{Products} \tag{2.13}$$

$$C_4^+ \xrightarrow{K_2} \text{Coke} \tag{2.14}$$

Pramanik and Kunzru also proposed a model for the pyrolysis of ethane [39], based on equations (2.15) and (2.16). The chosen coke precursor was ethylene. In contrast to the models of Sundaram and Froment, the reaction order of ethylene is 2.4.

$$C_6H_{14} \xrightarrow{K_1} \text{Products} \tag{2.15}$$

$$C_2H_4 \xrightarrow{K_2} \text{Coke} \tag{2.16}$$

Zou et al. [40] derived another model for coke formation of propane, in which two precursors (i.e. ethylene and propylene) are taken into consideration. The mechanism is presented in equations (2.17) and (2.18), and the expression for the coking rate, depicting the individual contributions of each precursor in the overall coke formation rate, is presented in Table 2.1.

$$C_2H_4 \xrightarrow{K_1} \text{Coke} \tag{2.17}$$

$$\frac{1}{3}C_3H_6 \xrightarrow{K_2} \text{Coke} \tag{2.18}$$

Additionally, a kinetic model for coke deposition during AGO pyrolysis was developed by Zou et al. [41]. Given the nature of the feed, ethylene and aromatics (Arom.) were taken as precursors, as can be seen from equations (2.19) and (2.20). They considered that aromatics have a more significant role in the coke deposition than ethylene.

$$C_2H_4 \xrightarrow{K_1} \text{Products} \tag{2.19}$$

$$\text{Arom.} \xrightarrow{K_2} \text{Coke} \tag{2.20}$$

2.3.2 Semi-empirical models

These models involve the determination of the coking rate based on a simple model that includes the most important reactions involved.

Plehiers developed a model for coke formation during steam cracking of light feeds [42], based on the rate expressions for coke formation in the thermal cracking of propane and ethane derived by Sundaram and Froment [37] and Sundaram et al. [38]. Further experiments carried out with mixtures of light hydrocarbons and naphthas in a microreactor and in a pilot plant led to a coking model in which a number of precursors contribute to the formation of coke. No specific

information of the details of the model is given in open literature, but a number of precursors contribute to the formation of coke in this model. It has been represented by equation (2.21), where $r_{C,i}$ are the individual rates of coke deposition for each precursor.

$$R_C = \sum r_{C,i} \xrightarrow{K_1} \text{Coke} \tag{2.21}$$

The good estimation of run lengths that this model has achieved, has made it widely used for other works presented in literature [36, 42-44].

Another model was developed by Reyniers et al. [18] for the simulation of coke formation during steam cracking of naphthas. Due to the nature of the feed, and as was explained in Section 2.1.3, the coke precursors for this model are olefins and aromatics. To limit the number of reactions to be considered, the number of precursors was restricted to 12. The C_5^+ olefins were excluded because typically they are present in very low concentrations and because their paraffinic branch is usually cracked, yielding a C_4^- olefin. To reduce the parameters to be estimated, the precursors are grouped depending on their characteristic function (double bond, triple bond, aromatic ring, …). The activation energy for the reactions of coke radicals with elements of a same group are all assumed to have the same activation energy.

This model assumes that all the radicals at the surface have the same reactivity. The precursors are assumed to add to these sites, continuously regenerating the radical positions. Also, the number of carbon atoms adding to the coke on each reaction layer equals the carbon of the precursor. An example of the reaction between a precursor (C_2H_4 in this case) and a surface site is presented in equation (2.22), in which the sites are represented by R•.

$$R\bullet + C_2H_4 \longrightarrow R\bullet + 2C + 2H_2 \tag{2.22}$$

The rate of coke deposition for this reaction is presented in equation (2.23).

$$R_C = 2\, k_{C_P} \cdot C_{C_2H_4} \tag{2.23}$$

Since the most abundant and active radicals in the gas phase are H and CH_3 and they are the main species abstracting hydrogen from the coke surface to generate surface radicals, the concentration of hydrogen and methane are taken to be proportional to that of H' and CH3', respectively. Equation (2.23) can then be rewritten as follows:

$$R_C = \left(C_{H_2}\, C_{CH_4}\right) k_{C_2H_4} C_{C_2H_4} \tag{2.24}$$

Using the same approach for all the other precursors, the global rate of coke formation can be expressed as

$$R_C = C_{H_2}\, C_{CH_4} \sum_{i=1}^{12} k_i C_i \tag{2.25}$$

The values of k_i are estimated by means of the relative rate constants estimated by Kopinke et al. [17, 21, 22].

Another model has been presented by Towfighi et al. [45], based on data obtained from a small steam cracking unit. In a very similar manner to the work of Reyniers et al. [46], seven precursors (ethylene, propylene, 1,3-butadiene, benzene, toluene, xylene and styrene) were selected, and then grouped into three classes of precursors of equal activation energy: olefins, dienes and aromatics. Using the relative rates of coking of Kopinke et al [17], an expression for the coking rate can be obtained, and is presented in equation (2.26):

$$R_c = \left(C_{CH_4}\, C_{H_2}\right)\{A_1 e^{\left(-\frac{E_1}{RT}\right)}\left[k_{C_2H_4}\, C_{C_2H_4} + k_{C_3H_6} C_{C_3H_6}\right] + A_2 e^{(-E_2/RT)}\, C_{C_4H_6} + A_3 e^{(-E_3/RT)}\left[k_{C_6H_6}\, C_{C_6H_6} + k_{C_7H_8}\, C_{C_7H_8} + k_{Xylenes}\, C_{Xylenes} + k_{C_8H_8}\, C_{C_8H_8}\right] \quad (2.26)$$

The parameters for this model are presented in Table 2.2.

Table 2.2: Parameters for the coking model of Towfighi et al. [45].

i	E_i	A_i	Component	k [-]
	[kJ·mol^{-1}]	[kg·m^{-2}·s^{-1}·(m^3·mol^{-1})^3]		
1	74.16	2.183×10^{-4}	C_2H_4	0.73
2	127.94	5.831×10^{-1}	C_3H_6	1.03
3	29.98	1.163×10^{-4}	C_6H_6	0.30
			C_7H_8	0.62
			Xylenes	1.00
			C_8H_8	0.80

2.3.3 Fundamental models

The coking models that have been presented so far take into consideration experimental observations and data regressions, in order to provide coking rate values for a certain gas phase or temperature. Although they can simulate industrial run lengths quite accurately, the semi-empirical models lack sufficient fundamental background to make them robust and applicable under a wider set of conditions and feedstocks.

With these considerations, Wauters and Marin developed a fundamental model based on elementary reactions between process gas components and the surface species on the coke

surface [19, 20]. No lumps are introduced but the specific reaction possibilities of each component are incorporated. This way, the kinetic parameters are independent of the feedstock.

This model accounts only for the heterogeneous non catalytic mechanism, due to its largely predominant role throughout the run length of the coil, as discussed in Sections 2.1.4 and 2.2. The coke layer is represented by a flat polyaromatic structure consisting of conjugated benzene rings.

The elementary reactions that are taken into consideration have been classified into 5 classes of reversible reactions, already listed in Section 2.1.2. The cleavage of C-C and C-H bonds was not taken into account, because their rates are much lower than those of the considered reaction classes.

The coke precursors in this model are H, CH_3, C_2H_5 and C_3H_5 radicals, as well as acetylene, ethylene, propadiene and propylene. Also, it was assumed that the coke surface is exclusively formed by six membered rings. According to Frenklach et al. [47], gas phase kinetic data can be used to describe reactions involving solid reagents if accurate alterations based on collision theory are applied to the gas-phase kinetic data to account for the presence of the solid.

In total, more than 14000 reactions between more than 2000 species constituted the network for ethane cracking. The large number of kinetic parameters that they would require was largely reduced by selecting a reference molecule in each of the five considered reaction classes. The difference between the reactions in the same class were accounted for using structural contribution theory described in the work of Willems and Froment [48, 49].

Based on a sensitivity analysis, this model indicated that addition by gas phase radicals to unsaturated bonds in the surface has a minor influence in the deposition of coke, compared to the importance of hydrogen abstractions, substitutions, and addition to gas phase olefins.

SPYRO is another model, developed by Pyrotec [50]. It describes not only the coke formation, but also the thermal cracking itself, with the ultimate purpose of industrial coil simulations.

It uses seven classes of elementary reactions, both radical and molecular. To reduce the amount of data that is required, the kinetic parameters of a single hydrogen abstraction are assumed to depend only on the type of H (primary, secondary, …) and the attacking radical, with no influence of the molecule to which H is attached. This approach is also taken for the other classes of elementary reactions.

Three main assumptions are made in this model. The first one is that the coke layer is covered with a continuous layer of polymeric material, that eventually transforms into coke. Steam is practically inactive for coke removal under these conditions. Secondly, the addition of unsaturated radicals or molecules to the surface of the polymeric layer is the limiting step. Vinylic and phenylic radicals are coke precursors, whereas unsaturated hydrocarbons react via Diels-Alder reactions and get integrated directly into the growing surface. Finally, the effective radicals are produced by reactions in the gas phase very close to the surface, which occur therefore at temperatures very close to those of the coke deposit.

2.4 Effect of temperature on the coking rate

To illustrate the large impact that temperature has on the rate of coke deposition, the model for coke deposition developed by Plehiers, presented in Section 2.3.2, can be applied to the conditions of a simulated ethane cracking furnace, like the one used in Section 1.3.

Three different coil outlet temperatures are tested (i.e. 1103 K, 1123 K and 1143 K). The temperature profile along the reactor for each COT is presented in Figure 2.16. The inlet temperature was 929 K for all cases.

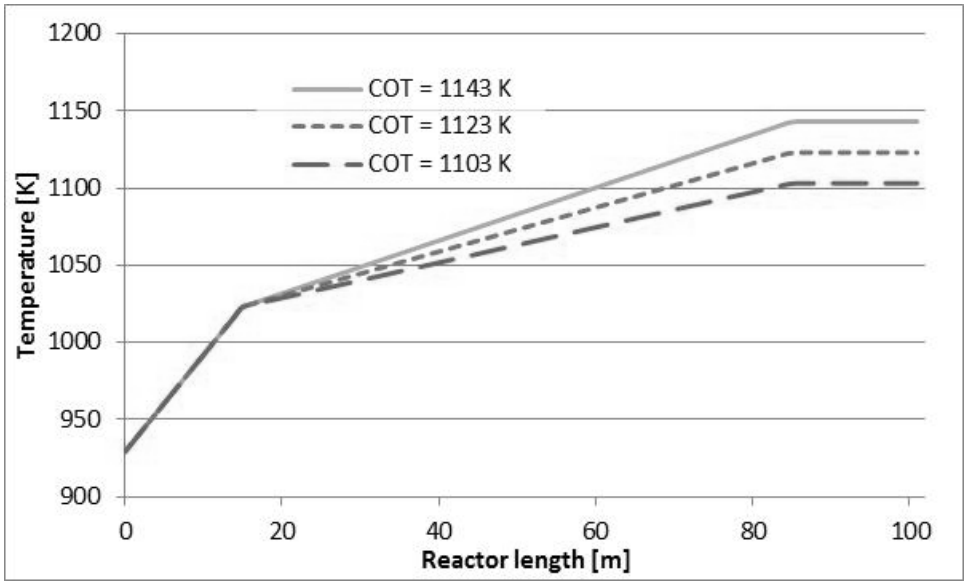

Figure 2.16: Temperature of the gas phase as a function of the reactor length for three different COTs.

Evidently, different reactor temperatures lead also to different gas phase compositions. Using the reaction network developed for ethane cracking by Sabbe et al. [51], the molar fractions of ethylene and propylene have been estimated as a function of the reactor length for each COT, and are presented in Figure 2.17 and Figure 2.18, respectively.

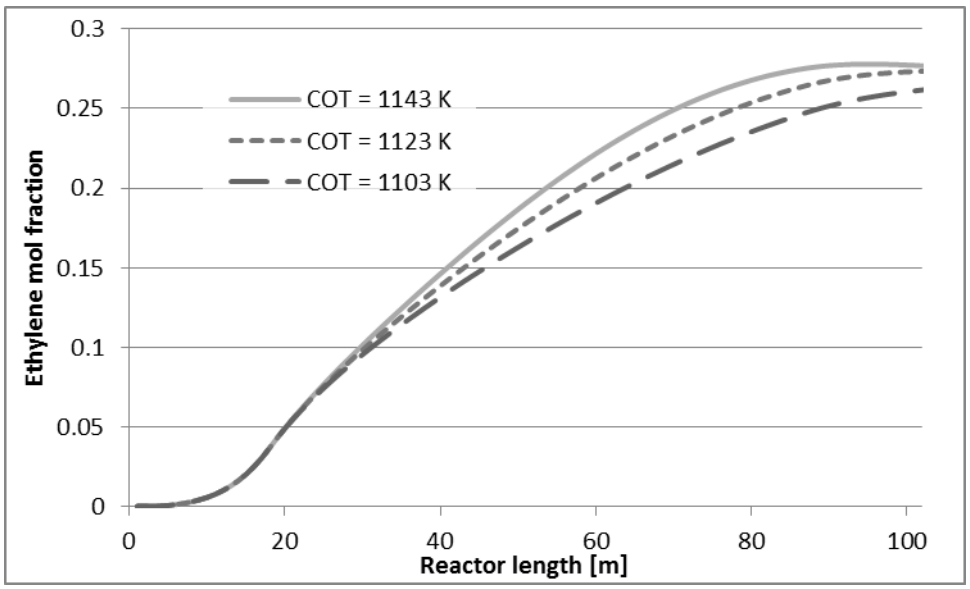

Figure 2.17: Ethylene mol fraction (wet) as a function of reactor length.

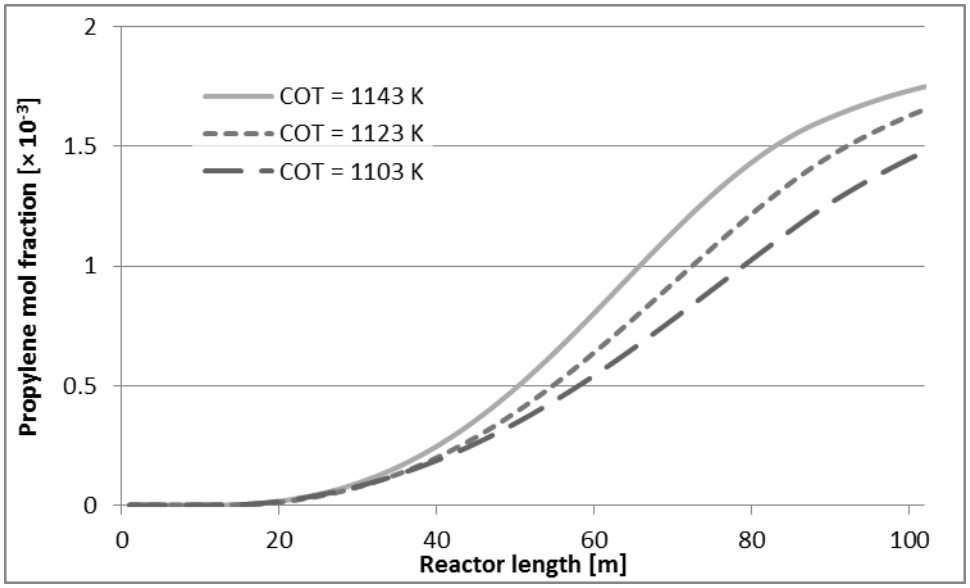

Figure 2.18: Propylene mol fraction (wet) as a function of reactor length.

Ethylene and propylene are the only coke precursors considered in the model of Plehiers. Since the gas phase temperature and the concentration of these components is known for each point of the reactor, the coking rate can be easily calculated. The calculated coking rate is plotted as a function of the reactor length in Figure 2.19.

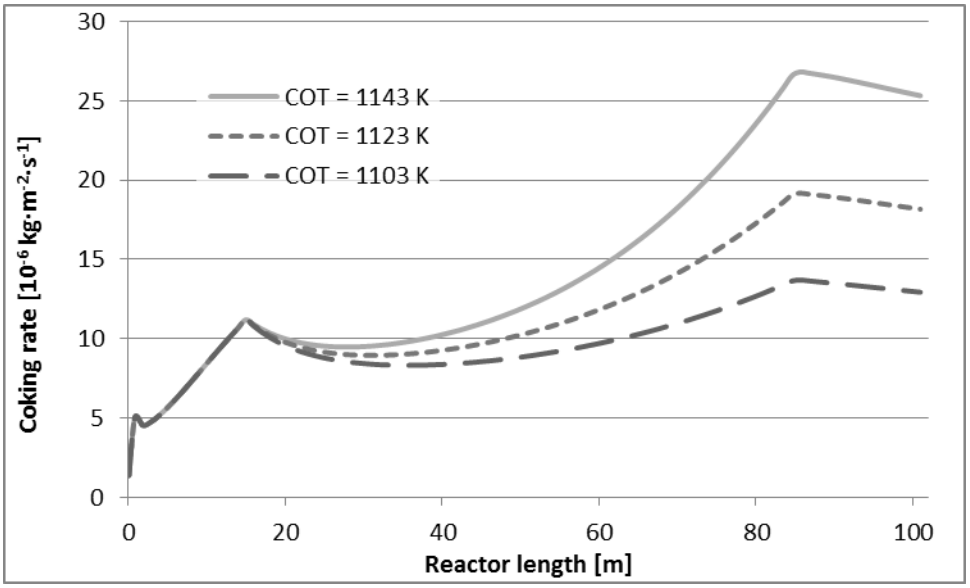

Figure 2.19: Coking rate as a function of reactor length, using the coking model of Plehiers.

It is clear that the calculated coking rates increase dramatically with increasing temperature. Comparison of the calculated coking rates indicates that for a COT of 1143 K the rate is twice as high as the one calculated for an outlet temperature of 1103 K.

Although the temperature has a certain effect on the gas phase composition, Figure 2.17 and Figure 2.18 clearly indicate that for the three tested temperatures the gas phase is not significantly changed. The effect of these small changes can thus be practically neglected, attributing the large change of coking rate to the effect of temperature variations only.

These observations are logical considering the form of the rate equation. There, the temperature affects the kinetic coefficients exponentially, whereas the concentration of precursors are raised to the power of the reaction order. It is evident from this point of view that temperature has a larger impact on the rates of coke deposition than the gas phase composition.

2.5 Reactor materials and their pretreatments

2.5.1 Materials development

In Section 1.2, the usual operating conditions of steam cracking units were presented. Clearly, the reactor coil is subjected to very aggressive conditions: Very high temperatures (reaching even 1425 K) are combined with alternating highly carburizing and highly oxidizing atmospheres during cracking and decoking operations, respectively. This is very harmful for the lifetime of alloys.

The material from which the reactor is constructed has to be, therefore, very resistant to high temperatures. Other properties must also be taken into consideration too, such as weldability, high resistance to carburization, thermal fatigue and creep, while trying to develop surface compositions that are as inert as possible to the deposition of carbon. Sometimes enhancing one

of these properties affects another characteristic, making it very complicated to find an adequate tradeoff that maximizes the performance and lifetime of the coils, while being still economically competitive [52-56].

The reactors are typically constructed of a steel comprised of iron, nickel and chromium with small additions of other elements, intended to enhance various properties of the alloy. The composition of the materials has evolved with time, as a response to the imposition of higher cracking severities aimed at process intensification.

Verdier and Carpentier [56] presented a brief review of the history of the materials for steam cracking coils, like the one presented in Figure 2.20. The first alloy mentioned is HK40. Its formulation has 25 wt% of chromium and 20 wt% of nickel, with 0.4 wt% of carbon [54]. Later, HP alloys were developed to reach higher temperatures and improve the resistance to creep. These alloys increased nickel and chromium contents to 35 wt% and 25 wt%, respectively, having a carbon content of 0.5 wt% [57]. Ibarra [52] suggested that, among this kind of alloys, an alloy (Supertherm) with 28 wt% Cr, 35 wt% Ni, 5 wt% W, 15 wt% Co and 0.5 wt% C showed the best protection to carburization, but its cost was high.

Further improvement of alloys was made by adding niobium to HP alloys, which increased creep resistance. In parallel, new alloys with higher contents in chromium (35 wt%) and nickel (45 wt%) were developed. They are commonly called 35/45 alloys, and their main objective is to increase protection to carburization by formation of a layer of chromium oxide at their surface [54, 56, 58].

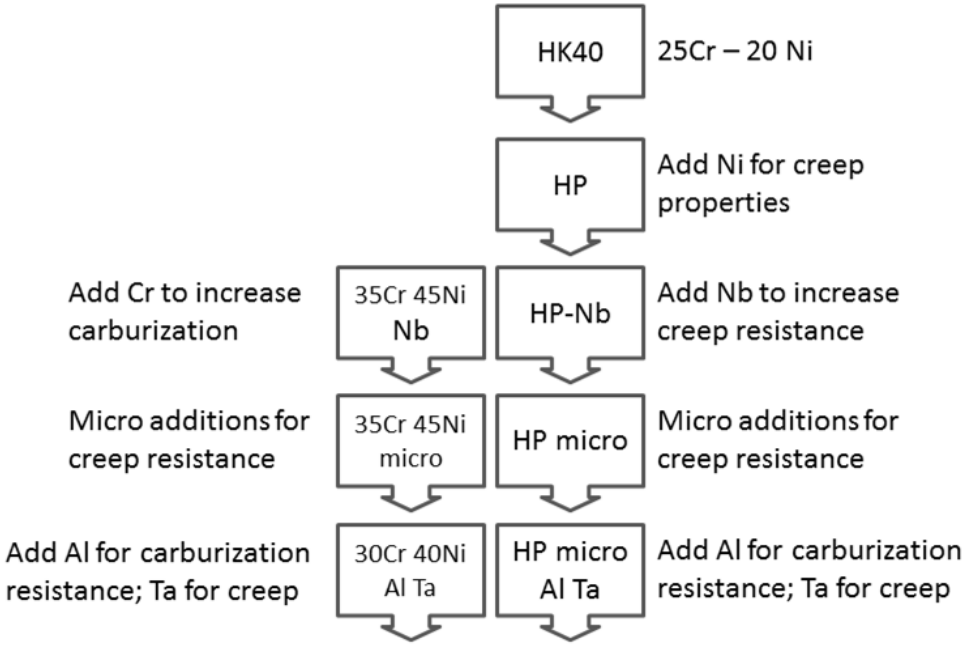

Figure 2.20: Historical summary of the evolution of steam cracking coil alloys [56].

Other improvement to the 25/35 and 35/45 alloys was made by inclusion of micro additions, e.g. Si, Mn, Nb, Mo, W, Ti, mainly intending to increase creep resistance and mechanical properties [55].

Finally, the inclusion of aluminum in the formulation of alloys has been the latest trend. Aluminum is included so that it can form a layer of aluminum oxide at the surface, protecting the reactor from carburization. Alumina is reported to be very stable at high temperatures, and remarkably inert to the deposition of coke [59-62].

It becomes obvious that, at the current state of the art, two main trends exist in the formulation of alloys for reduction of coke deposition. The first one comprises the group of alloys that rely on the formation of chromium oxides in the surface. The second group relies on surface aluminum oxides, instead.

2.5.2 Pretreatments and coatings

The bulk composition of the alloys largely determines their mechanical properties. However, it is the composition of the internal surface of the coil that affects the rates of coke deposition [63-65]. Consequently, significant efforts have been made to determine pretreatments [3, 66-68] that could modify the surface composition and form thermally stable and inert layers. Also coatings [5, 33, 69-75] have been developed aiming at reducing coke deposition by applying protective layers at the internal surface of the reactor.

2.5.2.1 Preoxidation

The most frequent way to pretreat a coil is preoxidation. It intends to form a protective layer of oxides that covers the bulk, and prevents the gas phase from being in contact with the coke promoting metals that constitute the alloy. The preoxidation is usually carried out by feeding air, steam, or a mix thereof to the reactor [76].

Two main characteristics can be typically identified in oxidized Fe-Cr-Ni alloys: the alloy surface is enriched with chromium, whereas iron and nickel are significantly depleted from the chromium-rich surface. This occurs due to the formation of a chromium oxide layer (chromia, Cr_2O_3) [34, 66, 77-80]. Holmen and Lindvåg [57], Browne et al. [4], and Wu et al. [81] have attributed lower coking rates in oxidized steels to the formation of a chromia layer that reduces or eliminates the contact between the gas phase and the active metals of the coil, like nickel and iron. Nevertheless, chromia layers eventually carburize[77] and spall as a consequence of, e.g. thermal changes [82], affecting the behavior of the alloy. Chromia evaporation is also a potential problem at high temperatures [83].

The elements that are added in small amounts (mainly Si and Mn) to these so-called "chromia-forming" alloys aid stabilizing their surface oxides. Manganese helps to form a spinel structure,

namely manganese chromite ($MnCr_2O_4$) which, besides being inert to the deposition of cokes, is very stable under a wide range of temperatures and atmospheres [84-86]. Formation of this spinel occurs by reaction of MnO and Cr_2O_3 [78]. Since the amount of manganese in the coils is much lower than that of chromium, significant amounts of chromia can still be present below the layer of manganese chromite [84].

The addition of silicon is also important for the coking resistance: under oxidizing atmospheres, it forms silica (SiO_2). This compound is a very good barrier to diffusion of carbon inwards, preventing carburization of the alloy [4, 62, 78, 86]. When present in enough quantities in the alloy, silica can form a uniform layer underneath the chromia offering a good protection. However, Liu et al. [78] mentioned that this layer could also block the migration of chromium and manganese to the uppermost surface of the alloy, not allowing the $MnCr_2O_4$ and Cr_2O_3 layers to regenerate, which could cause a negative impact in the long-term behavior of the alloy.

As mentioned in section 2.5.1, adding aluminum to the alloys is a recent trend in alloy development. When these alloys are exposed to oxidizing atmospheres, they form a layer of alumina (Al_2O_3) at the uppermost surface [87]. Alumina is very inert towards coke formation, and has a very high thermal stability [88]. Various authors [5, 59, 60, 89, 90] have, indeed, reported lower coking rates when performing steam cracking of hydrocarbons over Al-containing alloys. Jakobi et al. [91] compared alumina-forming alloys with chromia-forming alloys under a simulated cracking atmosphere. The results favor the stability of alumina over chromium and manganese chromite layers at high temperatures. However, excessive contents of aluminum in the alloy can lead to internal oxidation, which is very harmful for the alloys [56, 61].

Alumina forming alloys can also form other surface oxides, such as the spinel-structured manganese aluminate ($MnAl_2O_4$) and nickel aluminate ($NiAl_2O_4$) [76, 87, 92]. Manganese aluminate can easily migrate to the surface of the alloys, and is also resistant to the deposition of

coke [93]. Manganese aluminate, however, has been reported to decompose under reducing conditions leading to the formation of particles of elemental Ni [94], significantly enhancing coke deposition as a consequence [95].

The kinetics of the growth of oxide layers follows a parabolic rate, and the temperature and partial pressure of oxygen are the most determining factors [76, 96]. According to Koshelev et al. [77], during the initial stages of oxidation of Fe-Cr-Ni alloys, Fe_2O_3 is abundant at the surface. However, as time elapses and an oxide layer is formed at the surface, its abundance relative to that of Cr_2O_3 decreases significantly, because the rate is controlled by solid-state diffusion in the oxide [80], and chromium can diffuse much faster through the oxide layer than iron. Practically no Fe_2O_3 can be found in the oxide layer after oxidation at 1023 K during 16 hours [77]. Under highly carburizing environments and at temperatures above 1173 K, chromia is prone to carburize, significantly affecting the properties of the alloy [80, 91].

The protectiveness of an oxide layer is not only determined by its composition, but also by its uniformity and adhesiveness to the bulk, as these two properties ensure that the protection to coking is effective over the entire surface of the coil [91]. A slow-growing and thin but uniform oxide layer is the most desirable, because it offers a uniform coverage of the coil, and thin oxide layers are more adhesive than thicker ones [76].

2.5.2.2 Prereduction

This type of pretreatment is typically carried out by feeding hydrogen to the reactor at high temperature. Holmen et al. [64, 66] and Reyniers et al. [3] have studied prereduction and have compared it with preoxidation. The results of these studies are not so easy to compare, due to the differences in experimental procedures and feeds. The work of Holmen et al. [64] showed that, when cracking propane at high conversions, prereduced coupons of nickel exhibited lower coking

rates than preoxidized coupons. Propane cracking over preoxidized Sandvik 15Re 10 steel showed lower coking rates than for the prereduced nickel foils, which suggests that prereduction can be beneficial only for materials with high-Ni content. The work of Reyniers et al. [3] was more methodically performed, and seems to partially confirm the previous results. When cracking hexane over samples of Inconel 600 (72.5 wt% Ni; 16 wt% Cr), the prereduced coupons had significantly lower coking rates than the preoxidized ones. However, when comparing the coking rates of prereduced and preoxidized samples of Incoloy 800H (31 wt% Ni; 25 wt% Cr), the preoxidized samples had significantly lower coking rates. This could be explained considering that preoxidation of a high-Ni alloy like Inconel 600 possibly leads to the formation of a non-uniform layer, with mixed chromium and nickel oxides that could be easily damaged under the reducing steam cracking atmosphere; oxidation of alloys with higher contents of chromium and lower amounts of nickel can enhance the resistance to coking if compared to prereducing them.

This suggests that, in cases where preoxidation does not lead to the formation of a uniform protective oxide layer, prereduction may be a better pretreatment.

2.5.2.3 Presulfidation

In industrial practice, it is not uncommon to presulfide the reactor by feeding diluted dimethyl disulfide (DMDS) to the reactor before the cracking runs [97]. This pretreatment intends to form surface metal sulfides that could passivate the reactor, and reduce therefore the deposition of coke. Other frequently used sources of sulfur are dimethyl sulfide (DMS) and hydrogen sulfide (H_2S) [54]. Contradictory reports about the performance of these components have been presented, and the effect of sulfur on steam cracking of hydrocarbons is not completely understood yet, but

significant efforts have been conducted by various authors to try to improve the understanding in the field [3, 97-103].

Presulfidation of the reactor has proven to be a very effective way of reducing the initial peak of CO that is detected during the initial stages of a cracking run. However, the coking rates after presulfidation are strongly dependent on the duration of the pretreatment, amounts of sulfur during pretreatment and to the feed during cracking [3, 97, 98, 103]. The reduction of CO yields cannot be taken as an indication of coke reduction [28].

Recently, Li and Chen [104] studied the corrosive effect of H_2S on high temperature Fe-Ni-Cr alloys. Their work showed that the effect of sulfur is harmful for the alloys, except when working in a very narrow window of operating conditions, i.e. a ratio of P_{H2S}/P_{H2} close to 1.7×10^{-5}. When lower than this value, the oxide layer becomes porous and forms carbides in carburizing environments. On the other hand, when the amount of sulfur is too high, sulfide and oxides layers spall. This could explain the difficult balance between all the conditions that make presulfidation so unpredictable in terms of resistance to coke formation.

2.5.2.4 Coatings

Besides pretreatments, another way to obtain a modified composition of the internal coil surface is the application of coatings over the internal surface of the coils [54]. The main advantage that coatings offer is that they can be applied (often in-situ) over a regular base alloy. Two main kinds of coatings have been developed: inert and active coatings.

As their name suggests, when inert coatings are applied over the internal coil surface, they passivate the surface due to their inertness, limiting the amount of coke that deposits. Beneficial effects of various inert coatings have been presented in literature [5, 33, 69, 71, 89, 105]. The

main concern about these coatings seems to be their long-term performance, determined by their uniform coverage and adhesiveness.

Active coatings, on the other hand, are those that intend to gasify the deposited coke by reaction with oxygen. Two recent examples of these technologies are the Catalyzed-Assisted Manufacture of Olefins (CAMOL) [106], recently acquired by BASF, and YieldUp, property of General Electric Company [107, 108]. Both technologies use a catalyst deposited over the surface, which converts the carbon into CO and CO_2. CAMOL has been claimed to reach 1-2 year run lengths for light feedstocks, when using appropriate feedstock qualities and operation conditions [106]. YieldUp, on the other hand, has been reported to reduce coking 2 to 4 times, compared to an uncoated reference reactor[108].

As for the inert coatings, a big concern is also the long-term performance of the coatings. Additionally, the levels of CO_2 and mainly CO are expected to generate operational difficulties. However, reports on the performance of CAMOL-coated coils claim that impact on total CO/CO2 is both manageable and tunable in terms of level and relative make-up [106]. YieldUp increased the yields of CO and CO_2 too, but due to the high surface to volume ratio of the used reactor, this effect should be significantly reduced when applying the coating in an industrial reactor. Additionally, tuning of the coating formulation could further reduce the yields of CO [108].

The tests conducted on these coatings suggest that the coatings are durable and that their activity is good over time. Further testing at industrial scale and over long periods of time with cyclic operation could confirm the promising results that have been presented so far.

2.6 Conclusions

Coke formation is a very complex phenomenon, that is unfortunately unavoidable when carrying out steam cracking of hydrocarbons. Three mechanisms combine, shaping the deposits of coke that can be observed after a cracking run in a coil. However, during industrial operations, the available literature suggests that the prevalent, accounting for practically all the coke deposited, is the heterogeneous noncatalytic. This was confirmed with the calculations presented in Section 2.2. For ethane and naphtha cracking, the catalytic mechanism was estimated to be prevalent for 4% and 1% of the typical run length of a coil, respectively.

With this in mind, several coking models with different levels of complexity have been proposed, to provide tools to predict coke formation and industrial run lengths as a function of operation parameters such as concentration of precursors (typically light olefins and aromatics) in the gas phase and temperature. In Section 2.4 it has been demonstrated, using one of these coking models, that the effect of temperature is the most significant for the rate of coke deposition.

Among the many factors influencing the rates of coke deposition, the reactor coil materials are of large significance. Consequently, different alloy compositions have been developed throughout time by manufacturers, aiming to increase their high temperature properties, while at the same trying to generate internal surfaces with little or no coke-enhancing properties. Such properties are not only determined by the chemical composition of the bulk of the alloys, but are strongly dependent on the pretreatment applied to the coil. The formation of oxide layers after preoxidation is beneficial when a uniform and inert layer is formed. Presulfiding alloys has been studied too, leading –in general– to contradictory results. It seems clear, however, that presulfiding the coil leads to a reduction of the characteristic peak of CO at the beginning of a cracking run.

Also coatings can be used to reduce the deposition of coke in radiant coils. Inert coatings act as passivated layers, whereas active coatings catalytically remove the carbon deposited, forming CO and CO_2. The high yields of these components, together with the possible deactivation or removal of the coatings in the long term are factors that limit their large scale use in industry.

References

[1] Geurts, P.; Vanderavoird, A. Hartree-Fock-Slater-LCAO studies of the acetylene-transition metal interaction. 2. Chemisorption on Fe and Cu; Cluster models. *Surf. Sci.* **1981**, *103* (2-3), 416-430.

[2] Geurts, P.; Vanderavoird, A. Hartree-Fock-Slater-LCAO studies of the acetylene-transition metal interaction. 1. Chemisorption on Ni surfaces; Cluster models. *Surf. Sci.* **1981**, *102* (1), 185-206.

[3] Reyniers, M.-F.; Froment, G. F. Influence of metal-surface and sulfur addition on coke deposition in the thermal-cracking of hydrocarbons. *Ind. Eng. Chem. Res.* **1995**, *34* (3), 773-785.

[4] Browne, J.; Broutin, P.; Ropital, F. Coke deposition under steam cracking conditions - Study of the influence of the feedstock conversion by micropilots experiments. *Mater. Corros.* **1998**, *49* (5), 360-366.

[5] Ganser, A.; Wynns, K. A.; Kurlekar, A. Operational experience with diffusion coatings on steam cracker tubes. *Mater. Corros.* **1999**, *50* (12), 700-705.

[6] Helveg, S.; Sehested, J.; Rostrup-Nielsen, J. R. Whisker carbon in perspective. *Catal. Today* **2011**, *178* (1), 42-46.

[7] Baker, R. T. K.; Barber, M. A.; Waite, R. J.; Harris, P. S.; Feates, F. S. Nucleation and growth of carbon deposits from nickel catalyzed decomposition of acetylene. *J. Catal.* **1972**, *26* (1), 51-&.

[8] Yang, R. T.; Chen, J. P. Mechanism of carbon-filament grwoth on metal catalysts. *J. Catal.* **1989**, *115* (1), 52-64.

[9] Nielsen, J. R.; Trimm, D. L. Mechanisms of carbon formation on nickel-containing catalysts. *J. Catal.* **1977**, *48* (1-3), 155-165.

[10] Sacco, A.; Thacker, P.; Chang, T. N.; Chiang, A. T. S. The initiation and growth of filamentous carbon from alpha-iron in H2, CH4, H2O, CO2 and CO gas mixtures. *J. Catal.* **1984**, *85* (1), 224-236.

[11] Kock, A.; Debokx, P. K.; Boellaard, E.; Klop, W.; Geus, J. W. The formation of filamentous carbon on iron and nickel catalysts. 2. Mechanism. *J. Catal.* **1985**, *96* (2), 468-480.

[12] Alstrup, I. A new model explaining carbon-filament growth on nickel, iron and Ni-Cu alloy catalysts. *J. Catal.* **1988**, *109* (2), 241-251.

[13] Snoeck, J. W.; Froment, G. F.; Fowles, M. Filamentous carbon formation and gasification: Thermodynamics, driving force, nucleation, and steady-state growth. *J. Catal.* **1997**, *169* (1), 240-249.

[14] Keep, C. W.; Baker, R. T. K.; France, J. A. Origin of filamentous carbon formation from reaction of propane over nickel. *J. Catal.* **1977**, *47* (2), 232-238.

[15] Baker, R. T. K.; Harris, P. S.; Thomas, R. B.; Waite, R. J. Formation of filamentous carbon from iron, cobalt and chromium catalyzed decomposition of acetylene. *J. Catal.* **1973**, *30* (1), 86-95.

[16] Albright, L. F.; Marek, J. C. Mechanistic model for formation of coke in pyrolysis units producing ethylene. *Ind. Eng. Chem. Res.* **1988**, *27* (5), 755-759.

[17] Kopinke, F. D.; Zimmermann, G.; Nowak, S. On the mechanism of coke formation in steam cracking - Conclusions from results obtained by tracer experiments. *Carbon* **1988**, *26* (2), 117-124.

[18] Reyniers, G. C.; Froment, G. F.; Kopinke, F. D.; Zimmermann, G. Coke formation in the thermal-cracking of hydrocarbons .4. Modeling of coke formation in naphtha cracking. *Ind. Eng. Chem. Res.* **1994**, *33* (11), 2584-2590.

[19] Wauters, S.; Marin, G. B. Computer generation of a network of elementary steps for coke formation during the thermal cracking of hydrocarbons. *Chem. Eng. J.* **2001**, *82* (1-3), 267-279.

[20] Wauters, S.; Marin, G. B. Kinetic modeling of coke formation during steam cracking. *Ind. Eng. Chem. Res.* **2002**, *41* (10), 2379-2391.

[21] Kopinke, F. D.; Zimmermann, G.; Reyniers, G. C.; Froment, G. F. Relative rates of coke formation from hydrocarbons in steam cracking of naphtha .2. Paraffins, naphthenes, monoolefins, diolefins, and cycloolefins, and acetylenes. *Ind. Eng. Chem. Res.* **1993**, *32* (1), 56-61.

[22] Kopinke, F. D.; Zimmermann, G.; Reyniers, G. C.; Froment, G. F. Relative rates of coke formation from hydrocarbons in steam cracking of naphtha .3. Aromatic-hydrocarbons. *Ind. Eng. Chem. Res.* **1993**, *32* (11), 2620-2625.

[23] Wang, J. D.; Reyniers, M. F.; Marin, G. B. The influence of phosphorus containing compounds on steam cracking of n-hexane. *J. Anal. Appl. Pyrolysis* **2006**, *77* (2).

[24] Dente, M.; Bozzano, G.; Faravelli, T.; Marongiu, A.; Pierucci, S.; Ranzi, E., Kinetic Modelling of Pyrolysis Processes in Gas and Condensed Phase. In *Advances in Chemical Engineering*, Marin, G. B., Ed. Academic Press: **2007**; Vol. 32, pp 51-166.

[25] Van Geem, K. M.; Dhuyvetter, I.; Prokopiev, S.; Reyniers, M. F.; Viennet, D.; Marin, G. B. Coke Formation in the Transfer Line Exchanger during Steam Cracking of Hydrocarbons. *Ind. Eng. Chem. Res.* **2009**, *48* (23), 10343-10358.

[26] Kopinke, F. D.; Zimmermann, G.; Ondruschka, B. Tendencies of aromatization in steam cracking of hydrocarbons. *Ind. Eng. Chem. Res.* **1987**, *26* (11), 2393-2397.

[27] Sakai, T.; Soma, K.; Sasaki, Y.; Tominaga, H.; Kunugi, T. Secondary reactions of olefins in pyrolysis of petroleum hydrocarbons. *Adv. Chem. Ser.* **1970**, (97), 68-&.

[28] Froment, G. F. Coke Formation in the Thermal-Cracking of Hydrocarbons. *Rev. Chem. Eng.* **1990**, *6* (4), 293-328.

[29] Frenklach, M.; Clary, D. W.; Gardiner Jr, W. C.; Stein, S. E. Effect of fuel structure on pathways to soot. *Symp. (Int.) Combust., [Proc.]* **1988**, *21* (1), 1067-1076.

[30] Lahaye, J.; Badie, P.; Ducret, J. Mechanism of carbon formation during steam-cracking of hydrocarbons. *Carbon* **1977**, *15* (2), 87-93.

[31] Lahaye, J. Particulate carbon from the gas phase. *Carbon* **1992**, *30* (3), 309-314.

[32] Lahaye, J.; Aubert, J. P.; Buscailhon, A. Interaction between a coke and a tar. 2. Limit of tar penetration in coke porosity. *Fuel* **1977**, *56* (2), 188-191.

[33] Broutin, P.; Ropital, F.; Reyniers, M. F.; Froment, G. F. Anticoking coatings for high temperature petrochemical reactors. *Oil Gas Sci. Technol.* **1999**, *54* (3), 375-385.

[34] Bennett, M. J.; Price, J. B. A physical and chemical examination of an ethylene steam cracker coke and of the underlying pyrolysis tube. *J. Mater. Sci.* **1981**, *16* (1), 170-188.

[35] Schietekat, C. M.; van Goethem, M. W. M.; Van Geem, K. M.; Marin, G. B. Swirl flow tube reactor technology: An experimental and computational fluid dynamics study. *Chem. Eng. J.* **2014**, *238* (0), 56-65.

[36] Van Geem, K. M.; Heynderickx, G. J.; Marin, G. B. Effect of radial temperature profiles on yields in steam cracking. *Aiche J.* **2004**, *50* (1), 173-183.

[37] Sundaram, K. M.; Froment, G. F. Kinetics of coke deposition in the thermal-cracking of propane. *Chem. Eng. Sci.* **1979**, *34* (5), 635-644.

[38] Sundaram, K. M.; Vandamme, P. S.; Froment, G. F. Coke deposition in the thermal-cracking of ethane. *Aiche J.* **1981**, *27* (6), 946-951.

[39] Pramanik, M.; Kunzru, D. Coke formation in the pyrolysis of normal-hexane. *Ind. Eng. Chem. Proc. D. D.* **1985**, *24* (4), 1275-1281.

[40] Zou, R. J.; Lou, Q. K.; Liu, H. C.; Niu, F. H. Investigation of coke deposition during the pyrolysis of hydrocarbon. *Ind. Eng. Chem. Res.* **1987**, *26* (12), 2528-2532.

[41] Zou, R. J.; Lou, Q. K.; Mo, S. H.; Feng, S. B. Study on a kinetic model of atmospheric gas oil pyrolysis and coke deposition. *Ind. Eng. Chem. Res.* **1993**, *32* (5), 843-847.

[42] Plehiers, P. M.; Reyniers, G. C.; Froment, G. F. Simulation of the runlength of an ethane cracking furnace. *Ind. Eng. Chem. Res.* **1990**, *29* (4), 636-641.

[43] Van Geem, K. M.; Zajdlik, R.; Reyniers, M. F.; Marin, G. B. Dimensional analysis for scaling up and down steam cracking coils. *Chem. Eng. J.* **2007**, *134* (1-3), 3-10.

[44] Hu, G. H.; Wang, H. G.; Qian, F.; Zhang, Y.; Li, J. L.; Van Geem, K. M.; Marin, G. B. Comprehensive CFD simulation of product yields and coking rates for a floor- and wall-fired naphtha cracking furnace. *Ind. Eng. Chem. Res.* **2011**, *50* (24), 13672-13685.

[45] Towfighi, J.; Sadrameli, M.; Niaei, A. Coke formation mechanisms and coke inhibiting methods in pyrolysis furnaces. *J. Chem. Eng. Jpn.* **2002**, *35* (10), 923-937.

[46] Reyniers, G. Cokesvorming bij de Thermische Kraking van Koolwaterstoffen. PhD Thesis, Universiteit Gent. Faculteit van de Toegepaste Wetenschappen Ghent, Belgium, **1992**.

[47] Frenklach, M.; Wang, H. Detailed surface and gas-phase chemical kinetics of diamond deposition. *Phys. Rev. B* **1991**, *43* (2), 1520-1545.

[48] Willems, P. A.; Froment, G. F. Kinetic modeling of the therma cracking of hydrocarbons. 1. Calculation of frequency factors. *Ind. Eng. Chem. Res.* **1988**, *27* (11), 1959-1966.

[49] Willems, P. A.; Froment, G. F. Kinetic modeling of the thermal cracking of hydrocarbons. 2. Calculation of activation energies. *Ind. Eng. Chem. Res.* **1988**, *27* (11), 1966-1971.

[50] Goossens, A. G.; Dente, M.; Ranzi, E. Improve steam cracking operation. *Hydrocarb. Process.* **1978**, *57* (9), 227-236.

[51] Sabbe, M. K.; Van Geem, K. M.; Reyniers, M. F.; Marin, G. B. First Principle-Based Simulation of Ethane Steam Cracking. *Aiche J.* **2011**, *57* (2), 482-496.

[52] Ibarra, S., Materials of construction in ethylene pyrolysis-heater service. In *Pyrolysis - Theory and industrial practice*, Albright, L. F.; Crynes, B. L.; Corcoran, W. H., Eds. ACADEMIC PRESS, INC: New York, **1983**; pp 427-436.

[53] Tillack, D. J.; Guthrie, J. E. Select the right alloys for refineries and petrochemical plants. *Chem. Eng. Prog.* **1999**, *95* (2), 59-66.

[54] Wysiekierski, A. G.; Fisher, G.; Schillmoller, C. M. Control coking for olefins plants. *Hydrocarb. Process.* **1999**, *78* (1), 97-100.

[55] Zimmermann, H.; Walzl, R., Ethylene. In *Ullmann's Encyclopedia of Industrial Chemistry*, Wiley-VCH Verlag GmbH & Co. KGaA: Weinheim, **2009**.

[56] Verdier, G.; Carpentier, F. Consider new materials for ethylene furnace applications. *Hydrocarb. Process.* **2011**, *90* (5), 61-62.

[57] Holmen, A.; Lindvag, O. A. Coke formation on nickel-chromium-iron alloys. *J. Mater. Sci.* **1987**, *22* (12), 4518-4522.

[58] Smith, G. M.; Young, D. J.; Trimm, D. L. Carburization kinetics of heat-resistant steels. *Oxid. Met.* **1982**, *18* (5-6), 229-243.

[59] Albright, L. F.; McGill, W. A. Aluminized Ethylene Furnace Tubes Extend Operating Life. *Oil Gas J.* **1987**, *85* (35), 46-50.

[60] Jakobi, D., van de Moesdijk C., Karduck, P., von Richthofen A. Tailor - Made Materials for High Temperature Applications: New Strategies for Radiant Coil Material Development. NACE, Atlanta, GA, **2009.** NACE International.

[61] Asteman, H.; Hartnagel, W.; Jakobi, D. The Influence of Al Content on the High Temperature Oxidation Properties of State-of-the-Art Cast Ni-base Alloys. *Oxid. Met.* **2013**, *80* (1-2), 3-12.

[62] Yan, J. B.; Gao, Y. M.; Yang, F.; Bai, Y. P.; Liu, Y. H.; Yao, C. Y.; Hou, S. Z.; Liu, G. Z. Cyclic carburizing behaviour of Al modified high Si-containing HP40 alloy. *Corrosion Sci.* **2013**, *67*, 161-168.

[63] Nishiyama, Y.; Tamai, Y. Wall effects during thermal reactions. *Chemtech* **1980**, *10* (11), 680-684.

[64] Holmen, A.; Lindvaag, O. A.; Trimm, D. L. Surface effects on the steam cracking of propane. *ACS Sym. Ser.* **1982**, *202*, 45-58.

[65] Marek, J. C.; Albright, L. F., Formation and removal of coke deposited on stainless steel and vycor surfaces from acetylene and ethylene. In *Coke Formation on Metal Surfaces*, American Chemical Society: **1983**; Vol. 202, pp 123-149.

[66] Holmen, A.; Lindvaag, O. A.; Trimm, D. L. Coke formation during steam cracking of hydrocarbons .2. Effect of preoxidation and prereduction of the reactor surface *J CHEM TECH BIOT A* **1985**, *35* (7), 358-364.

[67] Luan, T. C.; Eckert, R. E.; Albright, L. F. Gaseous pretreatment of high-alloy steels used in ethylene furnaces: Pretreatment of Incoloy 800. *Ind. Eng. Chem. Res.* **2003**, *42* (20), 4741-4747.

[68] Zhang, Z. B.; Albright, L. F. Pretreatments of Coils to Minimize Coke Formation in Ethylene Furnaces. *Ind. Eng. Chem. Res.* **2010**, *49* (4), 1991-1994.

[69] Brown D, E.; Clark J. T, K.; Foster A, I.; Mc, C. J. J.; Sims M, L., Inhibition of coke formation in ethylene steam cracking. In *Coke Formation on Metal Surfaces*, AMERICAN CHEMICAL SOCIETY: **1983**; Vol. 202, pp 23-43.

[70] Redmond, T.; Bergeron, M. P. Tests demonstrate anticoking capability of new coating. *Oil Gas J.* **1999**, *97* (19), 39-42.

[71] Zychlinski, W.; Wynns, K. A.; Ganser, B. Characterization of material samples for coking behavior of HP40 material both coated and uncoated using naphtha and ethane feedstock. *Mater. Corros.* **2002**, *53* (1), 30-36.

[72] Li, C. S.; Yang, Y. S. A glass based coating for enhancing anti-coking and anti-carburizing abilities of heat-resistant steel HP. *Surf. Coat. Technol.* **2004**, *185* (1), 68-73.

[73] Zhou, J. X.; Wang, Z. Y.; Luan, X. J.; Xu, H. Anti-coking property of the SiO2/S coating during light naphtha steam cracking in a pilot plant setup. *J. Anal. Appl. Pyrolysis* **2011**, *90* (1), 7-12.

[74] Chasselin, H. Carburization in Ethylene radiant coils. the 25th. Ethylene Producers' Conference, San Antonio, TX, 04-May-2013, **2013.**

[75] Tang, S.; Gao, S.; Hu, S.; Wang, J.; Zhu, Q.; Chen, Y.; Li, X. Inhibition Effect of APCVD Titanium Nitride Coating on Coke Growth during n-Hexane Thermal Cracking under Supercritical Conditions. *Ind. Eng. Chem. Res.* **2014**, *53* (13), 5432-5442.

[76] Fedorova, E.; Monceau, D.; Oquab, D. Quantification of growth kinetics and adherence of oxide scales formed on Ni-based superalloys at high temperature. *Corrosion Sci.* **2010**, *52* (12), 3932-3942.

[77] Koshelev, I. K.; Paulikas, A. P.; Beno, M.; Jennings, G.; Linton, J.; Grimsditch, M.; Uran, S.; Veal, B. W. Chromium-oxide growth on Fe-Cr-Ni alloy studied with grazing-emission X-ray fluorescence. *Oxid. Met.* **2007**, *68* (1-2), 37-51.

[78] Liu, Y. C.; Wei, W. F.; Benum, L.; Oballa, M.; Gyorffy, M.; Chen, W. X. Oxidation Behavior of Ni-Cr-Fe-Based Alloys: Effect of Alloy Microstructure and Silicon Content. *Oxid. Met.* **2010**, *73* (1-2), 207-218.

[79] Pujilaksono, B.; Jonsson, T.; Heidari, H.; Halvarsson, M.; Svensson, J. E.; Johansson, L. G. Oxidation of Binary FeCr Alloys (Fe-2.25Cr, Fe-10Cr, Fe-18Cr and Fe-25Cr) in O-2 and in O-2 + H2O Environment at 600 degrees C. *Oxid. Met.* **2011**, *75* (3-4), 183-207.

[80] Young, D. J.; Zurek, J.; Singheiser, L.; Quadakkers, W. J. Temperature dependence of oxide scale formation on high-Cr ferritic steels in Ar-H-2-H2O. *Corrosion Sci.* **2011**, *53* (6), 2131-2141.

[81] Wu, X. Q.; Yang, Y. S.; He, W. Y.; Zhan, Q.; Hu, Z. Q. Morphologies of coke deposited on surfaces of pure Ni and Fe-Cr-Ni-Mn alloys during pyrolysis of propane. *J. Mater. Sci.* **2000**, *35* (4), 855-862.

[82] Steurbaut, C.; Grabke, H. J.; Stobbe, D.; van Buren, F. R.; Korf, S. J.; Defrancq, J. Kinetic studies of coke formation and removal on HP40 in cycled atmospheres at high temperatures. *Mater. Corros.* **1998**, *49* (5), 352-359.

[83] Grabke, H. J.; Jakobi, D. High temperature corrosion of cracking tubes. *Mater. Corros.* **2002**, *53* (7), 494-499.

[84] Benum, L.; Chen, W.; Oballa, M.; Petrone, S. Process of treating a stainless steel matrix U.S. Patent Application **2002**.

[85] Li, H.; Zheng, Y.; Benum, L. W.; Oballa, M.; Chen, W. Carburization behaviour of Mn-Cr-O spinel in high temperature hydrocarbon cracking environment. *Corrosion Sci.* **2009**, *51* (10), 2336-2341.

[86] Li, H.; Chen, W. X. Stability of MnCr2O4 spinel and Cr2O3 in high temperature carbonaceous environments with varied oxygen partial pressures. *Corrosion Sci.* **2010**, *52* (7), 2481-2488.

[87] Prescott, R.; Graham, M. J. The formation of aluminum oxida scales on high-temperature alloys. *Oxid. Met.* **1992**, *38* (3-4), 233-254.

[88] Jedlinski, J. The oxidation behaviour of FeCrAl 'alumina forming' alloys at high temperatures. *Solid State Ionics* **1997**, *101*, 1033-1040.

[89] Kurlekar, A.; Bayer, G. T. Enhance furnace tube resistance to carburization and coke formation - Applying diffusion coatings on ethylene furnace tubes may increase run times between decoking. *Hydrocarb. Process.* **2001**, *80* (1), 80-84.

[90] Jakobi, D.; Ganser, B. Centralloy 60 HT. Alloy Development for High Temperature Operation and Reduced Coking. Spring National Meeting: 17th Annual Ethylene Producers Conference, 2005/01/01/, **2005.**

[91] Jakobi, D.; Karduk, P.; von Richthofen, A. F. The high-temperature corrosion resistance of spun-cast materials for steam cracker furnaces - A comparative study of alumina- and chromia-forming alloys. NACE, Orlando, FL, **2013.** NACE International.

[92] Edrissi, M.; Soleymani, M.; Naderi, M. Synthesis of MnAl2O4 nanocrystallites by Pechini and sequential homogenous precipitation methods: characterization, product comparison, photocatalytic effect, and Taguchi optimization. *J. Sol-Gel Sci. Technol.* **2012**, *64* (2), 485-492.

[93] Jianguo, Z.; Hui, W.; Chunyu, X.; Mohsen, S.; Yongfeng, H.; Ajay, K. D., Design and preparation of Ni-Co bimetallic nanocatalyst for carbon dioxide reforming of methane. In *Nanocatalysis for Fuels and Chemicals*, American Chemical Society: **2012**; Vol. 1092, pp 195-221.

[94] Salhi, N.; Boulahouache, A.; Petit, C.; Kiennemann, A.; Rabia, C. Steam reforming of methane to syngas over NiAl2O4 spinel catalysts. *Int. J. Hhydrogen Energ.* **2011**, *36* (17), 11433-11439.

[95] López-Fonseca, R.; Jiménez-González, C.; de Rivas, B.; Gutiérrez-Ortiz, J. I. Partial oxidation of methane to syngas on bulk NiAl2O4 catalyst. Comparison with alumina supported nickel, platinum and rhodium catalysts. *Appl. Catal. A-Gen.* **2012**, *437–438* (0), 53-62.

[96] Nicholls, J. R.; Newton, R.; Simms, N. J.; Norton, J. F. Modelling the oxidation of FeCrAl-RE ODS alloys in simulated natural gas combustion environments. *Mater. High Temp.* **2003**, *20* (2), 93-108.

[97] Wang, J.; Reyniers, M. F.; Marin, G. B. Influence of dimethyl disulfide on coke formation during steam cracking of hydrocarbons. *Ind. Eng. Chem. Res.* **2007**, *46* (12), 4134-4148.

[98] Shah, Y. T.; Stuart, E. B.; Sheth, K. D. Coke formation during thermal cracking of n-octane. *Ind. Eng. Chem. Proc. D. D.* **1976**, *15* (4), 518-524.

[99] Bajus, M.; Vesely, V. Pyrolysis of hydrocarbons in the presence of elemental sulfur. *Collect. Czech. Chem. Commun.* **1980**, *45* (1), 238-254.

[100] Bajus, M.; Vesely, V.; Leclercq, P. A.; Rijks, J. A. Steam cracking of hydrocarbons. 3. Straight-run naphtha. *Ind. Eng. Chem. Prod. R. D.* **1980**, *19* (4), 556-563.

[101] Trimm, D. L.; Turner, C. J. The pyrolysis of propane. 2. Effect of hydrogen sulfide. *J. Chem. Technol. Biotechnol.* **1981**, *31* (5), 285-289.

[102] Trimm, D. L.; Holmen, A.; Lindvag, O. Coke formation during cracking of hydrocarbons. 1. The effect of pre-sulphiding on coke formation on a nickel-chromium-iron alloy under steam cracking conditions. *J. Chem. Technol. Biotechnol.* **1981**, *31* (6), 311-316.

[103] Dhuyvetter, I.; Reyniers, M. F.; Froment, G. F.; Marin, G. B.; Viennet, D. The influence of dimethyl disulfide on naphtha steam cracking. *Ind. Eng. Chem. Res.* **2001**, *40* (20), 4353-4362.

[104] Li, H.; Chen, W. X. Effect of H2S on High Temperature Corrosion of Fe-Ni-Cr Alloys in Carburizing/Oxidizing Environments. *Oxid. Met.* **2012**, *77* (3-4), 107-127.

[105] Niaei, A.; Salari, D.; Daneshvar, N.; Chamandeh, A.; Nabavi, R. Effect of Tube Materials and Special Coating on Coke Deposition in the Steam Cracking of Hydrocarbons. Conference of the World Academy of Science Engineering and Technology, Berlin, **2007.** Ardil, C., Ed.

[106] Petrone, S.; Deuis, R. L.; Kong, F.; Unwin, P. Catalyzed-assisted manufacture of olefins (CAMOL): Year-(4) update on furnace commercial installations. 2010 Spring National Meeting, San Antonio, TX, **2010.**

[107] Gu, Y.; Peng, W.; Wang, S.; Lin, C.; Kool, L.; Wu, Z.; Fu, Q.; Deng, Z. Method and reactor for cracking hydrocarbon and method for coating the reactor. U.S. Patent Application US20130267750A1, **2013**.

[108] Schietekat, C. M.; Reyniers, P. A.; Sarris, S. A.; Van Geem, K. M.; Marin, G. B.; Kool, L.; Peng, W.; Lucas, P.; Zhou, H.; Gu, Y. Catalytic coating for reduced coke formation in ethylene-producing steam crackers: experimental and model validation. 26th. Ethylene Producers' Conference, New Orleans - LA, USA, April, **2014.**

Chapter 3: Experimental procedures

Abstract:

In this chapter, the experimental setup used is presented, together with the procedures applied during the coking experiments. A quartz jet stirred reactor (JSR) is used to perform steam cracking experiments of ethane and naphtha over small rectangular coupons made of different materials. Measuring the mass increase of the coupons throughout the experiments allows to determine the rates of coke deposition as a function of time. These coupons are analyzed ex-situ at three different stages of the experiments: blank, i.e. after being cut and machined, preoxidized and coked. The analyses are carried out combining scanning electron microscopy (SEM) and energy dispersive X-ray analysis (EDX). The morphology and chemical composition of the top surface and cross section of the coupons are determined. Additionally, the processing of the data from the electrobalance reactor and the X-ray analyzes is explained.

Keywords: Experimental setups; jet stirred reactor; coupons; scanning electron microscopy; energy dispersive X-ray analysis; data processing.

3.1 Jet stirred reactor (JSR) setup

The JSR setup of the Laboratory for Chemical Technology was built to allow the continuous measurement of the coke depositing over samples of different materials of interest while performing steam cracking of hydrocarbons. This way, the influence of the studied material in coke formation can be quantitatively assessed.

The cracking conditions can be easily modified, as this setup allows the use of a wide range of conditions, i.e. temperatures, feeds (gaseous or liquids), dilutions. Usage of additives is also possible.

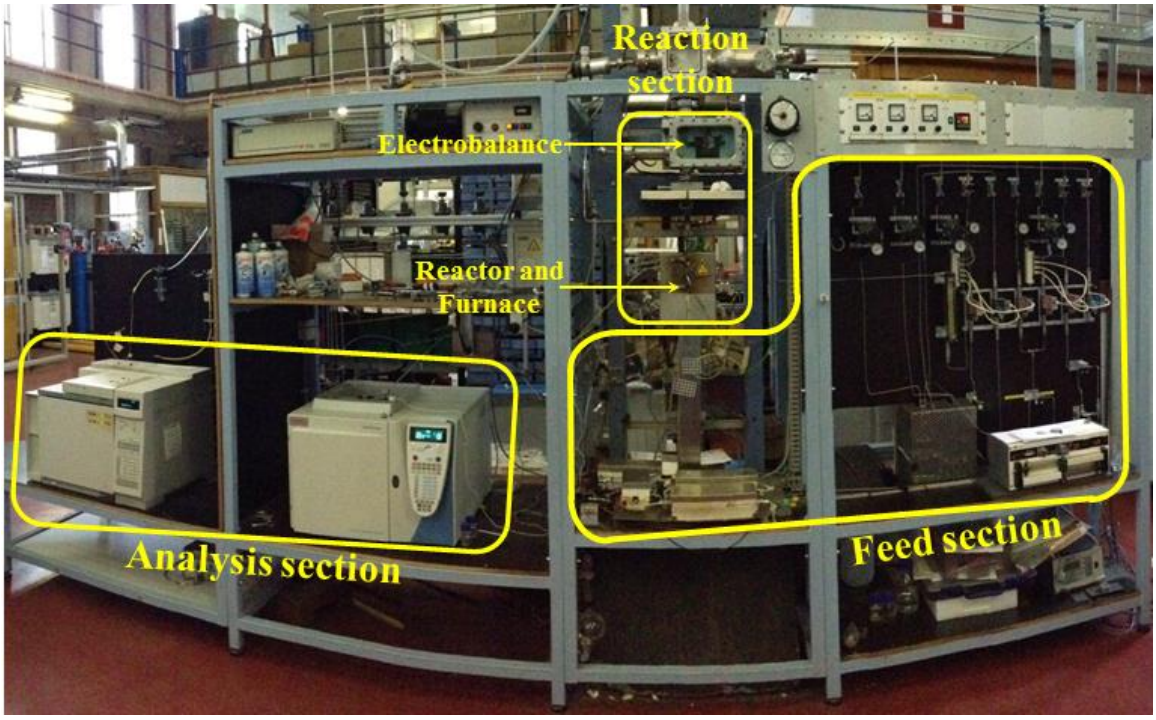

Figure 3.1: The JSR setup, divided into three sections

A picture of the JSR setup is presented in Figure 3.1, which also depicts the three sections in which the setup can be divided. They are described in Sections 3.1.1, 3.1.2 and 3.1.3, respectively. The operating conditions are presented in Section 3.2.

3.1.1 Feed section

This section involves all the elements of the setup that are upstream of the reactor.

The setup receives helium, hydrogen, nitrogen and compressed air from a centralized battery that serves the entire building. Gaseous hydrocarbons, on the other hand, are fed directly from cylinders, placed in a safety cabinet next to the setup. The lines of each individual gas entering the reactor reach a ball valve, that acts as an on/off switch. Each gas line is then directed to a pressure reducer. After the reducers, Bronkhorst thermal mass flow controllers (MFC) are installed, which regulate the flow rates of the gas streams.

Water and naphtha are stored in glass bottles. They are pressurized with an inert gas at 0.12 MPa, so that these liquids can be transported from their reservoirs to either a mass flow controller, or a regulating pump. A scheme of this arrangement is presented in Figure 3.2.

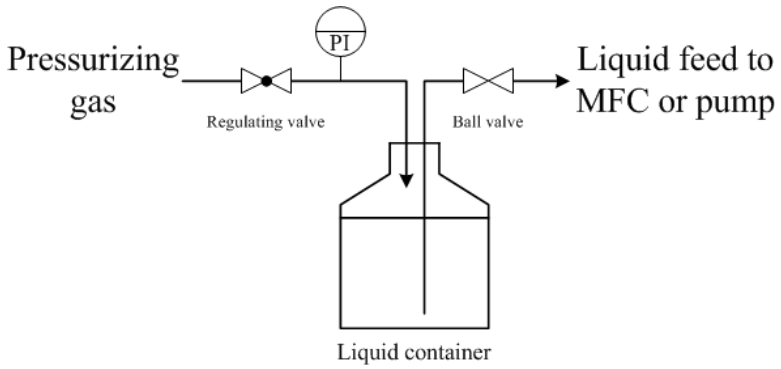

Figure 3.2: Scheme of the mechanism used for transport of liquids in the electrobalance setup

To regulate the water flow, a Bronkhorst Liquiflow MFC is used, whereas for naphtha, a high-precision piston pump (Pharmacia LKB P500) is used.

Two parallel evaporators filled with small glass pearls are used to evaporate the liquid feeds. When feeding a liquid hydrocarbon, water is fed to one evaporator, and the hydrocarbons to the other. The two gaseous streams are merged into one after evaporation. When feeding a gaseous hydrocarbon, the two evaporators are connected in-series, feeding only water to the first one, and

ethane to the second one. This way water is completely evaporated, and a good mixing with the hydrocarbons can be achieved.

The vaporized feeds are then directed to a heated switch valve, which can direct the reaction mixture to the vent, or to the reactor for cracking operation. For the feed to reach the reactor, it is firstly passed by a concentric tubes mixer, which takes the feed to two preheaters in series which heat up the mixture to temperatures slightly lower than those required for cracking. This heating step is very important, because it ensures that the feed is as hot as possible when entering the reactor, yet still unconverted. This minimizes the heat duty in the reactor, thus reducing temperature gradients that could affect the measurements inside the reactor to a minimum. A scheme of the feed section is presented in Figure 3.3.

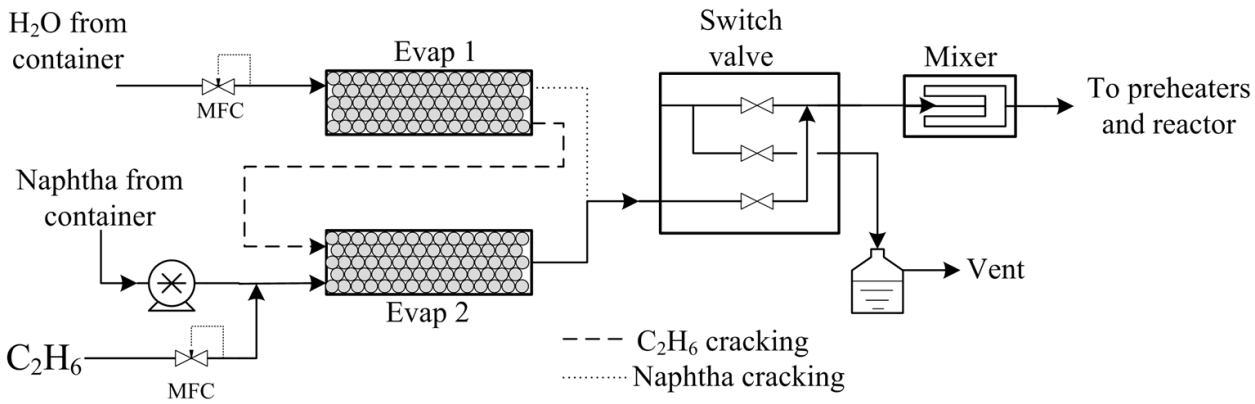

Figure 3.3: Schematic diagram of the feed section

3.1.2 Reactor section

This can be considered as the most important section of the setup. As its name suggests, it is where the cracking reactions take place. The type of reactor that has been selected is a jet stirred reactor (JSR). The reactor and the dimensions (in mm) of its components are schematically presented in Figure 3.4.

A small coupon made of the material to study is placed inside the reactor, hanging from the arm of an electrobalance. This way, the coke that deposits over the surface of the coupon can be

continuously measured during cracking operation. To measure the temperature inside the reactor, a thin thermocouple is placed inside a thermowell, directed to the center of the reactor, as can be observed in Figure 3.4.

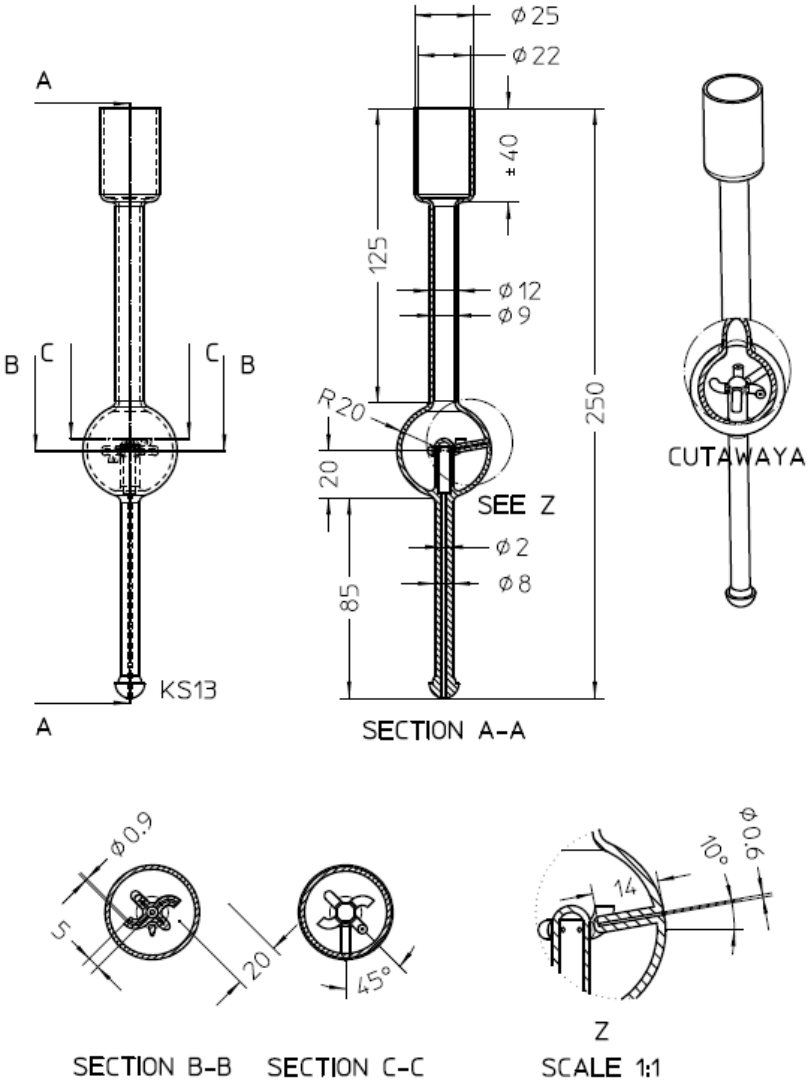

Figure 3.4: Schematic drawings used for the manufacturing of the JSR reactor

A picture of the JSR with a coupon placed inside is presented in Figure 3.5. The sample is connected to the electrobalance by a 0.25 mm thick Kanthal A wire. The composition of Kanthal A (in wt%) is, approximately, 71.4 % Fe, 22 % Cr, 5.3% Al, 0.7% Si, 0.5 % Mn, and 0.08% C [1].

The coupons placed inside the reactor are cut from new industrial steam cracking coils of the materials of interest. The cutting is outsourced to Verbeeken Precisiemechaniek, where the small coupons are cut by means of electro-erosion to final dimensions 1 mm × 8 mm × 10 mm, (total surface area S = 1.96×10^{-4} m^2). A picture of the coupons and the tubes they are cut from is presented in Figure 3.6. Polishing and cleaning of the coupons is performed before placing them inside the reactor. These procedures are explained in sections 3.2.1 and 3.2.2.

Figure 3.5: Picture of a coupon placed inside the quartz JSR.

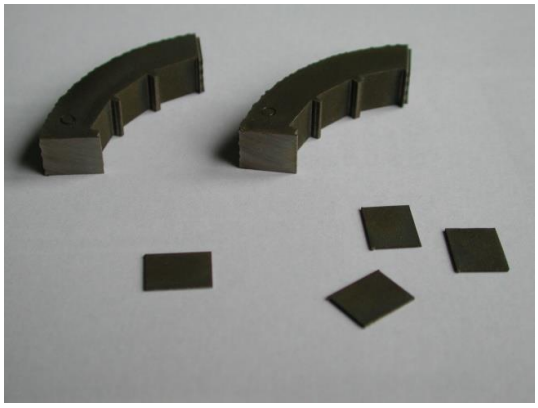

Figure 3.6: Samples cut from the inner surface on an industrial coil

It was explained in Chapter 2 that the reactor material has a large influence on the coking rate. The JSR is entirely made of quartz. This ensures that the amount of coke being measured over the coupon is not influenced by metals present in the formulation of the reactor material.

This type of reactor has been successfully used for various gas phase kinetic studies [2-6]. The main advantage it offers when compared to the typically used plug flow reactor (PFR) is that the JSR can achieve a very good mixing of the gas phase, leading to a very similar behavior to that of a continuously stirred tank reactor (CSTR). Consequently, temperature measurements can be made at practically any position inside the reactor, and the gas phase composition in the reactor can be easily determined by sampling the outlet stream, provided that reaction takes place only inside the reactor. An additional practical implication for the measurements of coke deposition is that the position of the coupon inside the reactor is not as crucial as would be for a PFR, where axial and radial gradients can largely influence the measured results. Computational Fluid Dynamics (CFD) simulations have been carried out for the JSR [7]. They have shown that the mixing is very good, and that concentration and temperature gradients are practically negligible.

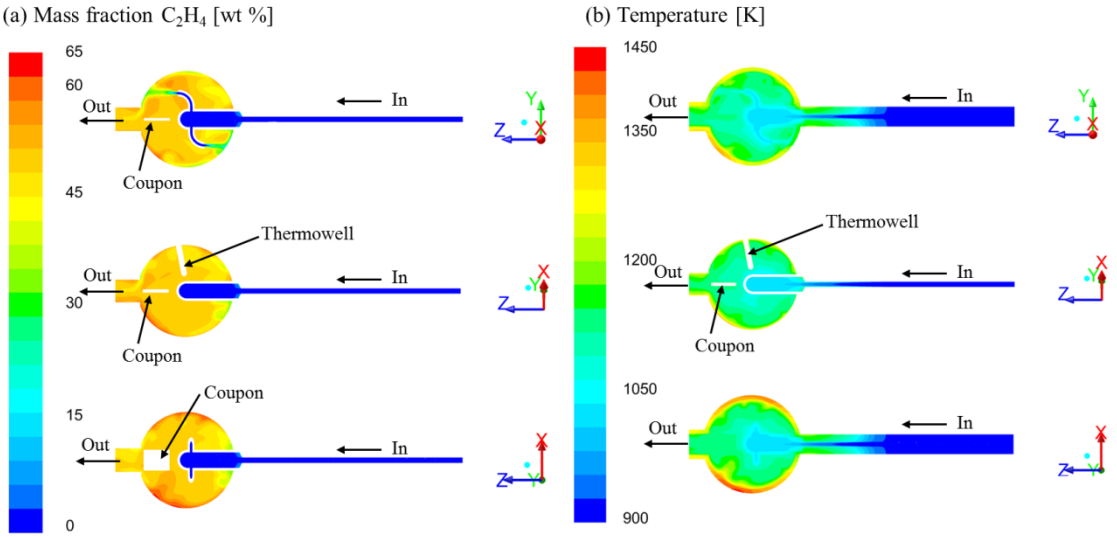

Figure 3.7: CFD simulation of (a) ethylene mass fraction [wt %] and (b) temperature [K] distribution in the JSR during ethane cracking **[7]**.

The simulated fraction of ethylene inside the JSR is presented in Figure 3.7(a) for ethane steam cracking. It is taken as a representative indicator of the uniformity of the gas phase composition. The color-scale indicates the ethylene mass fraction at a given position. It can be seen that, for both feeds, a very uniform gas phase composition is achieved. Figure 3.7(b) shows the simulated temperature distribution inside the JSR reactor for ethane steam cracking. The uniform color distribution inside the reactor can therefore be interpreted as a uniform temperature inside the reactor. This confirms the benefits of the JSR for the coke deposition measurement.

The reactor is heated by a closed electric furnace, with a customized shape that fits the reactor, as can be seen in Figure 3.5. The heating elements are blocks of refractory material that have a resistance inside that heats up when an electric current is passed through. Their maximum operating temperature is 1373 K.

The metal coupon is placed inside the reactor, suspended at the arm of an electrobalance. A Cahn D-200 electrobalance is used, and a schematic diagram of its configuration is presented in Figure 3.8. Briefly explained, the electrobalance works under the principle of maintaining both of its arms (sample and tare) balancing in equilibrium. The equilibrium of both arms is determined by action of a photocell. To do this, an electric current is passed through an electromagnetic coil, which generates a force capable of counteracting the weight of the sample, taking the arms to equilibrium. Knowing the amount of electric current passing through the coil, the mass of the sample can be determined.

The readout of the electrobalance is sent to a computer which plots the mass of the coupons in real time, and stores the data throughout the entire experimental run.

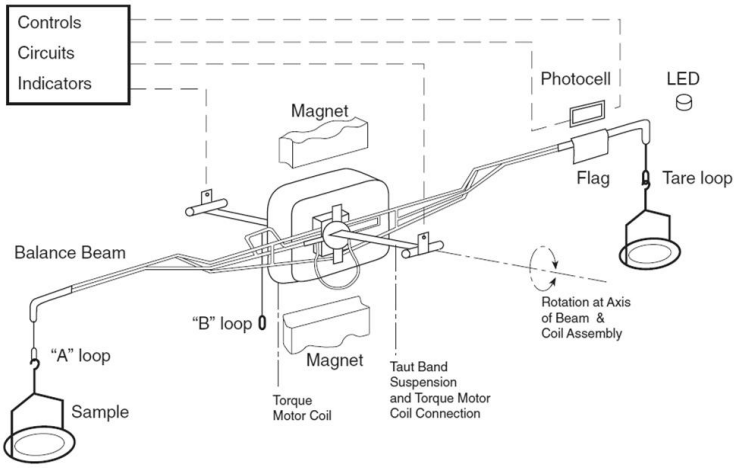

Figure 3.8: Schematic diagram of the electrobalance [8].

3.1.3 Analysis section

This section receives the effluent leaving the reactor, quenches it and analyzes it to determine its composition, using two gas chromatographs (GC). A schematic diagram of this section is presented in Figure 3.9.

Once the cracking effluent leaves the reactor it is rapidly quenched to stop the cracking reactions. During the experiments, this cooling is carried out by using a core and shell oil cooler, presented in Figure 3.10. Cooling oil is pumped by a Lauda Proline P5 pump at a temperature of 426 K.

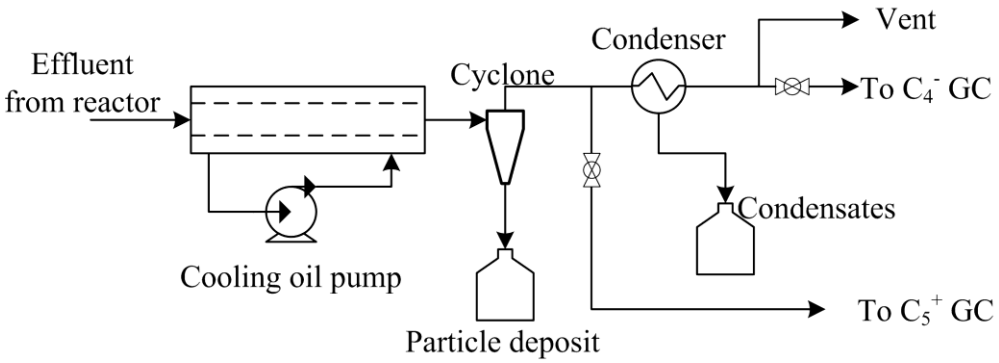

Figure 3.9: Schematic diagram of the analysis section

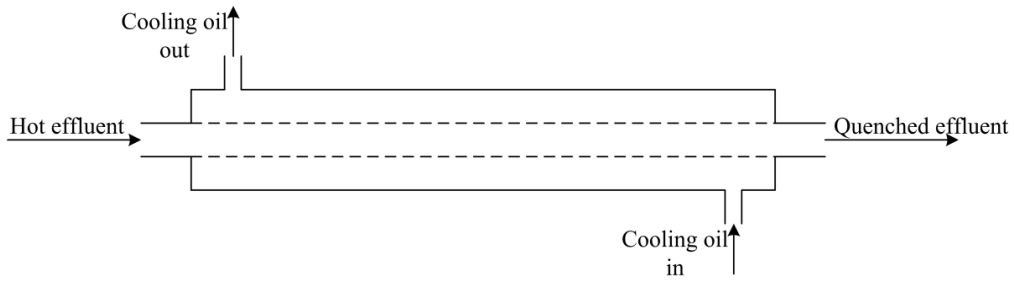

Figure 3.10: Schematic diagram of the core and shell oil cooler.

Downstream of the oil cooler, a known flow of nitrogen is added to the effluent, in order to apply the internal standard method for quantification of the relative fractions of each component in the effluent [9]. The effluent is then directed to a cyclone, to remove any particles.

Immediately downstream of the cyclone, a sampling valve is installed, which allows to extract a small fraction of the effluent, so that it can be analyzed in a Trace GC ultra GC, which is used to quantify the heavier hydrocarbons in the effluent.

The rest of the effluent is directed to two in-series condensers, whose purpose is to condensate all the non-permanent gases. The cooling fluid is propylene glycol, and a Fryka DLK 402 pump is used to transport and cool it. The temperature of the propylene glycol is set to 273 K.

The non-condensed fraction of the effluent is analyzed by a Refinery Gas Analyzer (RGA). The carrier gas is helium. Separation of nitrogen, carbon monoxide, carbon dioxide and hydrocarbons up to C_2 occurs on a Molsieve 5Å and a Porapack N column and a thermal conductivity detector (TCD) is used. Separation of C_3 and C_4 components occurs on a HP-PLOT Al_2O_3 - S25 column (50 m × 0.53 mm) and a Flame Ionization Detector (FID) is used. The Trace GC ultra GC is equipped with a PONA column (50 m × 0.25 mm, 0.5 µm film), used for quantitative determination of the C_{5+} hydrocarbons. A FID is used to measure the concentration of the hydrocarbons in the reaction mixture. A summary of the characteristics of the gas chromatographs is presented in Table 3.1.

Table 3.1: Summary of the conditions used by the gas chromatographs

	RGA			GC Trace GC
Detector	TCD		FID	FID
Column type	Molsieve 13X packed	Porapack N packed	HP-PLOT Al_2O_3	HP-PONA
Length [m]	1.5	3	50	50
Internal diameter [10^{-6} m]	320	320	530	250
Carrier gas	He	He	He	He
Flow rate of carrier gas [10^{-3} l·min^{-1}]	42	42	5.1	0.7
Temperature [K]				
Column	313-443	313-443	313-443	233-523
Detector	473	473	523	523
Injector	398	398	473	523
Run duration [min]	25	25	25	60

3.2 Experimental procedures and conditions

In this section, all the stages that the coupons undergo after being cut are explained. These stages can be divided into four categories: machining, cleaning, preoxidation, and cracking and decoking.

3.2.1 Machining

The coupons have a high and variable surface roughness (R_a) after cutting. To ensure that all the coupons have comparable surface roughness, a polishing procedure is carried out. This is done for all coupons, except those that are delivered directly from the manufacturer and have a special surface that could be destroyed during polishing.

To carry out the polishing, SiC sandpaper grade 220 is used. A circular sheet of sandpaper is attached to a rotating disk using double sided adhesive tape. The coupon is firmly attached to a cylindrical block using the same double sided adhesive tape. This block serves as a handle to manipulate the coupon, and to ensure that the coupon lies flat against the rotating disk, avoiding

excessive polishing on one edge. Although the coupons have to be pressed against the rotating disk, it is important to avoid excessive pressure, as this leads to scratching of the surface.

The disk rotation speed is 250 rpm, and a continuous stream of water is directed to the disk for cooling and to remove the dusts that form as consequence of polishing. This is typically done for approximately 5 minutes on each side of the coupon.

The surface roughness is measured after polishing, by means of a Mitutoyo surface roughness meter Surftset SJ-30. The desired surface finish is a measured surface roughness $R_a \sim 0.15$ µm. If after polishing the surface roughness is higher on either side of the coupon, such side is polished again for a shorter period of approximately 2 minutes, after which the surface roughness is controlled again. R_a is automatically calculated by the surface roughness meter. The R_a value is the arithmetic average of the absolute values of height and depth of the peaks and valleys present along the surface profile.

3.2.2 Cleaning

The first step is to clean the coupon to be placed in the reactor by means of an ultrasonic bath in acetone for two hours, followed by washing in isopropyl ether for five minutes, and then drying in air.

Then, the coupon undergoes an electrolytic scouring in a solution of sulfuric acid (1.5 wt %). To do this, a small graphite stick is connected to the anode of a battery capable of providing an 8V potential, whilst the coupon is connected to the cathode. The coupon and the graphite bar are submerged in the sulfuric acid solution, and the 8V are applied for 15 minutes.

The coupon is then removed from the solution and rinsed with demineralized water and dried in air.

3.2.3 Preoxidation

Industrially, the surface of the reactor is in an oxidized state before starting a cracking run. To mimic this, an in-situ preoxidation of the coupons is carried out. Once the coupon is placed inside the reactor, the latter has to be heated up. To prevent high thermal shocks in the reactor, the coupon and the furnace heating elements, a heating ramp of 300 $K \cdot h^{-1}$ is applied for each heating and cooling operation in the reactor. Using this ramp, the reactor is heated up until it reaches 1023 K. During this heat-up stage, a constant flow of nitrogen (6.7×10^{-3} $Nl \cdot s^{-1}$) is fed to the reactor, to ensure an inert gas phase, avoiding any reactions between the coupon surface and the gas phase. No nitrides are expected to form, based on thermodynamic calculations. The heat-up has a total duration of approximately 2.5 hours.

As the temperature of the reactor increases, the temperature of the preheaters also has to be increased. This has to be done in steps, as no heating ramp control is available for these elements. The protocol followed is, once the reactor reaches 473 K, to set the temperature on both preheaters to 373 K. Later, after every increase of 100 K of the reactor temperature, the temperature of the preheaters can also be increased by 100 K. This is repeated until preheaters 1 and 2 reach the desired temperatures of 623 K and 723 K , respectively.

Once the temperatures of the reactor and preheaters are stable, the nitrogen feed is switched to a constant flow of air (6.7×10^{-3} $Nl \cdot s^{-1}$). The duration of the preoxidation is 12 – 14 hours and it is, therefore, performed mostly overnight. Once the preoxidation period is completed, the air feed is stopped and replaced by nitrogen (6.7×10^{-3} $Nl \cdot s^{-1}$).

3.2.4 Cracking and decoking

After preoxidation, a cracking cycle is carried out, followed by a decoking procedure. This allows to burn off the coke deposited during cracking, in order to start a new cracking run. During the

experiments here described, three consecutive cracking cycles are carried out, with a decoking procedure in between them. After the third cycle no decoking operation is performed, in order to retrieve coupons from the reactor that have coke deposited on their surface, so that they can be analyzed by SEM and EDX.

To start a cracking run, all the elements of the feed section have to be heated to their operation temperatures, which are presented in Table 3.2. At the same time, the reactor is heated to 1173 K, under a constant flow of nitrogen (6.7×10^{-3} Nl·s^{-1}).

Table 3.2: Operation temperatures of the heated elements of the feed section for ethane and naphtha cracking

Element	HC Feed	
	Ethane	Naphtha
Evaporator 1	473 K	473 K
Evaporator 2	523 K	523 K
Valve	473 K	473 K
Mixer	543 K	543 K
Preheater 1	823 K	773 K
Preheater 2	903 K	823 K

The reactor reaches its set temperature after approximately 30 minutes. This time is enough for the elements of the feed section to reach their set points too. At 1173 K, the balance is electronically tarred, to have a reference for comparison with the mass of the coupon after cracking. From this point on, the procedure and operation conditions are slightly different for ethane and naphtha cracking.

Once the mass of the coupon is registered, the temperature of the reactor is set to 1283 K. This high temperature is used in order to counteract the drop of temperature that occurs as soon as the cracking mixture is fed to the reactor, due to their high flow rates compared to that of nitrogen, and the endothermicity of the cracking reactions. The time to reach this set point is approximately 15 minutes.

While the reactor reaches its new set point, water and the hydrocarbons are fed to the evaporators. Since the switch valve is not yet in cracking position, the feed mixture goes to the vent. This is necessary because a few minutes are required for the evaporation to reach a stable and uniform regime, avoiding pulses. This is of utter importance for the cracking of liquid hydrocarbons, e.g. naphtha.

When the reactor reaches its set temperature and the evaporation is already stable, cracking can be started. This is done by changing the position of the switch valve, which allows the cracking mixture to go to the reactor. The temperature rapidly drops in the reactor, and it has to be regulated to reach its operating set point. The experimental conditions used during cracking of ethane and naphtha are summarized in Table 3.3.

Table 3.3: Experimental conditions used for ethane and naphtha steam cracking

	Ethane cracking		Naphtha cracking	
	Value	Units	Value	Units
HC flow rate	2.75×10^{-2}	$Nl \cdot s^{-1}$	1.04×10^{-5}	$kg \cdot s^{-1}$
H2O flow rate	1.11×10^{-5}	$kg \cdot s^{-1}$	2.78×10^{-5}	$kg \cdot s^{-1}$
Dilution (δ)	0.33	kg_{H2O} / kg_{C2H6}	0.375	$kg_{H2O} / kg_{Naphtha}$
Temperature	1159	K	1098	K
Pressure	1.03×10^{5}	Pa	1.02×10^{5}	Pa

The duration of each cracking run is 6 hours for both feeds. During this period, several GC injections are made, in order to constantly monitor the conversion (73%) or P/E ratio (0.4) during ethane and naphtha cracking, respectively, and to control that the gas phase composition is consistent during the run. Typically, an injection can be made every 30 minutes for the RGA, and every 75 minutes for the Trace GC. This way, approximately ten injections can be made every coking cycle with the RGA, and four can be made with the Trace GC.

Cracking is stopped by changing again the position of the switch valve. Immediately, the reactor temperature set point is changed to 1173 K, the hydrocarbon feed is stopped, and nitrogen is fed to the reactor (6.7×10^{-3} Nl·s^{-1}).

Once the reactor temperature is stable at 1173 K, the mass of the coupon is registered and compared with the reference mass recorded before the cracking run. This difference represents the amount of coke deposited during the entire cracking run, thus verifying that the obtained coking curve provided reliable data.

Then, the temperature of the reactor is reduced to 1023 K to carry out decoking operations. This low temperature is selected in order to prevent a very violent burning of the coke, which could cause thermal shocks in the coupon and the reactor. When this temperature is reached, decoking is started by feeding a mixture of air (8.3×10^{-3} Nl·s^{-1}) and nitrogen (8.3×10^{-3} Nl·s^{-1}) to the reactor. At the same time, the temperature of the reactor is set to 1173 K, so that decoking takes place with increasing temperatures to ensure complete but smooth burning of the coke. After approximately 30 minutes, the temperature set point is reached. As soon as the temperature is stable, the so-called steam treatment is started by changing the feed to the reactor to a mix of air (8.3×10^{-3} Nl·s^{-1}) and steam (6.67×10^{-6} kg·s^{-1}) while maintaining a constant temperature of 1173 K. The steam treatment has a duration of exactly 15 minutes.

To stop the steam treatment, the feed is switched back to nitrogen (6.7×10^{-3} Nl·s^{-1}), and the flows of air and steam are stopped. Then, the mass of the coupon is recorded again to compare it with the reference value before cracking, to confirm that all the coke has been removed.

After the steam treatment, a new cracking cycle can be started again. If the third coking cycle has been carried out, no decoking is performed. Instead, the temperature of the reactor and of all the heating elements is set to room temperature, so that the coupon can be extracted and stored in a

vacuum desiccator once all the elements have cooled down. The reactor cooling rate is 300 $K \cdot h^{-1}$, to prevent spalling of the coke layer.

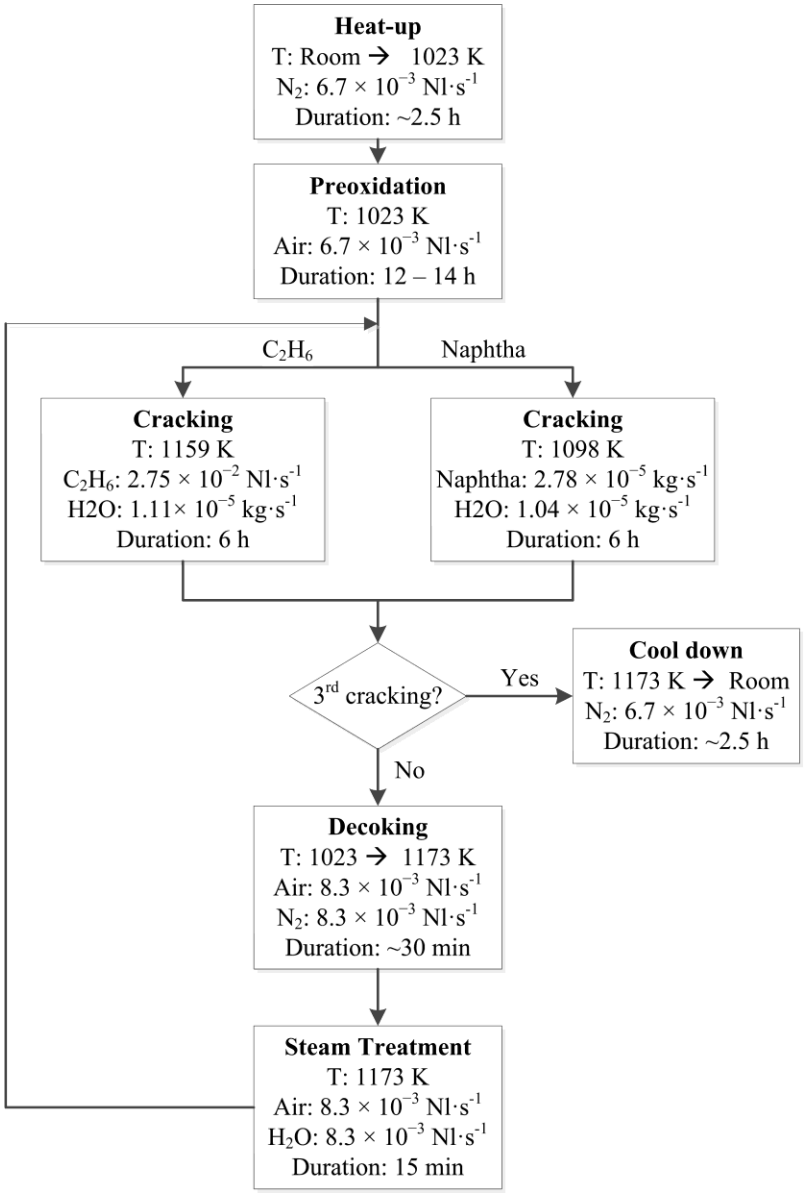

Figure 3.11: Simplified flowchart of the experimental procedure for cracking-decoking operation

The coke layer over the surface of the reactor is removed by an ex-situ decoking, carried out in a small Heraeus muffle furnace, where it is heated to 1133 K, kept at that temperature for approximately one hour, and cooled down. No automatic regulation for the heating ramp is available in the furnace, but due the power of its heating elements, heating takes approximately

3.5 hours before reaching the set point. Also cooling down takes longer than 3 hours because of the highly insulating construction of the furnace. Therefore, thermal shocks are not a concern during this operation.

A simplified summary of the procedure used during the experiments is presented in Figure 3.11.

3.3 Data processing

3.3.1 Coke formation data

A computer records all the data coming from the electrobalance setup. A large number of variables is recorded every second: temperatures of all the heated elements, as well as the mass of the coupon. No processing is required for the temperature measurements. However, the mass of the coupon needs to be processed in order to obtain the rates of coke deposition as a function of time. A Matlab code was developed for this purpose.

First, the outliers have to be eliminated. Sometimes the mass signal can exhibit upsets generated by, e.g., pressure changes as a consequence of GC injections. To reduce the effect of such upsets, the Matlab code allows to cut pieces of the raw signal so that they are not taken into consideration for filtering or further processing. Figure 3.12 shows two examples of raw signal of the mass of the coupon that exhibit some upsets, identified by arrows. Using the cutting feature of the data processing code, such upsets can be easily removed, as can be seen on the right side of Figure 3.12.

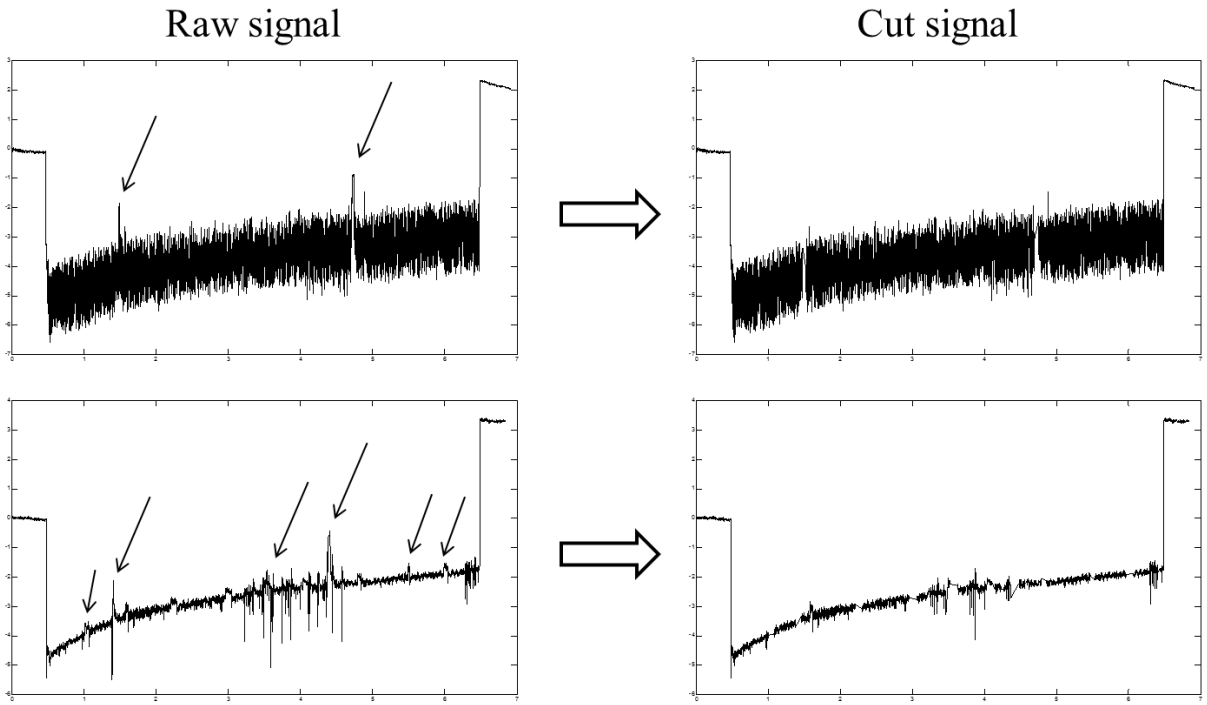

Figure 3.12: Raw signal of the balance (left) and signal after manual cutting of upsets (right). The upsets of the raw signal are identified with small arrows

To filter the raw signal, a function included in Matlab (lsim) is used. This function takes the values of the raw data as input, and returns a new set of data in which the mass is significantly smoother. Since the cracking runs last for 6 hours, the amount of data that are returned exceeds 20000 time-mass pairs. Working with such a large number of data takes a significant amount of time. Consequently, to facilitate the data processing, one data point of the smoothened set is taken for every 10 seconds interval. This reduces the amount of data to approximately 2000 points. This does not affect the quality of the dataset, as can be observed in Figure 3.13, where the cut and smoothened data are plotted as a function of time.

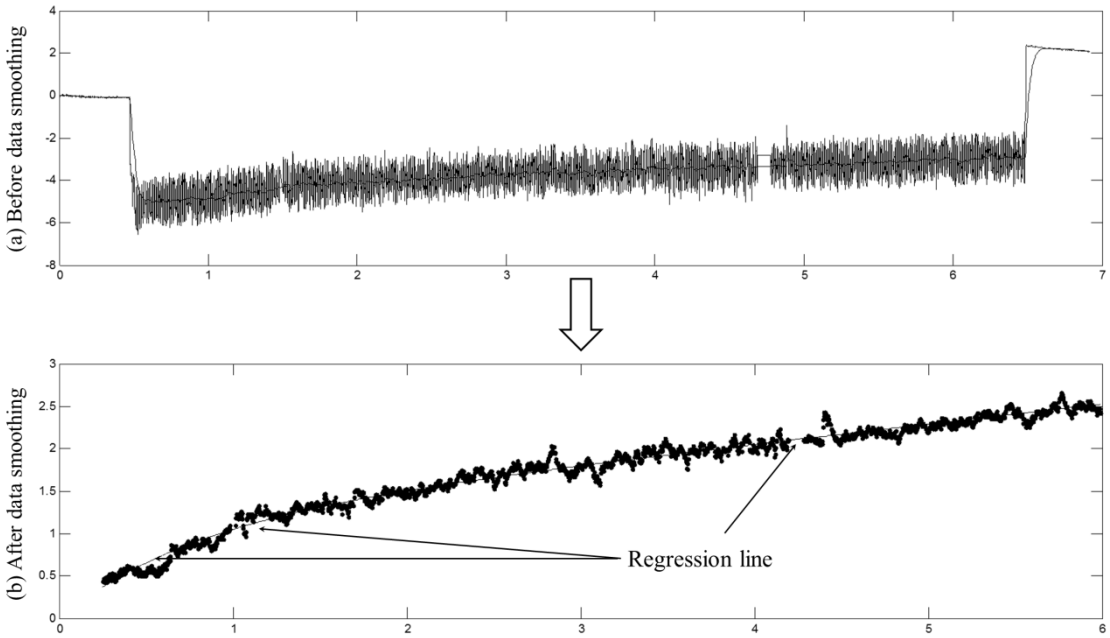

Figure 3.13: Effect of reducing the number of data points. (a) mass measurements every second after cutting; (b) smoothened mass measurement with data points every ten seconds

A routine for square-root minimization available in Matlab is used to make a regression of the smoothened mass of coke as a function of time. The data is fitted to equation (3.1), in which four parameters (A, B, C, D) are used. A constraint implemented to the routine is presented in equation (3.2). It implies that the difference between the mass function evaluated at 6 hours and 0 hours, respectively, must be equal to the measured amount of coke deposited during the experiment (m_f). This amount of coke is provided manually to the program by the user.

$$\text{Mass (t)} = \mathbf{A}\,t + \mathbf{B} - e^{-\mathbf{C}\,t + \ln\left(\frac{\mathbf{B}}{2}\right)} - e^{-\mathbf{D}\,t + \ln\left(\frac{\mathbf{B}}{2}\right)} \quad (3.1)$$

$$\text{Mass (6 h)} - \text{Mass (0)} = m_f \quad (3.2)$$

To evaluate the quality of the fit, the regression line constructed with the four parameters is plotted together with the smoothened mass of coke, as shown in Figure 3.13. If the fit needs to be

improved, parameters A, B, C and D are recalculated by running the Matlab program again, after performing a better elimination of outliers.

Once the minimization is finalized and parameters A, B, C and D are determined, the data processing program creates an output file that can be read in Microsoft Excel. This file presents the four parameters of the regression, as well as a table with the smoothened mass as a function of time, i.e. the data points that form the curve presented in Figure 3.13(b).

With equation (3.1) a continuous curve for the mass of coke as a function of time can be constructed. The coking rate can be easily calculated at any time, using equation (3.3), where S is the surface area of the tested coupon and m_{tj} is the mass of coke at time j.

$$R_c = \frac{m_{t_2} - m_{t_1}}{t_2 - t_1} \cdot \frac{1}{S} \tag{3.3}$$

Two rate values are reported for each coking experiment, i.e. the initial and asymptotic coking rates. The initial rate is calculated implementing t_1 = 15 min and t_2 = 30 min in equation (3.3). The asymptotic rate is calculated using t_1 = 5 h and t_2 = 6 h.

Assuming a uniform distribution of coke over the surface of the coupon, a nominal thickness of the coke layer (h) can be estimated with equation (3.4), in which δ_{coke} is the density of coke, and S is the surface area of the coupon. A value of $\delta_{coke} = 1.6\times10^3$ kg·m^{-3} has been reported by Bennett and Price [10].

$$h = \frac{m_f}{\delta_{coke} \cdot S} \tag{3.4}$$

3.3.2 Gas chromatography data

The chromatograms obtained from both gas chromatographs are stored in a computer, which uses Thermo Scientific's Chrom-Card Data System for integration of the obtained peaks. Typical chromatograms obtained with the three detectors are presented in Figure 3.14, Figure 3.15 and Figure 3.16.

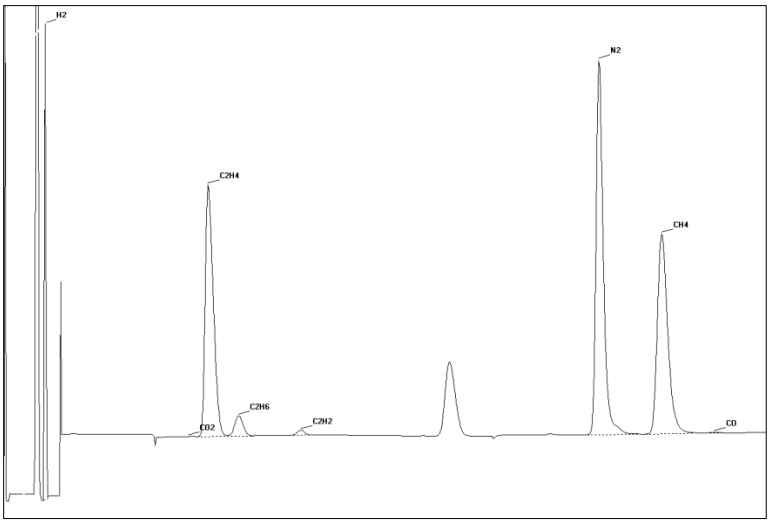

Figure 3.14: Example of a chromatogram obtained with the TCD of the RGA

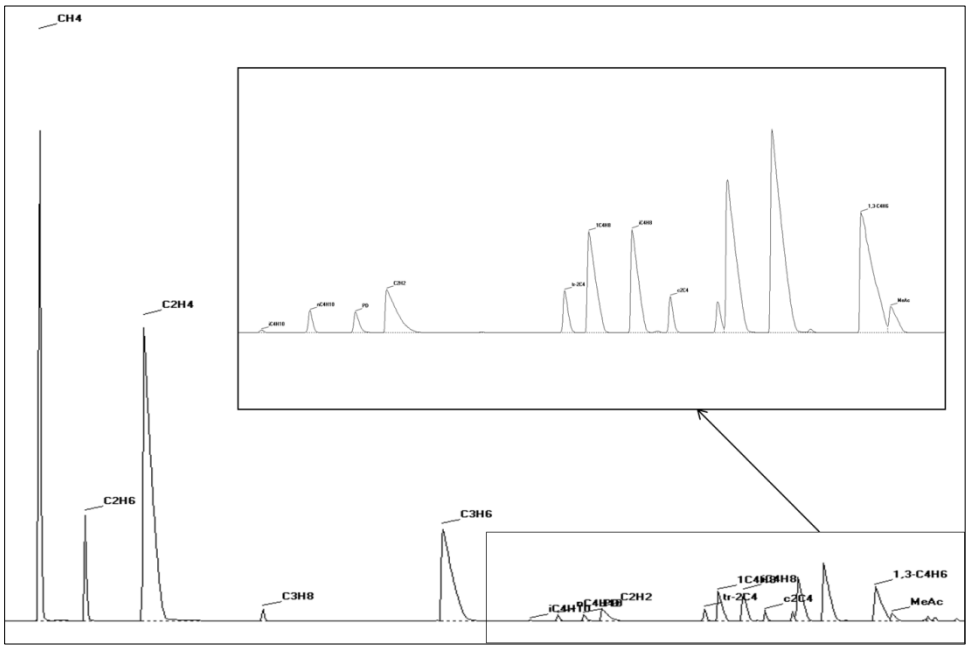

Figure 3.15: Example of a chromatogram obtained with the FID of the RGA.

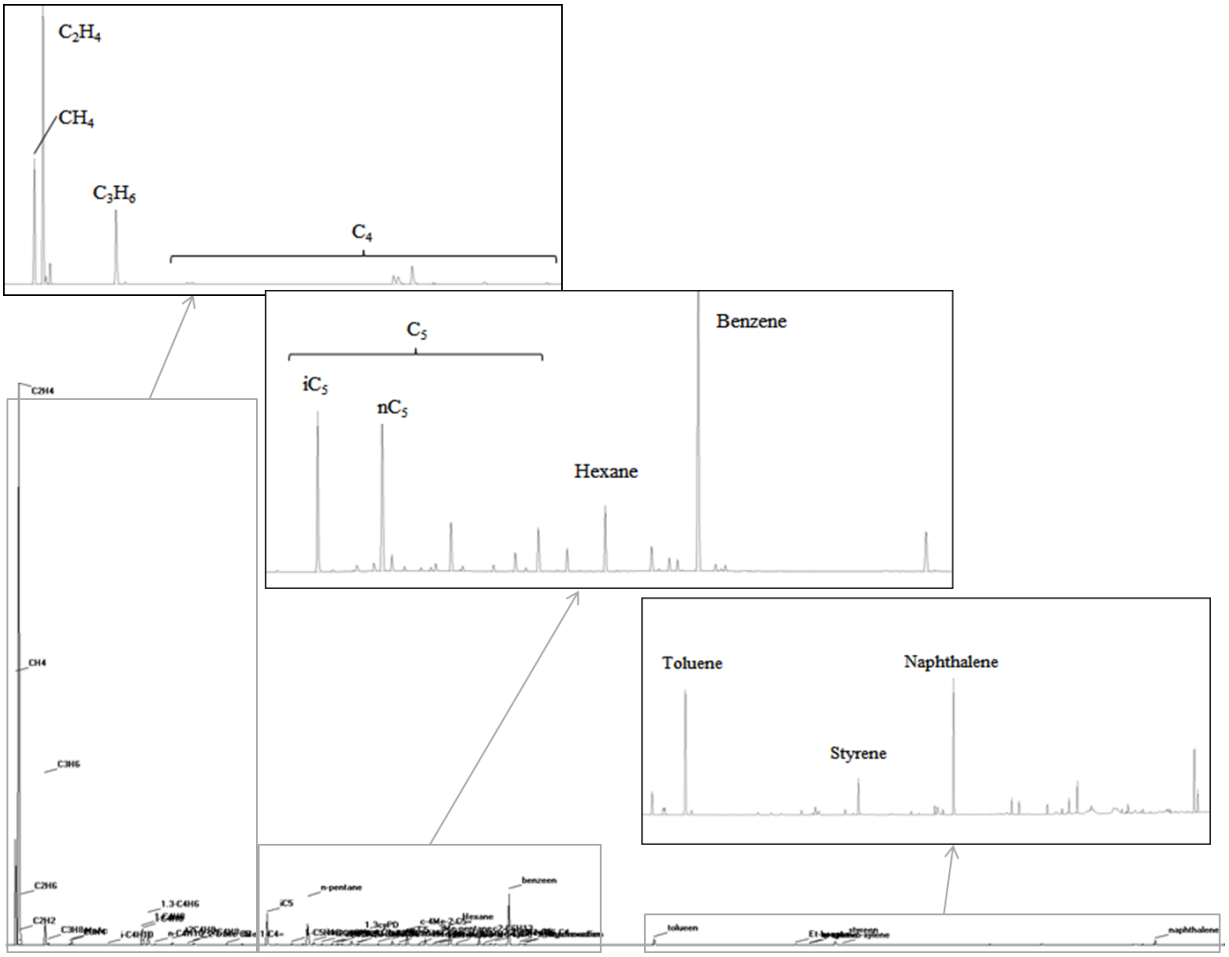

Figure 3.16: Example of a chromatogram obtained with the FID of the Trace Ultra GC

As mentioned in section 3.1.3, a small amount of nitrogen is added to the effluent to quantify the relative abundance of each component in the effluent, using the internal standard method. This method has been described in detail by Van Geem et al. [9]. Briefly explained, it relies on the fact that the flow rate of nitrogen that is added to the effluent is known. This way, the relative abundance of the rest of the components can be easily quantified.

In Section 3.1.3 it was said that three different chromatographs are obtained (two from the RGA, and one from the Trace GC), and nitrogen is only detected in one of them. Therefore, quantification of all the components follows the scheme presented in Figure 3.17.

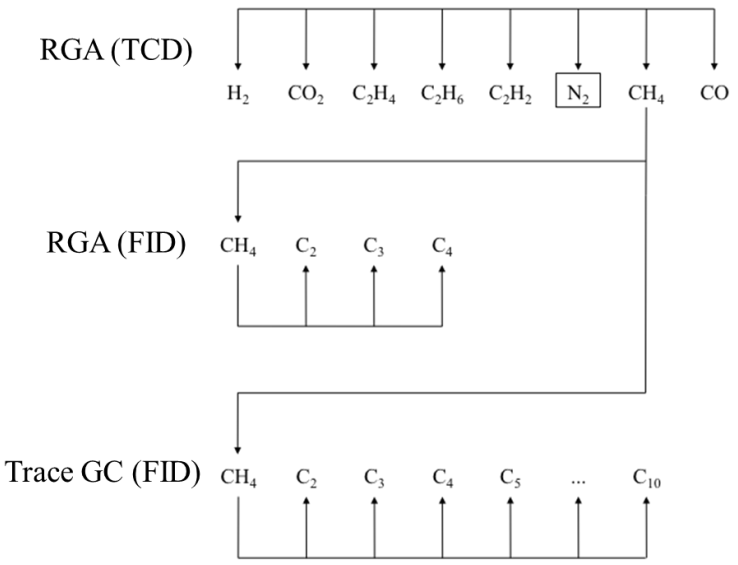

Figure 3.17: Use of reference components for quantitative on-line effluent analysis [9]

Knowing the amount of nitrogen added to the effluent, all the other components detected by the TCD of the RGA (H_2, CO, CO_2, CH_4, …) can be quantified, using equation (3.5).

$$F_i = \frac{f_i\, A_i}{f_{\text{Int Std}}\, A_{\text{Int Std}}}\, F_{\text{Int Std}} \tag{3.5}$$

In which F_i is the mass flow rate of component i, f_i is the relative response factor for component i, used to correct the corresponding total peak area A_i of component i in the chromatogram being quantified. The subscript Int Std refers to the internal standard. The response factors for the C_4^- fraction of the effluent are determined experimentally. For the heavier hydrocarbons, approximated response factors can be used [11]. They are approximated using equation (3.6), in which M_i is the molecular mass of component i, which has $N_{C,i}$ carbon atoms.

$$f_i = \frac{M_i}{N_{C,i}\, M_{CH_4}} \tag{3.6}$$

Taking advantage of the fact that methane is abundant in the gas phase, and that it is detected by the other two detectors, methane is used as an internal standard for the FIDs of the RGA and Trace GC. Quantification of the components detected with the other channels is also made using equation (3.5), in which the response factor of methane is chosen to be unity, i.e. $f_{CH4} = 1$.

As a verification of the results, the quantification of other molecules common to multiple channels, e.g. C_2H_4, can be made.

The yields of each component are reported as a wt % of the effluent. The calculation of the yield x_i for component i is done following equation (3.7).

$$x_i = \frac{F_i}{F_{feed}} \tag{3.7}$$

3.4 SEM and X-ray analysis

In order to study the morphologic and structural changes that the tested coupons undergo throughout the experimental runs, scanning electron microscopy and EDX analyses are performed. The former helps to observe the coupons with high magnifications, and the latter determines the elemental composition of the observed surfaces.

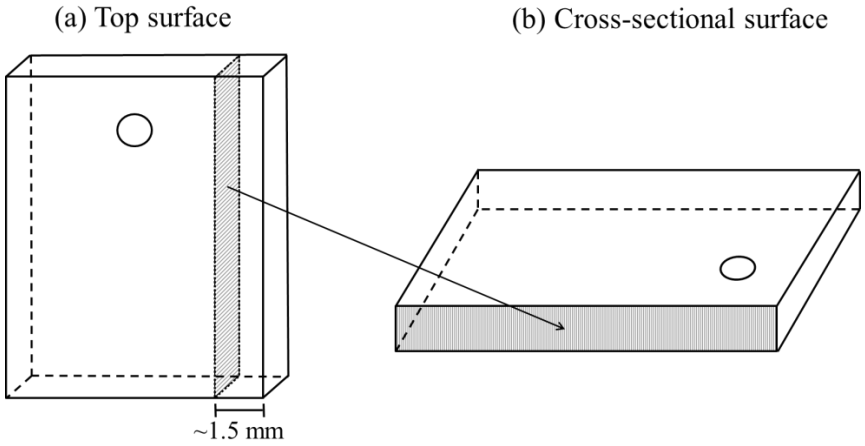

Figure 3.18: Schematic diagram indicating the top surface and the cross section of the coupons, both analyzed by means of SEM and EDX.

The top surface of the coupons, as well as the cross section are analyzed. Both surfaces are presented in Figure 3.18.

3.4.1 Description of the equipment

Two different types of microscopes are used for the analysis of coupons:

- The first one is a JEOL type JSM-5400, scanning electron microscope with a LaB6 crystal source. It is equipped with an INCA x-act detector, type 51-ADD0021SEM, as EDX detector. This is the microscope normally used to make images of the top surface of the coupons.
- The second type of microscopes are a FEI, type Quanta™ 450 FEG scanning electron microscope equipped with an Apollo X v6.5.3 detector for EDX analyses, and a FEI, type Quanta™ 200 FEG equipped with an EDAX Genesis 2000 detector. Both microscopes use a Schottky field emission gun as electron source. They can apply accelerating voltages ranging from 0.2 kV up to 30 kV. These are much more modern microscopes than the JEOL, allowing them to make sharper pictures at high magnifications, as well as element mappings with good resolution over highly magnified surfaces. Therefore, this microscopes were used when analyzing the cross sections of coupons by means of line scans and element mappings.

3.4.2 Pretreatment of the samples

The pretreatment of the coupons differs depending on the kind of analysis to be performed. For top surface analyses, the coupons are covered with a thin gold layer, to make sure that their surface is conductive and to prevent charging, which strongly affects the analyses. The gold-coating process is carried out using a JEOL JFC-1100E ion sputtering device.

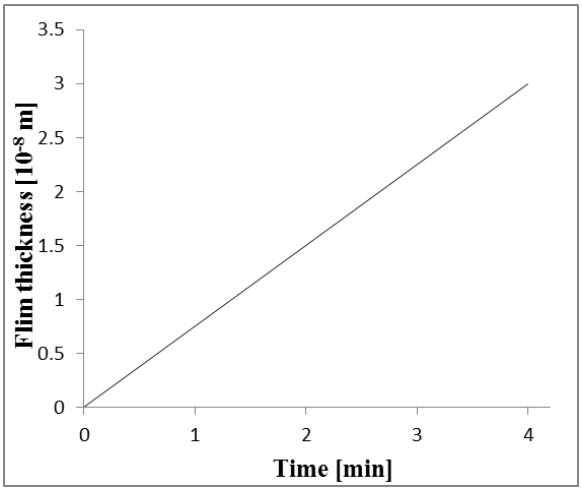

Figure 3.19: Thickness of the gold coating when using a current of 10^{-3} A [12].

A current of 10^{-3} A is used during the coating process. An estimation of the thickness of the gold layer as a function of the coating time is presented in Figure 3.19. The coating time for the coupons is 15 seconds, which leads to an estimated gold layer thickness of 2×10^{-9} m.

Once the coupon is coated, it is attached to a metallic cylinder made of a conductive metal, e.g. copper or steel, by means of double-sided carbon tape. The metallic cylinder acts as a support for the coupon to place it inside the microscope, and the carbon tape ensures good conductivity between the coupon and the support.

The pretreatment to analyze the cross section of a coupon is more complicated. It starts by cold-embedding the coupon in a strong resin, so that the coupon is not damaged by the following stages of the pretreatment. A cold embedding is performed, to prevent thermal shocks that could affect the morphology of the coupons. The embedment used is a commercial resin (Varidur 3000). It is prepared by mixing 15 g of its powder component with 7.6 g of its liquid component. They have to be mixed in a small cup for approximately two minutes with a manual stirrer, until a very homogeneous phase is formed. Using a small metallic holder, the coupon is placed lying over its long edge inside a cast, and the resin is poured. The embedment takes approximately two hours to

solidify at room temperature. Figure 3.20(a) shows how an embedded coupon looks once the resin has solidified.

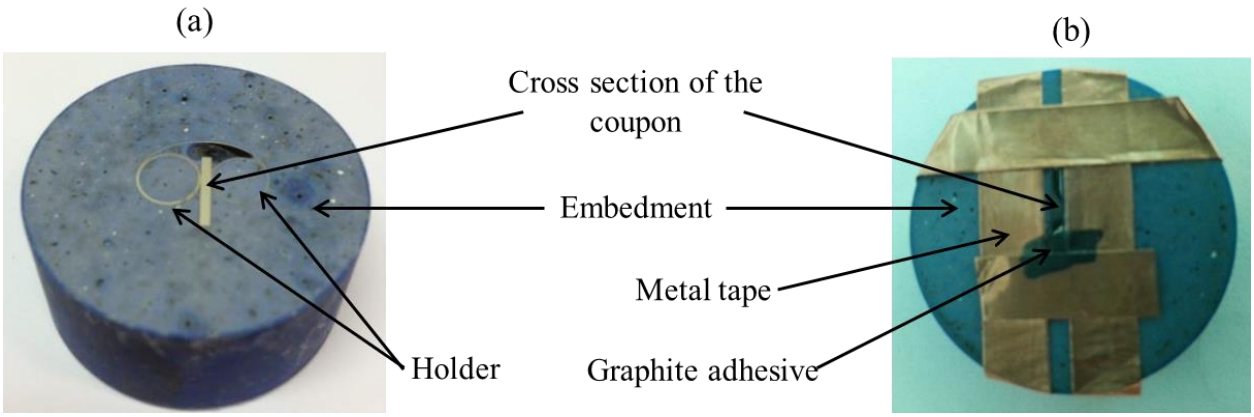

Figure 3.20: (a) Embedded coupon and (b) embedded coupon with metal tape and graphite adhesive to ensure good conductivity.

Before placing the embedded coupons in the microscope for analysis, they have to be ground and polished. This allows to observe the cross sections at a depth approximately 1.5 mm from the original edge (see Figure 3.18). The grinding and polishing is carried out in a Struers Tegrami-30 machine, in which an automated program is used. For the first three steps, water is used as coolant, and the last two include the addition of a suspension that includes small particles of different sizes, which facilitate the polishing.

- 2 minute grinding with a grit 200 disc.
- 1 minute grinding with a grit 600 disc.
- 1 minute grinding with a grit 1200 disc.
- 3 minutes polishing with a “mol” clothe, adding a suspension with 3 µm particles
- 5 minutes polishing with a “nap” clothe, adding a suspension with 1 µm particles.

Finally, the embedded coupons are partly covered with a metallic double-sided adhesive tape to prevent electric charging. To enhance the contact between the coupon and the tape, a graphite

conductive adhesive is applied in between them. An embedded coupon after application of the metal tape and graphite adhesive can be seen in Figure 3.20 (b).

3.4.3 Imaging and EDX scans

Three types of coupons are studied by means of SEM and EDX: blank, preoxidized, and coked. Blank coupons are those that have undergone the machining step described in section 3.2.1, but have not been washed or electro-scoured. They are studied to determine the appearance and surface composition of the material before being placed in the reactor, so that later the effect of the preoxidation step can be determined. Preoxidized coupons are those recovered from the reactor after being submitted to the in-situ preoxidation described in Section 3.2.3. Finally, coked coupons are those that, after undergoing 3 coking-decoking cycles, are recovered from the setup. Since no decoking is carried out after the third cycle, the coupons have a coke layer covering them.

The top surface of the coupons can be observed and photographed with various magnifications, ranging from 35X to 1000X or higher. Typically, an accelerating voltage of 10 kV is used for these images, because with higher accelerating voltages, the level of detail of the observed surface is reduced.

The penetration depth D of the electrons increases with higher accelerating voltages. It can be calculated using the Kanaya-Okayama correlation [13], presented in equation (3.8). For the studied metals, the accelerating voltages of 10 kV and 20 kV lead to penetration depths of approximately 0.5 μm and 1.7 μm, and of 1.5 μm and 5 μm for coke.

$$D = \frac{0.0267\, W_a\, E^{1.67}}{Z^{0.89}\rho} \tag{3.8}$$

Where W_a is the atomic mass of the metal, E is the accelerating voltage of the electron beam [kV], Z is the atomic number of the element, and ρ is the density of the material [$kg \cdot m^{-3}$].

For EDX determination of the surface composition, at least three rectangular EDX scans of the surface, see Figure 3.21, are carried out with two accelerating voltages (10 kV and 20 kV). Also, to increase the representativity of the analyses, the lowest magnification possible is used, so that the scans cover as much surface as possible. The scans are usually performed over rectangles of approximately 2 mm × 3mm.

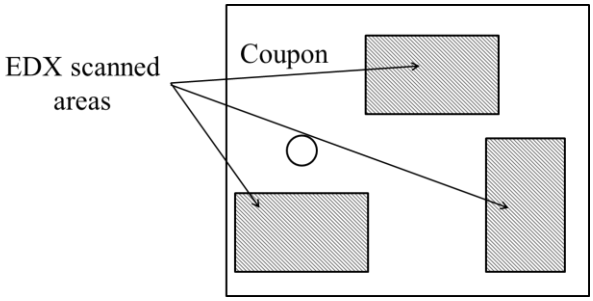

Figure 3.21: Example of the rectangular surfaces in which EDX scans are carried out to determine surface composition of coupons.

The cross sections of coupons are analyzed by means of line scans and element mappings. Both are carried out using an accelerating voltage of 15 kV. To perform a line scan, the line is drawn starting slightly above the uppermost layer of the sample (i.e. coke or oxide layer for coked or preoxidized coupons), and ending in the bulk of the material. The duration of a line scan depends on the length of the line and the resolution. For the typical cross section of coupons, this takes approximately 4 minutes.

To perform an element mapping, a rectangular area must be selected over the cross section. It is important to consider that mapping large areas can take a very long time (more than an hour per surface) to obtain an acceptable resolution.

Various images of cross sections, line scans and element mappings are presented in sections 4.3.2, 4.3.4 and 5.3.2.3, as well as in Appendices B and C.

3.4.4 Data processing

Identification and quantification of the X-ray spectra obtained during the EDX scans of top surfaces is automatically performed by the INCA software. The results can be extracted in a .txt file, which can be read in Microsoft Excel. This file includes the relative weight percentage of each element of interest for each scan performed. Sometimes, the reported concentration of an element is a small negative value. This is related with the numerical interpretation that the software makes of a small decrease of the baseline of the spectrum at the energy level corresponding to the element of interest. To correct this, the negative weight percentages are considered to be zero, and all the positive concentrations are re-normalized, in order to obtain a sum of all the concentrations of the elements that adds up to 100%. The surface compositions reported in this text correspond to the average of all the measurements made at the surface of a coupon with a given accelerating voltage.

The results of the EDX line scans are also quantified and processed by the software TEAM (Texture & Elemental Analytical Microscopy), installed in the computer linked to the FEI microscopes. This program generates a sheet in Microsoft Excel, reporting the number of counts received by the detector, as a function of the length of the line scan, or the position (in the x,y plane) for a mapping. This allows to create figures in which the number of counts for each element in the detector is plotted as a function of the length of the line scan. For the mappings, also a Microsoft Word document is automatically created by the software. It includes the image of the surface in which the mapping is carried out, as well as the individual mappings of each element of interest.

References

[1] Kanthal A (resistance heating wire and resistance wire) datasheet. Sandvik. URL: www.kanthal.com, last accessed: 16/06/2014.

[2] Matras, D.; Villermaux, J. Continuous reactor perfectly agitated by gas jets for kinetic study on rapid chemical reactions. *Chem. Eng. Sci.* **1973**, *28* (1), 129-137.

[3] Dagaut, P.; Cathonnet, M.; Rouan, J. P.; Foulatier, R.; Quilgars, A.; Boettner, J. C.; Gaillard, F.; James, H. A jet-stirred reactor for kinetic-studies of homogeneous gas-phase reactions at pressures up to 10-atmospheres (Approximately 1 MPa). *J. Phys. E Sci. Instrum.* **1986**, *19* (3), 207-209.

[4] Sobati, M. A.; Dehkordi, A. M.; Shahrokhi, M.; Ebrahimi, A. A. Novel Type of Four-Impinging-Jets Reactor for Oxidative Desulfurization of Light Fuel Oils. *Ind. Eng. Chem. Res.* **2010**, *49* (19), 9339-9348.

[5] Karsenty, F.; Sarathy, S. M.; Togbe, C.; Westbrook, C. K.; Dayma, G.; Dagaut, P.; Mehl, M.; Pitz, W. J. Experimental and Kinetic Modeling Study of 3-Methylheptane in a Jet-Stirred Reactor. *Energ. Fuel.* **2012**, *26* (8), 4680-4689.

[6] Veloo, P. S.; Dagaut, P.; Togbe, C.; Dayma, G.; Sarathy, S. M.; Westbrook, C. K.; Egolfopoulos, F. N. Jet-stirred reactor and flame studies of propanal oxidation. *P. Combust. Inst.* **2013**, *34*, 599-606.

[7] Schietekat, C. M.; Reyniers, P. A.; Sarris, S. A.; Van Geem, K. M.; Marin, G. B.; Kool, L.; Peng, W.; Lucas, P.; Zhou, H.; Gu, Y. Catalytic coating for reduced coke formation in ethylene-producing steam crackers: experimental and model validation. 26th. Ethylene Producers' Conference, New Orleans - LA, USA, April, **2014.**

[8] Shriner, K. A.; Curtis, R. A.; Falls, T. F., Apparatus for determining the moisture content of solids over a range of relative humidities and temperatures. In Google Patents: 1997.

[9] Van Geem, K. M.; Pyl, S. P.; Reyniers, M. F.; Vercammen, J.; Beens, J.; Marin, G. B. On-line analysis of complex hydrocarbon mixtures using comprehensive two-dimensional gas chromatography. *J. Chromatogr. A* **2010**, *1217* (43), 6623-6633.

[10] Bennett, M. J.; Price, J. B. A physical and chemical examination of an ethylene steam cracker coke and of the underlying pyrolysis tube. *J. Mater. Sci.* **1981**, *16* (1), 170-188.

[11] Beens, J.; Boelens, H.; Tijssen, R.; Blomberg, J. Quantitative aspects of comprehensive two-dimensional gas chromatography (GC x GC). *HRC-J. High Resolut. Chromatogr.* **1998**, *21* (1), 47-54.

[12] Jeol, *Instructions manual of Fine Coat JFC-1100E, ion sputtering device.*

[13] Goldstein, J.; Newbury, D.; Echlin, P.; Joy, D.; Lyman, C.; Lifshin, E.; Sawyer, L.; Michael, J., *Scanning Electron Microscopy and X-Ray Micro-analysis.* 3rd. ed.; Plenum Publishers: New York, **2003**.

Chapter 4: Ethane steam cracking

This chapter includes the following paper:

Muñoz Gandarillas A. E.; Van Geem, K. M.; Reyniers, M-F.; Marin, G. B., "Influence of the reactor material composition on coke formation during ethane steam cracking." *Industrial & Engineering Chemistry Research* **2014**, 53 (15), 6358-6371 **DOI:** 10.1021/ie500391b

Abstract:

An experimental study of the coking tendency of nine different materials and a reactor coating was carried out in a quartz electrobalance setup with a jet stirred reactor (JSR) under industrially relevant ethane steam cracking conditions: $T_{material}$ = 1159 K, P_{tot} = 0.1 MPa, X_{ethane} = 73%, dilution δ = 0.33 kg_{H2O}/kg_{HC}. A strong influence of the composition of the materials on the coking rate as a function of time on-stream was observed. The initial coking rate varied from 5×10^{-4} $g\cdot m^{-2}\cdot s^{-1}$ to 27×10^{-4} $g\cdot m^{-2}\cdot s^{-1}$, while the asymptotic coking rate changed in the range of 2×10^{-4} $g\cdot m^{-2}\cdot s^{-1}$ to 6×10^{-4} $g\cdot m^{-2}\cdot s^{-1}$. SEM and EDX analyses of coked and uncoked coupons revealed that the composition of the oxide layer in contact with the cracked gas, formed after the initial preoxidation or decoking, has an important influence on the amount of coke deposited. Materials that formed a thin Al_2O_3 layer on the coupon surface showed a higher coking resistance. A uniform surface composition and a high resistance to spalling and fractures are other important characteristics of good materials.

Keywords: Ethane steam cracking; coke formation; alloys; jet stirred reactor; electrobalance setup; SEM-EDX

4.1 Introduction

Steam cracking of hydrocarbons is the most important process for manufacturing many base chemicals such as light olefins (i.e. ethene, propene and butadiene) and aromatics (i.e. benzene, toluene and xylenes). Crackers account for about 8% of the primary energy consumption of the whole Chemical Process Industries sector [1]. A major influence on the energy efficiency and economics is the formation of coke on the inner wall of the tubular reactors in the gas fired furnaces. This carbonaceous coke layer reduces the cross-sectional area, leading to an increased reactor pressure drop. The latter promotes bimolecular over monomolecular reactions, resulting in a loss of olefin selectivity [2]. Moreover, coke functions as an insulator, affecting the conductive resistance against heat transfer from the furnace to the process gas [3]. To maintain the same cracking severity, the increased heat transfer resistance is compensated by increasing the fuel input to the furnace burners [4, 5]. This leads to higher tube metal temperatures (TMT). Eventually either the metallurgic constraints of the reactor material or an excessive pressure drop over the reactor will force the operators to cease production and decoke the reactors. Typically this requires production to be halted for 48 hours, and has a considerable adverse effect on the economics of the process [6].

In light of the negative effects of coke on the process performance coking has been extensively investigated [3, 7-35]. In general, three coke formation mechanisms have been delineated: the heterogeneous catalytic mechanism, the heterogeneous free-radical mechanism, and the homogeneous droplets condensation/tar deposition mechanism. The catalytic mechanism, schematically illustrated in Figure 4.1, accounts for the coil materials, with nickel and iron acting as catalysts for the formation of carbonaceous deposits in carbon-rich atmospheres [7, 21, 22]. In this mechanism, hydrocarbons are chemisorbed on the metal surface, subsequently losing

hydrogen atoms which react and desorb into the gas phase. The carbons left at the surface start diffusing into the alloy, lifting small metallic particles off the surface if the pressure they exert is higher than the tensile strength of the metal [21]. As carbon keeps depositing, the particles keep being lifted by carbon filaments growing out of the surface. Simultaneously, the radical carbon formation increases the diameter of the filament, and eventually covers the particle, encapsulating it. Therefore, the relative importance of radical coking compared to that of catalytic coking increases over time [7, 12, 21, 22].

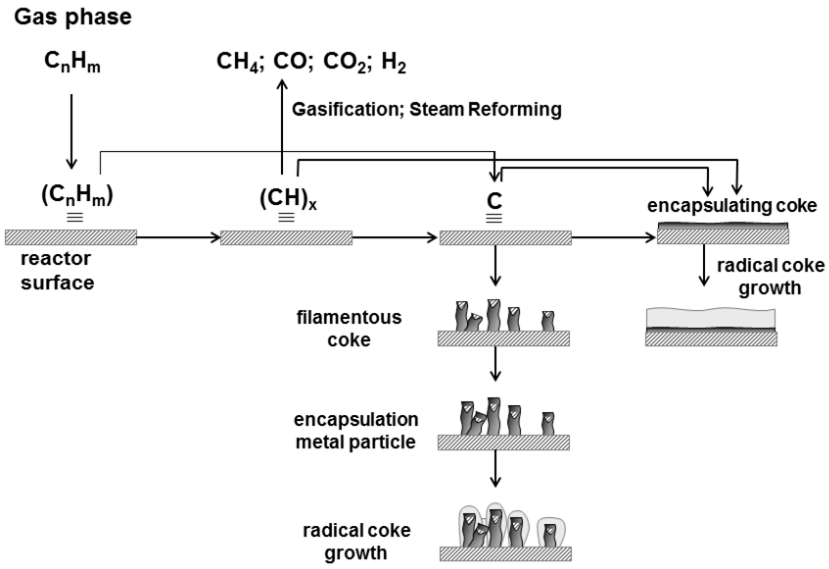

Figure 4.1: Schematic diagram of the heterogeneous catalytic mechanism for coke deposition

On the other hand, the growth of the radical coke layer can be explained by elementary radical reactions, which can be divided into five classes of reversible reactions (hydrogen abstraction, substitution, addition by gas phase radicals, addition to gas phase olefins and cyclization) as described by Wauters and Marin [28, 36]. The radical mechanism is present throughout the entire run length of the coil, and its relative importance increases over time as the catalytic sites of the surface are covered.

The droplet condensation mechanism applies when heavy polynuclear aromatics, either present in the feed or formed as a result of secondary chemical condensation reactions, e.g. by Diels-Alder reactions, condense either directly on the wall or in the bulk gas phase, and subsequently collect on the wall [26-28, 31, 33]. This mechanism is mainly important when cracking heavier feeds, such as gas oils, vacuum residue, and bitumen, and where gases are cooled [34-41].

Many efforts have been made towards the development of technologies to reduce coke formation. These technologies can be divided in three groups: the use of additives, the use of 3D reactor technologies and surface technologies. Mainly sulfur containing compounds are used as additives [34]. While a general consensus exists on the beneficial effect for the suppression of CO production, the reported effect on coke formation is contradictory [21, 33]. Next to additives, the application of three-dimensional reactor configurations such as the MERT technology [37] is increasing. These 3D geometries can result in improved heat transfer, leading to lower temperatures at the coke-gas interface, and hence, lower coking rates compared to conventional tubular reactors [38-40].

In the present work, the focus is on the third group, i.e. the application of advanced surface technologies such as coatings [41-43] and high performance alloys. Although coatings are not widely applied in industry, there is a strong interest in using innovative reactor alloys [44-50]. In most furnaces traditional Fe-Cr-Ni alloys are still used. Their ability to reduce coking and resist carburization has been attributed to the formation of a protective oxide layer, typically chromia (Cr_2O_3) on the surface [44, 46].

The addition of aluminum to Fe-Cr-Ni alloys can be highly beneficial for reducing coke formation and carburization. Aluminum forms alumina (Al_2O_3) on the surface when exposed to an oxidizing atmosphere. Alumina is much more stable than chromia at temperatures higher than 1200K [46, 51, 52]. However, the development of inhomogeneous non protective surfaces in Al-

enhanced alloys as a consequence of internal oxidation of the alloy has been reported [46]. Indeed, besides the composition, the uniformity and adhesiveness of the surface oxide layer to the bulk are also of great importance. These properties determine if the protection is only local or effective over the entire surface of the metal [53-55].

When manganese is included the high-temperature equilibrium under highly oxidizing atmospheres shifts towards the formation of a spinel, namely manganese chromite ($MnCr_2O_4$). This spinel is very stable under carbon-rich atmospheres and has been reported to significantly reduce the buildup of coke [20]. The formation of this spinel prevents the formation of chromia at the surface, which is prone to spall with temperature changes [24], and carburize weakening the alloy [56]. Nevertheless, it has been reported that chromia can be found below the manganese chromite, since the amount of chromium in the alloys is much larger than that of manganese [57]. If silicon is also included in small amounts, a thin layer of silica (SiO_2) has been observed to form below the chromium and manganese oxides layer [58]. It acts as a barrier for the possible migration of iron and nickel to the uppermost surface, but is also believed to block further migration of chromium to the surface, possibly affecting the long-term performance of the alloy [59].

The previous studies illustrate that many alloys can be used as reactor material. However, to the best of the authors' knowledge, at present no systematic comparison of the coking tendency of a wide range of traditional and more recently developed alloys has been reported yet. Only a limited amount of data from tubes withdrawn from service has been reported [24, 46, 60, 61]. However, those results are very dependent on how the furnaces were operated. Therefore in the present work an extensive dataset of coking rates has been obtained using coupons positioned in an electrobalance setup. Nine commercially available materials have been tested for ethane steam cracking under industrially relevant operating conditions, making this the most extensive

systematic evaluation of the coking tendency of different reactor materials under industrially relevant conditions. The effect of aging of the material is assessed by carrying out three coking and decoking cycles for each material. Both Al-enhanced alloys and alloys that do not contain aluminum are compared with silicon carbide. The influence of the chromium, iron and nickel content is also investigated. SEM and EDX analyses were used to evaluate the effect of preoxidation and coking/decoking cycles on the surface and bulk composition, complemented with thermodynamic calculations.

4.2 Experimental Section

4.2.1 Electrobalance setup

The experiments are carried out in a new electrobalance setup. The unit is especially designed to investigate the relation between the reactor material and the coking tendency. It consists of three parts: a feed section; a reactor section and an analysis section. A simplified flow diagram of the setup is shown in Figure 4.2.

4.2.1.1 Feed section

The feed section consists of a set of pressurized gas containers and a reservoir for water, two evaporators, a four-way switch valve, a heated mixer and two preheaters. The flow rates of the gases (i.e. N_2, C_2H_6, Air) and liquids (i.e. H_2O) are regulated by Bronkhorst thermal mass flow controllers. Water is evaporated in evaporator 1 (T = 473 K).

To avoid flow oscillations, the evaporators are filled with small glass pearls. The generated steam is then fed to evaporator 2 (T = 523 K), where ethane is also fed and heated. This mixture is sent to a heated four-way switch valve (V1, T = 473 K). This valve can send the feed either to a

condenser to stabilize the feed flow rates prior to cracking, or to the reactor to start the cracking experiments. To ensure proper mixing, the feed is then directed to a heated mixer (T = 543 K) located immediately downstream of V1.

Having a heat flux as low as possible in the reactor leads to a smaller temperature gradient inside the reactor, which is necessary to perform experiments at well-defined conditions. In order to prevent too high heat fluxes over the reactor wall, the feed is preheated in two separate preheating elements. The first preheater raises the temperature of the feed to 823 K. The second preheater further increases the temperature of the feed, yet holding it below cracking temperatures to prevent reactions taking place before the feed reaches the reactor. It is set at T = 903 K.

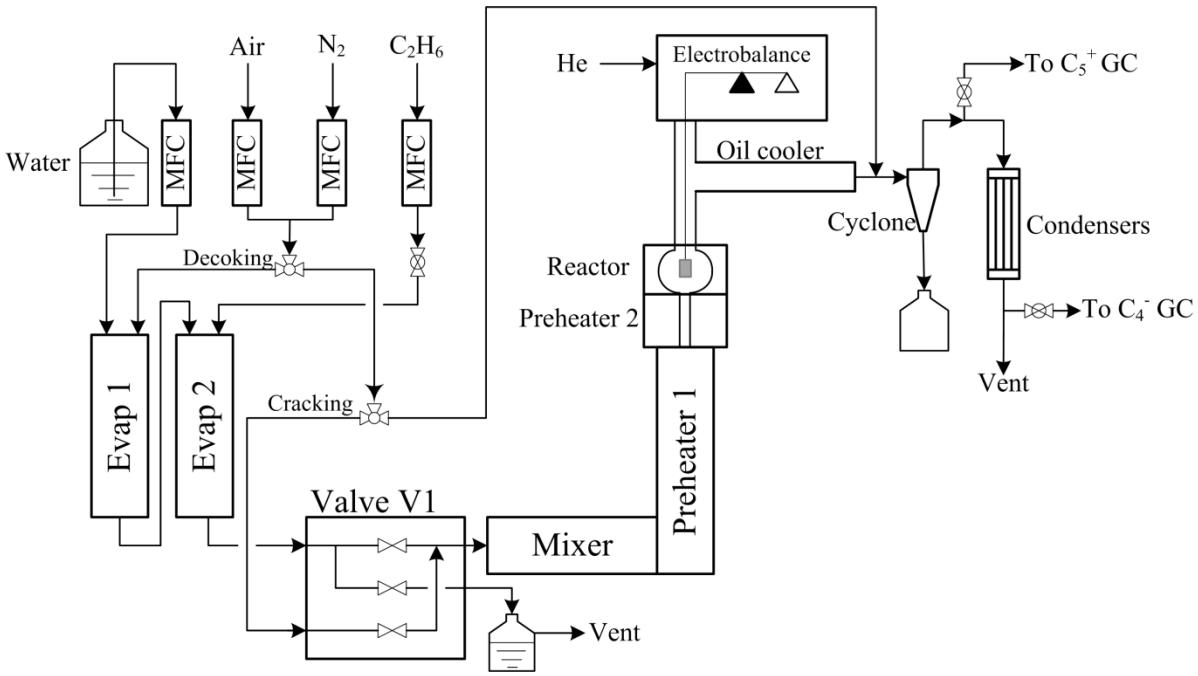

Figure 4.2: Overview of the electrobalance setup for studying coke formation on different reactor materials

4.2.1.2 Reaction section

Coke deposition is measured on small flat coupons (see Figure B.1(b) in Appendix B) made of different materials, suspended from the arm of an electrobalance. The dimensions of the samples (10 mm × 8 mm × 1 mm) were chosen as a trade-off between the specifications of the reactor (maximum size of the sample), the electro-balance (maximum mass of the sample, balance sensitivity and accuracy) and accounting for the mass of coke deposited that is required for an accurate measurement. The coupons were obtained from the internal surface of industrial tubes and were cut by electro-erosion into small flat rectangles. Except when coated, all coupons were polished using sandpaper grade 220 to ensure a similar surface roughness. Prior to placing them inside the reactor, all coupons were successively washed in water, isopropyl ether and acetone. The uncoated coupons underwent an additional 15 minute electrolytic scouring in a diluted solution of sulfuric acid. The main characteristics of the nine studied materials are presented in Table 4.1, together with the surface composition that has been measured for the blank coupons, i.e. prior to being placed in the reactor, using EDX with accelerating voltages of 10 and 20 kV.

A jet stirred reactor made out of quartz was used for studying coke formation because of the almost perfect mixing achieved in this type of reactor [62, 63]. More details of the used JSR reactor are presented in Section B.1 in Appendix B.

Table 4.1: Bulk composition and main characteristics of the tested materials

Material	Characteristics	Acc. V.	Measured Composition (wt %)					
			Cr	Fe	Ni	Mn	Si	Al
A	Centricast 35% Ni / 25% Cr micro alloy	10 kV	27.6	35.3	36.0	0.2	0.9	-
		20 kV	27.9	34.9	33.6	1.4	2.2	-
B	Multi-layered alloy	10 kV	28.4	34.8	36.8	0.0	0.0	-
		20 kV	28.7	36.1	35.2	0.0	0.0	-
C	Carburization resistant alloy	10 kV	29.0	33.3	36.2	0.0	1.5	-
		20 kV	28.5	34.2	33.8	1.5	2.0	-
D	Oxide layer on top of base alloy	10 kV	20.6	39.8	1.9	37.5	0.2	-
		20 kV	65.2	5.0	10.3	17.7	1.8	-
E	Al-enhanced alloy (Type 1)	10 kV	31.0	20.9	44.3	0.3	1.5	2.0
		20 kV	34.9	19.7	39.2	1.4	2.1	2.7
F	Al-enhanced, Nickel-free alloy	10 kV	25.2	70.3	-	0.0	0.4	4.1
		20 kV	22.9	71.2	-	0.2	0.5	5.2
G	Al-enhanced alloy (Type 2)	10 kV	31.1	21.8	44.7	0.0	0.2	2.2
		20 kV	32.4	20.4	43.3	0.1	0.2	3.6
H	Al-enhanced alloy (Type 3)	10 kV	30.1	36.1	32.2	1.1	0.0	0.5
		20 kV	23.5	38.1	33.2	3.1	1.0	1.1
I	Ceramic	-	SiC					

4.2.1.3 Analysis section

The analysis section consists of an oil cooler, set to a temperature T = 426 K, located immediately downstream of the reactor, which quenches the effluent impeding any further cracking reactions from taking place after the effluent leaves the reactor. This section also includes two Gas Chromatographs (GC): a Refinery Gas Analyzer (RGA), capable of detecting and quantifying permanent gases (up to C_4), and a Trace GC ultra GC, which measures the effluent from methane up to heavy hydrocarbons using nitrogen as internal standard for quantification [64]. Additionally, a propylene glycol cooled condenser (T = 274 K) is located right before the RGA to condense non-permanent gases and prevent heavy fractions from

reaching this chromatograph. The characteristics of the GCs are presented in Section B.2 of Appendix B.

4.2.2 Operating procedure and conditions

Figure 4.3 shows the timeline of an experiment carried out in the electrobalance setup. It consists of eight steps in which, after preoxidation, cracking and decoking cycles are repeated. The coked coupon is extracted from the reactor after the third cracking cycle for ex-situ analysis.

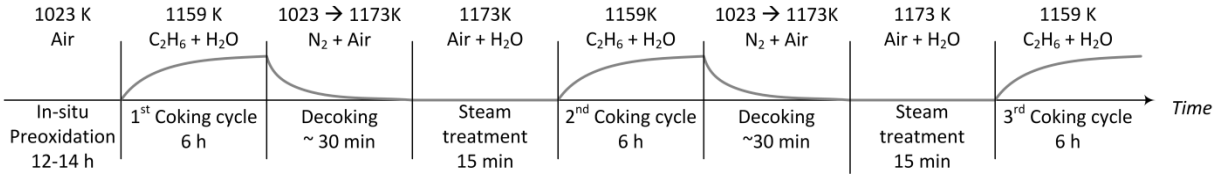

Figure 4.3: Timeline of the coking – decoking experiments in the Electrobalance setup.

4.2.2.1 Preoxidation

To mimic the surface state of an industrial cracking coil the samples were first oxidized in-situ prior to a cracking run. For that purpose, the reactor temperature was first raised to 1023 K with a heating ramp of 300 K/h and a constant nitrogen flow of 6.7×10^{-3} Nl·s^{-1}. Once this temperature was reached, the feed to the reactor was switched to a constant flow of 6.7×10^{-3} Nl·s^{-1} air. This preoxidation lasts 12 hours, after which, keeping the temperature fixed at 1023 K, 6.7×10^{-3} Nl·s^{-1} nitrogen was fed to the reactor. Although frequently in industry the coils are also presulfided, no presulfidation of the coupons was performed, since the effect of the presulfidation conditions on the coil surface composition and the coking rate is still not well understood. Hence, to obtain more insight in the effect of the coil material on the coking behavior, we have restricted this study to typically used oxidative pretreatment conditions.

4.2.2.2 Cracking

Before feeding ethane to the reactor the temperature of the reactor was raised to 1173 K under a nitrogen atmosphere, i.e. the reference state for mass difference measurement. After the mass of the sample was recorded the reactor was further heated to 1283 K. At this point water (1.11×10^{-2} $g\cdot s^{-1}$) and ethane (2.75×10^{-2} $Nl\cdot s^{-1}$) were sent to the evaporators (dilution $\delta = 0.33$ kg_{H2O}/kg_{C2H6}) in order to obtain a steady evaporation and then to a mixer before sending the stream to the reactor. Once the reactor temperature was stable at 1283 K, valve V1 was switched, allowing the cracking mixture to enter the reactor. Each cracking run lasted 6 hours, throughout which the temperature was controlled at 1159 K and residence time was set to 0.1s in order to maintain the conversion fixed at 73%. A detailed composition of the typical reactor effluent is presented in Table B.1 in Appendix B.

After cracking for 6 hours, the reactor effluent was sent to the vent, and nitrogen to the reactor. At the same time, the reactor temperature was set to 1173 K, and the flow of ethane was stopped. Once the set temperature was reached, the mass of the sample was registered, to calculate the mass difference between the start and the end of the cracking run, thus verifying that the obtained coking curve provided reliable data. The method to calculate the coking rates can be consulted in Section B.3 of Appendix B, as well as the mass gain as a function of time for each tested material. In total, more than 50 experiments (3 cycles each) were carried out. The standard deviations (σ) on every material amounted at most to 20% and 10% of the initial and asymptotic rates, respectively.

4.2.2.3 Decoking and steam treatment

Before decoking the reactor was cooled down to 1023 K, and once that temperature was reached, a mix of air (8.3×10^{-3} $Nl\cdot s^{-1}$) and nitrogen (8.3×10^{-3} $Nl\cdot s^{-1}$) was fed to the reactor.

Simultaneously the temperature of the reactor was set to 1173K using a heating ramp of 300 K/hour. As soon as the reactor reached 1173 K, the air flow was maintained, but the nitrogen was replaced by steam (6.67×10^{-6} kg·s^{-1}) to mimic industrial decoking practice. These conditions were kept fixed for 15 minutes, and then the feed to the reactor was switched back to nitrogen (3.8×10^{-3} Nl·s^{-1}). During decoking (N_2 and air) the mass of the coupon was monitored continuously enabling to confirm that all the coke was burned off. Additional visual inspection confirmed this. Finally, in "overnight mode", the reactor was cooled down to 1023 K with nitrogen flowing through, and kept like that until the next cracking run would start. Once the third cycle was completed, the reactor was cooled down to room temperature instead of going to the overnight mode. The samples were rarely decoked after the 3 coking cycles, to have coupons with coke on their surface once the experiments stopped. The samples were then removed and stored in a vacuum desiccator waiting for further analysis.

4.2.3 Scanning electron microscope and energy dispersive X-ray analysis

Coked and preoxidized samples were analyzed by means of Scanning Electron Microscopy (SEM) and Energy Dispersive X-ray (EDX) analyses. Scans of the top surfaces were carried out for the blank, preoxidized and coked coupons. Cross sectional analyses were carried out over preoxidized and coked coupons, to obtain line scans and element mappings over these surfaces. To avoid electric charging of the coupons during the analysis, they were covered with a thin gold layer, by means of sputtering to avoid electric charging of the surface.

EDX surface scans were carried out with two different accelerating voltages (10 kV and 20 kV), to evaluate the surface and sub-surface composition of the studied coupons. These scans were performed over three to five different rectangular regions for each coupon and the results were averaged in order to get a representative surface composition of the entire coupon.

The cross-sectional analyses of the coupons were carried out on selected materials (A, C, D, G, H). To observe the cross section of the coupons, they were first cold-embedded in a fast-curing resin (Varidur 3000) to ensure minimum damage to the coke layer in the further steps of the sample preparation. Once the resin had hardened, the coupons were ground and polished in order to expose a cross-section of the coupon at a depth of approximately 1.5 mm. Line scans and element mappings on such surfaces were obtained, to determine the profile of the metal concentrations along the depth of the coupons.

4.3 Results and Discussion

4.3.1 Coke deposition on different reactor materials

The total mass of coke deposited on the tested coupons after each cycle is shown in Table 4.2. The amount of coke depends on the composition of the material and the number of coking/decoking cycles. Based on the total amount of coke the ceramic material I is superior to all the alloys. Moreover, the mass of coke deposited on material I and also on material D remained almost unaffected after each cycle at around 1.5 mg and 1.8 mg, respectively. For E, F, G and H, small increments in the amount of coke were observed. The coke ranged from 1.3 to 2.6 mg. Finally, A, B and C showed significantly large increments of the coke deposited after every cycle (even 2 mg per cycle) and also the largest amounts of coke of all the tested materials, reaching values as high as 4.8 mg in the case of B. As a group, the Al-enhanced materials seemed to deposit less coke and deteriorate less over time than the non-Al containing materials under the experimental conditions.

Considering that the amount of coke deposited during the relatively short cracking experiments is determined by the effect of both the initial and asymptotic regimes, and that the asymptotic rate is

the one that in practice determines the amount of coke deposited in industrial coils [21], Table 4.2 also includes the values measured on each material for the initial and asymptotic regimes. Figure 4.4 shows a comparison of the mean measured initial and asymptotic coking rates. The size of the error bars corresponds to one standard deviation on both sides. Materials with and without aluminum in their formulation are grouped to better illustrate similarities and differences.

Table 4.2: Mean measured surface roughness, mass of deposited coke, and initial and asymptotic coking rates for the tested materials

		Non-Al-containing				Al-enhanced				SiC
		A	B	C	D	E	F	G	H	I
R_a Surface roughness [10^{-6} m]		0.15	0.16	0.17	0.72	0.18	0.17	0.19	0.14	1.38
Mass of coke [10^{-6} kg]	1st CC	1.75	2.09	2.17	1.91	1.93	1.32	1.57	1.74	1.48
	2nd CC	2.28	2.79	2.67	1.76	2.57	1.58	2.27	1.83	1.54
	3rd CC	2.99	4.86	3.70	1.78	2.64	1.69	2.62	2.03	1.42
R_c, init. [10^{-7} kg·s^{-1}·m^{-2}]	1st CC	6.8	7.3	7.7	6.2	6.5	5.1	5.4	6.5	3.5
	2nd CC	13.0	12.4	16.1	7.9	11.1	6.6	11.3	10.5	3.6
	3rd CC	17.9	26.8	23.7	6.0	12.2	5.3	16.4	13.8	3.6
R_c, asym. [10^{-7} kg·s^{-1}·m^{-2}]	1st CC	3.1	3.5	4.1	3.8	3.9	2.5	3.0	3.3	2.4
	2nd CC	3.3	4.8	4.1	3.4	3.8	2.7	3.6	2.6	2.4
	3rd CC	4.2	5.9	4.6	3.4	3.6	3.5	3.7	2.1	2.1

*Reported coking rates pertain to averaged values over 3-7 experiments.

The initial coking rates of materials A, B, C, E and G increase with the number of coking cycles, as is expected for alloys: Zimmermann et al. [60] showed that an increase of the initial coking rate is expected when materials age because of the increase in surface roughness by coking/decoking. However for materials D, F and I the initial coking rate remains almost

unchanged with an increasing number of cycles. Hence, the latter behavior does not seem to be related to the presence of aluminum.

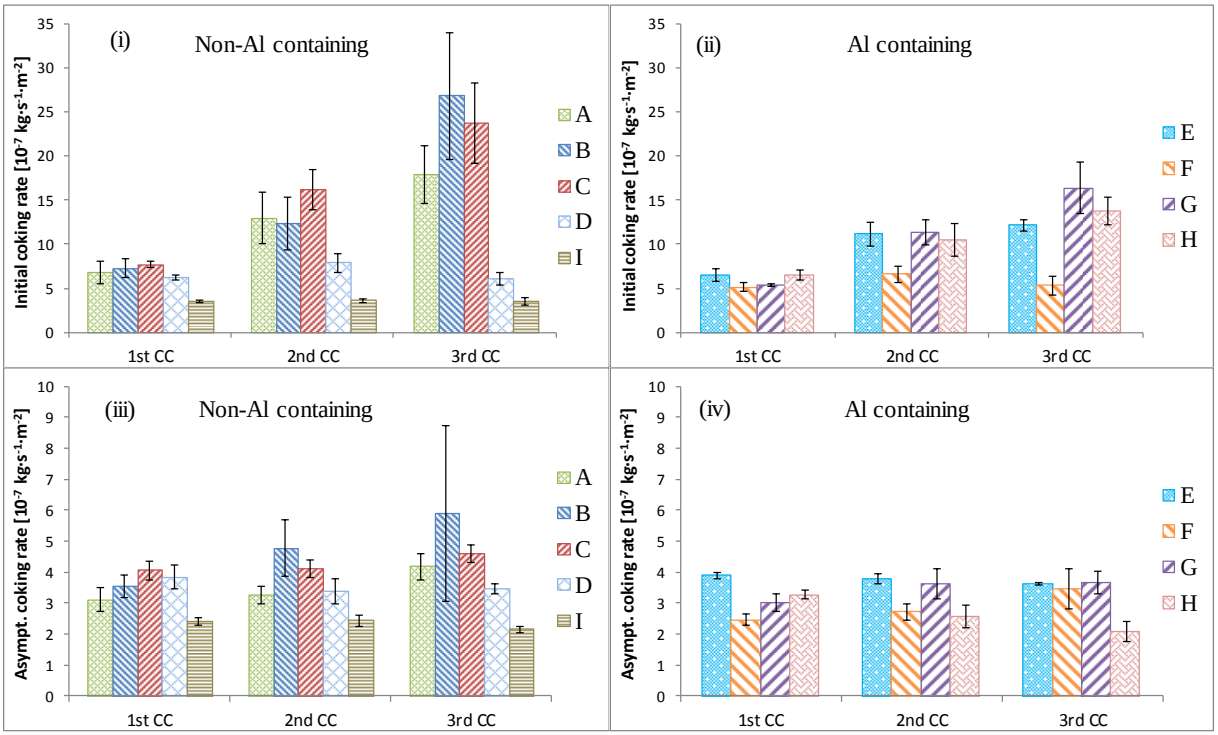

Figure 4.4: Comparison of the initial and asymptotic coking rates for non-Al containing alloys (i, iii) and Al-enhanced alloys (ii, iv) during ethane steam cracking in the electrobalance setup. The error bars correspond to the standard deviation (σ) of the experiments of each material.

A similar behavior was observed for the asymptotic coking rate. For some materials, the asymptotic rates increased with increasing coking cycles (A, B, C, F), while for others a minor decrease of the coking rate (E, H, I) as function of the number of decoking cycles was observed. Materials D and G exhibited a very stable asymptotic coking rate from the second cycle onwards. These observations are again not related to the presence of aluminum. It is well established that the asymptotic coking regime determines the run length of a reactor in an industrial cracker [21]. Based on this insight the following over-all ranking of the materials in increasing order of coke deposition is proposed under the studied conditions: B > C > A > G > E > F > D > H > I. The

high coking resistance exhibited by material I is not remarkable as this ceramic material is reported to be inert to the deposition of coke [23].

Material H is the least coking of all the studied alloys. Material D could be considered as the best of the non-Al containing alloys, as it showed stable and low asymptotic coking rates. The results presented in Figure 4.4 suggest that as a group, the Al-containing alloys tend to coke less than the non-Al alloys. However, this statement should not be taken as definitive, considering that some alloys containing aluminum had higher coking rates than materials with none. Materials B and C are particularly prone to coke formation under the used experimental conditions. Others, such as E, G and A, did not show a significant difference in performance. To better understand and explain these differences in coking behavior SEM and EDX analyses of coked and preoxidized coupons have been carried out.

4.3.2 SEM and EDX analyses of reactor materials

It is clear that the properties of the metal exert an important influence on catalytic carbon formation as was shown in Section 3.1. Other factors, such as surface roughness and grain size, chemisorption and dehydrogenation properties of the surface are also very important [22, 35, 65]. To gain further insight in which factors strongly affect the coking tendency of the different materials SEM and EDX analyses have been carried out on preoxidized and coked coupons. The SEM images presented in Figure 4.5 indicate the morphology of the coke deposited on the surface after three coking cycles for materials A (i, ii), D (iii, iv), H (v, vi), C (vii, viii) and G (ix, x). Very similar coke morphologies were observed in all of them, independent of the material of the coupon. On all the materials a layer of globular coke could be observed, formed by the interweaving of small coke filaments. However, the degree of packing of these filaments differed from coupon to coupon. It could be noticed, for instance, that the coke filaments in material A

were more closely packed than in material D, which is in line with the observed higher initial coking rate of material A compared to material D in Figure 4.4.

To retrieve additional information about the role of preoxidation of the coupons and how they aged under a cracking atmosphere, EDX analyses were performed on the top surfaces of various coupons: Blank (already polished, but not yet cleaned or preoxidized); preoxidized; and lastly coked (after 3 consecutive coking cycles). These analyses were performed using two different accelerating voltages for each coupon, i.e., 10 kV and 20 kV. The penetration depths of the electrons were calculated to be approximately 1.5 μm and 5 μm, respectively, by using the equation of Kanaya-Okayama, as described by Wang et al. [66] The results of these analyses are presented in Table 4.3, and then discussed in detail below. There are separate sections for the non-Al containing and Al-enhanced alloys. Top-view analyses were made for all the studied materials except material I, since this material is composed of silicon carbide and carbon cannot be properly quantified by EDX.

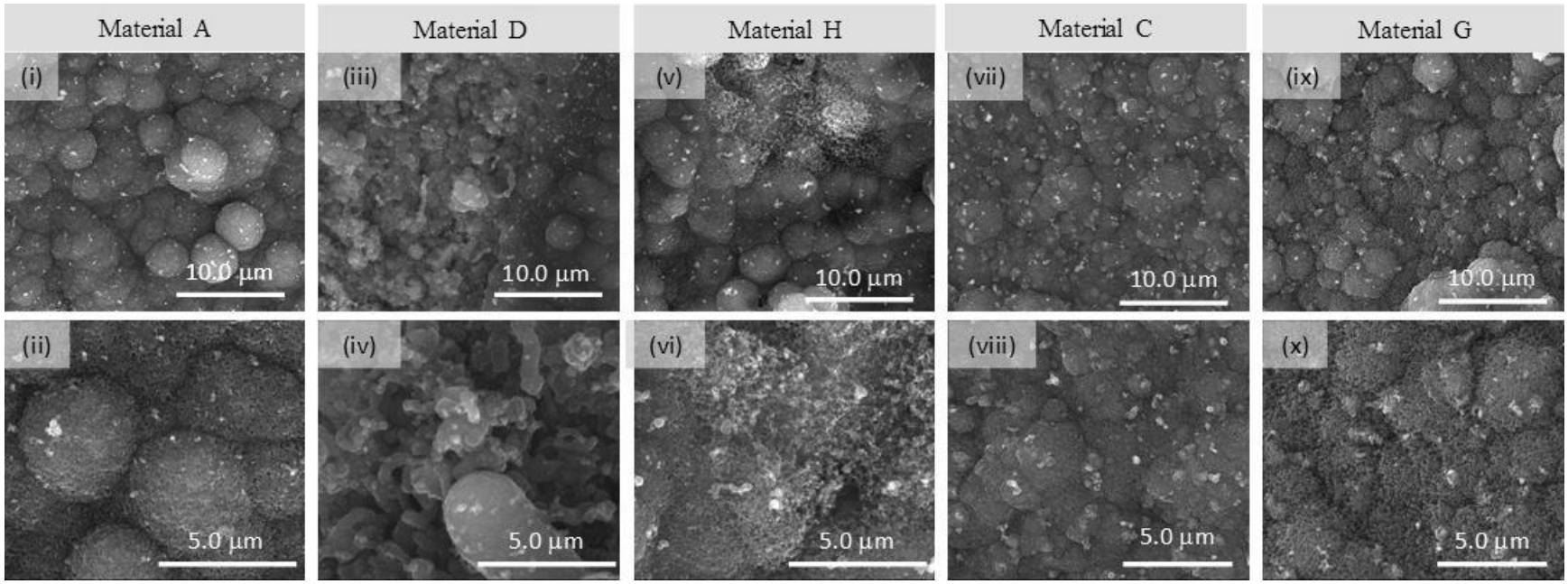

Figure 4.5. SEM images of the surface of coked coupons of material A (i, ii), material D (iii, iv), material H (v, vi), material C (vii, viii) and material G (ix, x). Magnification: 10000X (top row); 25000X (bottom row ii, iv, vi); 20000X (viii, x).

4.3.2.1 Non-Al-containing materials

The analyses of these coupons indicated that the preoxidation step had a significant impact on their surface composition. After preoxidation, the EDX surface scans showed a larger concentration of chromium and manganese in the outermost surface when compared to the blank coupons, accompanied by a depletion of iron and nickel. The only material for which preoxidation seemed not to have this impact was D. This is not surprising as this material had already undergone an oxidation during its manufacturing process which resulted in a developed oxide layer. The objective of such an oxidation is to develop a layer that is able to resist the influence of a carbon-rich atmosphere.

For example, for material A the concentration of chromium at the preoxidized surface was twice the concentration of the blank, while the concentration of manganese rose from almost zero in the blank to approximately 28% in the preoxidized sample. Iron and nickel decreased from approximately 35% to values as low as zero for nickel. The migration of elements leads to the formation of surface oxides of these elements or combinations of them.

Table 4.3: Top-view EDX analyses of blank, preoxidized and coked coupons of the studied materials (wt %)

		A			B			C			D		
		Blank	Preox.	3CC	Blank	Preox.	3CC	Blank	Preox.	3CC	Blank	Preox.	3CC
Cr	10 kV	27.6	56.4	82.8	28.4	62.5	98.8	29.0	60.2	84.9	20.6	69.1	47.4
	20 kV	27.9	45.8	78.5	28.7	47.5	91.4	28.5	73.3	80.4	65.2	66.0	59.1
Fe	10 kV	35.3	15.7	3.7	34.8	16.9	0.0	33.3	10.3	2.5	39.8	3.2	4.8
	20 kV	34.9	25.1	5.4	36.1	23.9	1.1	34.2	4.4	2.8	5.0	5.7	3.4
Ni	10 kV	36.0	0.0	1.1	36.8	0.0	1.2	36.2	0.0	3.5	1.9	4.9	8.7
	20 kV	33.6	22.3	4.5	35.2	23.5	7.5	33.8	10.9	11.8	10.3	11.1	5.9
Mn	10 kV	0.2	27.8	12.2	0.0	20.4	0.0	0.0	29.4	8.4	37.5	22.1	39.0
	20 kV	1.4	5.1	10.9	0.0	3.3	0.0	1.5	10.3	3.8	17.7	15.6	30.1
Si	10 kV	0.9	0.1	0.2	0.0	0.2	0.0	1.5	0.1	0.6	0.2	0.7	0.0
	20 kV	2.2	1.7	0.8	0.0	1.9	0.0	2.0	1.1	1.3	1.8	1.6	1.5

		E			F			G			H		
		Blank	Preox.	3CC	Blank	Preox.	3CC	Blank	Preox.	3CC	Blank	Preox.	3CC
Cr	10 kV	31.0	54.6	52.7	25.2	19.8	75.1	31.1	53.8	68.3	30.1	56.2	48.5
	20 kV	34.9	37.0	60.2	22.9	52.4	17.9	32.4	32.8	63.8	23.5	28.5	33.2
Fe	10 kV	20.9	9.3	10.8	70.3	55.8	0.0	21.8	9.9	6.7	36.1	13.5	19.3
	20 kV	19.7	18.6	4.8	71.2	18.1	47.9	20.4	20.0	7.9	38.1	28.6	14.2
Ni	10 kV	44.3	23.9	1.3	-	-	-	44.7	24.7	4.8	32.2	0.0	0.6
	20 kV	39.2	31.7	9.2	-	-	-	43.3	37.6	15.9	33.2	25.4	14.0
Al	10 kV	2.0	8.6	0.1	4.1	23.7	24.5	2.2	11.4	0.4	1.1	11.2	0.7
	20 kV	2.7	7.4	2.3	5.2	13.2	32.7	3.6	9.3	9.4	3.1	13.1	16.4
Mn	10 kV	0.3	1.5	35.0	0.0	0.3	0.0	0.0	0.0	19.1	0.0	18.8	30.2
	20 kV	1.4	2.1	21.4	0.2	16.2	0.5	0.1	0.2	0.7	1.0	3.1	16.2
Si	10 kV	1.5	2.1	0.2	0.4	0.4	0.4	0.2	0.2	0.7	0.5	0.3	0.6
	20 kV	2.1	3.1	2.0	0.5	0.1	0.9	0.2	0.1	2.3	1.1	1.3	5.9

The coked coupons also showed that chromium and manganese were the most abundant elements at the surface, similarly to what was observed after preoxidation. Therefore it could be assumed that no major changes took place in the surface composition of the coupons during coking, although small fractures of the oxide layer that cannot be detected by the scans might have occurred.

To better understand the surface composition of the coupons after preoxidation and coking, thermodynamic calculations were performed using Ekvicalc [67]. The thermodynamically-favored species are identified in the preoxidation atmosphere and then in the cracking atmosphere, by minimizing the Gibbs free energy of the gas-solid system. The conditions used for these calculations are given in Table 4.4. A molar ratio of 100 mol_{gas}/mol_{solid} was used to assure a large excess of the gas phase, in line with the experiments. The cracking atmosphere was modeled using the relative concentrations of ethylene, hydrogen, ethane, methane and water, as measured in the effluent.

Table 4.4: Conditions used for the Ekvicalc calculations

	Preoxidation	Cracking
Temperature [K]	1023	1159
Pressure [Pa]	10^5	1.03×10^5
Gas phase	21 mol O_2	21.84 mol C_2H_4
	79 mol N_2	39.03 mol H_2
		10.74 mol C_2H_6
		6.03 mol CH_4
		22.36 mol H_2O

Table 4.5: Solid phase input (mole fraction) for preoxidation and cracking calculations

		Preoxidation						Cracking					
		Cr	Fe	Ni	Al	Mn	Si	Cr	Fe	Ni	Al	Mn	Si
Non-Al	A	0.579	0.150	-	-	0.269	0.002	0.835	0.035	0.010	-	0.116	0.004
	C	0.616	0.098	-	-	0.284	0.002	0.853	0.024	0.031	-	0.080	0.012
	D	0.701	0.030	0.044	-	0.213	0.013	0.491	0.047	0.08	-	0.382	-
Al	G	0.502	0.086	0.204	0.205	-	0.003	0.691	0.063	0.043	0.008	0.183	0.013
	H	0.517	0.115	-	0.199	0.164	0.006	0.495	0.183	0.005	0.014	0.291	0.011

The input values for the preoxidation and cracking calculations, tabulated in Table 4.5, were obtained from the top-view 10 kV EDX analyses of the preoxidized and coked surfaces for each material. All the components that were calculated to be thermodynamically stable are tabulated in Table 4.6 for each material, for the preoxidation and cracking atmospheres.

Table 4.6: Normalized Ekvicalc-calculated surface composition (mole fraction) under preoxidation and cracking atmospheres for five different alloys

	Preoxidation					Cracking				
	Non-Al			*Al-enhanced*		*Non-Al*			*Al-enhanced*	
	A	**C**	**D**	**G**	**H**	**A**	**C**	**D**	**G**	**H**
Al_2O_3	-	-	-	-	0.225	-	-	-	-	-
Al_2SiO_5	-	-	-	-	0.014	-	-	-	0.008	-
Cr_2O_3	0.055	0.067	0.300	0.483	0.228	0.647	0.702	-	0.351	-
Fe	-	-	-	-	-	0.075	0.048	0.092	0.136	0.391
Fe_2O_3	0.204	0.137	-	-	0.139	-	-	-	-	-
$MnAl_2O_4$	-	-	-	-	-	-	-	-	-	0.015
$MnCr_2O_4$	0.736	0.792	0.585	-	0.394	0.249	0.163	0.482	0.393	0.528
MnO	-	-	-	-	-	-	-	0.269	-	0.031
Mn_2SiO_4	-	-	-	-	-	-	-	-	-	0.024
Ni	-	-	-	-	-	0.021	0.063	0.157	0.092	0.012
$NiAl_2O_4$	-	-	-	0.257	-	-	-	-	-	-
$NiCr_2O_4$	-	-	0.079	0.145	-	-	-	-	-	-
$NiFe_2O_4$	-	-	-	0.108	-	-	-	-	-	-
SiO_2	0.004	0.005	0.036	0.008	-	0.008	0.024	-	0.020	-

The Ekvicalc calculations suggest that, for most of the alloys after preoxidation, manganese chromite can be expected to be the most favored compound. Chromia was another important component that was observed in all the alloys after preoxidation. Silica seemed also to form in all of them. Finally, some Fe_2O_3 was also suggested to have formed, except on material D.

The cracking atmosphere calculations gave an indication of the stability under cracking conditions of the oxides formed during preoxidation. Manganese chromite is undoubtedly very stable, as it remained present in all the alloys in significant quantities.

The relative concentration of the manganese chromite spinel seems to have decreased during cracking for materials A, C or D, if compared to its abundance after preoxidation. This was accompanied by a significant increase in materials A and C of the relative amount of chromia, which is consequently assumed to coexist with the spinel. Also, elemental iron and nickel were determined to be stable under the cracking conditions.

The cross-sectional analyses shown in Figure 4.6 support the previous calculations. The preoxidation step had undoubtedly a significant effect on the surface composition, as can be seen in Figure 4.6(i). On top of the coupon, a darker region was formed, corresponding to the development of an oxide layer of roughly 2 μm thickness. This oxide layer seems to exhibit no discontinuities, and remained attached to the bulk metal. An EDX line scan was also performed across this cross section, and its results are presented in Figure 4.6(iv). As expected from the previous analyses, and in agreement with the results of the top-view EDX scans and the thermodynamic calculations, a large accumulation of oxygen, chromium and manganese could be detected in the uppermost surface of the coupon. This confirms the formation of a chromia layer and of the manganese chromite spinel that was suggested by the thermodynamic calculations. However, no underlying silica layer could be observed. It can also be seen that this oxide layer is free of nickel and iron, as the relative concentrations of these two elements seem to be significant only below the oxide layer.

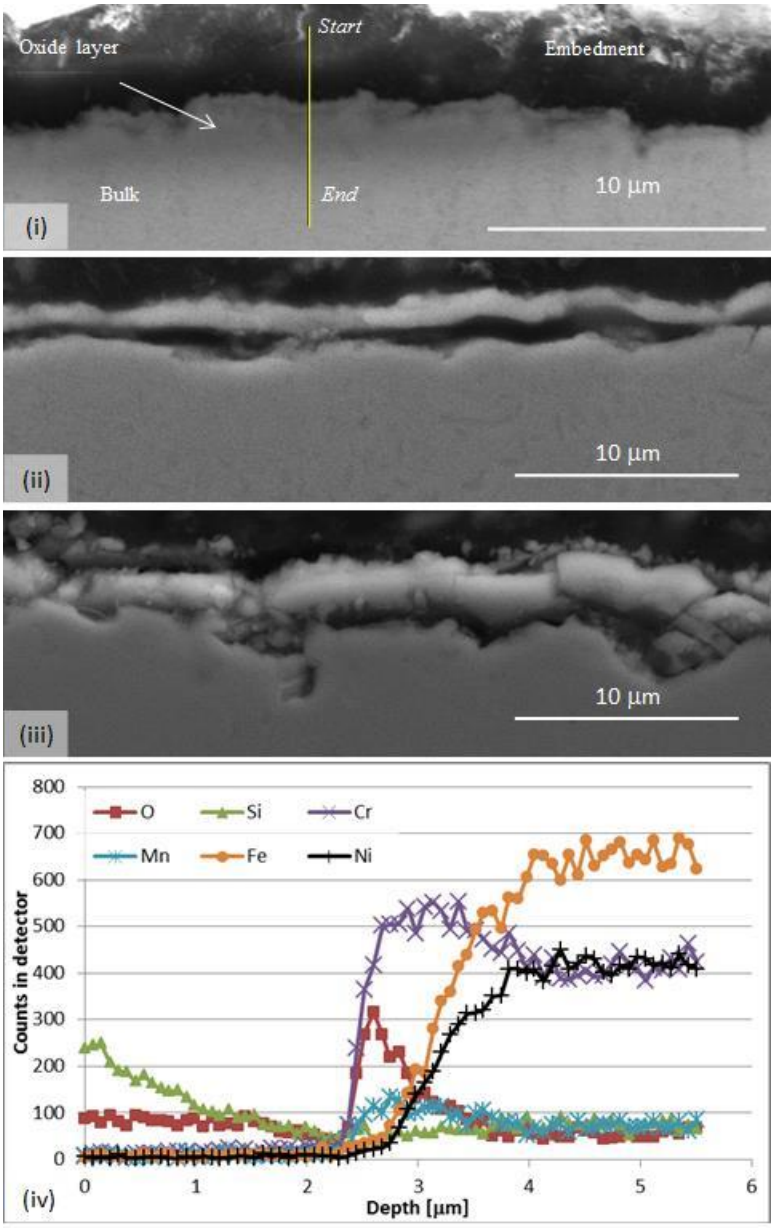

Figure 4.6: Cross sections of preoxidized coupons of materials A (i), C (ii), D (iii) and the EDX line scan analysis performed along the cross section of material A (iv).

Similar observations were made after preoxidation for the other two non-Al studied alloys inspected by EDX, namely C and D. Although the composition of these layers was similar in every case, it was interesting to notice that the oxide layer of C spalled from the bulk of the metal, leaving a gap between the bulk and the layer, as shown in Figure 4.6(ii). The cross section of D, presented in Figure 4.6(iii) shows a granular oxide layer noticeably thicker than in the case of A

or C. Line scans over cross sections of D determined that a very large amount of manganese chromite formed on top, with some chromia below it. For C, a thin manganese chromite layer was also formed on top, and a very significant amount of chromia was detected underneath. The line scans of preoxidized coupons of C and D (see Figures B.12 and B.13 in Appendix B) indicated the presence of a thin silica layer underneath the manganese chromite and chromia.

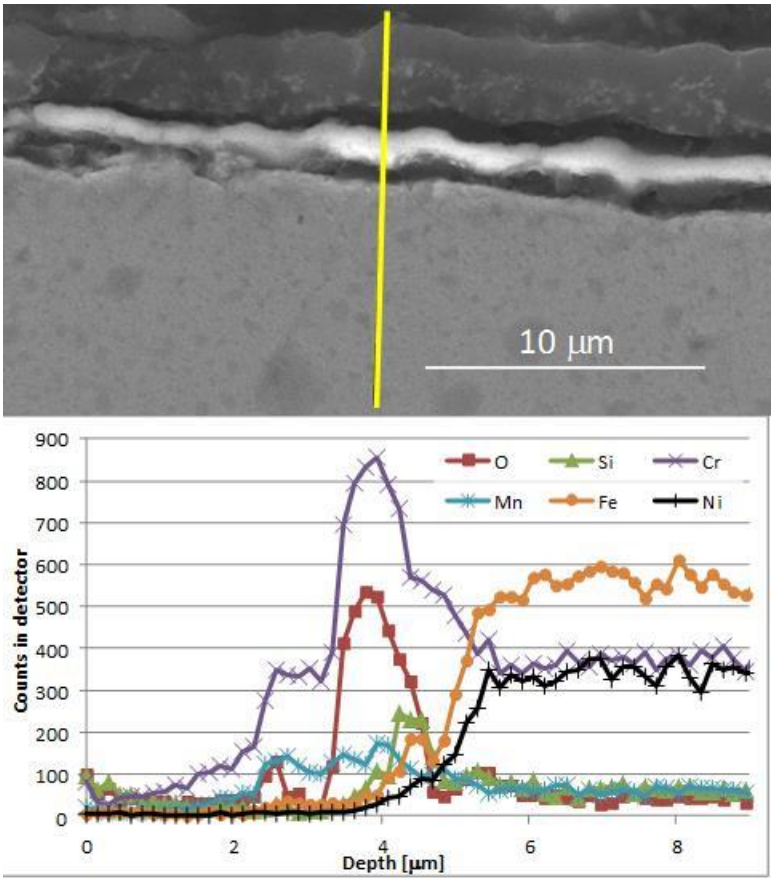

Figure 4.7: Cross section of a coked coupon of material A with the results of its EDX line scan

In line with the thermodynamic calculations, some differences in the surface composition could be observed between the preoxidized and coked coupons. Figure 4.7 showed that a void appeared between the coke and the oxide layer, and also between the oxide and the coupon itself. This can be related to the difference in thermal expansion coefficients between them and could be enhanced by the procedure used to remove them from the reactor after a coking run. Figure 4.7

illustrates this, and includes an EDX line scan that was performed along the cross section of a coked coupon of material A. However, the void between the metal and the oxide depends also on the material. Indeed, for material D (see Figure B.16 in Appendix B) the void was significantly smaller.

The line scans of the cross section also showed that some chromium and manganese are present in the coke layer in agreement with the observations of Bennett and Price [61]. The oxide layer was identified to be a chromium-manganese oxide, logically assumed to be manganese chromite. In accordance with the Ekvicalc calculations, the concentration of chromium was significantly higher than that of manganese, suggesting the formation of large amounts of chromia as well. Below the chromium and manganese rich area a silicon oxide is present, that forms a second diffusion barrier for carbon inwards and metals outwards. No relevant amounts of iron or nickel were detected in the oxide layer, as expected from literature [68]. However, right below the oxide layers, the concentration of these two elements became significant, together with chromium, in their usual bulk values. This confirmed that the oxide layers acted as a good barrier between the catalytically active metals iron and nickel and the gas phase.

The element mappings of Figure 4.8 complement the information provided by the line scans. Firstly, they show that carbon was restricted only to the coke layer. This element has not been detected throughout or underneath the oxide, showing that such layer acts as a very good barrier against carburization [69]. Additionally, the oxygen mapping showed that the oxide layer exerted an uninterrupted coverage of the metal. Reduced chromium and manganese that were embedded in the coke can be identified in the element mappings. The silica at the bottom of the oxide could be also clearly seen as a very thin but intense and continuous line. This confirms that a thin silica layer is indeed formed and acts as a barrier between the layer of chromium and manganese oxides and the bulk.

The main differentiating factor between A, C and D, that could explain the good performance of D and the rather poor one of C, seems to be related to the relative concentrations of chromia and manganese chromite on the surface. Based on the mappings and line scans, C seemed to be the one with the most chromia in the surface, while D exhibited the most manganese chromite. The element mappings of the three alloys indicated that silica formed in all of them, below the chromia and manganese chromite.

Hence, it can be concluded that at the applied experimental conditions all the non-Al containing alloys formed similar structures on their surface after preoxidation as shown schematically in Figure 4.9(a): a chromium-manganese spinel on top, which coexists with chromia (their relative abundance varies), followed by a thin layer of silica. Below, a region in which iron and nickel are relatively enriched was formed, as a consequence of the migration of chromium and manganese to the outermost layer. The long-term behavior of these materials could be however questionable, as the silica layer may block further migration of chromium and manganese to regenerate the surface during decoking operations.

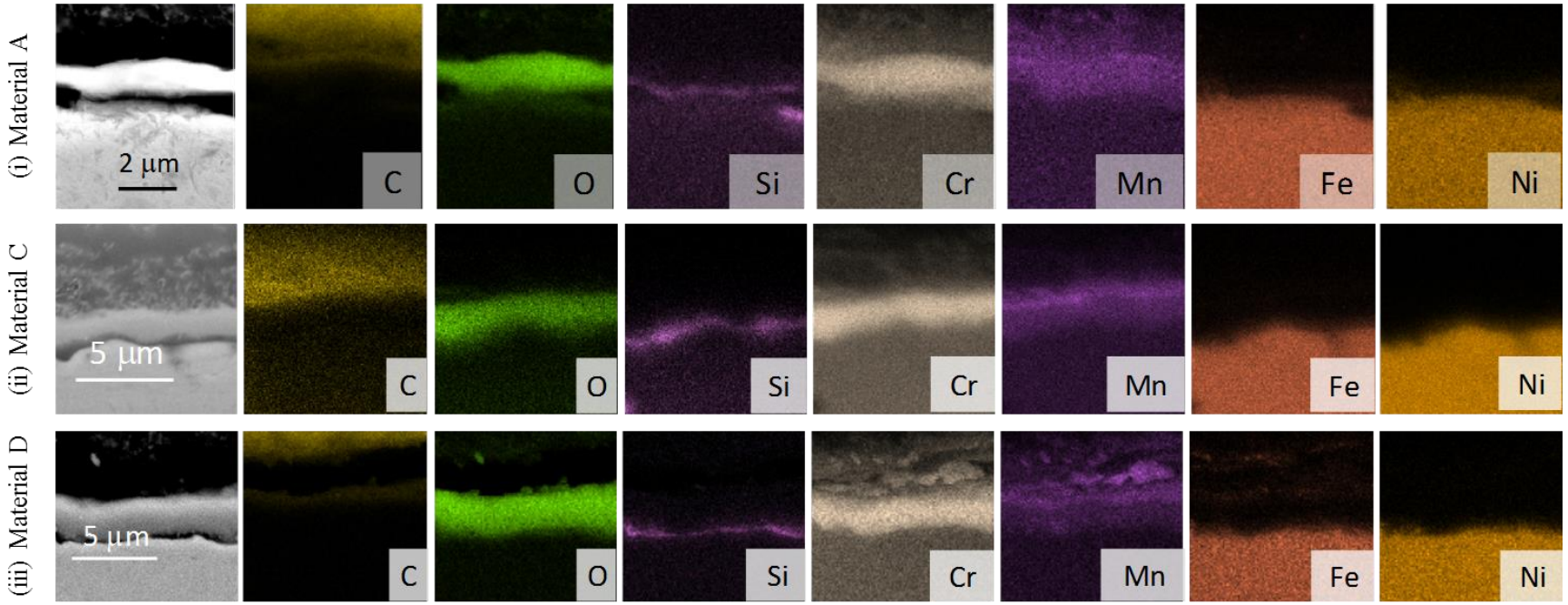

Figure 4.8: Element mappings of cross sections of coked coupons of material A (i), material C (ii) and material D (iii).

It can be noticed from Figure 4.9(b) that the coked coupons of non-Al materials showed a more defined division between the manganese chromite and the chromia than the one observed after preoxidation. This is most likely due to the high temperatures and steam content of the decoking atmosphere. The latter favors the formation of the manganese chromite. Interestingly, no carbon was observed penetrating the oxide. It was confined uniquely to the coke layer.

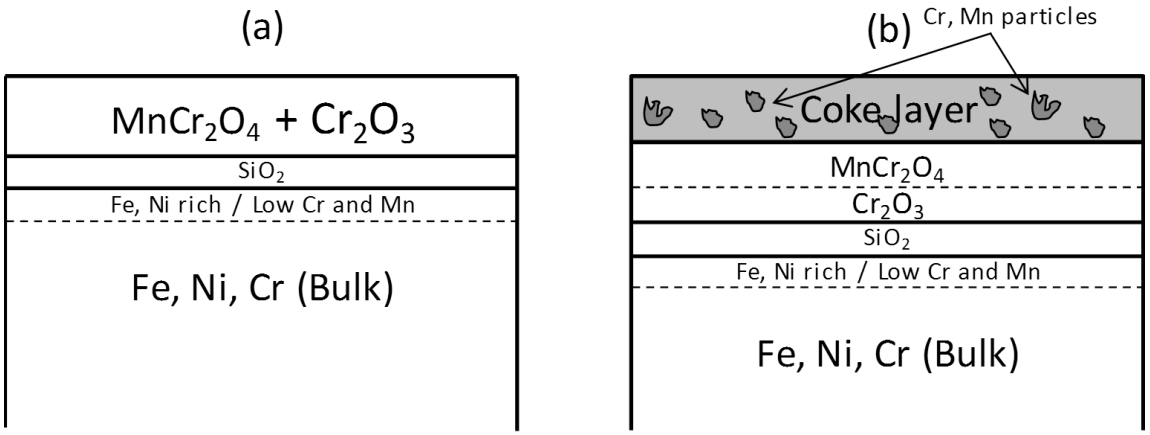

Figure 4.9: Simplified diagram of the observed surface state of material D (a) after preoxidation and (b) after coking. The layer thicknesses are not to scale.

4.3.2.2 Al-containing materials

The top-view EDX analyses of alloys E, F, G and H reported in Table 4.3 showed that besides the enrichment of manganese and chromium, that was discussed in section 3.2.1, now also aluminum is enriched on the surface of the preoxidized coupons [52].

Comparison of the preoxidized with the coked coupons indicated that chromium and manganese remained the most abundant metals on the uppermost surface of the coked coupons. Additionally, G and H showed significant amounts of aluminum close to the surface. Surprisingly, nickel had also a relevant concentration in the preoxidized coupons, particularly in G.

The Ekvicalc calculations for the Al-containing alloys indicated that after preoxidation the surface of material G contained high amount of mixed oxides. Since no manganese was detected

during EDX analysis, no manganese chromite was suggested to form. Additionally, G did not form alumina. Instead a combined oxide, $NiAl_2O_4$, formed. Silica was also a favored compound, although in small concentrations.

The thermodynamic calculations indicated that H formed alumina and manganese aluminate ($MnAl_2O_4$). Both are considered to easily migrate to the surface [70] and to be significantly resistant to the deposition of carbon [71]. However, only a small amount of Al_2SiO_5 was predicted to form in G. In addition, the $NiAl_2O_4$ formed during preoxidation in material G was determined to be prone to disintegrate during cracking, which could cause the release of elemental nickel at the surface, or very close to it. Also, in contrast with what was observed for the non-Al materials, manganese chromite was suggested by the calculations to be more favored after coking, as its calculated relative concentration was higher than during preoxidation, suggesting that this spinel coexists with the aluminum oxides in the surface.

Besides the composition of the layers, another important property that should be considered to determine the resistance of the materials to coking is how the integrity of these layers is preserved after the consecutive coking and decoking cycles [55]. Therefore again cross-sections of preoxidized and coked coupons were analyzed.

After preoxidation a thin oxide layer could be seen on top of both alloys (see the bright thin line on top of the bulk in Figure 4.10 for G, and in Appendix B (Figure B.14) for H. Line scans along these cross sections indicated a high concentration of aluminum and oxygen on top of the metal. It could also be determined that H had a thicker Al-rich layer than G. Additionally, a separation between the aluminum oxide and the other metals was clearly visible for material H. Instead for material G, it was observed that along the aluminum-rich layer, also other metals overlapped with this oxide, such as chromium, iron and nickel. Silicon also exhibited a slight increase in

concentration in this region, confirming that some silica was formed in material G after preoxidation.

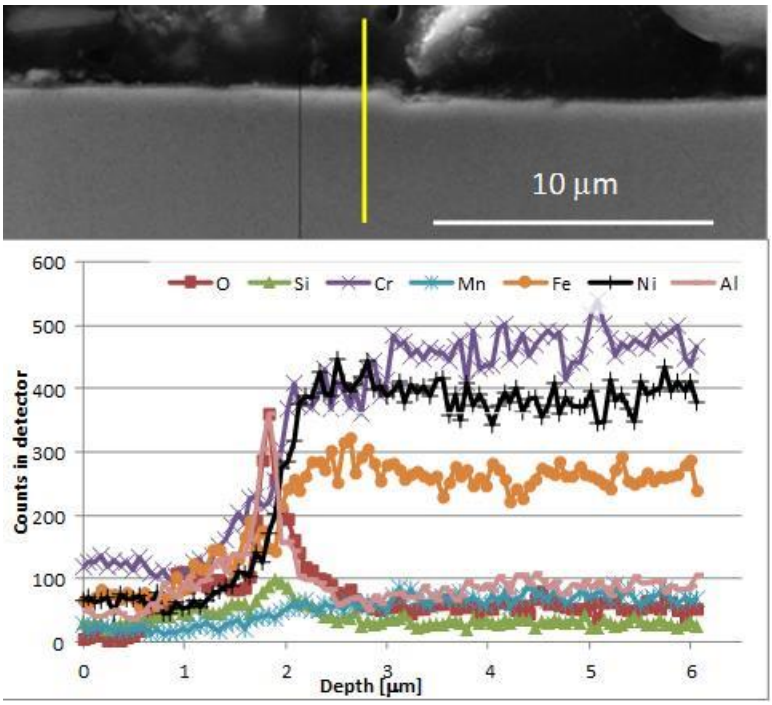

Figure 4.10. Cross section of a preoxidized coupon of material G, with the results of its EDX line scan.

The element mappings of the cross sections of coked coupons provided some fundamental insight in the different behavior of materials E, F, G and H. Material G conserved the presence of a thin but continuous oxide layer on its surface, as can be seen in Figure 4.11(i). The mappings and line scans of this material determined that this layer was mostly composed of an aluminum oxide. Some manganese was also detected in the layer which, based on the thermodynamic calculations, could be assumed to form manganese aluminate. A layer of chromia and manganese chromite spinel was formed as well, that partly overlaps with the Al-rich layer as indicated in the line scans. Consequently it can be assumed that, although the coupon was entirely covered by oxides, the surface composition varied locally between alumina, manganese chromite and manganese aluminate. As all of these oxides have a significant resistance to coke deposition, no carbon was

detected throughout or below the oxide layer. Iron and nickel were very well isolated from the gas phase.

The less promising coking properties of material G could be explained considering that its oxide layer did not remain intact after cracking, since internal oxidation can be observed in the coked coupons, forming channels perpendicularly oriented to the surface, instead of a uniform, continuous surface oxide. The element mappings presented in Figure 4.11 illustrate this very well. It can also be seen that on the uppermost surface nickel and iron were present, as well as some grains of chromium and Mn. This indicates that the $NiAl_2O_4$ predicted to form during preoxidation effectively decomposed and released elemental nickel at the surface. This was confirmed also with a line scan (see Appendix B, Figure B.17), which showed high amounts of oxygen on top of the bulk, accompanied by significant amounts of nickel and the main metals of the alloy. As observed in literature and shown in this work, internal oxidation of Al-enhanced alloys leads to poor resistance to coking and carburization [46].

When looking overall at the aluminum-enhanced alloys, aluminum migration to the surface after preoxidation was observed in all cases, along with the formation of a manganese chromite spinel.

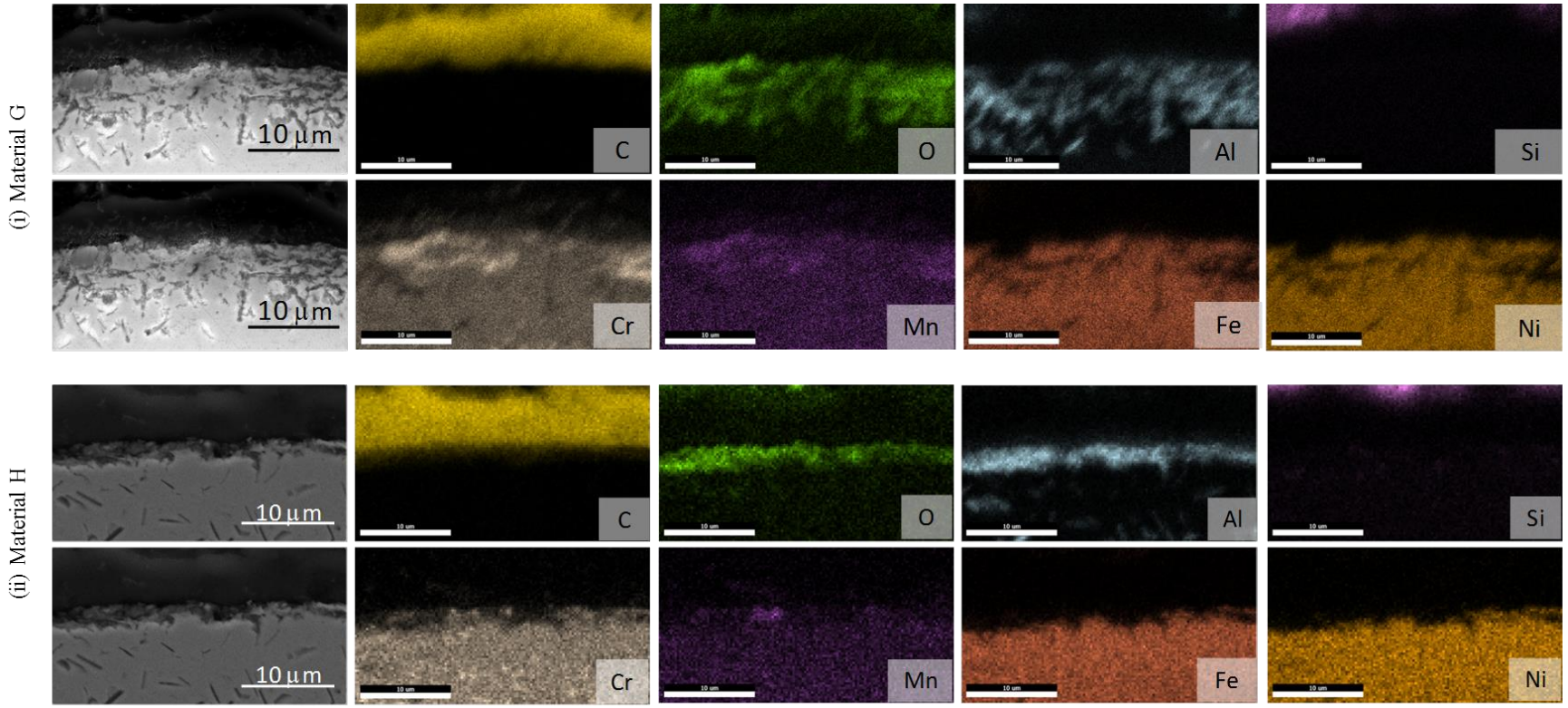

Figure 4.11: Element mappings of the cross section of a coupon of material G (i) and material H (ii).

Figure 4.12(a) presents a schematic of these different layers that can be developed during preoxidation. The element mappings further indicate that a continuous coverage of a thin alumina layer, combined with a mix of manganese chromite spinel and chromia underneath is desirable for this layer to be actually protective against coking. However, internal oxidation may lead to very poor results if it destroys the protective oxides and allows contact of the gas phase with, e.g., nickel or iron. Coked coupons seemed to form manganese chromite in the surface during the coking-decoking cycles in small amounts, in combination with alumina. This type of surface seemed to be the most coke resisting of all those that have been investigated, and is schematically illustrated in Figure 4.12(b). However, manganese aluminate did not achieve a total coverage of the surface.

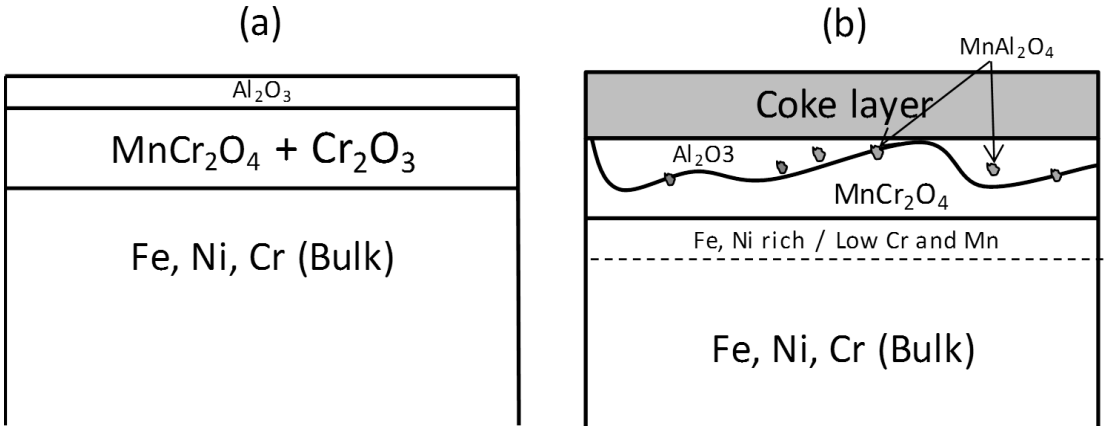

Figure 4.12. Simplified diagram of the observed surface state of material H (a) after preoxidation and (b) after coking. The layer thicknesses are not to scale.

4.3.3 Coke deposition on coated coupons

In Sections 2.5.2.4 and 4.1, it was stated that coatings can also be applied to the internal surface of the reactor to improve its coking resistance. A proprietary coating that was made available has been tested too, and is referred to as material J. This coating is applied over a typical heat-resistant alloy and, although its composition was not specified at delivery, it is known that it

consists of three different layers: an engineered surface at the gas-reactor interface, an enrichment pool underneath, and a diffusion barrier to separate the base alloy from the coating.

Coupons of base alloy were coated by the manufacturer and, applying the same pretreatment as the one explained in Section 2.1.2 and the experimental procedure of Section 2.2, absolute amounts of coke as well as coking rates were determined for three consecutive ethane cracking cycles. The coupons were not subjected to polishing or electro-scouring, and had a surface roughness R_a ~ 3.5 µm.

Table 4.7: Mean measured mass of deposited coke, initial and asymptotic rates for material J.

Mass of coke [10^{-6} kg]	1st CC	2.00
	2nd CC	2.36
	3rd CC	2.24
Rc, init. [10^{-7} kg·s^{-1}·m^{-2}]	1st CC	6.06
	2nd CC	8.28
	3rd CC	9.16
Rc, asym. [10^{-7} kg·s^{-1}·m^{-2}]	1st CC	4.19
	2nd CC	4.39
	3rd CC	4.23

Table 4.7 summarizes the coking rates measured during the experiments testing the coating. The results indicate that the amount of coke deposited over material J is not significantly influenced by the number of cycles, and could be considered stable between 2.0 and 2.4 mg. Comparing the mass of coke deposited over the coated coupons with those of the other studied materials it can be noticed that material J deposited less coke than material A, which had up to 3 mg of coke on the third cycle. However, other materials like D, G and I deposited less coke during the experiments.

To assist in the study of the coking resistance of this coating, Figure 4.13 presents the initial and asymptotic coking rates measured for material J, and includes also the rates measured over three

other materials: A base alloy (material A), and the two best performing materials of Section 4.3.1. One without aluminum in its formulation (material D) and one with this element (material H).

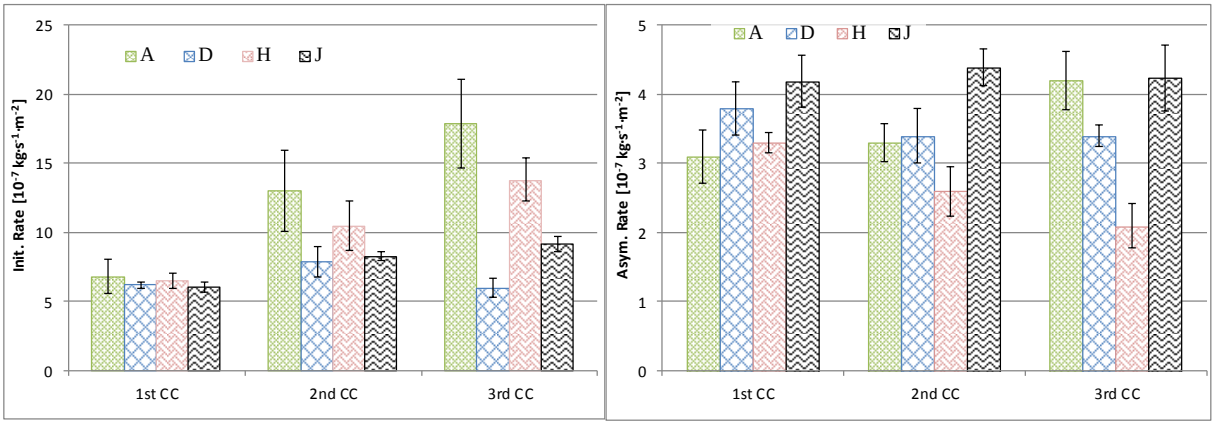

Figure 4.13: Comparison of the initial (left) and asymptotic (right) coking rates of materials J, A, D, and H.

Comparison of the initial coking rates indicates that material J has a lower rate of coke deposition than materials A and H, especially during the third cycle. It is also evident that this material exhibits an increase of its initial rate as the number of cycles increases. However, during the asymptotic regime, it can be observed that the asymptotic coking rate of J is very stable as the number of cycles increases, but higher than that exhibited by materials D and H, and comparable to that of material A, particularly in the third coking cycle.

If including material J in the ranking presented in Section 4.3.1, it can be ranked as the fourth most coke promoting material, in between materials A and G.

4.3.4 SEM and EDX analyses of coated coupons

To complement the information that the coking rates provided and to understand the evolution of the material throughout the experiments, the top and cross sectional surfaces of blank, preoxidized and coked coupons were analyzed by means of SEM and EDX.

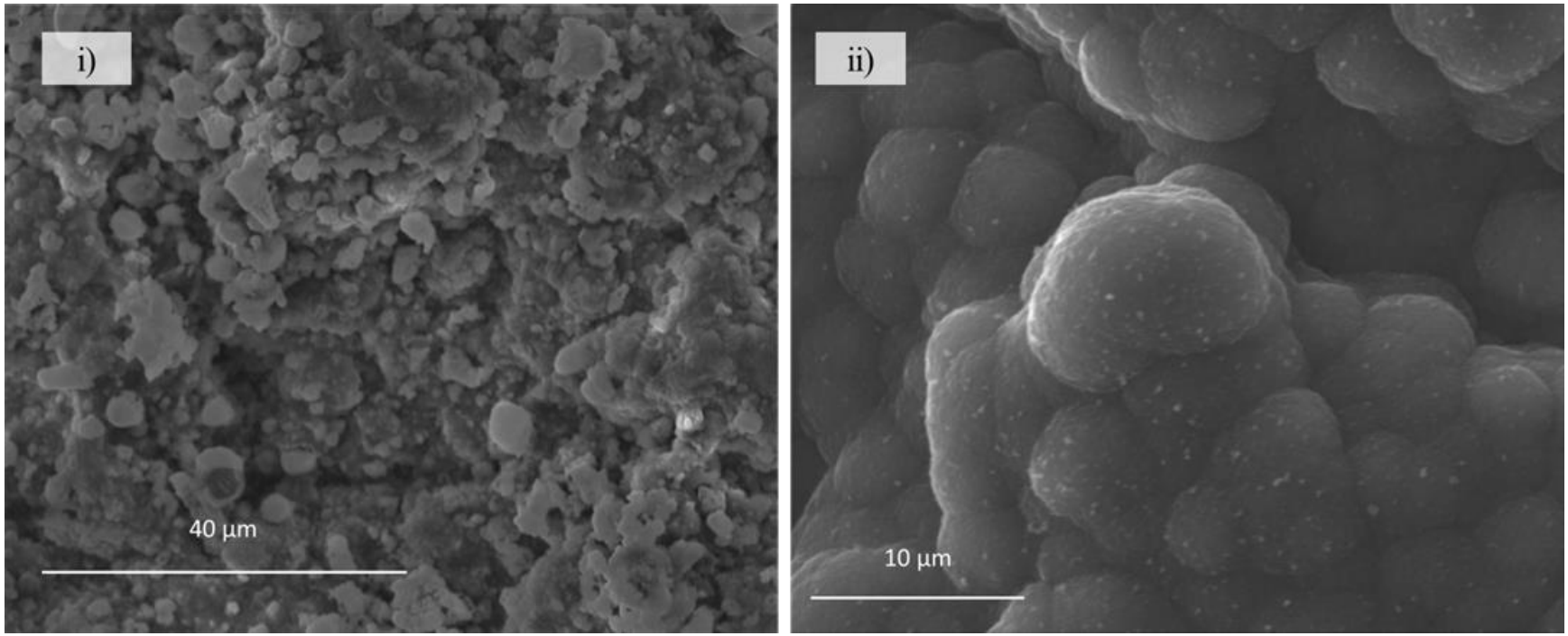

Figure 4.14: SEM images of the surface of (i) a blank coupons of material J, and (ii) a coked coupon of material J; Magnification: 10000X (i); 25000X (ii).

Figure 4.14 presents images of the surfaces of blank and coked coupons of material J. It can be clearly observed that the surface of the coating is constituted by small grains, and that cavities as well as mounds are present, due to the deposition of the coating over the base alloy. The coked coupon underwent three coking cycles, and the coke deposited on its surface is of the same type as that observed over the previously studied coupons, i.e. a granular structure. These grains, however, seem to be more packed than in, e.g., material A.

EDX analyses of the top surfaces were also carried out with accelerating voltages of 10 kV and 20 kV. The results of these analyses are presented in Table 4.8.

Table 4.8: Top-view EDX analyses of blank, preoxidized and coked coupons of material J

Element	Acc. Voltage [kV]	Type of coupon		
		Blank	Preox.	3CC
Cr	10	70.4	58.5	58.6
	20	3.8	3.8	5.3
Fe	10	10.2	0.0	17.4
	20	0.9	0.5	0.9
Ni	10	1.9	1.1	2.8
	20	15.0	13.4	21.7
Al	10	17.4	40.3	0.3
	20	71.0	76.0	64.5
Mn	10	0.0	0.0	20.6
	20	8.6	6.0	6.4
Si	10	0.1	0.1	0.3
	20	0.6	0.3	1.2

The first thing to notice is that the measurements performed over the coupons of material J significantly vary depending on the accelerating voltage used. In general, the uppermost layer of the coupons (corresponding to 10 kV) is very rich in chromium, but below (as indicated by the analyses at 20 kV), the most abundant element is aluminum, followed by nickel in smaller concentrations.

As for all the other materials tested, Ekvicalc calculations were carried out to evaluate the stability of the surfaces formed in material J at preoxidation and cracking atmospheres. The input

given to the software was the molar fraction corresponding to the compositions of the materials, determined through the top-view EDX of the coupons under such atmospheres. The results of the calculations are presented in Table 4.9.

Table 4.9: Thermodynamic calculations for coupons of material J after preoxidation and coking

	Preoxidized	Coked
Al_2O_3	0.274	-
Cr_2O_3	0.213	0.100
$NiAl_2O_4$	0.007	-
Al_2SiO_5	0.001	0.003
$MnCr_2O_4$	-	0.199
Fe	-	0.166
Ni	-	0.025
SiO_2	-	0.003

The results of these calculations suggest that, after the preoxidation step, material J forms alumina, chromia and two other mixed Al-oxides: $NiAl_2O_4$ and Al_2SiO_5.

This composition seemed to be very affected after cracking, especially concerning the Al compounds. Although the Al_2SiO_5 remained stable, the $NiAl_2O_4$ dissociated under the reducing cracking conditions and formed elemental nickel. High rates of coke formation have been attributed to the dissociation of $NiAl_2O_4$ [72], and the coking resistance exhibited by material G in Sections 4.3.1 and 4.3.2 seem to confirm this.

Additionally, manganese chromite and elemental iron are also predicted to be present after coking.

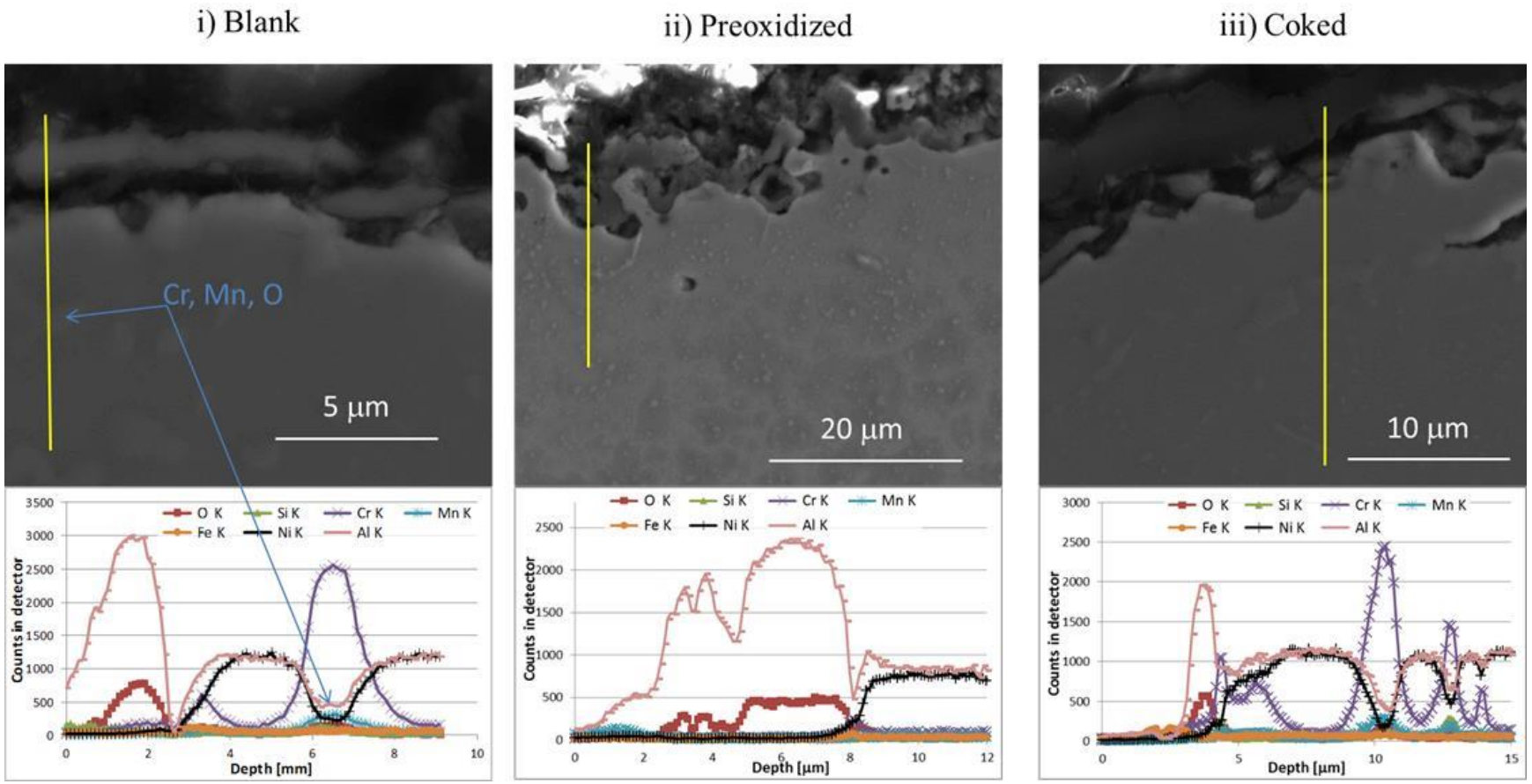

Figure 4.15: Cross section of (i) a blank coupon, (ii) a preoxidized, and (iii) a coked coupon of material J, with the results of their respective EDX line scans

The cross sectional analyses presented in Figure 4.15 help to better appreciate the changes that took place in material J throughout the experiments, using line scans that clearly indicate changes of composition in depth. Figure 4.15 and the mapping of Figure 4.16 confirm the conjectures made based on the top-view analyses, stating that a significant amount of aluminum is present on the uppermost surface of the blank coupon. The line scan and element mappings indicate that the surface aluminum is in an oxidized state, since oxygen is also detected in the uppermost layer of the blank coupon. This implies that the coupons of material J were delivered with an oxide layer already developed as a part of their manufacturing process. The oxide layer of the blank coupons has a granular structure, and is not well attached to the bulk of the material, since a void can be observed between the two sections. The line scan also indicates that the bulk of the blank coupons is mainly composed of aluminum and nickel, although some grains, rich in chromium and, to a lesser extent manganese, are also scattered in the bulk. The mapping of the blank coupon presented in Figure 4.16 (i) indicates that sections or pieces of the oxide layer cover the bulk, but do not achieve a uniform coverage of the surface. These gaps seem to be filled by chromium, manganese and small amounts of iron. Additionally, some nickel can be observed at the surface, possibly forming $NiAl_2O_4$ as the thermodynamic calculations predicted.

The cross section of a preoxidized coated coupon is presented in Figure 4.15 (ii). Visually, its surface oxide layer does not exhibit significant changes with respect to what the blank coupon presented. The line scan across the coupon seems also to confirm that no big changes occurred in the oxide layer: A significant concentration of aluminum and oxygen is observed in the uppermost surface, and the bulk below is composed almost exclusively of aluminum and nickel. The mappings of the preoxidized cross section (see Figure 4.16 (ii)) suggest that the oxide layer was slightly thicker after preoxidation. The coexistence of nickel and aluminum became quite evident with the mappings of these two elements. The Ekvicalc predictions are supported with

these mappings: a significant amount of alumina seems to be present in the uppermost surface, as well as $NiAl_2O_4$ in the areas where the alumina has not entirely covered the coupon. Very small particles of chromium and manganese could be observed dispersed through the bulk.

In order to evaluate the resistance during coking of the oxide layer, the cross section of a coked coupon was also analyzed. It is presented in Figure 4.15 (iii) and shows that the oxide layer has been largely affected during cracking, as only some oxide grains are visible but no continuous layer. The line scan performed across this surface and presented in Figure 4.15 (iii) indicates that aluminum and oxygen were still the most abundant species on top of the bulk. However it also indicates that, right below the surface, the bulk composition alternated nickel and aluminum rich sections with high concentrations of chromium and manganese.

The mapping presented in Figure 4.16 (iii) confirms that the oxide layer in the coked coupons was much more discontinuous than that seen after preoxidation, indicating that it has been significantly affected during cracking, triggering higher coking than in other Al-enhanced materials, e.g. Material H. The cokes seem, nevertheless, to have been confined only to the coke layer. Although the oxide still present at the surface is mostly alumina, chromium and manganese seem to have also reached the surface and oxidized, most likely forming chromia or manganese chromite. Elemental nickel seems also to have reached the surface, as expected from the Ekvicalc calculations that predicted decomposition of $NiAl_2O_4$.

It is also noticeable that silicon did not play any important role in material J. The line scans and element mappings of the blank, preoxidized and coked coupons showed no defined structures as the ones observed in other materials in Section 4.3.2.

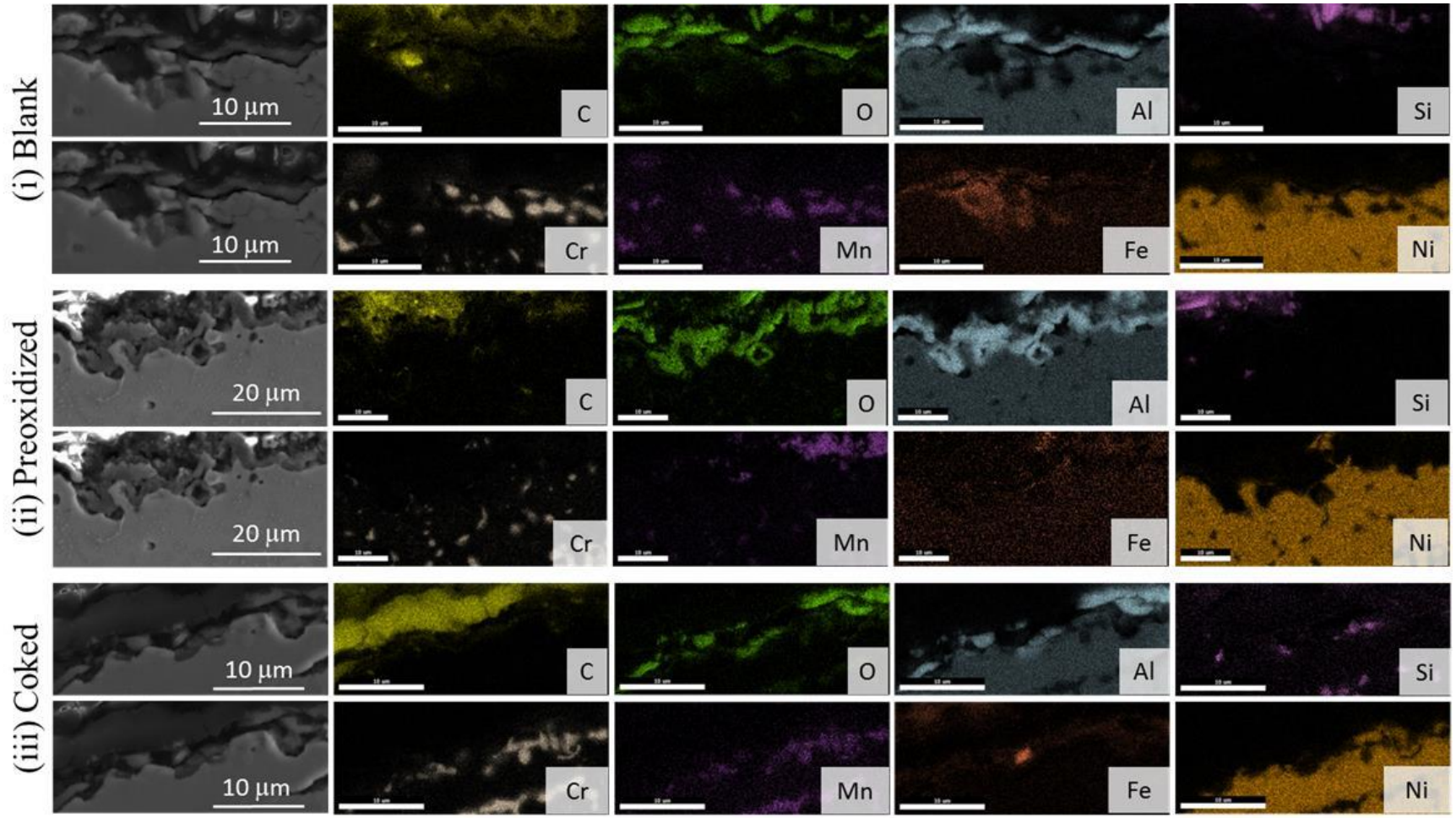

Figure 4.16: Element mappings of (i) blank, (ii) preoxidized and (iii) coked coupons of cross sections of coupons of material J.

4.4 Conclusions

A new electrobalance reactor setup has been used for studying the coking resistance of various materials by comparing their initial and asymptotic coking rates during ethane steam cracking. Reproducible results (± 20% for initial coking rate and ±10% for asymptotic coking rate) were obtained for industrially relevant conditions: $T_{material}$ = 1159K, P_{tot} = 0.1 MPa, X_{ethane} = 73%, δ = 0.33 kg_{H2O}/kg_{HC} and τ = 0.1 s.

For the nine studied materials the obtained experimental data revealed that coke deposition is strongly affected by the composition of the material, with a difference in asymptotic coking rate of more than 250% depending on the material. As a group, the Al-enhanced alloys showed a better resistance to coke formation than those without aluminum in their formulation. SEM and EDX analyses of blank, preoxidized and coked Al-enhanced coupons complemented with thermodynamic calculations, revealed that during preoxidation aluminum migration to the surface results in the formation of an alumina layer. In particular, reduced coking was observed when after cracking the alumina on the surface was present under the form of oxide, with a sub-layer of manganese chromite.

For the non-Al containing materials the relative concentration of chromia and manganese chromite in the surface strongly affects the coking resistance. The EDX mappings and line scans revealed that high chromia contents in the surface are undesirable, as large amounts of coke were found over this oxide, while the formation of manganese chromite reduces coke formation under the studied conditions. Good protection against coking was achieved on these materials when a layer of manganese chromite developed. A sub-layer of silica also enhances the coking resistance. The coated coupons of material J did not exhibit a remarkable resistance to coking. In fact, when including them in the ranking of coking resistance of all the tested coupons, the coating is the

fourth most coke promoting. The SEM and EDX analyses performed over the cross sections of the coated coupons indicated the formation of alumina at the surface during preoxidation. However, it practically disappears after the cracking runs. No manganese chromite and almost no chromia layers were detected either.

For all the tested materials, it was observed that the formation of a uniform layer of a protective oxide is essential, because the status of the surface after preoxidation or decoking has a significant impact on the coking rate, and not the bulk composition. Therefore no straightforward relationship can be made between the bulk composition and the initial and asymptotic coking rates. This implies that extensive testing under relevant conditions is required to assess the relative coking tendency of existing and new materials.

References

[1] Van Geem, K. M.; Marin, G. B.; Hedebouin, N.; Grootjans, J. Energy efficiency of the cold train of an ethylene cracker. *Oil Gas-Eur. Mag.* **2008**, *34* (2), 95-99.

[2] Van Geem, K. M.; Zajdlik, R.; Reyniers, M. F.; Marin, G. B. Dimensional analysis for scaling up and down steam cracking coils. *Chem. Eng. J.* **2007**, *134* (1-3), 3-10.

[3] Ranzi, E.; Dente, M.; Pierucci, S.; Barendregt, S.; Cronin, P. Coking simulation aids on-stream time. *Oil Gas J.* **1985**, *83* (35), 49-52.

[4] Rao, M. V. R.; Plehiers, P. M.; Froment, G. F. The coupled simulation of heat-transfer and reaction in a pyrolysis furnace. *Chem. Eng. Sci.* **1988**, *43* (6), 1223-1229.

[5] Stefanidis, G. D.; Merci, B.; Heynderickx, G. J.; Marin, G. B. CFD simulations of steam cracking furnaces using detailed combustion mechanisms. *Comput. Chem. Eng.* **2006**, *30* (4), 635-649.

[6] Heynderickx, G. J.; Schools, E. M.; Marin, G. B. Optimization of the decoking procedure of an ethane cracker with a steam/air mixture. *Ind. Eng. Chem. Res.* **2006**, *45* (22), 7520-7529.

[7] Baker, R. T. K.; Yates, D. J. C.; Dumesic, J. A. Filamentous carbon formation over iron surfaces. *ACS Sym. Ser.* **1982**, *202*, 1-21.

[8] Albright, L. F.; McGill, W. A. Aluminized ethylene furnace tubes extend operating life. *Oil Gas J.* **1987**, *85* (35), 46-50.

[9] Albright, L. F.; Marek, J. C. Coke formation during pyrolysis - roles of residence time, reactor geometry, and time of operation. *Ind. Eng. Chem. Res.* **1988**, *27* (5), 743-751.

[10] Albright, L. F.; Marek, J. C. Mechanistic model for formation of coke in pyrolysis units producing ethylene. *Ind. Eng. Chem. Res.* **1988**, *27* (5), 755-759.

[11] Albright, L. F.; Marek, J. C. Analysis of coke produced in ethylene furnaces - insights on process improvements. *Ind. Eng. Chem. Res.* **1988**, *27* (5), 751-755.

[12] Kopinke, F. D.; Zimmermann, G.; Nowak, S. On the mechanism of coke formation in steam cracking - conclusions from results obtained by tracer experiments. *Carbon* **1988**, *26* (2), 117-124.

[13] Froment, G. F. Coke formation in the thermal-cracking of hydrocarbons. *Rev. Chem. Eng.* **1990**, *6* (4), 293-328.

[14] Billaud, F.; Gueret, C.; Broutin, P.; Weill, J. Coke formation during hydrocarbons pyrolysis .1. Steam cracking. *Rev. I. Fr. Petrol.* **1992**, *47* (4), 537-549.

[15] Billaud, F.; Broutin, P.; Busson, C.; Gueret, C. Coke formation during hydrocarbons pyrolysis .2. Methane thermal-cracking. *Rev. I. Fr. Petrol.* **1993**, *48* (2), 115-125.

[16] Kopinke, F. D.; Zimmermann, G.; Reyniers, G. C.; Froment, G. F. Relative rates of coke formation from hydrocarbons in steam cracking of naphtha .3. Aromatic-hydrocarbons. *Ind. Eng. Chem. Res.* **1993**, *32* (11), 2620-2625.

[17] Kopinke, F. D.; Bach, G.; Zimmermann, G. New results about the mechanism of TLE fouling in steam crackers. *J. Anal. Appl. Pyrol.* **1993**, *27* (1), 45-55.

[18] Kopinke, F. D.; Zimmermann, G.; Reyniers, G. C.; Froment, G. F. Relative rates of coke formation from hydrocarbons in steam cracking of naphtha .2. Paraffins, naphthenes, monoolefins, diolefins, and cycloolefins, and acetylenes. *Ind. Eng. Chem. Res.* **1993**, *32* (1), 56-61.

[19] Reyniers, G. C.; Froment, G. F.; Kopinke, F. D.; Zimmermann, G. Coke formation in the thermal-cracking of hydrocarbons .4. Modeling of coke formation in naphtha cracking. *Ind. Eng. Chem. Res.* **1994**, *33* (11), 2584-2590.

[20] Bach, G.; Zimmermann, G.; Kopinke, F. D.; Barendregt, S.; Vandenoosterkamp, P.; Woerde, H. Transfer-line heat-exchanger fouling during pyrolysis of hydrocarbons .1. Deposits from dry cracked gases. *Ind. Eng. Chem. Res.* **1995**, *34* (4), 1132-1139.

[21] Reyniers, M. F.; Froment, G. F. Influence of metal-surface and sulfur addition on coke deposition in the thermal-cracking of hydrocarbons. *Ind. Eng. Chem. Res.* **1995**, *34* (3), 773-785.

[22] Snoeck, J. W.; Froment, G. F.; Fowles, M. Filamentous carbon formation and gasification: Thermodynamics, driving force, nucleation, and steady-state growth. *J. Catal.* **1997**, *169* (1), 240-249.

[23] Browne, J.; Broutin, P.; Ropital, F. Coke deposition under steam cracking conditions - Study of the influence of the feedstock conversion by micropilots experiments. *Mater. Corros.* **1998**, *49* (5), 360-366.

[24] Steurbaut, C.; Grabke, H. J.; Stobbe, D.; van Buren, F. R.; Korf, S. J.; Defrancq, J. Kinetic studies of coke formation and removal on HP40 in cycled atmospheres at high temperatures. *Mater. Corros.* **1998**, *49* (5), 352-359.

[25] Dhuyvetter, I.; Reyniers, M. F.; Froment, G. F.; Marin, G. B.; Viennet, D. The influence of dimethyl disulfide on naphtha steam cracking. *Ind. Eng. Chem. Res.* **2001**, *40* (20), 4353-4362.

[26] Cai, H. Y.; Krzywicki, A.; Oballa, M. C. Coke formation in steam crackers for ethylene production. *Chem. Eng. Process.* **2002**, *41* (3), 199-214.

[27] Towfighi, J.; Sadrameli, M.; Niaei, A. Coke formation mechanisms and coke inhibiting methods in pyrolysis furnaces. *J. Chem. Eng. Jpn.* **2002**, *35* (10), 923-937.

[28] Wauters, S.; Marin, G. B. Kinetic modeling of coke formation during steam cracking. *Ind. Eng. Chem. Res.* **2002**, *41* (10), 2379-2391.

[29] Luan, T. C.; Eckert, R. E.; Albright, L. F. Gaseous pretreatment of high-alloy steels used in ethylene furnaces: Pretreatment of Incoloy 800. *Ind. Eng. Chem. Res.* **2003**, *42* (20), 4741-4747.

[30] Abild-Pedersen, F.; Norskov, J. K.; Rostrup-Nielsen, J. R.; Sehested, J.; Helveg, S. Mechanisms for catalytic carbon nanofiber growth studied by ab initio density functional theory calculations. *Phys. Rev. B* **2006**, *73* (11).

[31] Wang, J. D.; Reyniers, M. F.; Marin, G. B. The influence of phosphorus containing compounds on steam cracking of n-hexane. *J. Anal. Appl. Pyrol.* **2006**, *77* (2), 133-148.

[32] Andersson, M. P.; Abild-Pedersen, F. Carbide induced reconstruction of monatomic steps on Ni(111) - A density functional study. *Surf. Sci.* **2007**, *601* (3), 649-655.

[33] Wang, J. D.; Reyniers, M. F.; Marin, G. B. Influence of dimethyl disulfide on coke formation during steam cracking of hydrocarbons. *Ind. Eng. Chem. Res.* **2007**, *46* (12), 4134-4148.

[34] Wang, J. D.; Reyniers, M. F.; Van Geem, K. M.; Marin, G. B. Influence of silicon and silicon/sulfur-containing additives on coke formation during steam cracking of hydrocarbons. *Ind. Eng. Chem. Res.* **2008**, *47* (5), 1468-1482.

[35] Van Geem, K. M.; Dhuyvetter, I.; Prokopiev, S.; Reyniers, M. F.; Viennet, D.; Marin, G. B. Coke formation in the transfer line exchanger during steam cracking of hydrocarbons. *Ind. Eng. Chem. Res.* **2009**, *48* (23), 10343-10358.

[36] Wauters, S.; Marin, G. B. Computer generation of a network of elementary steps for coke formation during the thermal cracking of hydrocarbons. *Chem. Eng. J.* **2001**, *82* (1-3), 267-279.

[37] Sugitani, J.; Mae, K. I.; Furuta, M. Method for producing ethylene. European Patent Application EP0692693B1, **2001**.

[38] Brown, D. J. Internally finned radiant coils: A valuable tool for Improving ethylene plant economics. 6th EMEA Petrochemicals Technology Conference, London, UK, **2004.**

[39] Albano, J. V.; Sundaram, K. M.; Maddock, M. J. Applications of extended surfaces in pyrolysis coils. *Energy Progress* **1988**, *8* (3), 9.

[40] Schietekat, C. M.; van Goethem, M. W. M.; Van Geem, K. M.; Marin, G. B. Swirl flow tube reactor technology: An experimental and computational fluid dynamics study. *Chem. Eng. J.* **2014**, *238* (0), 56-65.

[41] Broutin, P.; Ropital, F.; Reyniers, M. F.; Froment, G. F. Anticoking coatings for high temperature petrochemical reactors. *Oil Gas Sci. Technol.* **1999**, *54* (3), 375-385.

[42] Redmond, T.; Bergeron, M. P. Tests demonstrate anticoking capability of new coating. *Oil Gas J.* **1999**, *97* (19), 39-42.

[43] Zhou, J. X.; Wang, Z. Y.; Luan, X. J.; Xu, H. Anti-coking property of the SiO2/S coating during light naphtha steam cracking in a pilot plant setup. *J. Anal. Appl. Pyrol.* **2011**, *90* (1), 7-12.

[44] Verdier, G.; Carpentier, F. Consider new materials for ethylene furnace applications. *Hydrocarb. Process.* **2011**, *90* (5), 61-62.

[45] Jakobi, D.; Ganser, B. Centralloy 60 HT-alloy development for high temperature operation and reduced coking. Spring National Meeting: 17th Annual Ethylene Producers Conference, Atlanta, GA, USA, 10/April/2005, **2005.**

[46] Jakobi, D., van de Moesdijk C., Karduck, P., von Richthofen A. Tailor-made materials for high temperature applications: New strategies for radiant coil material development. NACE, Atlanta, GA, **2009.** NACE International.

[47] Pons, F.; Hugo, M.; Crambes, M.; Papapietro, M. Austenitic phase alloy containing chromium and aluminium; use in cracking furnaces and drilling pipes or cables. European Patent Application EP0169119A1, **1986**.

[48] Flahaut, D. High temperature alloys. WIPO Patent Application WO/2004/042101A2, **2004**.

[49] Terwijn, F. X.; Morii, K.; Takeuchi, Y.; Kato, Y.; Hayakawa, H.; Nishimura, N. Heat resisting metal tube and method for manufacturing same. European Patent Application EP1043084A3, **2001**.

[50] Benum, L. W.; Oballa, M. C.; Petrone, S. S. A.; Chen, W. Surface on a stainless steel matrix. U.S. Patent Application US20050077210A1, **2005**.

[51] Yan, J. B.; Gao, Y. M.; Yang, F.; Bai, Y. P.; Liu, Y. H.; Yao, C. Y.; Hou, S. Z.; Liu, G. Z. Cyclic carburizing behaviour of Al modified high Si-containing HP40 alloy. *Corros. Sci.* **2013**, *67*, 161-168.

[52] Jedlinski, J. The oxidation behaviour of FeCrAl 'alumina forming' alloys at high temperatures. *Solid State Ionics* **1997**, *101*, 1033-1040.

[53] Nicholls, J. R.; Newton, R.; Simms, N. J.; Norton, J. F. Modelling the oxidation of FeCrAl-RE ODS alloys in simulated natural gas combustion environments. *Mater. High Temp.* **2003**, *20* (2), 93-108.

[54] Fedorova, E.; Monceau, D.; Oquab, D. Quantification of growth kinetics and adherence of oxide scales formed on Ni-based superalloys at high temperature. *Corros. Sci.* **2010**, *52* (12), 3932-3942.

[55] Wu, X. Q.; Yang, Y. S.; He, W. Y.; Zhan, Q.; Hu, Z. Q. Morphologies of coke deposited on surfaces of pure Ni and Fe-Cr-Ni-Mn alloys during pyrolysis of propane. *J. Mater. Sci.* **2000**, *35* (4), 855-862.

[56] Koshelev, I. K.; Paulikas, A. P.; Beno, M.; Jennings, G.; Linton, J.; Grimsditch, M.; Uran, S.; Veal, B. W. Chromium-oxide growth on Fe-Cr-Ni alloy studied with grazing-emission X-ray fluorescence. *Oxid. Met.* **2007**, *68* (1-2), 37-51.

[57] Benum, L. W.; Oballa, M. C. Process of treating a stainless steel matrix U.S. Patent Application US6436202B1, **2002**.

[58] Li, H.; Chen, W. X. Stability of MnCr2O4 spinel and Cr2O3 in high temperature carbonaceous environments with varied oxygen partial pressures. *Corros. Sci.* **2010**, *52* (7), 2481-2488.

[59] Liu, Y. C.; Wei, W. F.; Benum, L.; Oballa, M.; Gyorffy, M.; Chen, W. X. Oxidation behavior of Ni-Cr-Fe-based alloys: Effect of alloy microstructure and silicon content. *Oxid. Met.* **2010**, *73* (1-2), 207-218.

[60] Zimmermann, G.; Zychlinski, W.; Woerde, H. M.; van den Oosterkamp, P. Absolute rates of coke formation: A relative measure for the assessment of the chemical behavior of high-temperature steels of different sources. *Ind. Eng. Chem. Res.* **1998**, *37* (11), 4302-4305.

[61] Bennett, M. J.; Price, J. B. A physical and chemical examination of an ethylene steam cracker coke and of the underlying pyrolysis tube. *J. Mater. Sci.* **1981**, *16* (1), 170-188.

[62] Matras, D.; Villermaux.J Continuous reactor perfectly agitated by gas jets for kinetic study on rapid chemical reactions. *Chem. Eng. Sci.* **1973**, *28* (1), 129-137.

[63] Dagaut, P.; Cathonnet, M.; Rouan, J. P.; Foulatier, R.; Quilgars, A.; Boettner, J. C.; Gaillard, F.; James, H. A jet-stirred reactor for kinetic-studies of homogeneous gas-phase reactions at pressures up to 10-atmospheres (Approximately 1 MPa). *J. Phys. E Sci. Instrum.* **1986**, *19* (3), 207-209.

[64] Van Geem, K. M.; Pyl, S. P.; Reyniers, M. F.; Vercammen, J.; Beens, J.; Marin, G. B. On-line analysis of complex hydrocarbon mixtures using comprehensive two-dimensional gas chromatography. *J. Chromatogr. A* **2010**, *1217* (43), 6623-6633.

[65] Nielsen, J. R.; Trimm, D. L. Mechanisms of carbon formation on nickel-containing catalysts. *J. Catal.* **1977**, *48* (1-3), 155-165.

[66] Wang, J. The influence of additives on the coke formation during steam cracking. Ph.D. Thesis, Ghent University, Belgium, **2006**.

[67] Nolang, B. *Ekvicalc and Ekvibase*, 4.30; Svensk Energi Data: Balinge, Sweden, **2013**.

[68] Li, H.; Zheng, Y.; Benum, L. W.; Oballa, M.; Chen, W. Carburization behaviour of Mn-Cr-O spinel in high temperature hydrocarbon cracking environment. *Corros. Sci.* **2009**, *51* (10), 2336-2341.

[69] Chauhan, A.; Anwar, M.; Montero, K.; White, H.; Si, W. Internal carburization and carbide precipitation in Fe-Ni-Cr alloy tubing retired from ethylene pyrolysis service. *J. Phase Equilib. Diff.* **2006**, *27* (6), 684-690.

[70] Edrissi, M.; Soleymani, M.; Naderi, M. Synthesis of MnAl2O4 nanocrystallites by Pechini and sequential homogenous precipitation methods: characterization, product comparison, photocatalytic effect, and Taguchi optimization. *J Sol-Gel Sci Technol* **2012**, *64* (2), 485-492.

[71] Jianguo, Z.; Hui, W.; Chunyu, X.; Mohsen, S.; Yongfeng, H.; Ajay, K. D., Design and preparation of Ni-Co bimetallic nanocatalyst for carbon dioxide reforming of methane. In *Nanocatalysis for Fuels and Chemicals*, American Chemical Society: **2012**; Vol. 1092, pp 195-221.

[72] López-Fonseca, R.; Jiménez-González, C.; de Rivas, B.; Gutiérrez-Ortiz, J. I. Partial oxidation of methane to syngas on bulk NiAl2O4 catalyst. Comparison with alumina supported nickel, platinum and rhodium catalysts. *Applied Catalysis A: General* **2012**, *437–438* (0), 53-62.

Chapter 5: Naphtha steam cracking

This chapter includes the following paper:

Muñoz Gandarillas A. E.; Van Geem, K. M.; Reyniers, M-F.; Marin, G. B., "Coking Resistance of Specialized Coil Materials During Steam Cracking of Sulfur-Free Naphtha." *Industrial & Engineering Chemistry Research* **2014**, 53 (35), 13644-13655 **DOI:** 10.1021/ie502277e

Abstract:

The reactor material strongly affects coke formation during steam cracking of hydrocarbons. Therefore, in the past decade several specialized reactor materials have been developed that have proven to be efficient in reducing coke formation for ethane steam cracking. However, their beneficial anti-coking properties are questioned when heavier feedstocks such as naphtha are cracked. Therefore the effect of the composition of the reactor material has been investigated for ethane and naphtha cracking in an electrobalance setup under industrially relevant conditions. A significant reduction of coke formation is obtained for specialized alloys compared to typical Fe-Cr-Ni heat resistant steels when a sulfur-free naphtha is cracked. A thin layer of alumina on the surface along with manganese chromite provides the highest resistance to coking, as was demonstrated by the SEM and EDX analyses. The decrease in coking rate translates in a run length increase of 50% for a typical naphtha furnace equipped with reactors made out of an Al-enhanced alloy instead of typically applied heat resistant steel.

Keywords: Naphtha steam cracking; coke formation; alloy; electrobalance setup; Jet stirred reactor; SEM-EDX

5.1 Introduction

Coke is a carbonaceous solid residue that deposits on the internal surface of the reactor and downstream equipment during steam cracking of hydrocarbons. Reducing coke formation is considered one of the main research areas where significant improvements of this mature process still seem to be possible. As coke accumulates, the pressure drop over the reactor coil increases gradually, lowering the ethylene selectivity, and thus the profit [1]. Additionally, the heat input to the reactor must increase because the coke layer functions as an extra resistance for heat transfer to the process gas. This leads to higher external tube wall temperatures over the course of time. Fuel consumption of the burners in the furnace increases by approximately 5% in comparison to start-of-run conditions if the same severity is desired [2]. When the maximum operation temperature (MOT) of the coil is reached, cracking is halted to remove the coke. MOTs are close to 1375 K for traditional alloys and can reach 1425 K for certain specialized alloys [3]. Decoking is carried out by feeding air and/or steam to the reactor [4, 5]. This cyclic coking and decoking operation causes aging of the material, which has a negative impact on the process by increasing the rates of coke formation [6-8]. Next to aging of the material, also the surface composition of the reactor material strongly affects coking [1, 9-12]. Typically, Fe-Cr-Ni alloys are used because of their good resistance to high temperatures. These alloys can be modified to create surfaces that are less prone to coke deposition [3, 13-19]. The usual method to form a protective surface on the inner wall of the coil is to carry out a preoxidation with air, steam or a mixture thereof [20], but other techniques such as prereduction [21-23] or presulfidation [24-26] are applied as well. Preoxidation leads to the formation of a variety of surface oxides. Usually, a layer of chromia (Cr_2O_3) is formed at the surface, but also manganese chromite ($MnCr_2O_4$) or alumina (Al_2O_3) can form depending on the conditions of the pretreatment and the composition of the bulk alloy. The

latter two oxides have exhibited remarkable resistance to coke formation [3, 7, 17]. Also coatings can be applied to make the internal coil surface more inert and resistant to coking [27-33].

Although plenty of studies report about new materials, only in a limited number of them the coking behavior has been investigated on different materials under identical cracking conditions and/or different pretreatments under identical cracking conditions [6, 7, 34-36]. Unfortunately, the results of these studies are virtually impossible to relate with each other due to differences of the experimental protocol. Some tests concerned industrial coils [28, 37, 38], whereas others used small lab-scale samples, with real [6, 23, 34, 35, 39] and simulated cracking atmospheres [3, 8, 40], in which the concentrations of radicals could be very largely different from the concentrations that are found when actually cracking a hydrocarbon feed [41] .

In Chapter 4, a study of the coking resistance of ten commercially available materials was carried out in an electrobalance setup under a fixed set of ethane cracking conditions. The tested materials were divided in Al-enhanced and non-Al containing materials but the observed coking behavior was strongly material dependent. A ranking of the alloys and materials based on their coking tendency was made, based among other things on the results of scanning electron microscopy (SEM) and energy dispersive X-ray (EDX) analyses. It was found that the best performing materials had a protective and continuous oxide layer at their outermost surface. Alumina and manganese chromite provided the highest resistance to coking. This suggested that, for ethane cracking conditions, some specialized materials exhibit a significant advantage compared to regular Fe-Cr-Ni alloys.

In the reactor two important mechanisms determine the amount of coke deposited on the coil material [23, 42, 43]. The first one, namely the heterogeneous catalytic mechanism, explains the catalytic formation of coke by action of Ni and Fe present in the heat-resistant alloys constituting the coils [44-47], whereas the second, namely the heterogeneous radical mechanism, regards the

radical reactions of species present in the gas phase with the radicals at the gas-coke interface, and with other radicals of the gas phase [48-51]. A third mechanism, the so-called homogeneous condensation mechanism, has been postulated but it is relevant only for heavy feedstocks or in the cold sections of a steam cracking unit [43, 52-55].

Experiments have shown that the type of hydrocarbons in contact with the reactor material also strongly affects coke formation. For example, it has been reported that unsaturated and aromatic hydrocarbons have the highest coking tendency [48, 56]. Therefore typically a distinction is made between coking models developed for gaseous feeds [57, 58] and liquid feeds [27, 56, 59, 60]. An additional complexity is the presence or addition of sulfur to the feed because this element typically increases coke formation [23-25], although it also causes a significant reduction of CO in the effluent stream. Straight run naphthas have sulfur concentrations usually ranging from 20 to 100 ppmw [2, 11], although values as high as 250 ppmw can be reached [61, 62]. It is thus obvious that the observations made for coking during ethane cracking cannot be simply translated to naphtha cracking. Hence, there is a clear need to study coke formation under naphtha cracking conditions on several alloys to determine if the material has an impact on coke formation during naphtha cracking as significant as during ethane cracking.

The present work builds upon earlier work for ethane cracking and evaluates the coking tendency of three selected alloys under naphtha cracking conditions using the same electrobalance setup and methodology. As reference a typical Fe-Cr-Ni heat-resistant alloy is used, while the two best performing materials from the ethane cracking study are also considered: an Al-enhanced and a non-Al containing material. Given the influence of sulfur on coking during steam cracking, a sulfur-free naphtha is used, to discard the effect of sulfur. This allows attributing all observations exclusively to the effect of the interplay between the feed and the materials, without interference of the effect of sulfur.

5.2 Experimental section

5.2.1 Electrobalance setup

The electrobalance setup described in detail in Chapter 3 was used. Minor modifications were made to the setup which allowed feeding, evaporating and cracking a liquid feedstock. Figure 5.1 presents a flow diagram of the setup, as configured for the naphtha cracking experiments.

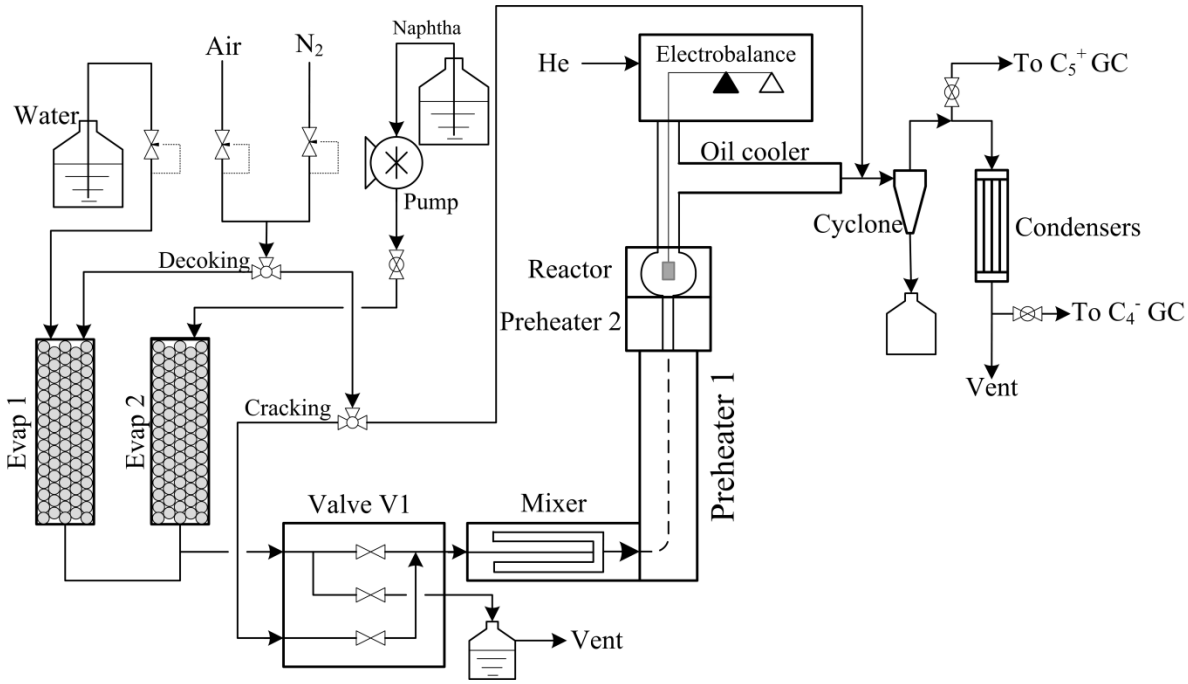

Figure 5.1: Overview of the electrobalance setup, configured to study coke formation on different reactor materials during naphtha steam cracking.

The setup can be divided into three main parts: feed, reaction and analysis section. The feed section consists of all the elements upstream of the reactor. It assures that steam and naphtha are fed at the desired flow rates, that they are properly mixed after evaporation and that there is no cracking before entering the reactor. Given the liquid nature of the feed used during the tests, a high-precision piston pump (Pharmacia LKB P500) was installed to regulate the naphtha flow rate. It is essential to have a uniform evaporation of the feed to avoid pressure oscillations in the

reactor. Oscillations affect the stability of the mass signal and could result in coke spalling from the coupon. Moreover, coke formation is strongly dependent on the pressure, and hence, oscillations of the pressure will surely increase the error bars on the measured coking rates. Therefore instead of using the evaporators in series as in Chapter 4, a parallel arrangement of the evaporators proved to be more stable as shown in Figure 5.1. In this configuration, water is fed to evaporator 1 (473 K), and naphtha to evaporator 2 (523 K). After leaving the evaporators, the two gasified streams were joined and directed to Valve V1 (473 K) to enable a stable gas flow. A mixer (543 K) ensures the uniformity of the mixture, and then two in-series preheaters (773 K and 823 K, respectively) are used to reduce the heating duty of the reactor furnace.

The reactor section consists of a jet stirred reactor made of quartz, heated by an electric furnace. Due to the action of the jets, good mixing of the gas phase can be achieved. A small rectangular coupon (10 mm × 8 mm × 1 mm) is placed inside a jet stirred reactor, hanging from the arm of an electrobalance, which continuously measures the mass increase of the coupon caused by the deposition of coke over time.

Finally, the analysis section allows the characterization of the effluent leaving the reactor by means of an online Refinery Gas Analyzer (RGA), which detects and quantifies permanent gases (up to C_4), and an online Trace GC ultra GC, which analyzes hydrocarbons ranging from methane up to heavy hydrocarbons.

5.2.2 Materials

Three different materials are investigated in this work, and they are referred to as materials A, D and H. The mean measured composition of these materials, as determined via EDX scans of top surfaces of coupons with accelerating voltages of 10 kV and 20 kV, is given in Table 5.1.

Material A is a typical heat resistant steel which showed a classical behavior during the ethane cracking tests. It is not based on a specially engineered surface technology and is used as reference material. Material D was among the best performing materials during the ethane cracking tests. It is a surface engineered material that has a protective oxide layer developed on its surface as a part of its manufacturing process. Material H, on the other hand, is an Al-enhanced alloy that was considered the most coking resistant of the materials tested during ethane cracking. Material A, D and H thus represent the main used materials in industrial steam crackers.

Table 5.1: Bulk composition and main characteristics of the tested materials.

Material	Characteristics	Acc. V.	Measured Composition (wt %)					
			Cr	Fe	Ni	Mn	Si	Al
A	Centricast 35% Ni / 25% Cr micro alloy	10 kV	27.6	35.3	36.0	0.2	0.9	-
		20 kV	27.9	34.9	33.6	1.4	2.2	-
D	Oxide layer on top of base alloy	10 kV	20.6	39.8	1.9	37.5	0.2	-
		20 kV	65.2	5.0	10.3	17.7	1.8	-
H	Al-enhanced alloy	10 kV	30.1	36.1	32.2	0.0	0.5	1.1
		20 kV	23.5	38.1	33.2	1.0	1.1	3.1

5.2.3 Procedure and conditions

A detailed description of the experimental cracking procedure was given in Chapter 4. For comparison, a similar procedure is used in this work with some small but significant modifications, adapted to the needs of working with a liquid feed.

5.2.3.1 Pretreatment of the coupons

The coupons of materials A and H were polished to ensure that the materials had similar surface roughness values (R_a ~ 0.15 µm). The coupons of D were not polished to avoid damaging their protective outermost surface. Once polished, the surface roughness of the coupons was measured using a Mitutoyo SJ-201 surface roughness meter.

The coupons of the three materials were then sequentially washed in demineralized water, diisopropyl ether and acetone. The coupons made out of A and H (D was excluded from this step too) were subjected to electro-scouring for 15 minutes in a diluted solution of sulfuric acid. Finally, all the coupons were rinsed in demineralized water and dried in air.

5.2.3.2 Preoxidation, cracking and decoking

After preoxidizing the coupons, naphtha cracking was started. Throughout the duration of an experiment the effluent composition was monitored, assuring its representativeness of industrial conditions, i.e. targeting at a ratio of propylene to ethylene of 0.4 at the reactor outlet [63]. Table 5.2 summarizes the conditions applied during preoxidation, as well as during cracking and decoking. The typical effluent composition measured during the experiments can be consulted in Table C.3 in Appendix C.

Table 5.2: Conditions applied during preoxidation, naphtha cracking and decoking.

Parameter	Preoxidation	Cracking	Decoking	
			Air	Steam
T [K]	1023	1098	1023-1173	1173
Heating ramp [$K \cdot h^{-1}$]	-	-	300	-
F_{air} [$Nl \cdot s^{-1}$]	6.7×10^{-3}	-	8.3×10^{-3}	-
F_{N2} [$Nl \cdot s^{-1}$]	-	-	8.3×10^{-3}	8.3×10^{-3}
F_{H2O} [$kg \cdot s^{-1}$]	-	1.04×10^{-5}	-	6.67×10^{-6}
$F_{Naphtha}$ [$kg \cdot s^{-1}$]	-	2.78×10^{-5}	-	-
Duration [h]	12	6	0.5	0.25

Three continuous cracking cycles were performed with decoking in between each cycle. The reproducibility was verified by performing 4 to 7 experiments per material. This allowed calculating standard deviations (σ) for the measurements on each cycle and material, and reporting them by error bars on the measured coking rates. Decoking consisted of a first stage, in which a mix of air and steam was fed to the reactor, while increasing its temperature from 1023 K to 1173 K, and a second stage in which a mix of air and steam was fed to the reactor for 15

minutes. After the third coking cycle, no decoking was carried out, so that the coked coupons could be analyzed by SEM and EDX.

5.2.3.3 Determination of the coking rate

The amount of coke deposited over the coupons during the naphtha cracking experiments was continuously measured. This enabled to determine the absolute amount of coke over each coupon after every cracking cycle, as well as an initial and asymptotic coking rate for each cycle, as shown in Section B.3 of Appendix B.

$$R_C = \frac{m_{t_2} - m_{t_1}}{t_2 - t_1} \cdot \frac{1}{S} \tag{5.1}$$

The initial coking rate is reported as the mean measured value between the first 15 and 30 minutes of cracking, and is taken as an indication of the catalytic mechanism. The asymptotic rate is related to the radical coking mechanism, and is reported as the mean measured coking rate between 5 and 6 hours. Both the initial and asymptotic coking rates are averaged values over 3-7 experiments.

5.2.4 Thermodynamic calculations

To gain insight into the surface composition of the materials after preoxidation and naphtha cracking, thermodynamic calculations were performed with Ekvicalc [64]. In these simulations 100 mol of gas and 1 mol of alloy were assumed, to assure large excess of gas phase in line with the experiments. The gas phase is a mixture of the four most abundant hydrocarbons in the effluent, together with hydrogen and steam, all in their respective relative concentrations. The mole fraction of metals in the coke layer is obtained from the EDX analysis of the coked coupons with 10 kV. In addition, a temperature T = 1098K and a pressure P = 1.02×10^5 Pa are used. A

summary of the composition of the materials and gas phase used as input values for the calculations is presented in Table 5.3.

Table 5.3: Input values used for Ekvicalc calculations of naphtha cracking

Gas phase		Material composition (mole fraction)			
Component	mol	Element	A	D	H
CH_4	23.5	Si	0.015	0.009	0.012
C_2H_4	25.6	Cr	0.738	0.616	0.547
C_3H_6	7.1	Mn	0.185	0.297	0.197
C_6H_6	1.9	Fe	0.037	0.036	0.220
H_2	9.3	Ni	0.025	0.041	0.014
H_2O	32.6	Al	-	-	0.010
TOTAL	100	TOTAL	1	1	1

5.2.5 Scanning electron microscope and energy dispersive X-ray analysis

SEM and EDX were used to obtain information concerning the morphology and composition of the coupons. Analyses of the top surface of the coked coupons were performed, as well as cross-sectional analyses. Blank coupons (i.e. coupons that did not undergo pre-oxidation or cracking operations) and pre-oxidized coupons were not analyzed, because the pretreatment and pre-oxidation procedures were the same during naphtha and ethane cracking, so the results reported in Chapter 4 were used.

The top surface scans were performed on a JEOL – JSM-5400 microscope, equipped with an INCA x-act 51- ADD0021 detector. SEM images revealed the morphology of the coke layers, while triplicate rectangular EDX scans determined the surface composition of the coked coupons. Two different accelerating voltages (10 kV and 20 kV) were used.

To analyze the cross sections two approaches were taken, namely line scans and element mappings. Line scans helped to evaluate the in-depth concentration profile of the studied elements, whereas element mappings provided information about the homogeneity of such profiles along the surface.

5.2.6 Naphtha composition and characterization

To determine the composition of the feed, comprehensive two-dimensional gas chromatography (GC×GC) coupled to a flame ionization detector (FID) was applied [65]. Duplicate analyses were carried out to assure good reproducibility. A PIONA analysis of the naphtha is presented in Table 5.4. A detailed composition of the feed, as well as the ASTM D 2887 boiling point curve [66] are given in Table C.1, and Table C.2 and Figure C.1 of Appendix C.

The naphtha was determined to be light (i.e. C_4 - C_7) and mostly paraffinic and isoparaffinic. Additional GC×GC analyses with an Agilent 355 sulfur chemiluminescence detector [67] (Agilent Technologies, Inc.) indicated that the sulfur content in the naphtha was below the detection limit of 10 ppb. This is of great importance as even ppm amounts of sulfur can have a significant influence on the coking rate.

Table 5.4: PIONA analysis of the naphtha used in the JSR cracking experiments

Carbon number	Paraffins [wt %]	Isoparaffins [wt %]	Olefins [wt %]	Naphthenes [wt %]	Aromatics [wt %]	TOTAL [wt %]
4	1.25	0.04	0.17	0	0	1.46
5	32.79	24.14	0	2.60	0	59.53
6	12.57	18.54	0	5.49	1.73	38.33
7	0.06	0.59	0	0.02	0.01	0.69
TOTAL [wt %]	46.66	43.32	0.17	8.11	1.74	100

To measure the density of the naphtha, triplicate analyses were performed using a Mettler Toledo DA100M density meter. It was determined to be $\rho = 661\ kg \cdot m^{-3}$ at a temperature of 288 K.

5.3 Results and discussion

5.3.1 Influence of the feed – coke deposition during naphtha cracking compared to ethane cracking

Table 5.5 summarizes the averaged values of the amount of coke deposited on the coupons, the initial coking rate and the asymptotic coking rate over three different runs under identical conditions for each material. For comparison, the coking rates determined during ethane steam cracking in Chapter 4 are included, as well as the mean measured surface roughness of the tested coupons, because the latter can have an influence on the coking rate [68, 69]. The coking rates as a function of time for the three cycles for the three tested materials are presented in Figures C.2-C.4 in Appendix C.

Comparison of the amount of coke deposited over each material shows that material H accumulates the least coke of the three tested materials, while A has the most coke on its surface in each of the three cycles. The number of cycles seems not to have a drastic effect on the amount of coke deposited. The mass of coke deposited on material H is more or less stable around 1.8×10^{-6} kg after each one of the three 6-hour cycles. Materials A and D exhibited small increments (i.e. maximum 0.3×10^{-6} kg per cycle) that can be attributed to the fact that, due to the coking and decoking cycles, the material ages and the surface roughness increases as suggested by Bach et al. [70].

Next to the total amount of coke also the initial and asymptotic coking rates are given in Table 5.5. The experiments on the electrobalance setup take only 6 hours, and consequently the amount of coke deposited over the coupons is determined by the combined action of the initial and asymptotic regimes. For industrial coils, however, the initial rate has a negligible contribution to

the final amount of coke deposited on the surface of the reactor throughout its lifetime [56]. Figure 5.2 presents the initial and asymptotic coking rates measured on the three tested materials during the naphtha cracking experiments. Also the results of ethane cracking from Chapter 4 have been included for comparison.

Table 5.5: Mean surface roughness, mass of coke and initial and asymptotic coking rates for the three tested materials during steam cracking of light naphtha

		A		D		H	
R_a Surface roughness* [μm]		0.15		0.72		0.14	
		Naphtha	Ethane*	Naphtha	Ethane*	Naphtha	Ethane*
Mass of coke [10^{-6} kg]	1st CC	2.70	1.75	2.20	1.91	1.85	1.74
	2nd CC	2.87	2.28	2.43	1.76	1.68	1.83
	3rd CC	2.93	2.99	2.76	1.78	1.92	2.03
$R_{c,\,init}$ [10^{-7} kg·s^{-1}·m^{-2}]	1st CC	8.2	6.8	7.1	6.2	7.0	6.5
	2nd CC	11.8	13.0	6.8	7.9	4.4	10.5
	3rd CC	9.1	17.9	6.6	6.0	6.3	13.8
$R_{c,\,asym.}$ [10^{-7} kg·s^{-1}·m^{-2}]	1st CC	5.7	3.1	4.4	3.8	3.4	3.3
	2nd CC	5.6	3.3	5.0	3.4	2.5	2.6
	3rd CC	5.5	4.2	4.8	3.4	3.1	2.1

*Values determined in Chapter 4

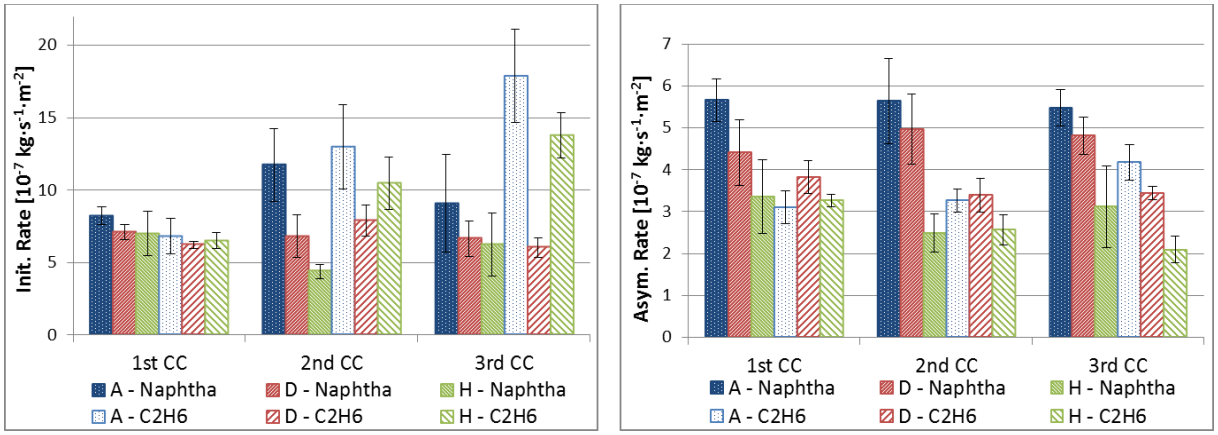

Figure 5.2: Mean measured initial and asymptotic coking rates during three cracking-decoking cycles on three materials during naphtha and ethane cracking in the electrobalance setup. The error bars correspond to the standard deviation (σ) of the experiments of each material. See Figures C.5 and C.6 in Appendix C for individual comparison plots of the coking rates as a function of the number of cycles and material, respectively.

The initial coking rates are not largely influenced by the number of coking cycles for naphtha cracking, as can be seen in Figure 5.2 (and more explicitly in Figure C.5 in Appendix C). Although the absolute values differ slightly from cycle to cycle, these differences are not larger than the standard deviations. Additionally, material A showed higher initial rates than materials D and H over the three coking cycles.

This behavior is very different than the one observed during ethane cracking, where the initial rate of materials A and H increased almost linearly with the number of cycles.

The asymptotic coking rates during naphtha cracking seem not to be influenced by the number of cycles either (see Table 5.5 and Figure C.5 in Appendix C). However, differences between the coking rates of the materials in the asymptotic regime are observed. Clearly, material H is the most coke resistant of the three tested during naphtha cracking. Material D showed slightly lower coking rates than A, although the differences between A and D are rather small, as can be seen in Figure C.6, in Appendix C. During ethane cracking, the asymptotic coking rates followed the same trend: material H performed better than D, which in turn performed better than A. The most remarkable coking rate reduction in the third coking cycle was achieved by material H for both feeds. During naphtha cracking, this reduction was approximately 40%, slightly lower than the 50% achieved during ethane cracking.

Comparison of the coking rates measured for both feeds indicates that the initial rates had similar values during the first cycle for ethane and naphtha cracking while for the second and third cycle, the initial rates were higher during ethane cracking. The aging effect seems to be more pronounced for ethane cracking. Higher asymptotic rates were observed during naphtha cracking. The different temperatures used for ethane (1159 K) and naphtha cracking (1098 K) lead to differences of the coking rates. Based on the coking model of Plehiers [58] such a difference in temperature (for identical gas phase compositions) causes a factor 3 difference for the asymptotic

coking rates. This effect is, however, compensated by the increase in concentration of more active coke precursors [48, 59, 60] (e.g. propylene, C_4^+ paraffins, benzene, naphthalene, …) that form during naphtha cracking, leading to the higher asymptotic rates observed. This agrees with typical observations from industry, where liquid feeds lead to lower run lengths (higher coking rates) than gas feeds [71].

To evaluate the effect of decreasing the coking rate on the run length of an industrial reactor, run length simulations of steam cracking of the naphtha used in the experiments were carried out using the simulation packages available at the Laboratory for Chemical Technology [41, 72], in line with the run length study presented by Wang et al. [73].

The reactor type and conditions for the simulations were taken from Dijkmans et al. [74]. The reactor was a 54 m long split coil, and a dilution $\delta = 0.375\ kg_{H2O}/kg_{naphtha}$ was applied, aiming at a P/E of 0.48. The run length was estimated to be 30 days, which was taken as a base case. A new simulation, implementing a coking rate 40% lower than the base case, predicted a run length of 45 days, i.e. 50% longer than the base case. Based on these values it is evident that coking rate reduction can significantly enhance production.

During the ethane cracking experiments, a rate reduction of 50% was achieved by material H with respect to material A. According to Wang et al. [73] this translates into a run length extension of almost 100%. The rate reduction achieved during naphtha cracking is, therefore, lower than during ethane cracking, but is still very significant.

5.3.2 Influence of the coil material – SEM, EDX and thermodynamic calculations

5.3.2.1 Analysis of top surfaces

Pictures of coked surfaces of the three tested materials obtained using SEM are presented in Figure 5.3. These images show that the coke morphology is very similar for each of the materials. The images with higher magnification, however, seem to indicate that the porosity of the coke is slightly different. Figure 5.3 suggests that the coke of material A has the highest density, whereas the lowest density was observed for material H. These observations are consistent with those made when cracking ethane over the same materials, although during ethane cracking the visual differences were somewhat more pronounced. No signs of coke spalling were observed at the surface of the coupons. EDX scans were performed over the surface of the coupons which underwent three consecutive cycles of naphtha cracking. The results of the scans are summarized in Table 5.6.

Preoxidation significantly changes the surface of materials A and H, compared to their raw or "blank" state. Migration of elements occurs, leading to the formation of oxide layers of some metals (Cr, Mn, Al) in the surface, whereas others (Ni, Fe) are depleted from the surface. This effect is less pronounced for material D because this material underwent an oxidation during its manufacturing which was intended to form a protective and stable oxide surface that can resist the influence of the cracking and decoking atmospheres.

Table 5.6: EDX-determined composition (wt %) of the surface of preoxidized* and ethane*and naphtha coked coupons. For the composition of blank coupons, see Table 5.1.

		A			**D**			**H**		
		Preox.*	3CC		Preox.*	3CC		Preox.*	3CC	
			Naphtha	Ethane*		Naphtha	Ethane*		Naphtha	Ethane*
Cr	10 kV	56.5	73.1	82.8	69.1	60.3	47.4	56.2	53.7	48.5
	20 kV	45.8	58.3	78.5	66	61.6	59.1	28.5	49.7	33.2
Fe	10 kV	15.7	3.9	3.7	3.2	3.8	4.8	13.5	23.2	19.3
	20 kV	25.1	9.3	5.4	5.7	3.6	3.4	28.6	11.6	14.2
Ni	10 kV	0.0	2.8	1.1	4.9	4.6	8.7	0.0	1.5	0.6
	20 kV	22.3	2.9	4.5	11.1	10.4	5.9	25.4	8.0	14.0
Mn	10 kV	27.8	19.4	12.2	22.1	30.8	39.0	18.8	20.4	30.2
	20 kV	5.1	29.1	10.9	15.6	22.8	30.1	3.1	21.3	16.2
Si	10 kV	0.1	0.8	0.2	0.7	0.5	0.0	0.3	0.7	0.6
	20 kV	1.7	0.5	0.8	1.6	1.7	1.5	1.3	1.6	5.9
Al	10 kV	-	-	-	-	-	-	11.2	0.5	0.7
	20 kV	-	-	-	-	-	-	13.1	7.8	16.4

*Retrieved from Chapter 4

The EDX analysis of coked coupons of the three materials revealed that, also after naphtha cracking, Cr and Mn were the most abundant elements at the surface. On the other hand, Fe and –more notoriously– Ni were depleted from the surface. Additionally, Al increased its concentration at the surface of material H during preoxidation and remained in a significant amount after cracking.

These trends are similar to those observed for the coupons after preoxidation, which suggests that the surface composition did not suffer major changes during cracking. Consequently, it can be assumed that the surface oxides that formed during preoxidation remained stable during naphtha cracking. This agrees with what was also observed for the coked coupons from the ethane cracking experiments, whose composition has also been included in Table 5.6 to facilitate comparison.

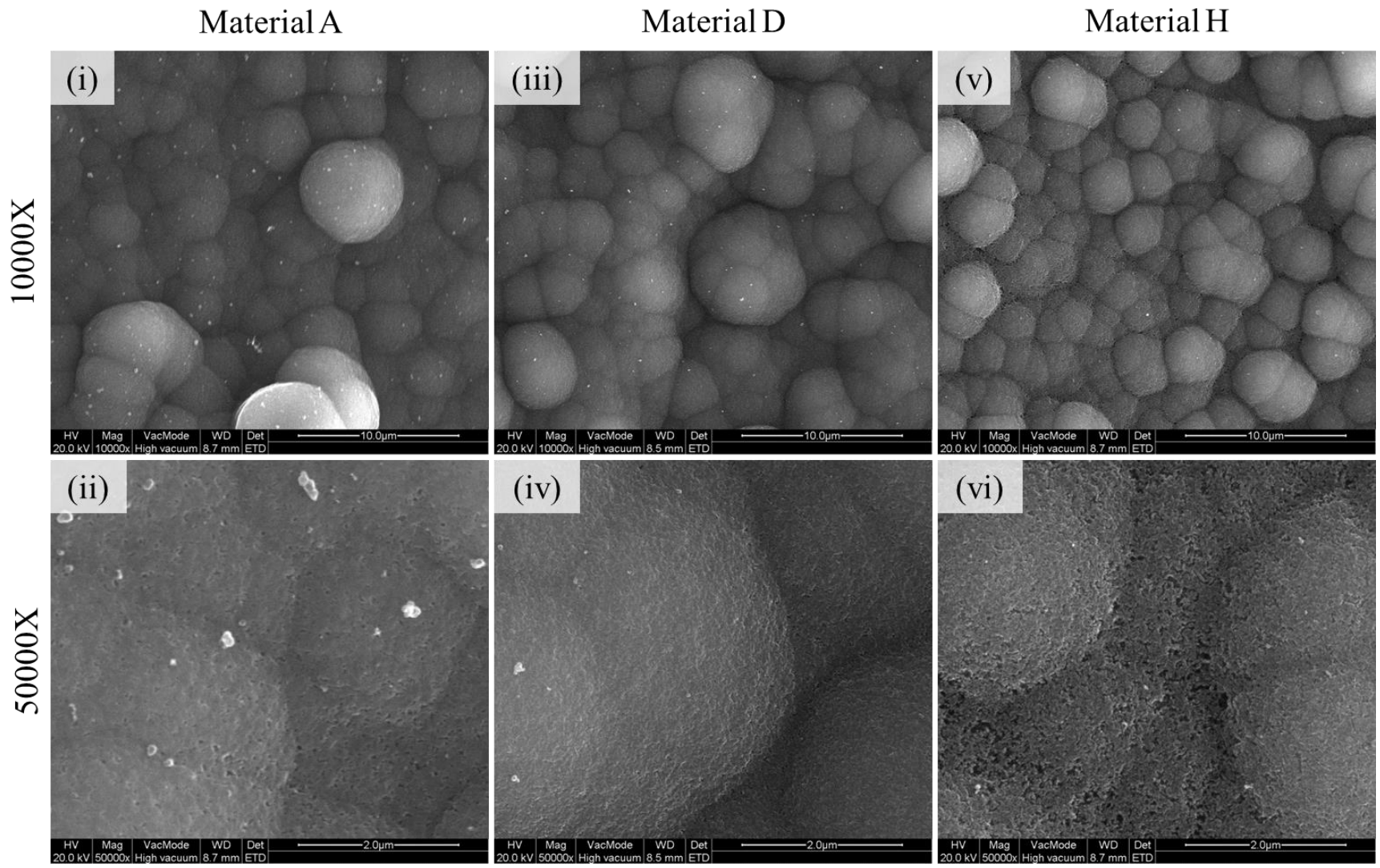

Figure 5.3: SEM images of coked coupons of material A (i, ii), material D (iii, iv) and material H (v, vi); Magnifications: 10000X (top row); 50000X (bottom row). See Table 5.6 for the EDX-determined surface composition of coked coupons of materials A, D and H.

5.3.2.2 Thermodynamic calculations

Table 5.7 presents the results of the thermodynamic calculations carried out for the three materials under naphtha cracking conditions.

Table 5.7: Normalized Ekvicalc-calculated surface composition (mole fraction) under oxidative and naphtha cracking conditions. See Table 5.2 for the experimental conditions and Table 5.3 for the input values used for the calculations.

	Preoxidation*			Cracking		
	A	D	H	A	D	H
Al_2O_3	-	-	0.225	-	-	0.010
Al_2SiO_5	-	-	0.014	-	-	-
Cr_2O_3	0.055	0.300	0.228	0.413	0.027	0.147
Fe_2O_3	0.204	-	0.139	-	-	-
$MnCr_2O_4$	0.736	0.584	0.394	0.415	0.754	0.379
$NiCr_2O_4$	-	0.080	-	-	-	-
Fe	-	-	-	0.082	0.092	0.423
Ni	-	-	-	0.056	0.104	0.027
SiO_2	0.004	0.036	-	0.034	0.023	0.014

*Retrieved from Chapter 4

The results of the calculations suggest that for each of the three tested materials, manganese chromite is the most abundant compound in the surface after pre-oxidation. Under the naphtha cracking conditions, manganese chromite is predicted to remain vastly abundant in the surface of the coupons. Additionally, the calculations predict the presence of chromia at the surface of all the materials, which coexists with the manganese chromite. The presence of a small amount of silica is also predicted for all the materials. Under the reducing conditions of cracking, iron and nickel are thermodynamically stable in their elemental form in the alloys, in contrast to their original oxidized state. A non-uniform surface oxide layer can therefore expose these elements to the gas phase and promote coking.

Furthermore, the calculations also predict that material H forms alumina on its outermost surface during preoxidation, which remains stable during the naphtha cracking experiments. The

presence of alumina at the surface could be the cause of the lower asymptotic coking rate that material H exhibits when compared to A and D. This is in line with the observations of the ethane cracking experiments over these materials, in which $MnAl_2O_4$ was suggested to form. This spinel was not predicted to form in the naphtha cracking coupons because all the Mn available (see Table 5.3) is used to form $MnCr_2O_4$, implying that the available Al forms alumina instead of $MnAl_2O_4$.

The beneficial effect of alumina layers has been suggested by various authors [3, 75]. Jakobi et al. [76] made a comparative study of selected alumina- and chromia-forming alloys, under a simulated cracking atmosphere. They determined that alumina shows a better resistance to coking than manganese chromite. Nevertheless, too large amounts of aluminum in the formulation are also harmful for the alloy, because they can lead to internal oxidation, affecting the uniformity of the uppermost oxide layer [19, 77].

5.3.2.3 Cross-sectional analysis

To validate the results of the thermodynamic EKVICALC calculations and to obtain additional information about the depth profile of metals and oxides, cross-sectional analyses of the coupons were performed with SEM and EDX. Figure 5.4 shows the images and the results of the EDX line scans performed over the cross sections of the three different types of coupons that underwent three naphtha cracking cycles. The trajectory of the line scans is represented by a yellow line and the initial point of the scan is the higher end of the line, which corresponds to the coke deposited on the uppermost surface of the coupons.

The EDX line scan across the coked coupon of material A in Figure 5.4(i) indicates that the coke layer, the oxide layer, and the bulk metal were almost entirely in contact with each other leaving

no voids between them, in contrast to what was observed on this material during the ethane cracking experiments.

The EDX analysis of the coked coupon of material A indicated that an oxide layer was present at the outermost surface of the coupon, since a significant increase in the concentration of oxygen was detected at the uppermost layer of the metal bulk. This increase of oxygen was accompanied by an increase in the concentration of chromium, and some manganese. The increase of chromium was much larger than that of manganese, confirming the results of the thermodynamic calculations: Manganese chromite and chromia coexist in the uppermost surface of material A. No iron or nickel were detected in the chromium-manganese rich zone, but these two elements rapidly increased their concentration right below the oxide layer to stable (bulk) values, showing that the spinel and chromia are a good barrier to prevent migration of iron and nickel to the surface. In agreement with the thermodynamic calculations, a small increase of silicon could be detected in between the bulk and the uppermost oxide layer, confirming that silicon also forms a silica layer, which could act as a second diffusion barrier preventing the migration of iron and nickel to the surface.

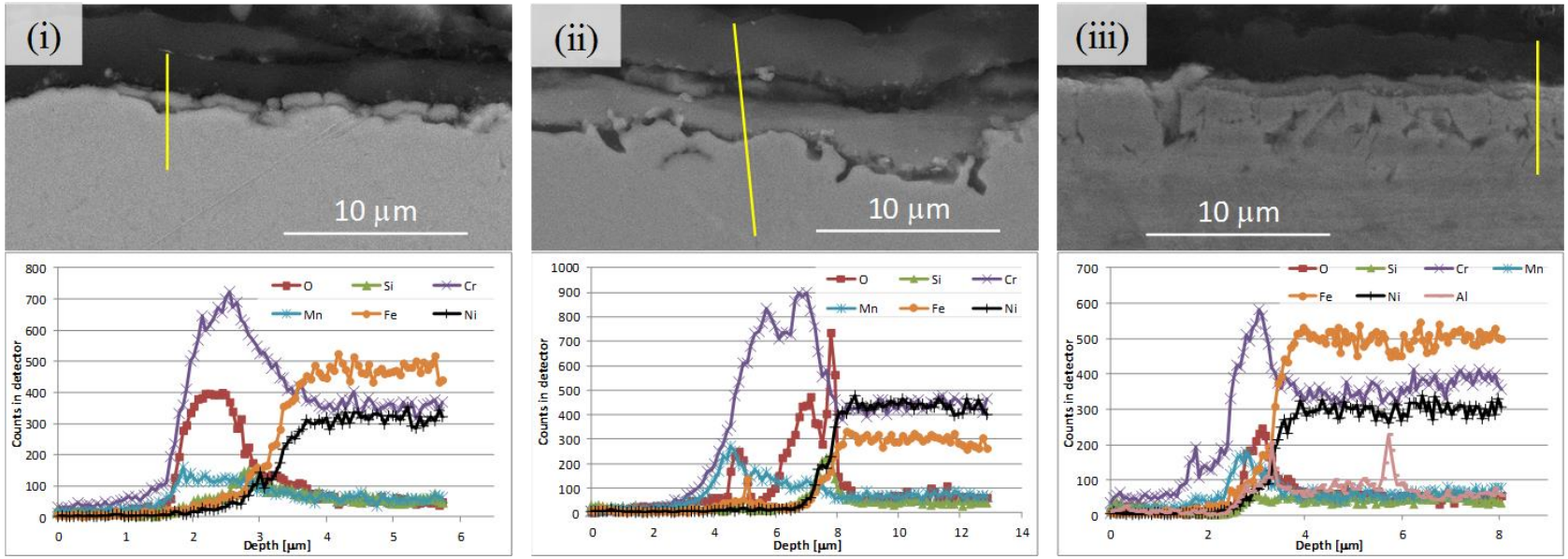

Figure 5.4: EDX line scans of cross sections of coked coupons after three cracking cycles for material A (i), material D (ii), and material H (iii). See Table 5.6 for the EDX-determined surface composition of coked coupons of materials A, D and H.

Element mappings of a cross section of material A were also performed, and are presented in Figure 5.5(i). They indicate that carbon remained restricted to the coke layer, and did not enter the oxide scale, nor the alloy. Below the carbon, a well-defined and continuous oxide scale is observed. This oxygen is perfectly matched by the chromium and manganese mappings. The chromium mapping shows a higher intensity than that of manganese in the oxide scale, which confirms the conjectures about a significant amount of chromia in the surface, coexisting with some manganese chromite spinel. Below this layer, a very thin line was detected in the silicon mapping, right above the iron and nickel, as can be seen from the mappings of these elements in Figure 5.5(i). Silica was effectively formed between the top layers and the bulk, rich in iron and nickel. The mappings of these two elements indicated that no iron or nickel were able to reach the surface, due to the effect of the oxide layers formed.

A cross section of material D is presented in Figure 5.4(ii). Its oxide layer seems thicker and better delineated than in material A. The EDX line scan analysis shows a large increase in the concentration of oxygen below the coke, confirming the presence of an oxide layer. This accumulation of oxygen is accompanied initially by high amounts of manganese and chromium. Below, the concentration of manganese decreased while that of chromium increased. This confirms the thermodynamic calculations for this material that predicted that manganese chromite and chromia should coexist in the surface. Below the chromia, a very narrow but pronounced increase of concentration of silicon can be observed confirming that a silica layer separated the bulk from the oxide scale in material D.

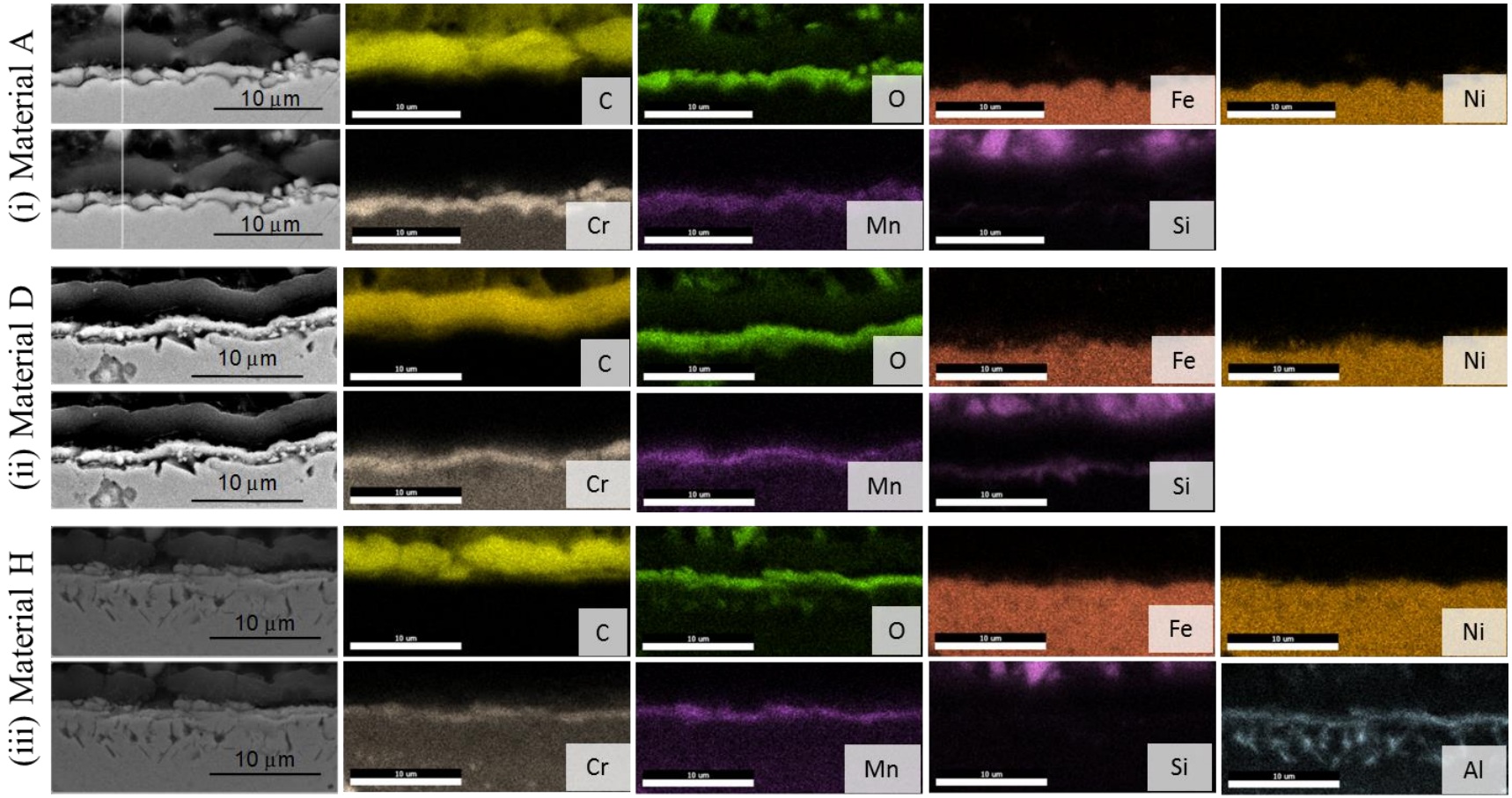

Figure 5.5: EDX element mappings of the cross section of coked coupons after three cracking cycles for material A (i), material D (ii), and material H (iii). See Table 5.6 for the EDX-determined surface composition of coked coupons of materials A, D and H.

The element mappings of a coked coupon of material D presented in Figure 5.5(ii) confirm the previous observations. The mappings of manganese and chromium for material D showed matching bright lines on the uppermost layer of the coupon, suggesting that the oxide layer in the surface is largely composed of manganese chromite and, consequently, the relative abundance of chromia in the surface is lower than in material A. Additionally, a bright line can be observed in the Si mapping, below the manganese chromite. This suggests that the silica layer in material D is more significant than in material A, thus forming a better barrier to prevent iron and nickel migration to the surface.

Inspection of the cross sectional analysis of material H indicates a thin and continuous oxide layer in between the coke and the bulk of the coupon. The EDX line scan performed on it (Figure 5.4(iii)) confirms that oxygen increased its concentration close to the surface. In the same region aluminum increased too, implying the presence of an aluminum oxide, most likely alumina, as predicted by the Ekvicalc calculations. However, together with this alumina, and even slightly closer to the outermost surface, chromium and manganese seem to have also appreciable concentrations, which suggests the presence of manganese chromite too.

The line scan detected no iron or nickel in the surface. The concentration of these two elements increases rapidly below the oxide layer, reaching the usual bulk values. It is also remarkable that no increase in the concentration of Si was detected, in contrast to what was observed in material D.

Figure 5.5(iii), which presents element mappings of the cross section of a coked coupon of material H, confirms that a thin continuous layer of aluminum is present on the outermost surface of the coupon, accompanied by an accumulation of oxygen. The bright line in the oxygen mapping is also matched by chromium and manganese, which confirms that alumina and manganese chromite coexist in the surface of the coupon. The aluminum mapping shows also that,

below the alumina layer, thin alumina-rich channels were encroached in the bulk, perpendicularly to the surface. This indicates internal oxidation of the alloy, which is considered to be the main cause for low coking resistance of some aluminum-enhanced alloys [3]. Its effect, however, is not expected to be significant because a uniform oxide layer still covers the surface of the coupon.

Silicon seems not to play any important role for material H, as no particular accumulation of this element was observed, confirming the observations made from the line scan analysis. The element mappings of iron and nickel indicated the presence of these two elements only below the top oxide layer. No overlapping of Fe or Ni with the alumina or manganese chromite could be detected, showing that both oxides are very protective and effectively impede the presence of Fe and Ni at the surface.

All these observations clearly indicate that the oxide layers developed over the surface of the coupons determine the differences in the coking behavior of the materials during naphtha cracking. The analyses of the cross sections of materials A and D suggest the presence of chromia and manganese chromite in their surfaces. However, these materials differ on the ratio of concentration of chromia to manganese chromite. Material D exhibited a higher concentration of manganese chromite than A. And hence, because chromia has been suggested not to be as resistant to coke deposition as manganese chromite, the differences between the measured coking rates of A and D could be explained in this way.

It is clear that material H shows a significantly higher coking resistance than materials A and D. Considering that the cross-sectional analysis of the coupons of H indicated the presence of alumina and manganese chromite, and in view of the positive impact in coking resistance that this surface has been reported to have, the good resistance of material H should be logically attributed to the alumina on its surface.

The results of the line scans and mappings show that the main characteristics of the studied materials are not drastically different for naphtha and ethane cracking. Nevertheless, the asymptotic coking rates of the three tested materials are higher during naphtha cracking than during ethane cracking. This implies that the material selection for the construction of naphtha cracking coils has an impact on their run length, although it is slightly less crucial than for ethane crackers, due to the higher asymptotic coking rates associated with heavier feeds.

5.4 Conclusions

A quantitative assessment of the coking resistance of three different industrial reactor materials has been presented when cracking ethane or naphtha. Although the naphtha cracking conditions were not identical to those of ethane cracking due to the intrinsic differences in reactivity of both feeds, the experiments revealed that material H, the best during ethane cracking, behaved also better than A and D for naphtha cracking.

The difference in coking tendency between the different materials under naphtha cracking conditions was only slightly less pronounced than under ethane cracking conditions. This difference cannot be attributed to a different coupon pretreatment, as the latter was identical in both cases. Even after cracking, the characteristic features of the coupons during naphtha and ethane cracking were essentially the same.

EDX analyses of the surface of coked coupons of the three materials indicated that chromium, manganese and aluminum (when available) are dominant in the uppermost layer while others, like iron and nickel, can be considered negligible in the surface. Thermodynamic calculations

indicate that the oxide layers formed during the preoxidation step, i.e. chromia and manganese chromite for materials A and D, and manganese chromite combined with alumina for material H are not largely affected by the coking and decoking cycles. Cross sectional analyses of the coked coupons confirmed the predictions of the thermodynamic calculations. Compared to material A, the slightly better behavior of material D is attributed to its high concentration of manganese chromite in the surface, accompanied by the presence of a layer of silica underneath. Material H exhibited a thin and continuous layer of alumina on its uppermost surface, coexisting with manganese chromite.

Despite the pronounced similarity of the experimental procedure during ethane and naphtha cracking, the observed coking behavior confirms industrial observations claiming that the coil material selection has a larger significance for ethane than for naphtha cracking. Nevertheless a run length increase of even 50% can still be achieved during naphtha cracking by selecting an adequate material.

Finally, it can be concluded that the differences in coking resistance observed during ethane and naphtha cracking are mainly related to the cracking conditions during the steam cracking of each feed, i.e. temperature and gas phase composition inside the reactor.

References

[1] Wysiekierski, A. G.; Fisher, G.; Schillmoller, C. M. Control coking for olefins plants. *Hydrocarb. Process.* **1999**, *78* (1), 97-100.

[2] Zimmermann, H.; Walzl, R., Ethylene. In *Ullmann's Encyclopedia of Industrial Chemistry*, Wiley-VCH Verlag GmbH & Co. KGaA: **2000**.

[3] Jakobi, D., van de Moesdijk C., Karduck, P., von Richthofen A. Tailor-made materials for high temperature applications: New strategies for radiant coil material development. NACE, Atlanta, GA, **2009.** NACE International.

[4] Schools, E. M.; Froment, G. F. Simulation of decoking of thermal cracking coils by steam/air-mixtures. *Aiche J.* **1997**, *43* (1), 118-126.

[5] Heynderickx, G. J.; Schools, E. M.; Marin, G. B. Optimization of the decoking procedure of an ethane cracker with a steam/air mixture. *Ind. Eng. Chem. Res.* **2006**, *45* (22), 7520-7529.

[6] Zimmermann, G.; Zychlinski, W.; Woerde, H. M.; van den Oosterkamp, P. Absolute rates of coke formation: A relative measure for the assessment of the chemical behavior of high-temperature steels of different sources. *Ind. Eng. Chem. Res.* **1998**, *37* (11), 4302-4305.

[7] Zychlinski, W.; Wynns, K. A.; Ganser, B. Characterization of material samples for coking behavior of HP40 material both coated and uncoated using naphtha and ethane feedstock. *Mater. Corros.* **2002**, *53* (1), 30-36.

[8] Nishiyama, Y.; Otsuka, N. Degradation of surface oxide scale on Fe-Ni-Cr-Si alloys upon cyclic coking and decoking procedures in a simulated ethylene pyrolysis gas environment. *Corrosion* **2005**, *61* (1), 84-93.

[9] Albano, J. V.; Sundaram, K. M.; Maddock, M. J. Applications of extended surfaces in pyrolysis coils. *Energy Prog.* **1988**, *8* (3), 9.

[10] Brown, D. J. Internally finned radiant coils: A valuable tool for Improving ethylene plant economics. 6th EMEA Petrochemicals Technology Conference, London, UK, **2004.**

[11] Dente, M.; Bozzano, G.; Faravelli, T.; Marongiu, A.; Pierucci, S.; Ranzi, E., Kinetic modelling of pyrolysis processes in gas and condensed phase. In *Advances in Chemical Engineering*, Guy, B. M., Ed. Academic Press: **2007**; Vol. Volume 32, pp 51-166.

[12] Schietekat, C. M.; van Goethem, M. W. M.; Van Geem, K. M.; Marin, G. B. Swirl flow tube reactor technology: An experimental and computational fluid dynamics study. *Chem. Eng. J.* **2014**, *238*, 56-65.

[13] Pons, F.; Hugo, M.; Crambes, M.; Papapietro, M. Austenitic phase alloy containing chromium and aluminium; use in cracking furnaces and drilling pipes or cables. European Patent Application EP0169119A1, **1986**.

[14] Terwijn, F. X.; Morii, K.; Takeuchi, Y.; Kato, Y.; Hayakawa, H.; Nishimura, N. Heat resisting metal tube and method for manufacturing same. European Patent Application EP1043084A3, **2001**.

[15] Flahaut, D. High temperature alloys. WIPO Patent Application WO/2004/042101A2, **2004**.

[16] Benum, L. W.; Oballa, M. C.; Petrone, S. S. A.; Chen, W. Surface on a stainless steel matrix. U.S. Patent Application US20050077210A1, **2005**.

[17] Jakobi, D.; Ganser, B. Centralloy 60 HT-alloy development for high temperature operation and reduced coking. Spring National Meeting: 17th Annual Ethylene Producers Conference, Atlanta, GA, USA, 10/April/2005, **2005.**

[18] Demarest, J.; Verdier, G. Apparatus for making centrifugally-cast tube. U.S. Patent Application US8070401B2, **2011**.

[19] Verdier, G.; Carpentier, F. Consider new materials for ethylene furnace applications. *Hydrocarb. Process.* **2011**, *90* (5), 61-62.

[20] Fedorova, E.; Monceau, D.; Oquab, D. Quantification of growth kinetics and adherence of oxide scales formed on Ni-based superalloys at high temperature. *Corros. Sci.* **2010**, *52* (12), 3932-3942.

[21] Holmen, A.; Lindvaag, O. A.; Trimm, D. L. Surface effects on the steam cracking of propane. *ACS Symp. Ser.* **1982**, *202*, 45-58.

[22] Holmen, A.; Lindvaag, O. A.; Trimm, D. L. Coke formation during steam cracking of hydrocarbons .2. Effect of preoxidation and prereduction of the reactor surface *J. Chem. Tech. Biot. A.* **1985**, *35* (7), 358-364.

[23] Reyniers, M.-F.; Froment, G. F. Influence of metal-surface and sulfur addition on coke deposition in the thermal-cracking of hydrocarbons. *Ind. Eng. Chem. Res.* **1995**, *34* (3), 773-785.

[24] Dhuyvetter, I.; Reyniers, M. F.; Froment, G. F.; Marin, G. B.; Viennet, D. The influence of dimethyl disulfide on naphtha steam cracking. *Ind. Eng. Chem. Res.* **2001**, *40* (20), 4353-4362.

[25] Wang, J.; Reyniers, M. F.; Marin, G. B. Influence of dimethyl disulfide on coke formation during steam cracking of hydrocarbons. *Ind. Eng. Chem. Res.* **2007**, *46* (12), 4134-4148.

[26] Li, H.; Chen, W. X. Effect of H2S on high temperature corrosion of Fe-Ni-Cr alloys in carburizing/oxidizing environments. *Oxid. Met.* **2012**, *77* (3-4), 107-127.

[27] Broutin, P.; Ropital, F.; Reyniers, M. F.; Froment, G. F. Anticoking coatings for high temperature petrochemical reactors. *Oil Gas Sci. Technol.* **1999**, *54* (3), 375-385.

[28] Ganser, A.; Wynns, K. A.; Kurlekar, A. Operational experience with diffusion coatings on steam cracker tubes. *Mater. Corros.* **1999**, *50* (12), 700-705.

[29] Redmond, T.; Bergeron, M. P. Tests demonstrate anticoking capability of new coating. *Oil Gas J.* **1999**, *97* (19), 39-42.

[30] Voisey, K. T.; Liu, Z.; Stott, F. H. Inhibition of metal dusting using thermal spray coatings and laser treatment. *Surf. Coat. Technol.* **2006**, *201* (3-4), 637-648.

[31] Zhou, J.; Xu, H.; Liu, J.; Qi, X.; Zhang, L.; Jiang, Z. Study of anti-coking property of SiO2/S composite coatings deposited by atmospheric pressure chemical vapor deposition. *Mater. Lett.* **2007**, *61* (29), 5087-5090.

[32] Wang, Z. Y.; Xu, H.; Luan, X. J.; Hou, F.; Zhou, J. X. Effect of Potassium Acetate on Coke Growth during Light Naphtha Thermal Cracking. *Ind. Eng. Chem. Res.* **2011**, *50* (17), 10292-10297.

[33] Zhou, J. X.; Wang, Z. Y.; Luan, X. J.; Xu, H. Anti-coking property of the SiO2/S coating during light naphtha steam cracking in a pilot plant setup. *J. Anal. Appl. Pyrol.* **2011**, *90* (1), 7-12.

[34] Browne, J.; Broutin, P.; Ropital, F. Coke deposition under steam cracking conditions - Study of the influence of the feedstock conversion by micropilots experiments. *Mater. Corros.* **1998**, *49* (5), 360-366.

[35] Luan, T. C.; Eckert, R. E.; Albright, L. F. Gaseous pretreatment of high-alloy steels used in ethylene furnaces: Pretreatment of Incoloy 800. *Ind. Eng. Chem. Res.* **2003**, *42* (20), 4741-4747.

[36] Zhang, Z. B.; Albright, L. F. Pretreatments of Coils to Minimize Coke Formation in Ethylene Furnaces. *Ind. Eng. Chem. Res.* **2010**, *49* (4), 1991-1994.

[37] Bennett, M. J.; Price, J. B. A physical and chemical examination of an ethylene steam cracker coke and of the underlying pyrolysis tube. *J. Mater. Sci.* **1981**, *16* (1), 170-188.

[38] Chauhan, A.; Anwar, M.; Montero, K.; White, H.; Si, W. Internal carburization and carbide precipitation in Fe-Ni-Cr alloy tubing retired from ethylene pyrolysis service. *J. Phase Equilib. Diff.* **2006**, *27* (6), 684-690.

[39] Wu, X. Q.; Yang, Y. S.; He, W. Y.; Zhan, Q.; Hu, Z. Q. Morphologies of coke deposited on surfaces of pure Ni and Fe-Cr-Ni-Mn alloys during pyrolysis of propane. *J. Mater. Sci.* **2000**, *35* (4), 855-862.

[40] Li, H.; Zheng, Y. J.; Benum, L. W.; Oballa, M.; Chen, W. X. Carburization behaviour of Mn-Cr-O spinel in high temperature hydrocarbon cracking environment. *Corros. Sci.* **2009**, *51* (10), 2336-2341.

[41] Van Geem, K. M.; Heynderickx, G. J.; Marin, G. B. Effect of radial temperature profiles on yields in steam cracking. *Aiche J.* **2004**, *50* (1), 173-183.

[42] Speight, J. G. The chemistry and physics of coking. *Korean J. Chem. Eng.* **1998**, *15* (1), 1-8.

[43] Cai, H. Y.; Krzywicki, A.; Oballa, M. C. Coke formation in steam crackers for ethylene production. *Chem. Eng. Process.* **2002**, *41* (3), 199-214.

[44] Nielsen, J. R.; Trimm, D. L. Mechanisms of carbon formation on nickel-containing catalysts. *J. Catal.* **1977**, *48* (1-3), 155-165.

[45] Baker, R. T. K.; Yates, D. J. C.; Dumesic, J. A. Filamentous carbon formation over iron surfaces. *ACS Symp. Ser.* **1982**, *202*, 1-21.

[46] Snoeck, J. W.; Froment, G. F.; Fowles, M. Filamentous carbon formation and gasification: Thermodynamics, driving force, nucleation, and steady-state growth. *J. Catal.* **1997**, *169* (1), 240-249.

[47] Reshetenko, T. V.; Avdeeva, L. B.; Ismagilov, Z. R.; Pushkarev, V. V.; Cherepanova, S. V.; Chuvilin, A. L.; Likholobov, V. A. Catalytic filamentous carbon structural and textural properties. *Carbon* **2003**, *41* (8), 1605-1615.

[48] Kopinke, F. D.; Zimmermann, G.; Nowak, S. On the mechanism of coke formation in steam cracking - conclusions from results obtained by tracer experiments. *Carbon* **1988**, *26* (2), 117-124.

[49] Glasier, G. F.; Pacey, P. D. Formation of pyrolytic carbon during the pyrolysis of ethane at high conversions. *Carbon* **2001**, *39* (1), 15-23.

[50] Dong, G. L.; Huttinger, K. J. Consideration of reaction mechanisms leading to pyrolytic carbon of different textures. *Carbon* **2002**, *40* (14), 2515-2528.

[51] Hemelsoet, K.; Van Speybroeck, V.; Van Geem, K. M.; Marin, G. B.; Waroquier, M. Using elementary reactions to model growth processes of polyaromatic hydrocarbons under pyrolysis conditions of light feedstocks. *Mol. Simulat.* **2008**, *34* (2), 193-199.

[52] Moszkowicz, P.; Witzel, L.; Claus, G. Modelling of very fast pyrolysis of heavy fuel oil droplets. *Chem. Eng. Sci.* **1996**, *51* (17), 4075-4086.

[53] Towfighi, J.; Sadrameli, M.; Niaei, A. Coke formation mechanisms and coke inhibiting methods in pyrolysis furnaces. *J. Chem. Eng. Jpn.* **2002**, *35* (10), 923-937.

[54] Wauters, S.; Marin, G. B. Kinetic modeling of coke formation during steam cracking. *Ind. Eng. Chem. Res.* **2002**, *41* (10), 2379-2391.

[55] Woerde, H. M.; Barendregt, S.; Humblot, F.; Brun, C. Mitigate coke formation. *Hydrocarb. Process.* **2002**, *81* (3), 45-50.

[56] Reyniers, G. C.; Froment, G. F.; Kopinke, F. D.; Zimmermann, G. Coke formation in the thermal-cracking of hydrocarbons .4. Modeling of coke formation in naphtha cracking. *Ind. Eng. Chem. Res.* **1994**, *33* (11), 2584-2590.

[57] Sundaram, K. M.; Froment, G. F. Kinetics of coke deposition in the thermal-cracking of propane. *Chem. Eng. Sci.* **1979**, *34* (5), 635-644.

[58] Plehiers, P. M.; Reyniers, G. C.; Froment, G. F. Simulation of the run length of an ethane cracking furnace. *Ind. Eng. Chem. Res.* **1990**, *29* (4), 636-641.

[59] Kopinke, F. D.; Zimmermann, G.; Reyniers, G. C.; Froment, G. F. Relative rates of coke formation from hydrocarbons in steam cracking of naphtha .3. Aromatic-hydrocarbons. *Ind. Eng. Chem. Res.* **1993**, *32* (11), 2620-2625.

[60] Kopinke, F. D.; Zimmermann, G.; Reyniers, G. C.; Froment, G. F. Relative rates of coke formation from hydrocarbons in steam cracking of naphtha. 2. Paraffins, naphthenes, monoolefins, iolefins, and cycloolefins, and acetylenes. *Ind. Eng. Chem. Res.* **1993**, *32* (1), 56-61.

[61] Miki, Y.; Toba, M.; Yoshimura, Y. Analysis of sulfur compounds in straight-run naphtha and FCC gasoline. *J. Jpn. Pet. Inst* **2008**, *51* (4), 225-233.

[62] Herrera, P.; Simanzhenkov, V.; Wong, C.; Benum, L. W. Feedstock Contaminants: A Case Study. Ethylene Producers' Conference, San Antonio, TX, USA, March 22nd, **2010.**

[63] Van Geem, K. M.; Reyniers, M. F.; Marin, G. B. Two severity indices for scale-up of steam cracking coils. *Ind. Eng. Chem. Res.* **2005**, *44* (10), 3402-3411.

[64] Nolang, B. *Ekvicalc and Ekvibase*, 4.30; Svensk Energi Data: Balinge, Sweden, **2013**.

[65] Van Geem, K. M.; Pyl, S. P.; Reyniers, M. F.; Vercammen, J.; Beens, J.; Marin, G. B. On-line analysis of complex hydrocarbon mixtures using comprehensive two-dimensional gas chromatography. *J. Chromatogr. A* **2010**, *1217* (43), 6623-6633.

[66] ASTM-D2887, Standard Test Method for Boiling Range Distribution of Petroleum Fractions by Gas Chromatography. In ASTM International, West Conshohocken, PA, 2003: 2013.

[67] Dijkmans, T.; Van Geem, K. M.; Djokic, M. R.; Marin, G. B. Combined comprehensive two dimensional gas chromatographic analysis of PAH/PASH compounds in complex matrices. *Ind. Eng. Chem. Res.* **2014**.

[68] Crynes, L. L.; Crynes, B. L. Coke formation on polished and unpolished Incoloy-800 coupons during pyrolysis of light-hydrocarbons. *Ind. Eng. Chem. Res.* **1987**, *26* (10), 2139-2144.

[69] Marek James, C.; Albright Lyle, F., Surface Phenomena During Pyrolysis: The Effects of Treatments with Various Inorganic Gases. In *Coke Formation on Metal Surfaces*, American Chemical Society: **1983**; Vol. 202, pp 151-175.

[70] Bach, G.; Zimmermann, G.; Kopinke, F. D.; Barendregt, S.; Vandenoosterkamp, P.; Woerde, H. Transfer-Line Heat-Exchanger Fouling During Pyrolysis of Hydrocarbons .1. Deposits from Dry Cracked Gases. *Ind. Eng. Chem. Res.* **1995**, *34* (4), 1132-1139.

[71] Petrone, S.; L., D. R.; Kong, F.; Unwin, P. Catalyzed-assisted manufacture of olefins (CAMOL): Year-(4) update on furnace commercial installations. 2010 Spring National Meeting, San Antonio, TX, **2010.**

[72] Van Geem, K. M.; Reyniers, M. F.; Marin, G. B. Challenges of modeling steam cracking of heavy feedstocks. *Oil Gas Sci. Technol.* **2008**, *63* (1), 79-94.

[73] Wang, J. D.; Reyniers, M. F.; Van Geem, K. M.; Marin, G. B. Influence of silicon and silicon/sulfur-containing additives on coke formation during steam cracking of hydrocarbons. *Ind. Eng. Chem. Res.* **2008**, *47* (5), 1468-1482.

[74] Dijkmans, T.; Pyl, S. P.; Reyniers, M. F.; Abhari, R.; Van Geem, K. M.; Marin, G. B. Production of bio-ethene and propene: alternatives for bulk chemicals and polymers. *Green Chem.* **2013**, *15* (11), 3064-3076.

[75] Yan, J. B.; Gao, Y. M.; Yang, F.; Bai, Y. P.; Liu, Y. H.; Yao, C. Y.; Hou, S. Z.; Liu, G. Z. Cyclic carburizing behaviour of Al modified high Si-containing HP40 alloy. *Corros. Sci.* **2013**, *67*, 161-168.

[76] Jakobi, D.; Karduk, P.; von Richthofen, A. F. The high-temperature corrosion resistance of spun-cast materials for steam cracker furnaces - A comparative study of alumina- and chromia-forming alloys. NACE, Orlando, FL, **2013.** NACE International.

[77] Asteman, H.; Hartnagel, W.; Jakobi, D. The Influence of Al Content on the High Temperature Oxidation Properties of State-of-the-Art Cast Ni-base Alloys. *Oxid. Met.* **2013**, *80* (1-2), 3-12.

Chapter 6: Conclusions and perspectives

6.1 Conclusions

In this thesis, the resistance to coke deposition of various materials specifically developed for the construction of steam cracking reactors has been systematically studied under a fixed set of industrially representative conditions. Using an electrobalance setup, initial and asymptotic rates of coke deposition were measured over 1 cm^2 rectangular coupons, that were exposed to the conditions of steam cracking of ethane and light naphtha inside a quartz JSR. Ten different materials (chromia-forming alloys, alumina-forming alloys and a coating) were tested under ethane cracking conditions.

A strong influence of the composition of the materials was observed. The initial coking rate measured during ethane cracking ranged from 5×10^{-7} $kg \cdot m^{-2} \cdot s^{-1}$ to 27×10^{-7} $kg \cdot m^{-2} \cdot s^{-1}$, and the asymptotic rate ranged from 2×10^{-7} $kg \cdot m^{-2} \cdot s^{-1}$ to 6×10^{-7} $kg \cdot m^{-2} \cdot s^{-1}$. Comparison of the coking rates allowed to rank the studied alloys, leading to place material H (an Al-enhanced alloy) as the one with the highest coking resistance, followed by material D (a pretreated alloy with Cr-Mn oxides at its surface). The coated coupons (material J) exhibited a similar resistance to that of material A, which was included in the study because of being a typical heat-resistant alloy. For the ethane cracking experiment, material H achieved a reduction in asymptotic rate of 50% compared to material A.

As a group, the alumina-forming alloys exhibited a slightly higher resistance to coking than the materials without aluminum in their formulation. However, no direct link can be made between the bulk composition of the alloys and their coking performance during cracking.

The three reactor materials tested under naphtha cracking conditions also exhibited different coking rates. Material H showed the lowest asymptotic coking rate followed by material D which, in turn, had a lower rate than material A. The asymptotic coking rate of material H was 40% lower than that of material A. This confirms that a significant reduction of coke deposition can be achieved by the usage of an effective reactor material for steam cracking of naphtha.

SEM and EDX analyses of blank, preoxidized, and coked coupons complemented with thermodynamic calculations revealed that the observed migration to the surface of chromium and manganese during preoxidation results in the formation of chromia and manganese chromite. For the Al-enhanced materials, migration of this element to the surface results in the formation of an alumina layer.

Reduced coking was observed when, after ethane and naphtha cracking, the aluminum on the surface was present under the form of a uniform oxide, with a sublayer of manganese chromite. However, excessive amounts of alumina caused internal oxidation, which is harmful for the coking resistance of alloys.

For the non-Al containing materials, the relative concentration of chromia and manganese chromite at the surface strongly affects the coking resistance. The EDX mappings and line scans revealed that high chromia contents at the surface are undesirable, as large amounts of coke were found over this oxide, while the formation of manganese chromite reduces coke formation. A sublayer of silica also seemed to enhance the coking resistance.

The small difference of coking rate reduction during ethane and naphtha cracking cannot be attributed to a different pretreatment, because the latter was exactly the same for the experiments

with both feeds. Even after cracking, the characteristic features of the coupons submitted to ethane and naphtha cracking were essentially the same. The differences in coking resistance observed during ethane and naphtha cracking can be attributed exclusively to the cracking conditions.

Run length simulations indicated that the reduction of the coking rates achieved during ethane and naphtha cracking leads to run length increases of, respectively, 100% and 50%. This indicates that the use of specialized coil materials is significantly beneficial for cracking of both feedstocks, although the effect of good materials on run length is reduced as the feed becomes heavier, due to the intrinsic differences of reactivity between lighter and heavier feeds.

6.2 Perspectives

The work presented in this thesis provided the first systematic study focused on determining which types of materials show the best resistance to coking and on explaining the characteristics that make them better than others.

Using the same methodology and conditions, it would be recommendable to study the performance of active coatings that gasify coke, which seem to be a recent trend in the market of coil surface technologies. The JSR setup provides the unique possibility of testing them to obtain information concerning their effect on coking rates and the yields of CO and CO_2. The effect of cyclic operation, i.e. consecutive cracking and decoking runs, on the integrity of the coatings can also be studied in this setup.

The coking resistance of alloys is often reduced by the effect of aging. Higher numbers of consecutive cycles could be carried out in order to study the long term performance of the tested materials, which is sometimes questioned.

Several experimental conditions, e.g. temperature, dilution, residence time, surface roughness, were fixed during this work, so that the observed differences in coking behavior could be attributed to the different materials or feeds used. However, studying the effect of varying these conditions could provide valuable insight concerning fundamentals of coke formation. For example, coupons of the same material could be polished to different roughness values and be tested during ethane and naphtha cracking experiments to provide the first quantification of the effect of surface roughness on coke deposition.

In industry, sulfur is usually present in the feed or is added deliberately in order to reduce the yields of CO. A comparative study of the effect of sulfur compounds on specialized coils (e.g. materials D and H) should be carried out to determine if alumina layers and mixed oxides are equally resistant to coking when sulfur is added. This could also help to clarify the so far contradictory reports on the influence of sulfur on coking. The effect of other additives can be studied in a similar manner.

Additionally, it is important to notice that coking rate values were determined for only two feeds in this thesis. Coking tests using other feeds could provide valuable quantitative information concerning the effect of different concentrations and types of coke precursors on the rates of coking.

The results presented in Chapters 4 and 5 showed that it is the surface composition rather than the bulk composition of the materials that influences the rates of coke deposition. The surface composition is mainly determined by the type of pretreatment the material undergoes. It is therefore very important to study the effect of different pretreatments on the coking behavior. Varying the temperature and duration of the preoxidation step, as well as the gas used for preoxidation (air, steam and various mixtures thereof) could allow to determine conditions that

form better oxide layers, consequently enhancing the coking resistance of the treated alloys. The decoking procedure and other pretreatments could also be studied in the same manner.

All the information retrieved by the studies suggested above could be used for the development of a kinetic coke model that takes all the parameters considered significant into account. This model would be able to predict coking rates and run lengths with great accuracy for a very wide range of operating conditions.

Appendix A: Calculation of activation energy

In Chapter 2, calculations to determine the duration of the catalytic regime are presented. These calculations require an activation energy. The calculation of this activation energy is made based on experimental measurements of coking rate as a function of cracking temperature in a CSTR reactor during steam cracking of hexane, which is a good surrogate for light naphtha.

The measured coking rates are plotted as a function of the inverse of temperature in Figure A.1.

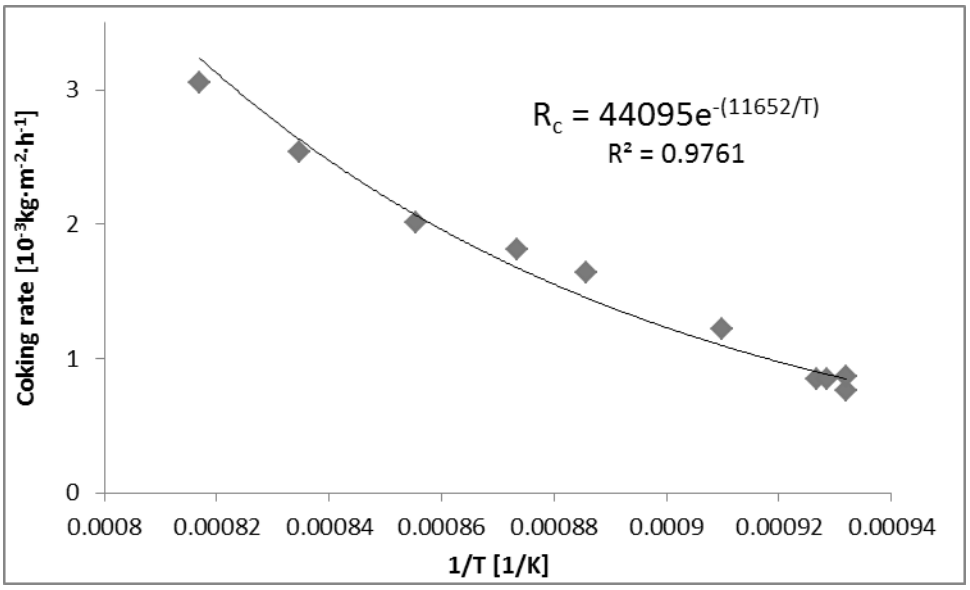

Figure A.1: Measured coking rate as a function of the inverse of the temperature for hexane cracking experiments.

Regression of the experimental data allows to form the equation presented in Figure A.1.

Using this regression, the following can be determined:

$$-\frac{E_a}{R\,T} = -\frac{11652}{T} \tag{A.1}$$

From equation (A.1), the activation energy is calculated to be

$$E_a = 96930\ J \cdot mol^{-1}$$

Appendix B: Supplementary information to Chapter 4

B.1 The JSR reactor

The JSR reactor (Figure B.1(a)) has four nozzles oriented in symmetrically opposite directions for good mixing of the gas. To prevent cracking reactions prior to entering the reactor, the internal diameter of the nozzles and the line transferring the feed to the reactor were kept as low as possible (approximately 1.8 mm).

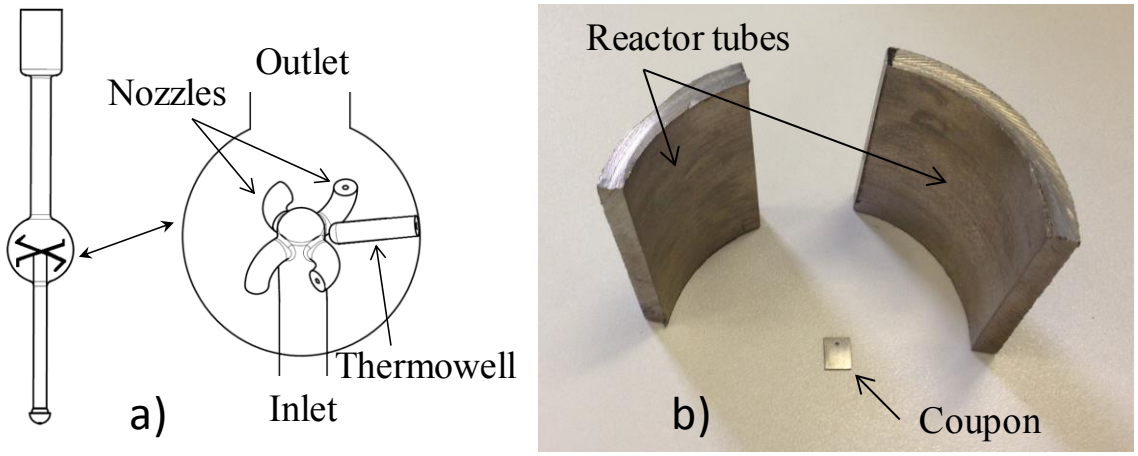

Figure B.1: (a) Diagram of the JSR Reactor; (b) Cut industrial tubes and a JSR coupon.

B.2 Characteristics of the gas chromatographs

The C_4^- sample is analyzed on the Refinery Gas Analyzer (RGA). The carrier gas is helium. Separation of nitrogen, carbon monoxide, carbon dioxide and hydrocarbons up to C2 occurs on a Molsieve 5Å (3 m × 3.0 mm) and a Porapack N column (3 m × 3.0 mm) and a thermal conductivity detector (TCD) is used. Separation of C_3 and C_4 components occurs on a HP-PLOT Al_2O_3 - S25 column (50 m × 0.53 mm) and a Flame Ionization Detector (FID) is used. The Trace GC ultra GC, equipped with a PONA column (50 m × 0.25 mm, 0.5 µm film), is used for quantitative determination of the C_{5+} hydrocarbons. A FID is used to measure the concentration of the hydrocarbons in the reaction mixture.

Integration and identification of peaks is performed by a commercial integration package, namely Chrom-Card Data System. Calculations are based on the absolute flow rates of the effluent components. This is made possible by the injection of a precisely known nitrogen flow, as an internal standard. From the peak areas of the RGA TCD, the experimentally determined calibration factors and the known flow rate of nitrogen, the flow rates of hydrogen, methane, CO_x, and C_2 hydrocarbons are calculated. Using the methane flow rate thus calculated, the flow rates of the other components can be calculated. With these data a product distribution in terms of mass fractions can be determined. As the feed flow rate is known, yields and a mass balance can also be calculated. The carbon mass balances closed between 97% and 102%.

B.3 Calculation of coking rates

The initial and asymptotic coking rates were calculated as a function of time for each experiment, by numerical differentiation of the mass of coke with respect to time over the entire length of the experiment. The length of the time intervals for differentiation was 10 seconds. Figures B.3 – B.11 depict the coking rates as a function of time for each tested material. The initial coking rate is taken as an indication of the deposition of catalytic coke and is calculated as the rate between cracking times t_1 = 15 min and t_2 = 30 min, using equation (B.1).

$$\mathbf{R_c} = \frac{\mathbf{m_{t_2} - m_{t_1}}}{\mathbf{t_2 - t_1}} \cdot \frac{\mathbf{1}}{\mathbf{S}} \qquad (B.1)$$

The asymptotic rate, on the other hand, is calculated between t_1 = 5 hours and t_2 = 6 hours, when the mass increase reaches a stable linear regime. Figure B.2 shows how the coking rate changed with time during the experiments, and indicates the derived coking rate, as well as the time intervals from which the initial and asymptotic rates were obtained. All reported coking rates and their standard deviations pertain to averaged values over at least three experiments per material.

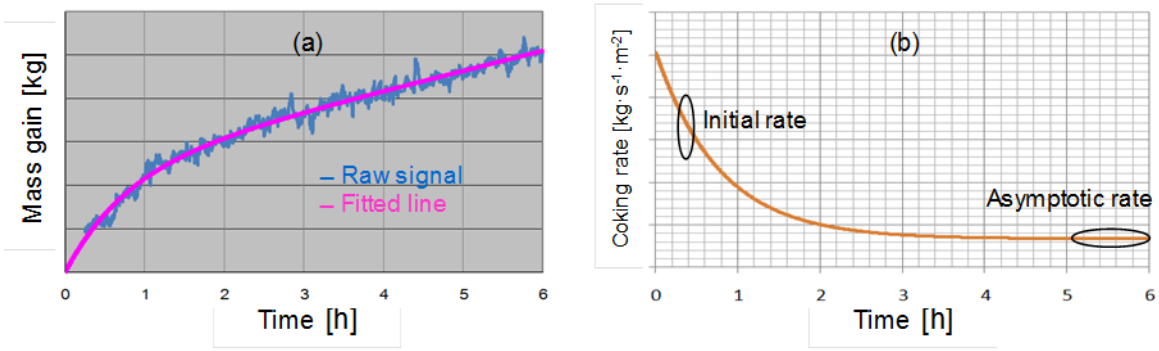

Figure B.2: Illustration of the measurements of the mass gain of the coupons (a), and the derivation leading to the coking rates in the initial and asymptotic regimes (b).

B.4 Tables

Table B.1: Mean measured effluent composition during ethane cracking experiments in the electrobalance setup (T=1159 K, δ=0.33 kg_{H2O}/kg_{C2H6}, τ~0.1s)

Component	Wt%	Component	Wt%
H_2	6.40	Propadiene	0.04
CO	0.01	C_2H_2	1.54
CO_2	0.00	t2-C_4H_8	0.04
CH_4	7.91	1-C_4H_8	0.07
C_2H_6	26.43	i-C_4H_8	0.00
C_2H_4	50.15	c2-C_4H_8	0.03
C_3H_8	0.11	1,3-C_4H_6	1.67
C_3H_6	0.88	Met. Acetylene	0.05
i-C_4H_{10}	0.00	C_5^+	4.58
n-C_4H_{10}	0.08		

B.5 Figures

B.5.1 Coking Results

The following Figures (Figure B.3 - Figure B.11) present the mean measured coking rates for each material as a function of time for three consecutive cycles during ethane cracking experiments performed in the electrobalance setup.

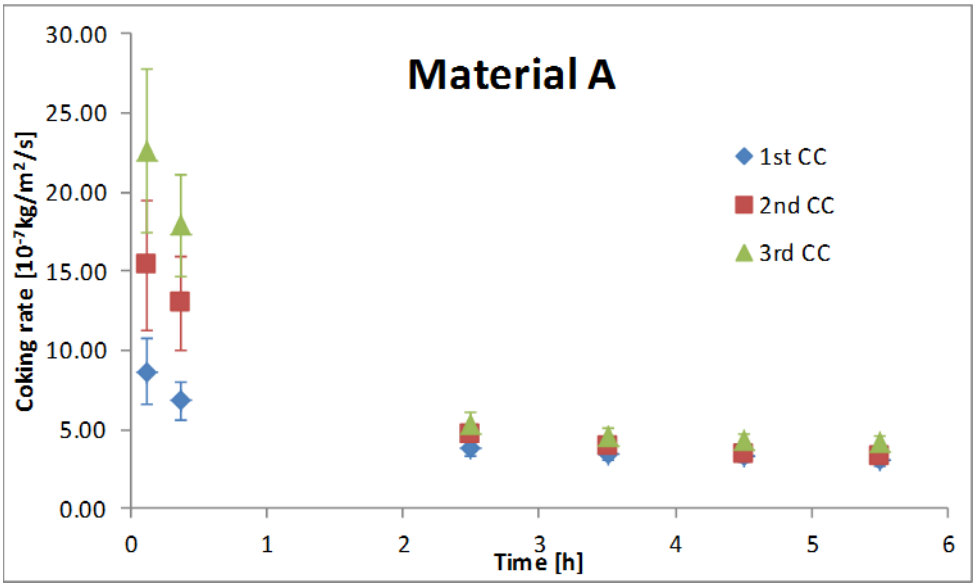

Figure B.3: Mean measured coking rate as a function of time for three consecutive coking cycles on material A during ethane cracking at 1159 K in the JSR reactor.

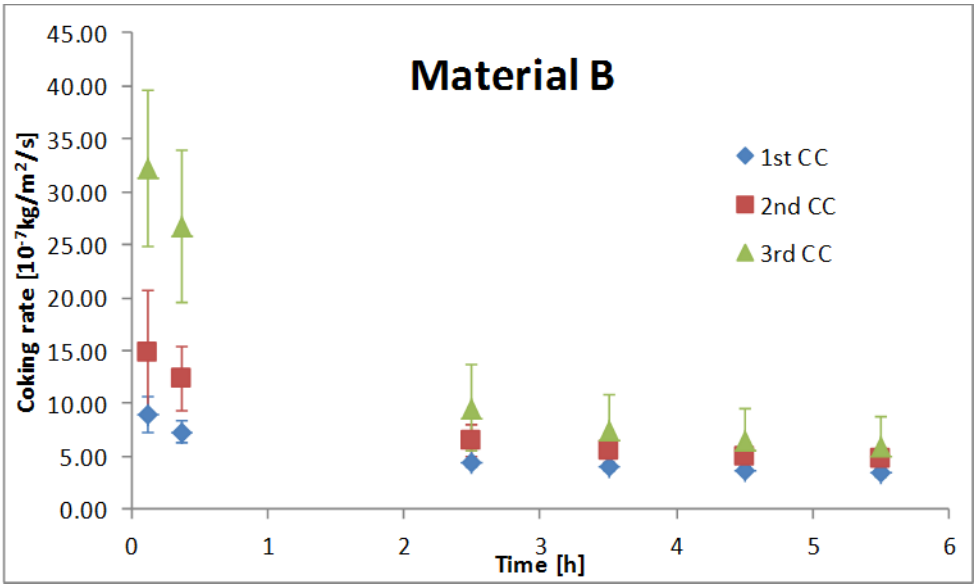

Figure B.4: Mean measured coking rate as a function of time for three consecutive coking cycles on material B during ethane cracking at 1159 K in the JSR reactor.

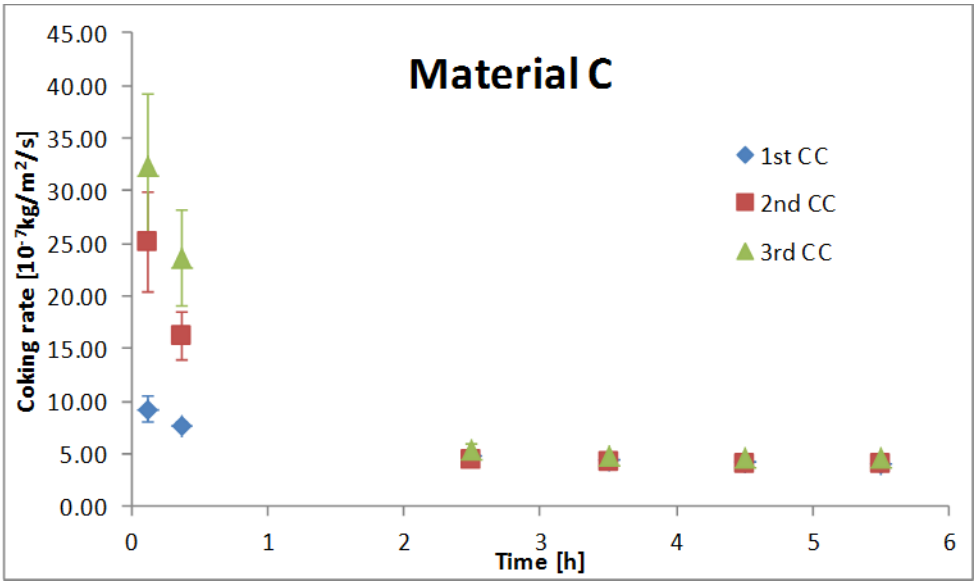

Figure B.5: Mean measured coking rate as a function of time for three consecutive coking cycles on material C during ethane cracking at 1159 K in the JSR reactor.

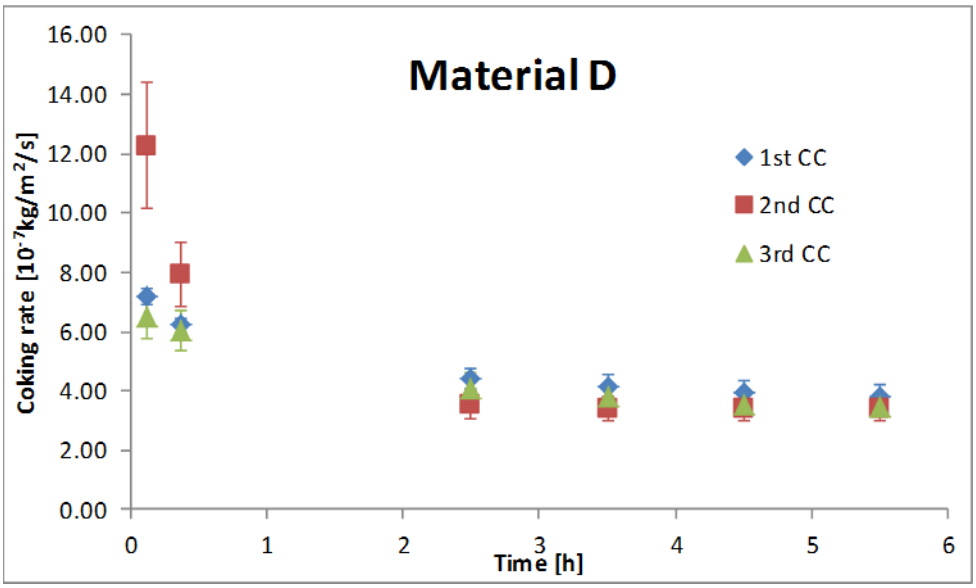

Figure B.6: Mean measured coking rate as a function of time for three consecutive coking cycles on material D during ethane cracking at 1159 K in the JSR reactor.

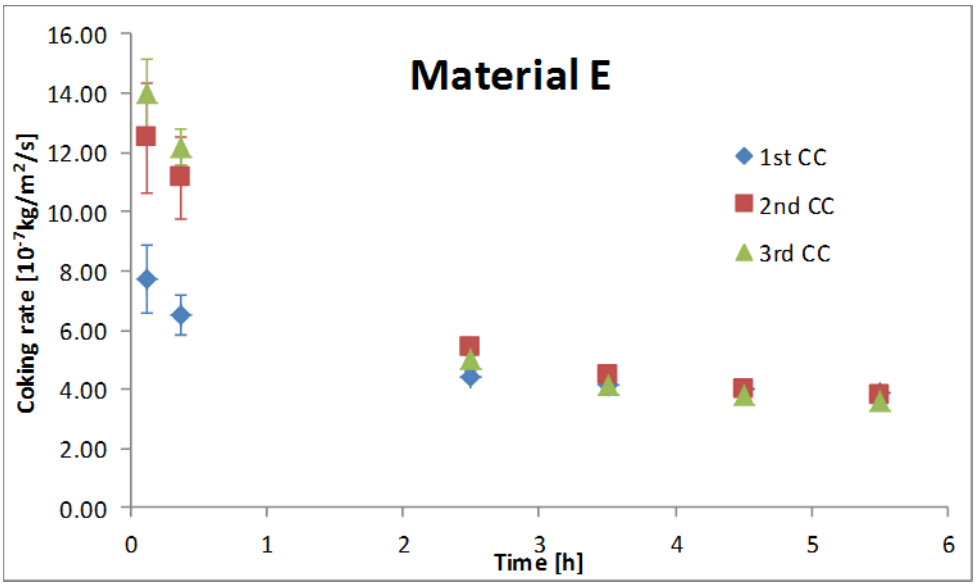

Figure B.7: Mean measured coking rate as a function of time for three consecutive coking cycles on material E during ethane cracking at 1159 K in the JSR reactor.

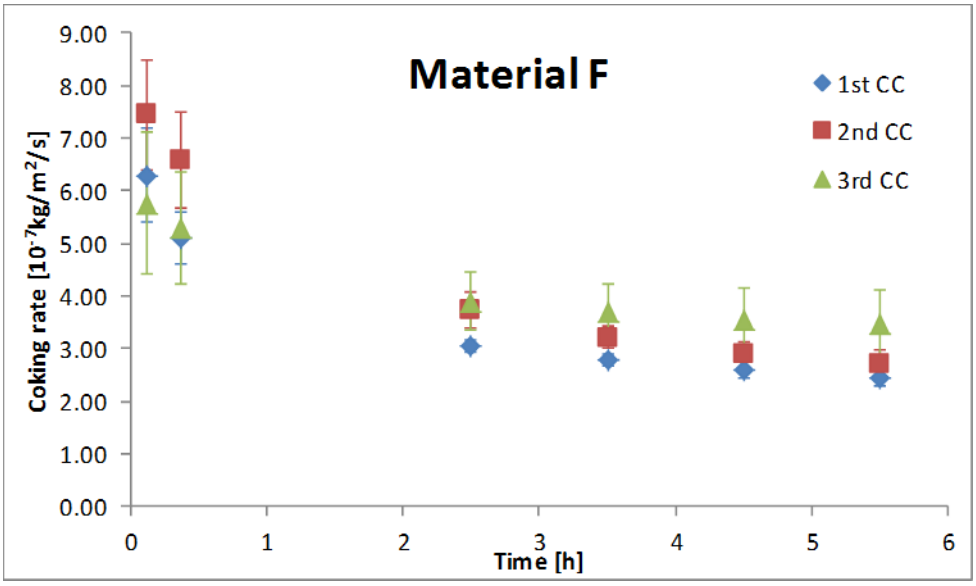

Figure B.8: Mean measured coking rate as a function of time for three consecutive coking cycles on material F during ethane cracking at 1159 K in the JSR reactor.

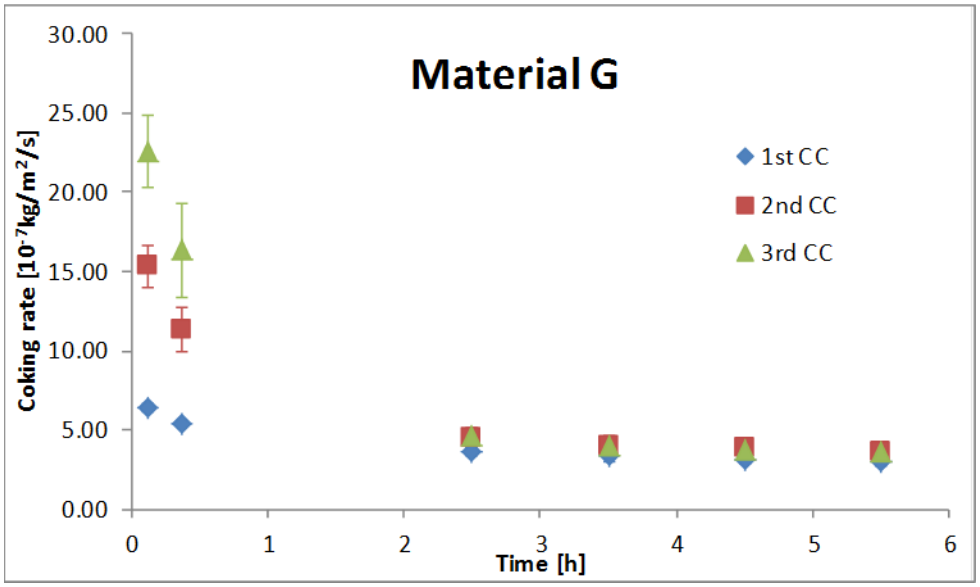

Figure B.9: Mean measured coking rate as a function of time for three consecutive coking cycles on material G during ethane cracking at 1159 K in the JSR reactor.

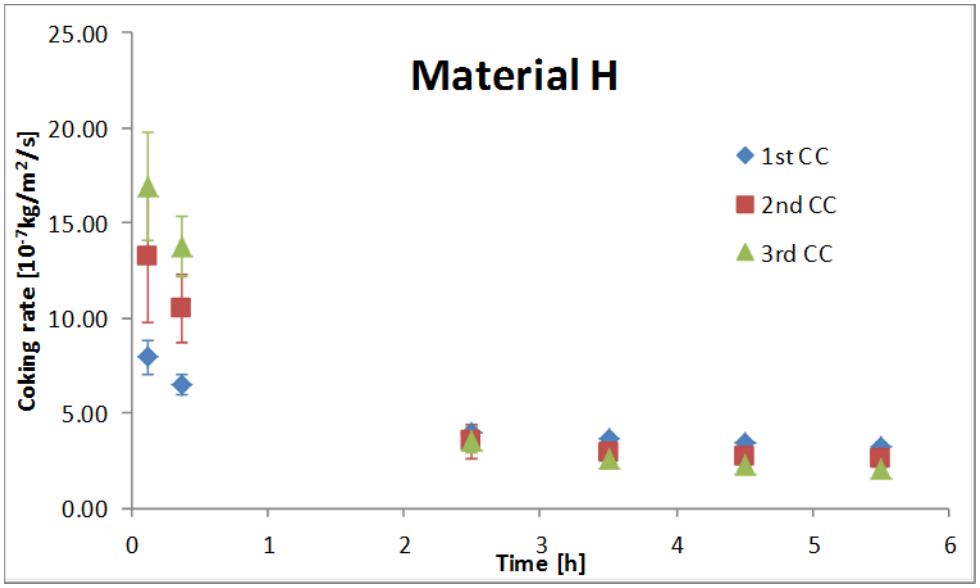

Figure B.10: Mean measured coking rate as a function of time for three consecutive coking cycles on material H during ethane cracking at 1159 K in the JSR reactor.

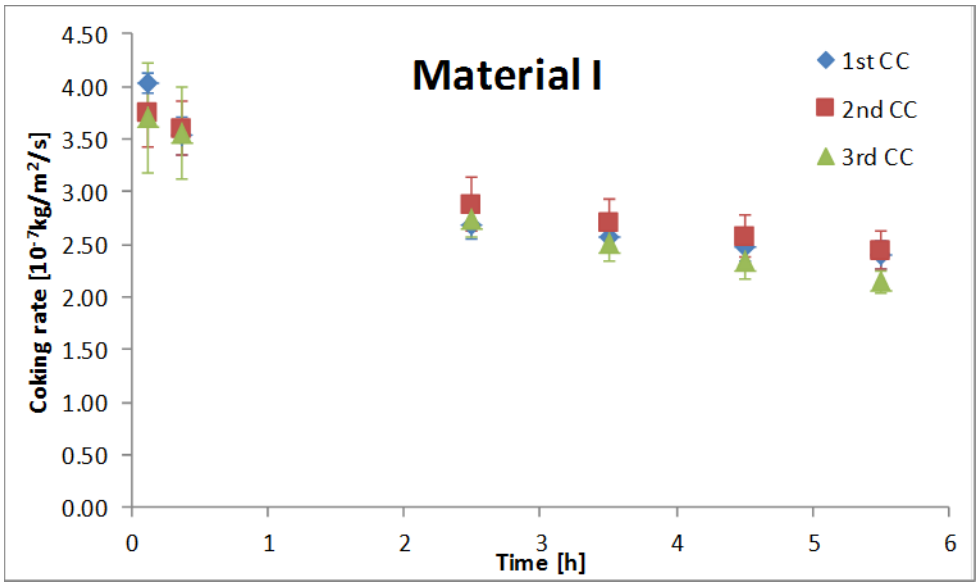

Figure B.11: Mean measured coking rate as a function of time for three consecutive coking cycles on material I during ethane cracking at 1159 K in the JSR reactor.

B.5.2 EDX Results

The following Figures (Figure B.12 - Figure B.18) present the EDX line scans of the cross section of various preoxidized and coked coupons of the tested materials.

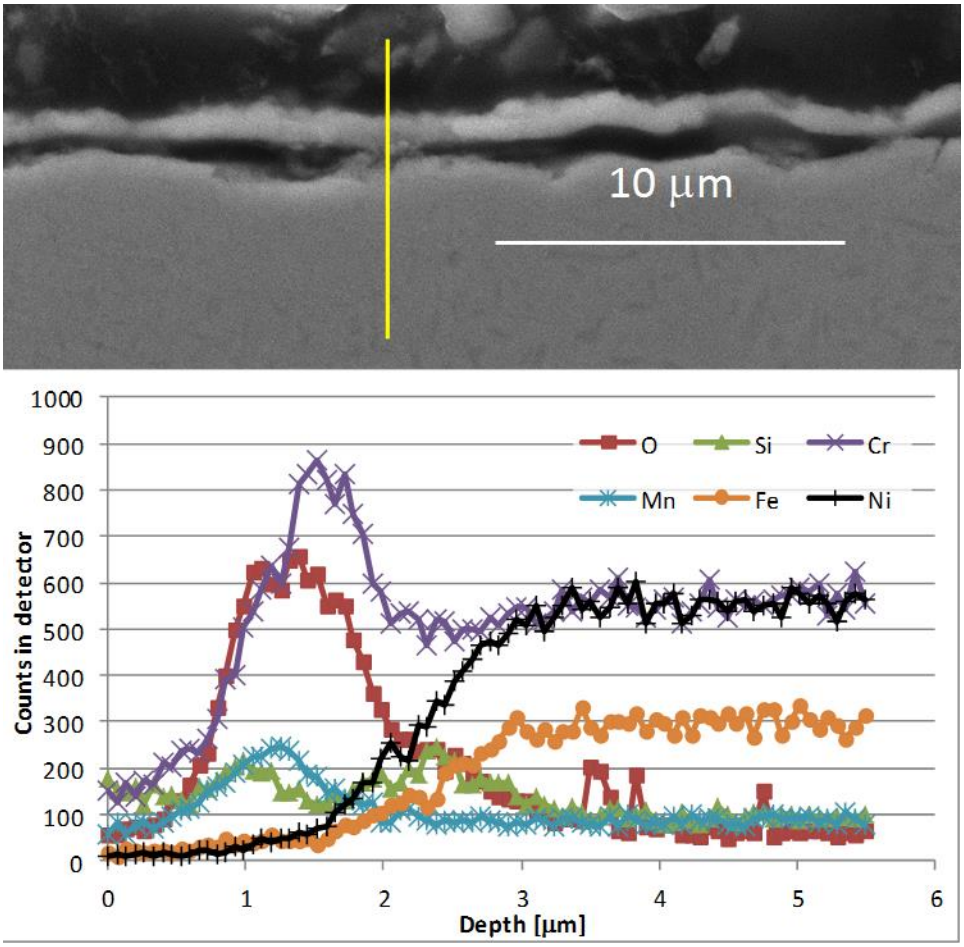

Figure B.12. Cross section of a preoxidized coupon of material C with the results of its EDX line scan

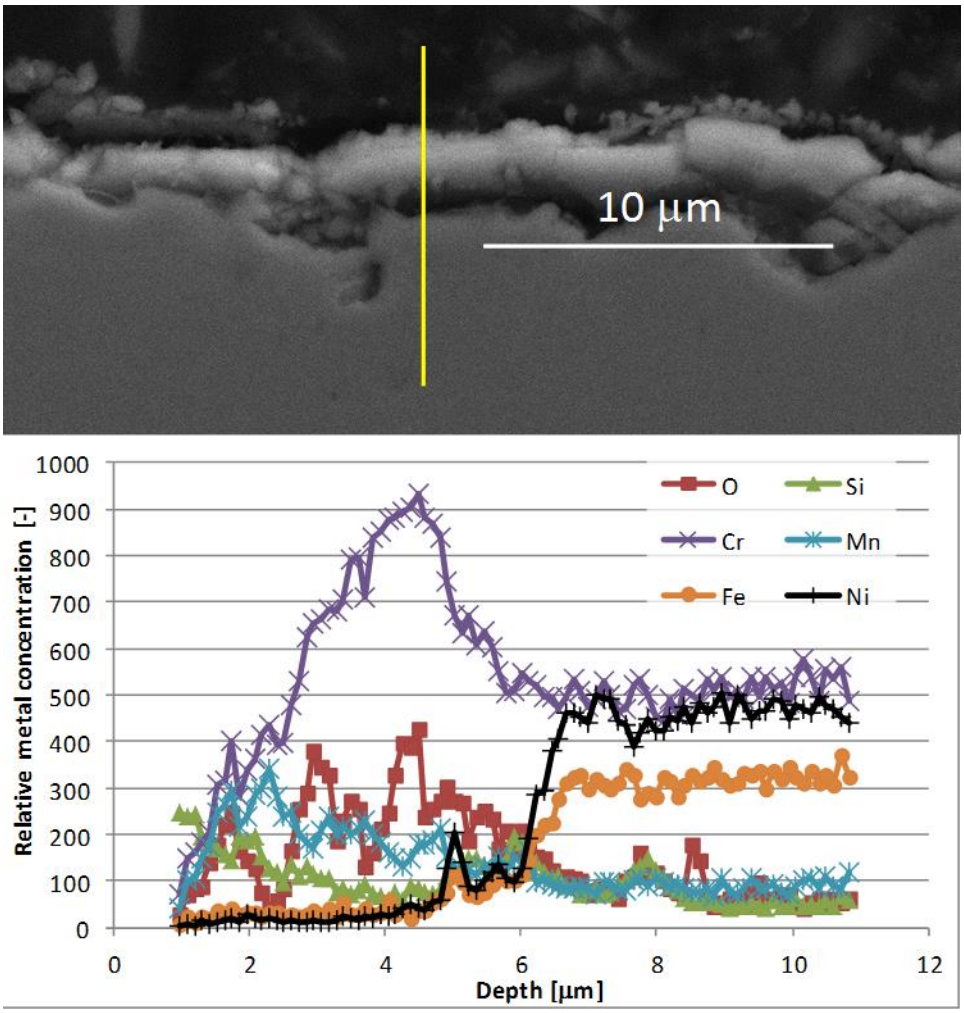

Figure B.13: Cross section of a preoxidized coupon of material D with the results of its EDX line scan

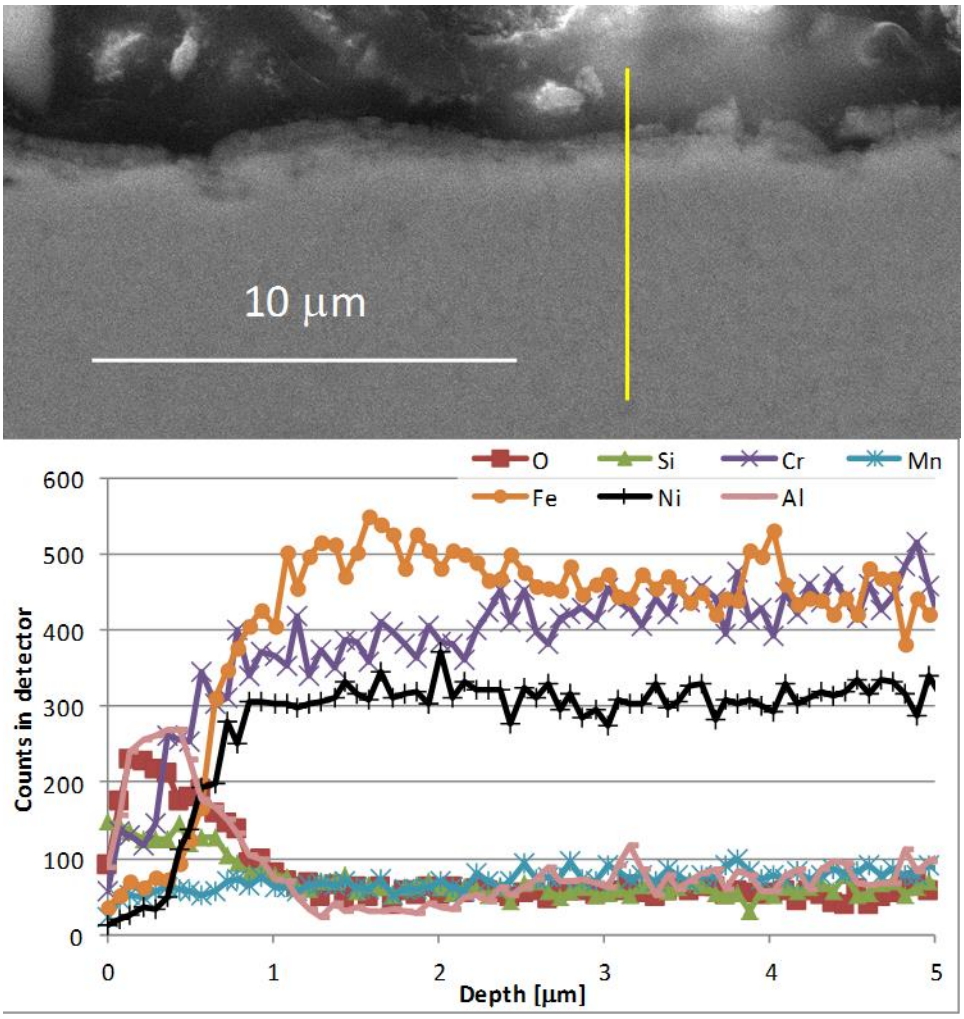

Figure B.14: Cross section of a preoxidized coupon of material H with the results of its EDX line scan

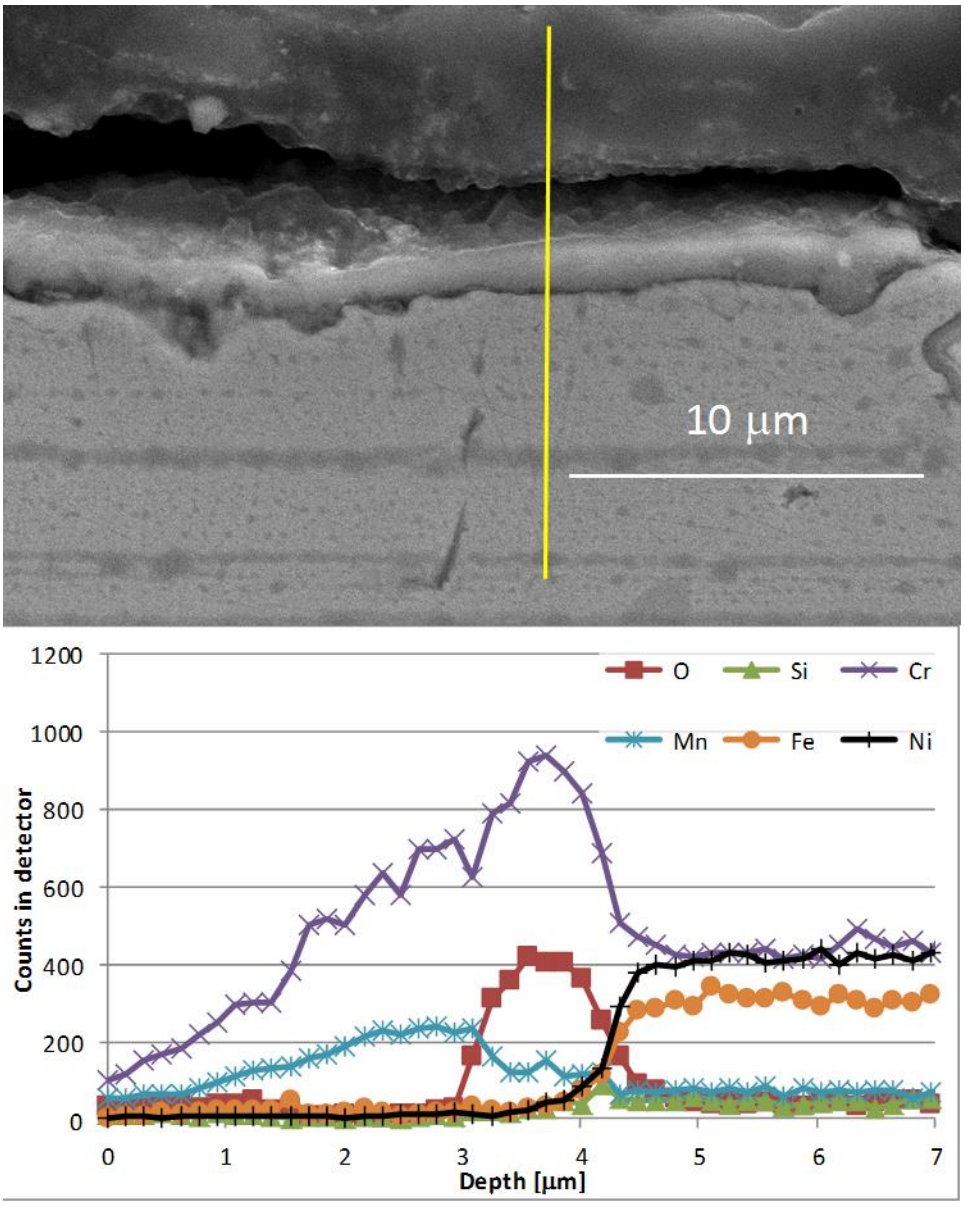

Figure B.15: Cross section of a coked coupon of material C with the results of its EDX line scan

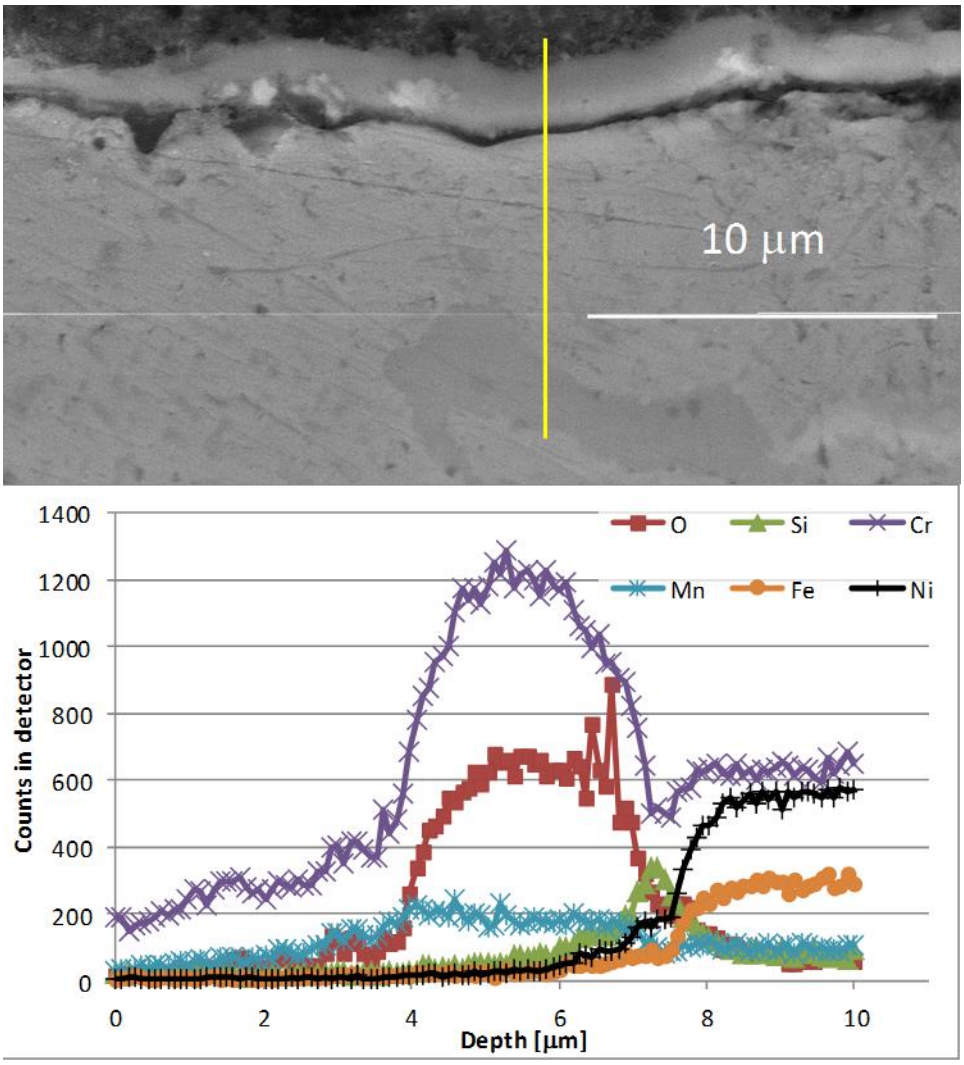

Figure B.16: Cross section of a coked coupon of material D with the results of its EDX line scan

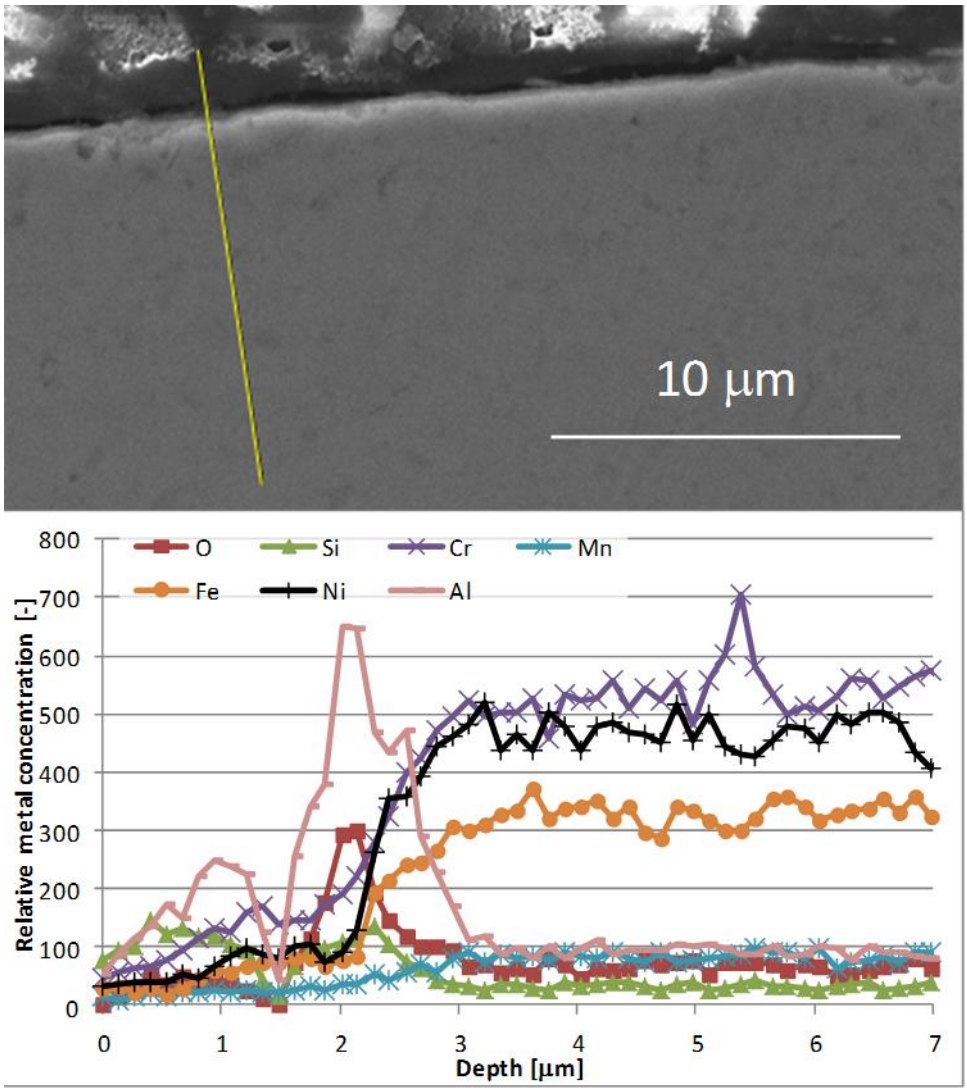

Figure B.17: Cross section of a coked coupon of material G with the results of its EDX line scan

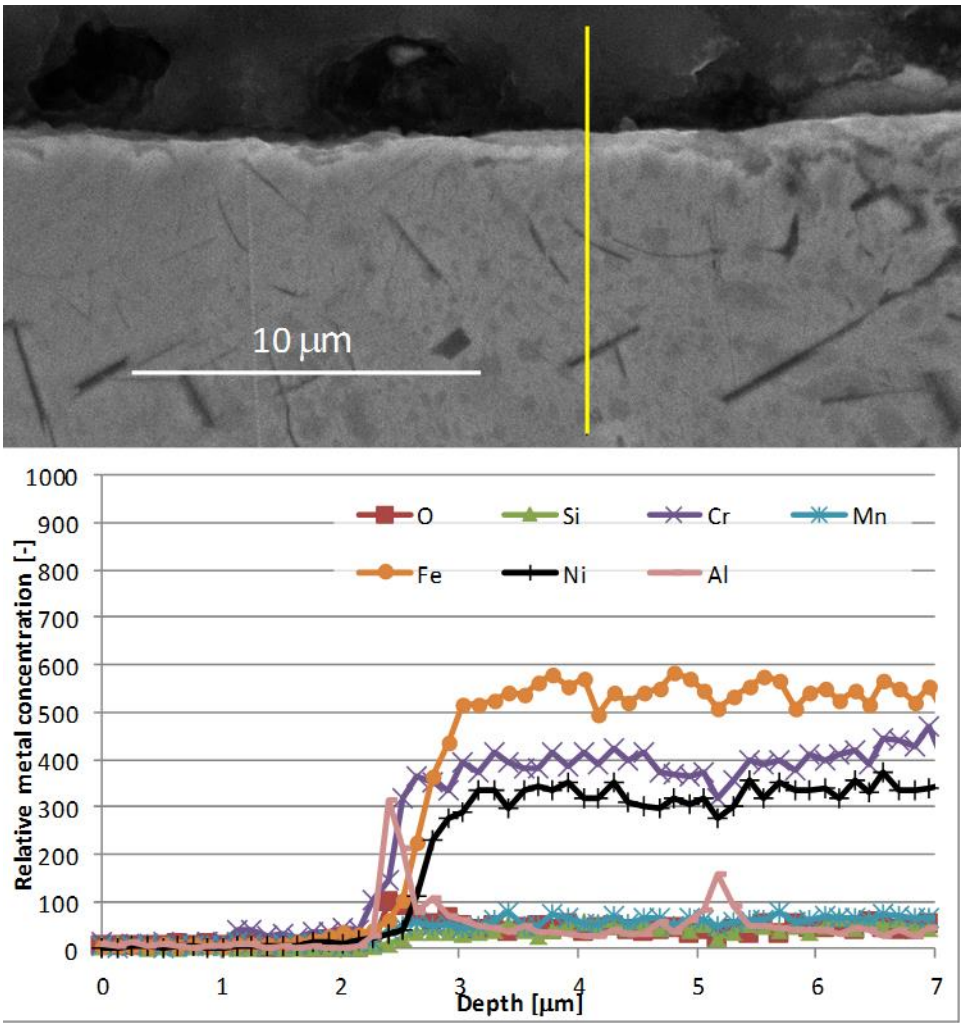

Figure B.18: Cross section of a coked coupon of material H with the results of its EDX line scan

Appendix C: Supplementary information to Chapter 5

C.1 Naphtha composition

Table C.1: Naphtha composition

Compound Name	Weight %
Isobutane	0.02
Cyclopentane	2.59
Hexane	13.27
3-methylpentane	5.82
Methylcyclopentane	4.02
2-methylpentane	10.40
2,4-dimethylpentane	0.10
Cyclohexane	1.29
Butane	1.64
2-methylhexane	0.20
2-methylbutane	24.42
Pentane	32.38
3-methylhexane	0.11
1,3-dimethylcyclopentane	0.05
2,3-dimethybutane	1.48
1,2-dimethylcyclopentane	0.03
Benzene	1.71
2,2-dimethylbutane	0.47

Table C.2: ASTM D 2887 Boiling point curve of the naphtha

Yield [wt %]	T [K]
0	266.5
10	294.3
30	308.2
50	317.1
70	330.2
90	347.4
100	388.9

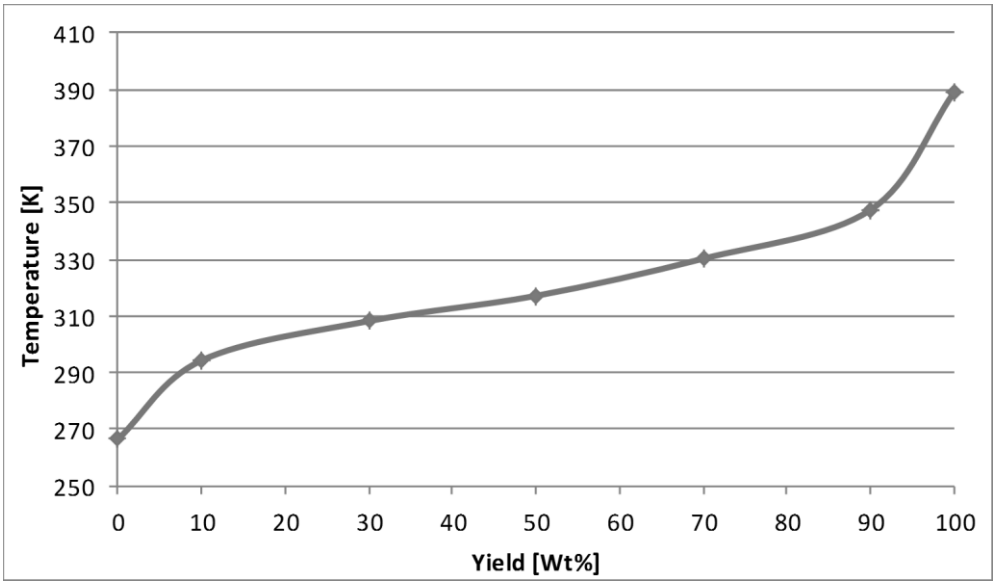

Figure C.1. ASTM D 2887 Boiling point curve of the naphtha

C.2 Reactor effluent

Table C.3: JSR effluent composition for naphtha cracking at T=1098 K, $\tau \sim 0.3$ s, δ=0.375 kg_{H2O}/kg_{C2H6}

Permanent gasses [C_0 - C_1]	**16.83**
H_2	0.79
CH_4	15.94
CO	0.09
CO_2	0.01
Light alkenes [C_2 - C_4]	**51.44**
Ethene	30.41
Propene	12.60
1-Butene	1.74
Iso-butene	1.77
1,3-Butadiene	3.07
Others	1.85
Light alkanes [C_2 - C_4]	**3.51**
Pyrolysis gasoline [C_5 – C_9]	**27.44**
n-pentane	5.94
i-pentane	4.19
n-hexane	1.86
Benzene	6.42
Toluene	1.00
Xylenes	0.11
Others	7.92
Pyrolysis fuel oil [C_{10} – C_{30}]	**0.78**
Naphthalene	0.57
Me-naphthalenes	0.21
Heavy paraffins	-
Heavy olefins	-

C.3 Coking rates

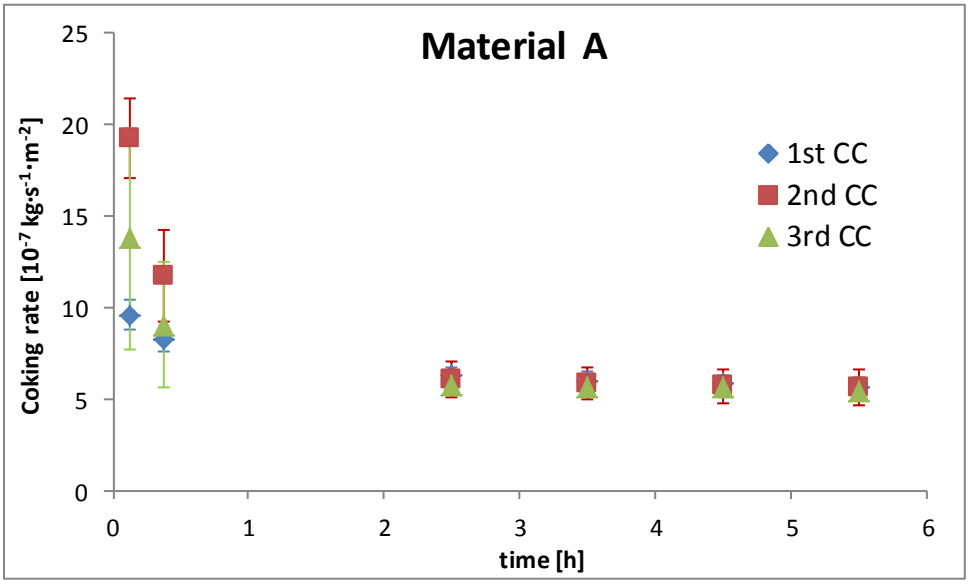

Figure C.2. Mean measured coking rate as a function of time for three consecutive coking cycles on material A during naphtha cracking at 1098 K in the electrobalance setup.

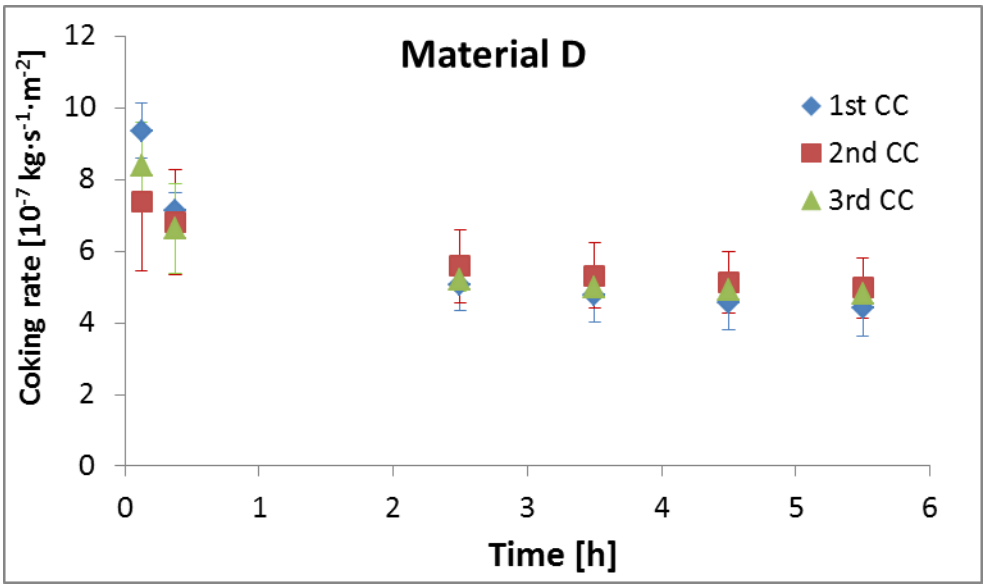

Figure C.3. Mean measured coking rate as a function of time for three consecutive coking cycles on material D during naphtha cracking at 1098 K in the electrobalance setup.

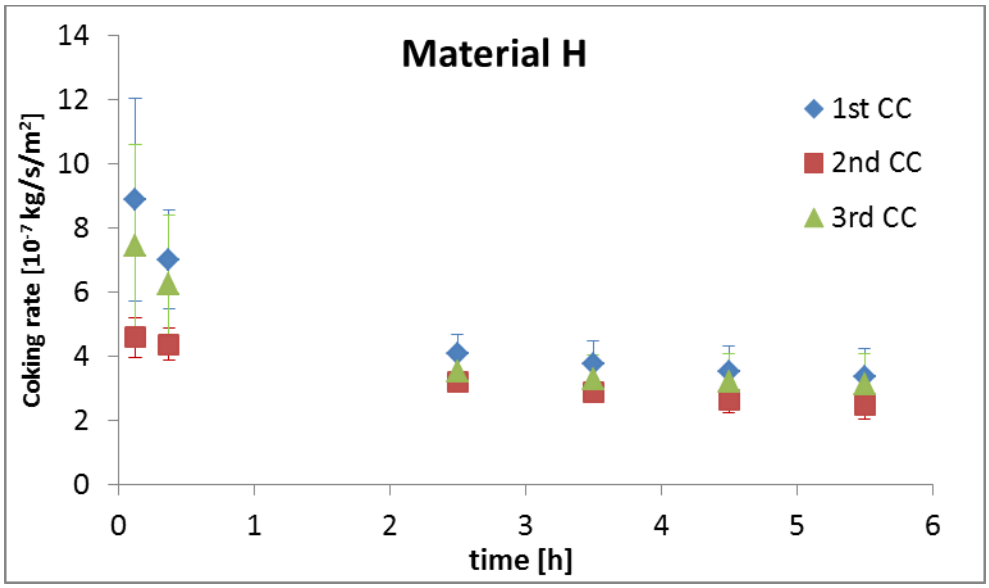

Figure C.4. Mean measured coking rate as a function of time for three consecutive coking cycles on material H during naphtha cracking at 1098 K in the electrobalance setup.

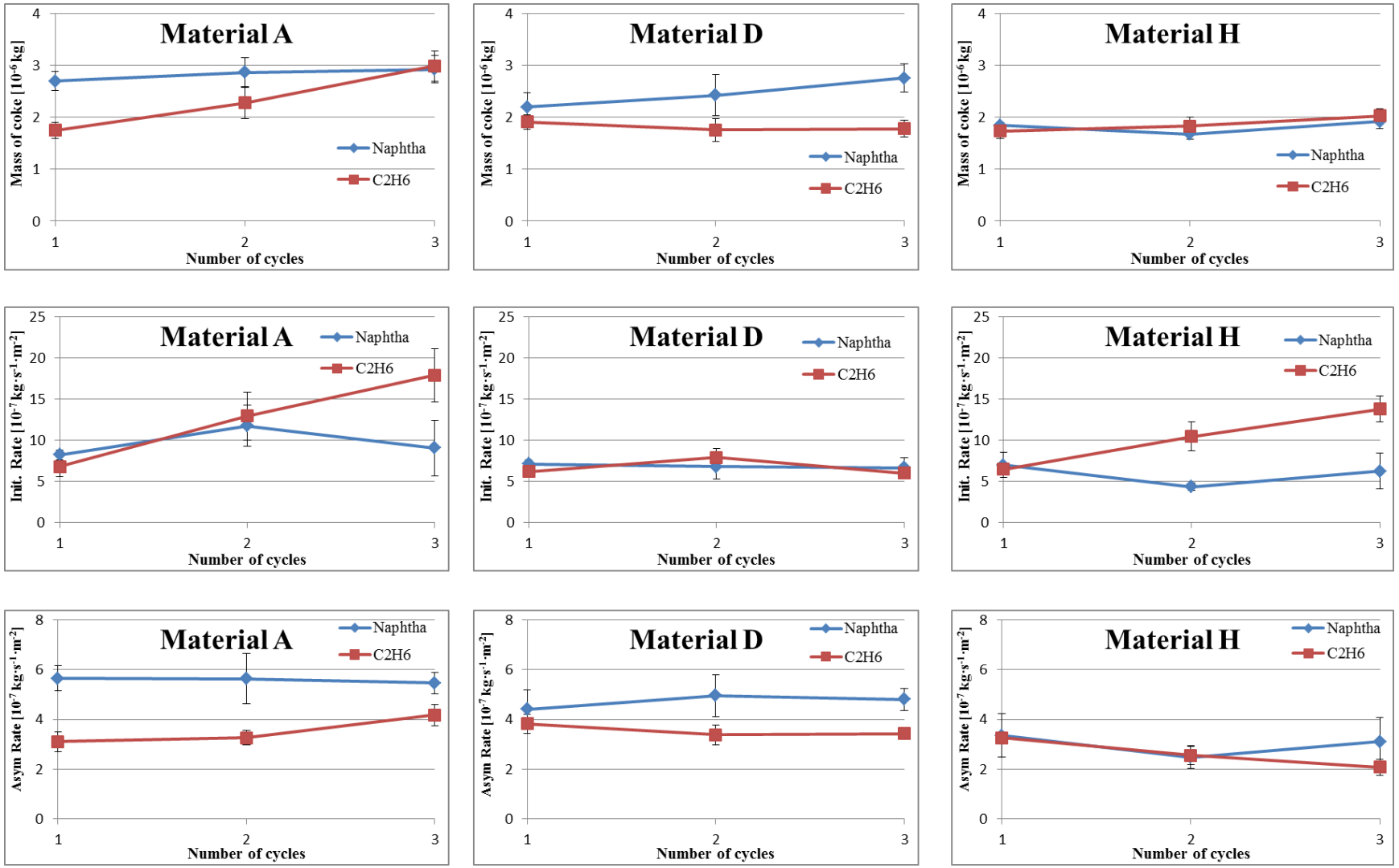

Figure C.5: Comparison of the mass of cokes, initial rate and asymptotic rate for materials A, D and H as a function of the number of coking cycles.

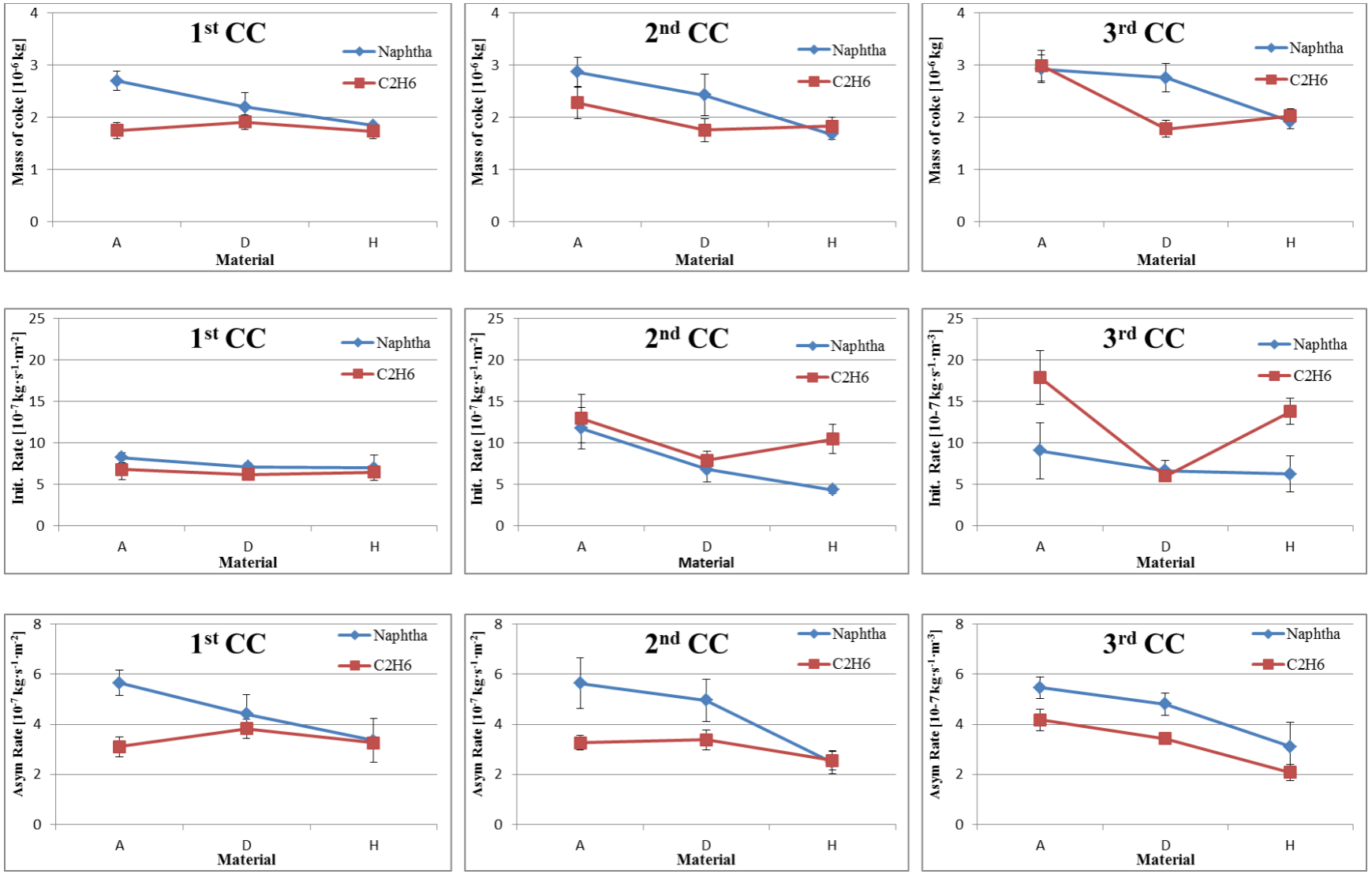

Figure C.6: Comparison of the mass of coke, initial coking rate and asymptotic coking rate for materials A, D and H for the first, second and third coking cycles, as a function of the tested material.

Appendix D: Brief explanation of Ekvicalc

Thermodynamic calculations were carried out in this work using Ekvicalc, in order to predict the composition of the surface of preoxidized and coked coupons. The elemental composition of the coupons determined by EDX is provided as input to the software, as well as the chemical composition of the gas phase to which the coupons are exposed. Temperature and pressure also have to be provided as input, since the Gibbs free energy is a state function. This software calculates the combination of species that minimizes the Gibbs free energy of the mixture, i.e. the most thermodynamically stable species at that particular pressure and temperature. The minimization routine is performed using the Lagrangian multiplier technique.

To clarify what this software does, the interaction between 1 mol of alpha-iron (Fe) and 1 mol of molecular oxygen (O_2) at 1000 K and 10^6 Pa is used as an example.

Once these species and their amounts are introduced to the program, all the combinations of Fe and O that could form if any reaction takes place are considered possible products: FeO, Fe_2O_3, Fe_3O_4, O and O_3. It is also possible that the original species are the most stable and, therefore, Fe and O_2 are also considered possible "products".

The Gibbs free energy of the mixture of all these products is minimized for the given pressure and temperature by iteratively correcting the number of moles of products. Obviously, these corrections are subjected to the constraint imposed by the mass balance of the elements involved.

In this example, minimization is achieved with 0.5 mol Fe_2O_3 and 0.25 mol O_2. The number of moles of all the other possible products is zero.

For simplicity, phases were not taken into account in this example. However, Ekvicalc considers also phase changes into its calculations: The alpha, delta and gamma phases of iron were also considered possible products, although the number of moles of these species after minimization was zero.